Propriétés électriques et optiques des nanofils uniques de silicium

Amit Solanki

To cite this version:

Amit Solanki. Propriétés électriques et optiques des nanofils uniques de silicium. Autre. Université de Grenoble, 2012. Français. NNT : 2012GRENY081 . tel-00846580

UNIVERSITÉ DE GRENOBLE

THÈSE

Pour obtenir le grade de

DOCTEUR DE L'UNIVERSITÉ DE GRENOBLE

Spécialité : **Nanophysique**

Arrêté ministériel : 7 août 2006

Présentée par

Amit SOLANKI

Thèse dirigée par **Noël MAGNEA**
codirigée par **Nicolas PAUC**

préparée au sein du **CEA Grenoble/INAC/SP2M**
dans **l'École Doctorale de Physique**

Propriétés Électriques et Optiques des Nanofils Uniques de Silicium

Thèse soutenue publiquement le **06 décembre 2012**
devant le jury composé de :

M. Henry MARIETTE
Directeur de recherche, Institut Néel, Grenoble, président
M. Georges BREMOND
Professeur, INL et INSA de Lyon, rapporteur
M. Philippe TORCHIO
Maître de conférences, IM2NP et Université d'Aix-Marseille, rapporteur
M. Taha BENYATTOU
Directeur de recherche, INL, Lyon, examinateur
M. Alain MORAND
Maître de conférences, IMEP-LAHC et Université de Grenoble, examinateur
M. Vincent PAILLARD
Professeur, CEMES et Université de Toulouse, examinateur
M. Nicolas PAUC
Ingénieur chercheur CEA, INAC/SP2M, Grenoble, co-encadrant de thèse
M. Noël MAGNEA
Ingénieur chercheur CEA, CEA Grenoble, directeur de thèse

Université Joseph Fourier / Université Pierre Mendès France /
Université Stendhal / Université de Savoie / Grenoble INP

Electrical and optical properties of single Si NWs

Amit Solanki

Doctoral Thesis

Director of thesis : Noël MAGNEA

Supervisor of thesis : Nicolas PAUC

Prepared at CEA Grenoble in

Doctoral School in Physics at University of Grenoble

ACKNOWLEDGMENTS

My days in CEA, Grenoble are very memorable, mainly due to all wonderful people that I have been able to interact with. It would not be possible to accomplish anything without contribution of many people whom I heartily thank for accommodating and acknowledging me in my efforts.

First and foremost, I would like to sincerely thank my advisor Nicolas. He has been a great mentor and I see myself extremely fortunate to be his first PhD student. I have learned a lot from his research experiences, unending stream of advices, and his remarkable intuition. It was his enthusiasm and supervision that resulted in this comprehensive work. His interest in science and strong inventive sense was very inspirational throughout my time working for him, making the research work intense, productive and fun. I really enjoyed and appreciated the vast number of hours spent toiling on the problems in lab together, all the lively discussions over the years and overcoming every obstacle to finally polishing this thesis to its completion. Most importantly he has a strong drive to ensure his students succeed. I am also really grateful for his continual support outside the lab. When I first arrived in France, being in a new country with no knowledge of the work, culture his friendly and professional support was something i could bank on. I have truly benefited from his simulation expertise and physics insight that greatly helped me with in all stages of this the PhD work.

The last few years has been an exciting journey, which is also due to the friendly colleagues in SiNaPS group. I am especially grateful to Quentin, Claude, Therese, Aurelie, Ludovic and Abhinav for making my stay enjoyable. I appreciate all interactions, discussions, and activities that I had with them. I am glad to have Quentin and Aurelie as friends and colleagues. They have been always there me whenever I need a help from them and were really fun to be with. I enjoyed the fruitful discussions with Claude and appreciate his dedication for research. Although I got know Therese well for shorter period then others, our time together was really enjoyable and I am very grateful for your endless endeavors for teaching me how to swim. It was a great pleasure working with Pascal and Ludovic who provided me the all the nanowires for all the experiments in the PhD. Thus honestly speaking they have the foremost contributions to the results attained by satisfying my endless list of different nanowire growths and thus giving me the freedom to test all the my ideas over time. During my tenure in the lab, Eric was particularly helpful, with his enormous expertise inseemingly any hardware, was a frequent source of relief whenever there was a need for custom tool or an informatics issue. He never seems to stop amaze me, it seemed every setup or concept could be realized as long as we had Eric ! I would also like to acknowledge the other Bassem and Guillaume who have been very helpful in their discussions and collaboration. This would surely have been a much much shorter thesis without them. I will cherish all the happy memories we had together.

I'm very grateful to my thesis director Noel and Lab head Emmanuel for their insightful discussions and support. Their fountain of knowledge on all things from physics to instrumentation vastly helped me by forecasting issues, vision of which problems need to be addressed, how to best go about solving them and the motivation behind them. I have matured a lot as a researcher owing to their insightful suggestions and generous supports in many aspects and the friendly personal interactions during the past couple of years. I would also like to thank Emmanuel for the very interesting lectures and asking appropriate questions which showed me how to convey ideas more clearly.

I was also given an exciting opportunity to spend few month in University of Sherbrooke in Canada working at the CR2N lab. I would like to thank Prof. Vincent and Prof. Dominique for their collaboration and invitation to visit Sherbrooke. Specifically I would like to thank Prof. Dominique for happily accommodating me in his busy schedule and teaching me EBIC. The short time I spent in Sherbrooke was worthwhile in every sense from learning new techniques to the opportunity of work outside Europe which I really enjoyed.

Lastly, I would like to thank my family and friends at home. My parents have always been a source of motivation. My success so far is solely due to their upbringing which instilled the importance of handwork and determination in me, also my younger brother and sister for always looking up to me giving me the strength to face any adversity and compelling me to continuously strive for the best. It is their care, love and faith in me that has pushed me so far and will continue to do so. I would like to thank them for always being supportive and providing me with so many wonderful opportunities throughout my life.

Contents

Part 1. Introduction 9

Chapter 1. Background 11

Chapter 2. The road to NWs : 3D to 1D 13
- 2.1. Si NWs 13
- 2.2. Engineering the NW growth and light absorption 24

Part 2. Doping of Si NWs 27

Chapter 3. Résumé 29

Chapter 4. Homogenously doped NWs 33
- 4.1. Challenges in doping of NWs 33
- 4.2. Electrical measurements 39
- 4.3. Diameter and axial dependence of doping 45

Chapter 5. NW growth with junctions 63
- 5.1. NW pin junctions 63
- 5.2. NW schottky diodes 63

Chapter 6. Conclusions 75

Part 3. Light absorption in single Si NWs 77

Chapter 7. Résumé 79

Chapter 8. Experimental setup & methods 85

Chapter 9. Photocurrent on single Si NW 89
- 9.1. NW photo-response 89
- 9.2. Theoretical interpretation 93

9.3. Tuning absorption: Diameter & polarization 104

9.4. EQE estimate: p-i-n coreshell system 111

Chapter 10. Engineering light absorption: Dielectric surrounding 115

10.1. Theory of light absorption in core-shell nanocylinders 116

10.2. Dielectric shell enhanced core absorption in core shell like NWs on a substrate 117

10.3. Quest for an ideal system: NWs and core shell structures in the air 134

Chapter 11. Conclusion 143

Part 4. Conclusion and Perspective 147

Part 5. Appendices 151

A Growth and methods 153

I CVD growth 153

II Nanofabrication 159

III Characterization 170

B NW Doping vs diameter 173

I K. Seo et al 173

II Uniform Potential Approach 175

C NW in polarized light 177

Bibliography 179

List of Publications 185

Part 1

Introduction

CHAPTER 1

Background

Since the advent of the industrial revolution in 17-18th century, the energy consumption in the world has been rising with current energy consumption rate greater than 132000 terawatt hours and increasing at the rate of 5% every year. This energy dearth is fueled by decreasing non renewable fuel sources such as coal, oil and natural gas. Further the environmental consequences of incessant use of non renewable fuel has pushed us to turn our focus on harvesting the renewable energy in the nature to our benefit.

One of the major sources of renewable energy is our Sun. The energy radiated by the Sun is above 7500 times the world's annual primary energy consumption of 450 exajoules[**1**]. Further the Sun can almost be considered as a perpetual energy source compared to our life scales. Thus serious efforts are being made towards harvesting this free energy with the help of photovoltaics[**2**], passive solar heating[**3**], or hydrogen fuel generation[**4**], etc.

The conversion from solar energy to electrical energy by photovoltaics/solar cells is currently the most efficient way to harvest solar energy. A typical photovoltaic cell consist of a semiconductor with p- and n-doped regions, where the junction between the two doped regions provides a space charge region. The absorbed photons creates photo-generated electrons and holes separated by the static electric field in this space charge region producing electrical energy. Thus in this way the free solar energy is converted into useful electricity. Majority of solar cells today employ some form of (crystalline or amorphous) silicon as the semiconductor material. Silicon with its band gap of 1.11 eV at room temperature is close to the energy maximum of solar energy spectrum radiated on earth. The band gap is an important criteria determining the energy efficiency since it determines the optimum wavelength for efficient light absorption in the semiconductor. In the case of Si, the photons with the energy below 1.11 eV are not energetic enough to be absorbed, whereas the photons with energy above the band-gap create high energy electrons which then thermalize and heat up the cell. Apart from the above losses due to the material absorption properties, the energy conversion efficiency is limited by internal recombination processes, resulting in non radiative electron hole pair recombination before separation by the junction. The upper bound for the conversion efficiency in silicon is reached when electron-hole pair lifetime is set only by the radiative recombination and is given by the Shockley–Queisser[**5**] limit at 33.7% for silicon single junction solar cells. Even so with the reduced cost and expertise in silicon processing due to its extensive use in the microelectronic industry, silicon still has majority of share in solar industry.

That being said, the bulk Si technology is reaching its limits on various fronts from microelectronics to photovoltaics. The standard CMOS structure with silicon dioxide as the gate dielectric reached its limits with the advent of 32 nm node by INTEL in 2010 where the quantum effects of charge tunneling through the gate oxide hindered further miniaturization. The photovoltaic technology follows a similar path with bulk Si solar cells already near the efficiency limits. As with the electronics industry a trend exists in the photovoltaic industry towards increasing the yields along with reducing the cost of solar cells. For this reduction in cost, the thin film technologies were sought and to increase the efficiencies, the light trapping mechanisms by nanostructuring were probed. An ideal architecture for solar cells would be one which does not reflects or transmits any light and in the process converting most of the absorbed light to electricity. Even maintaining the typical junction structure, one can play with the device morphology to have an efficient light coupling. Further nanostructuring from 2D films currently employed in industry to 1D NWs provides an extra degree of freedom to optimize light coupling in the solar cell. Such a system can be realized by arrays of NWs with predefined diameters where all the light is confined in the array by multiple internal reflections. Towards this, continued efforts are being made to optimize every aspect ranging from growth, designs, fabrication to packaging of solar cells. The several strategies sought for this purpose range from multijunction, tandem to up/down conversion solar cells for tailoring the absorption spectrum of the solar cell to match the solar spectrum. As an alternative route there are an effort put towards the improvement of the light coupling to the device (surface texturing, use of light diffusers, light concentrators, plasmonics, etc).

CHAPTER 2

The road to NWs : 3D to 1D

A majority of the current technological advances are being brought about by nanostructuring the semiconductor to increase the electrical and optical performance or reduce the cost of the system.

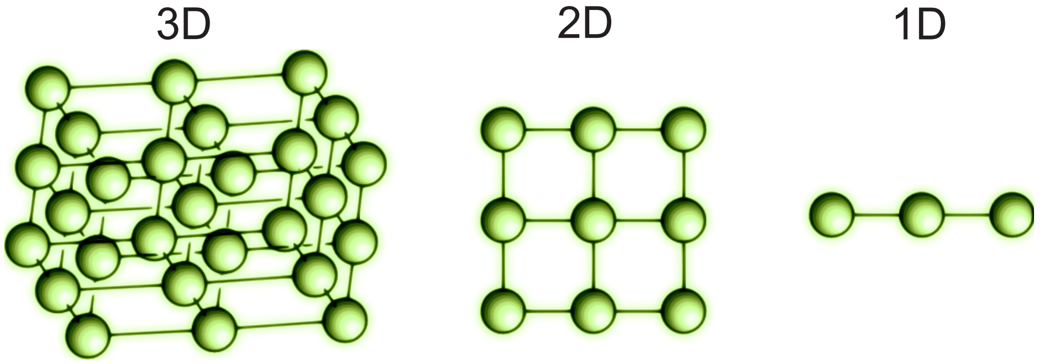

Figure 2.0.1. Schematic of 3D to 1D

When we go from 3-dimensional structure to 1-dimensional structure as in NWs we expose relatively more atoms to the surroundings/surface when compared to the bulk (see Fig 2.0.1), which results in an increase of the influence of the surface effects in a 1-D system. The ratio of the number of surface atoms to bulk atoms in bulk Si with x, y and z dimensions of 10μm is $\approx$0.00033 and for a Si film of 10 µm length and width with thickness of 100 nm thickness the same ratio is $\approx$0.011. Similarly for a NW of 10μm length with diameter of 100 nm the ratio is $\approx$0.022. This continuous increase in ratio depicts the relative gain in the influence of the surface phenomena, thus resulting in more dominant surface effects.

2.1. Si NWs

NWs are typically defined as quasi one dimensional structures with length dimension exceeding few micrometers and radius of a few tens of nanometers. In the last decade an explosion in NW related research has occurred due to the novel properties that nanostructuring and 1-D confinement has to offer. Actual 1-D confinement occurs when diameter of the NW is smaller than the exciton Bohr radius of the material (Si = 4.9 nm). In such a case, the quantum confinement of charge carriers in 1-D introduces new properties like ballistic transport, coulomb blockade and quantized conductance. Even in the case of quasi 1-D confinement, with the increase in the ratio of surface atoms to total atoms the surface increasingly plays an important role in charge carrier dynamics. These interesting properties provide enough reasons for studying the NW based devices even out of the quantum limit and thus make them the basic building blocks for the nanoscale research. Further interest has been fueled by the ease of fabrication of NWs by various bottom-up means as chemical vapor deposition (CVD), pulse laser deposition, template assisted growth and by top-down approach with reactive ion etching has led to their extensive proliferation in research.

The immense potential of NW has already been seen in research in various fields such as nanoelectronics, nanophotonics, photovoltaics, thermoelectric, sensors, etc. The typical materials that are grown/etched into NWs are endless starting from Si, Ge, InAs, GaAs, ZnO, GaN to Diamond. Among them, Si NWs enjoy a prominent place due to the success of Si in microelectronics and photovoltaics and the past century of effort in its study, making it one of the most well understood material.

There are various means for the synthesis of Si NWs by top down or bottom up approach. The top down approach provides better control on size, shape and positioning of the NWs whereas the bottom up approach provides more smoother NWs and more straightforward synthesis. The bottom up growth with vapor solid liquid mode predominates the other growth methods, mainly due to its ease of growth and the high density of NWs which can be obtained.

2.1.1. Si NW Growth: Bottom up approach.

The vapor solid liquid (VLS) growth starts with the deposition of a catalyst on a substrate (Fig. 2.1.1). The catalyst is normally Au but other metals like Al, Ag, Cu, Sn, etc have also shown a catalytic activity. Gold being a noble metal does not oxidize and further has a low temperature eutectic phase at 363 °C, which makes this catalyst the most used in the literature, see phase diagram in Fig. 2.1.2. The substrate is chosen carefully since the growth and orientation of the NWs greatly depend on it. A crystalline Si substrate with [111] orientation was used. The surface of the substrate is efficiently cleaned to remove any contaminants and surface native oxide, to have a nice catalyst interface with substrate and

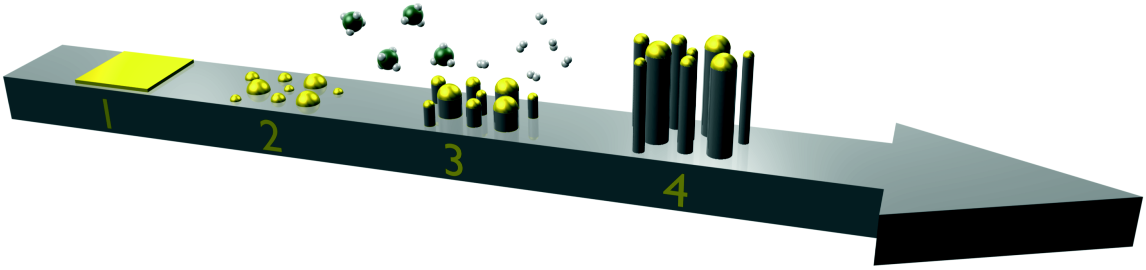

FIGURE 2.1.1. Schematic of VLS Growth of NWs. The step 1 shows the Au thin film deposited, step 2 shows the dewetting of the film after annealing, step 3 shows gaseous precursors cracked at the surface of the catalyst with epitaxial Si deposition below the catalyst and the last step shows the NWs finally obtained after growth.

to aid epitaxial growth for obtaining crystalline NWs. A schematic of the VLS process is shown in Fig 2.1.1. The 1-5 steps marked on the schematic suggest different process steps performed for the growth which begins with catalyst deposition (by thin film or colloids), then heating of chamber to form catalyst droplets followed by introduction of gaseous precursors resulting in NW growth. The growth can be performed in LPCVD, PECVD or other means. For high quality Si NWs, usually growth in LPCVD reactors is preferred due to lower contamination. The CVD chamber is heated higher than the eutectic temperature between the gold and Si to have both catalyst and silicon in liquid state.

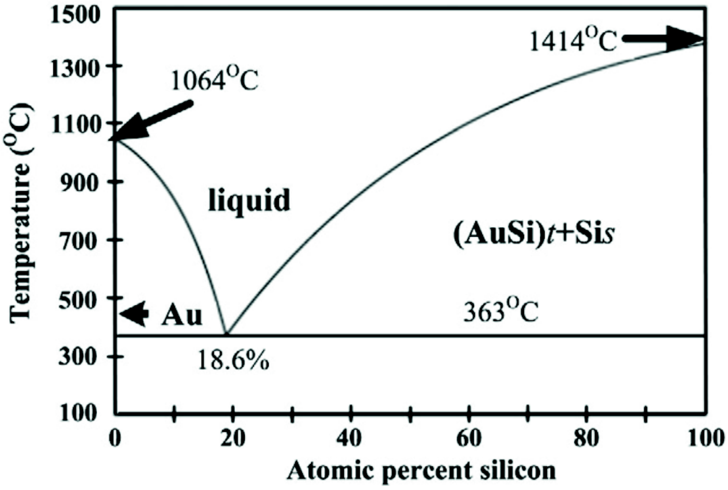

FIGURE 2.1.2. Eutectic diagram of Au-Si. Adapted from Ref. [6]

The growth begins with the nucleation and ripening of metal catalyst at the growth temperature. This step is followed by diffusion and decomposition or cracking of Silane on the catalyst. The incorporation of Si in catalyst proceeds until the catalyst is saturated and with further supersaturation the Si starts to precipitate at the base of the catalyst. As the catalyst releases this excess Si at its base, the Si recrystallizes epitaxially on the crystalline substrate forming a NW. The growth of the NW proceeds as more and more Si is expelled in NWs, which simultaneously lifts the catalyst droplet aiding the NW growth.

This mode of NW growth has a distinct advantage of ease of fabrication of heterostructures or junctions. The growth mode can also be easily switched between the 1D axial growth and 2D growth regime which makes it easy to obtain axial junction or radial junction in NWs. Also by switching of dopant gas or primary material gas e.g. Silane to Germane, various core shell and axial regimes can be obtained.

2.1.2. Si NW Growth: Top Down approach.

The top down approach of the NW fabrication relies on the etching of a Si substrate to yield NWs. Typically crystalline Si substrate is patterned by lithography or by other means to obtain small exposed areas on the surface masked by a metal. This can be followed by electroless etching technique to obtain a high density of NWs. Another technique is to use reactive ion etching to etch patterned NWs on Si substrate. A schematic of such a technique is shown in Fig. 2.1.3.

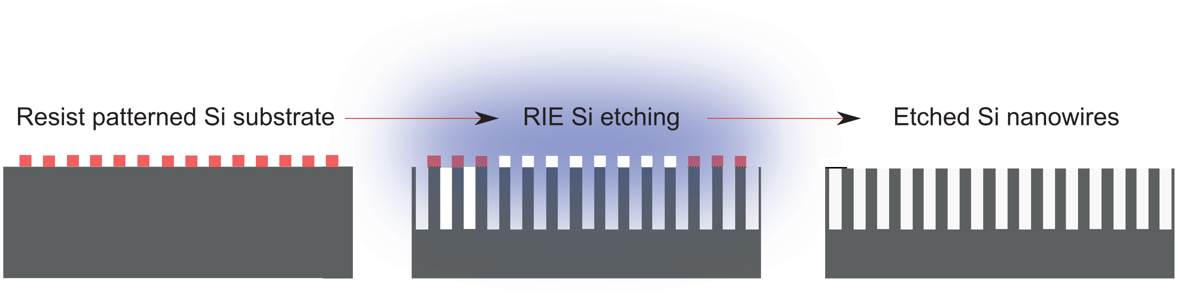

FIGURE 2.1.3. Template assisted Growth

In the top down approach it is easier to control the doping and contamination and crystal orientation of the NWs since high purity [111] or [100] oriented crystalline Si wafers can be used for etching as required.

2.1.3. Si NW Applications.

The NWs have various potentials ranging from field effect transistor, single electron devices, sensors, thermoelectric, solar cells. Their applications in nanoelectronics primarily arise from the nanoscale dimension, ease of fabrication of heterojunction and doping modulation. NWs are very promising in sensing application due to their enhanced surface to volume ratio which makes electrical properties highly dependent on the surrounding medium. A change in surrounding medium triggers a significant modulation in the charge carrier properties, thus making them ideal candidates for sensing. The surface roughness of NWs inducing strong phonon scattering dramatically drops the phonon conduction while keeping a reasonable level of electrical conductivity, making these structures extremely promising for thermoelectric applications. Their nanoscale geometry and light trapping properties have shown applications in the field of nanophotonics. A significant advantage of NWs is in their growth which can be performed on almost any type of substrates, as long as it can sustain the growth conditions, ranging from silicon wafers to glass[**7**] to for instance steel[**8**].

The current limits to inclusion of NWs in photovoltaics arise from the efficient growth and doping engineering of NWs and increasing the light absorption in NWs. For this, one needs to modulate the doping in the NWs to obtain devices with junctions (both axial and radial) where intrinsic field induced charge separation is done. Further, the study of the light-matter interaction at nanoscale in NWs is indispensable to understand how different photons with different energies interact with the NWs with different size parameters. Towards these goals several works were already published. The next section sums up a few of them in order to highlight the problems for the integration of NWs in solar cells

2.1.4. Si NWs from growth to solar cells.

In this section we briefly trace some historical steps dealing with the various difficulties, novel growth and fabrication techniques to the most recent advances in the field of doping of Si NWs and their use as photon to current converters in connection with the scope of this thesis.

The interest in the NW community was reignited by the highly cited work by Morales and Lieber[**9**] on the growth of various diameters Si and Ge NWs by laser ablation method. They presented Si NWs with nice crystalline core, albeit the NW was surrounded by a thick layer of SiO_x shell by this approach(see Fig 2.1.4I). The other methods such as CVD VLS

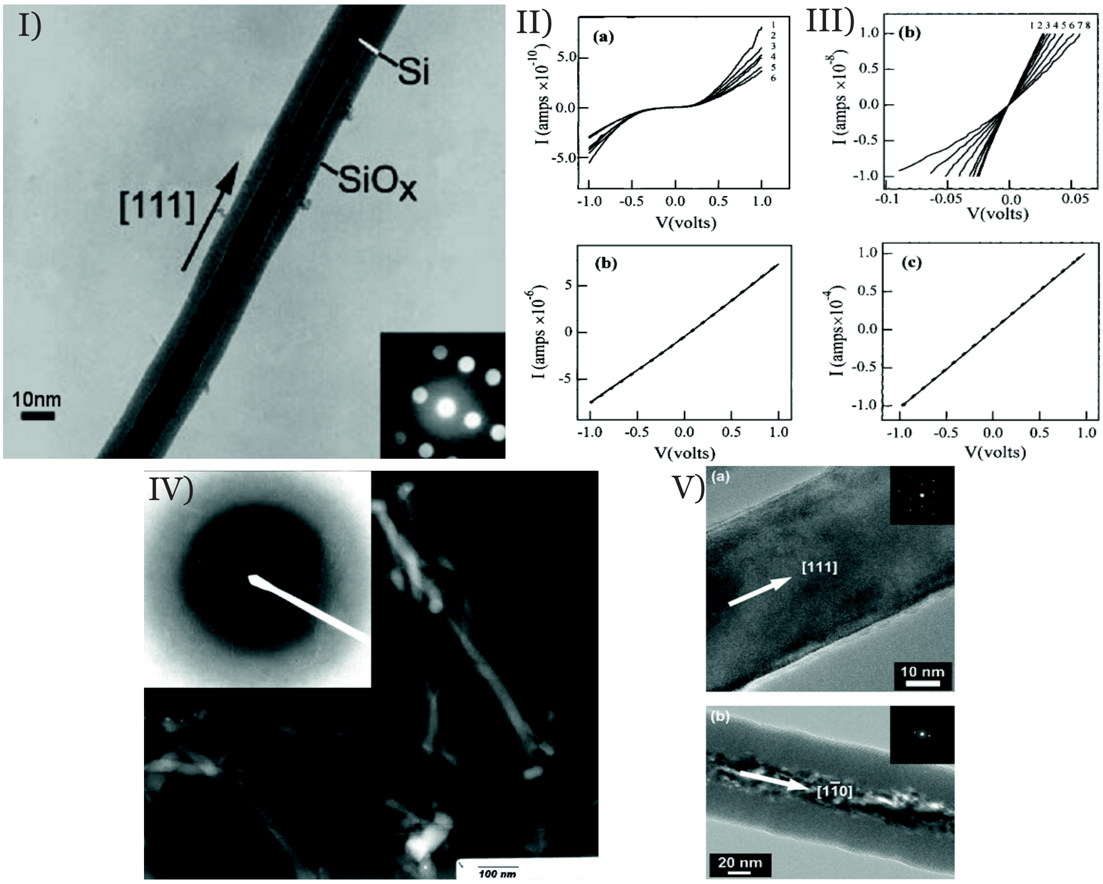

FIGURE 2.1.4. Growth and doping of Si NWs. I) Si NW with SiO_xshell[9] II) Id-Vg curves for 20V to -30 V in a) and I-V in b) on phosphorous doped NWs[10] III) Id-Vg curves for -30V to 30 V in a) and I-V on boron doped NWs[10] IV) TEM on boron doped NWs and inset showing diffraction pattern signifying amorphous NWs[11] V) TEM on Si NWs grown with TMB in a) and diborane in b) as boron precursor.[12]

growth did not show such thick shell of oxide and thus were extensively used for the NW growth. The electrical measurements on undoped Si NWs grown with CVD VLS method showed a p-type behavior with NWs being highly resistive making it unusable for fabricating devices as bulk Si (see [13]). Therefore doping incorporation was studied in the Si NW by different dopants such as boron, phosphorous, etc. The investigations of Y. Cui et al[10] (see Fig 2.1.4III,IV) show first studies on boron and phosphorous doping in Si NW confirming the possibility of dopant incorporation in VLS growth. In the literature there are various reports on the difficulty of obtaining a perfectly crystalline NW for boron doping using B_2H_6 gas, which shows either an amorphous shell (see Fig. 2.1.4V) or faceting on the entire NW. An alternative dopant recipe with trimethylborane was also studied and the amorphous shell was avoided in this case but the doping efficiency is reduced drastically making it very difficult to obtain high doping values[**12**]. With modification of the precursor partial pressure along with the use of chlorine recipe above mentioned problems can be easily countered[**14**].

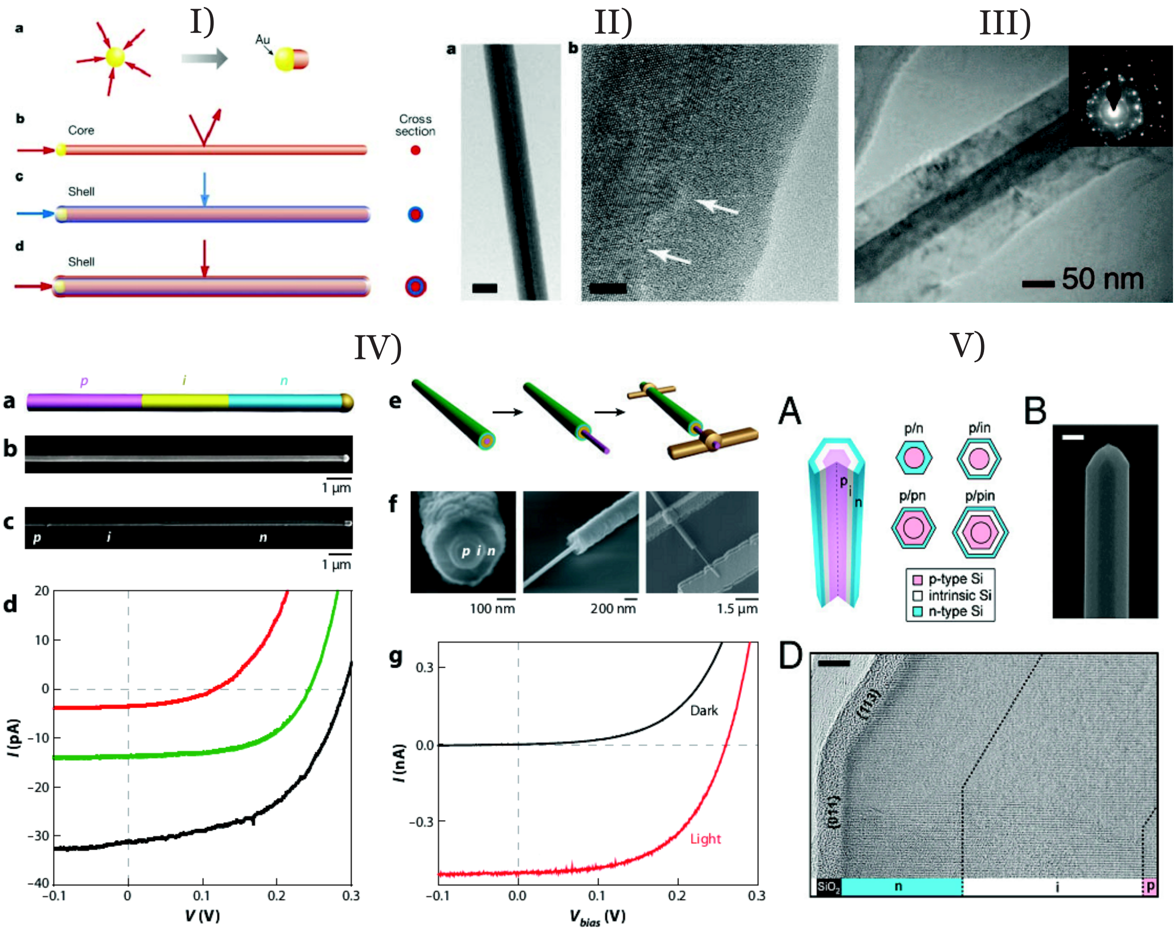

FIGURE 2.1.5. Axial and radial junction Si NW junctions. I) Shows the growth process for radial core shell junction in [**15**] II)TEM on Si NWs with amorphous shell[**15**] III) The core shell NWs with amorphous boron doped shell. The core was grown using electroless etching and boron doped shell was deposited by CVD[**16**] IV) pin axial and radial NWs and their I-V properties in dark and under illumination showing photo current[**17**] V) A pin core shell NW grown in CVD with both crystalline core and shell[**18**].

With the p and n type doping readily available, different types of radial and axial pin junctions were fabricated in NWs. The core-shell geometry of NWs was the easiest one to obtain as a simple switching of the preferred growth mode from 1D VLS to 2D growth by changing the process parameters results in the core shell geometry. The schematic of this process is shown in Fig 2.1.5I[**15**]. A Transmission Electron Microscope (TEM) image of as grown core shell NWs is shown in Fig. 2.1.5II. The core of the NW is grown with undoped silicon by VLS and thus shows a crystalline core, whereas the shell of the NW under 2D growth parameters (low growth temperature) formed an amorphous shell which could be crystallized by subsequent annealing. The further details can be seen from [**15**]. An alternative p-n core shell NWs grown by Garnett et al.[**16**] is shown in Fig 2.1.5III where an electroless etching technique was utilized to obtain the n-type crystalline core followed by the CVD VLS deposition of the p-type shell. Later, studies on axial doping of NWs has been performed by Kempa et al.[**18**], by growing pin axial junctions with crystalline p, i and n regions shown in Fig 2.1.5IV (left half)[**19**] and the core-shell p-i-n NWs with p doped cores and n doped Si shells are shown in Fig. 2.1.5IV (right half) by Tian et al[**20**]. The axial and radial NW shows excellent rectifying behavior with considerable photocurrent on illumination which can be seen in Fig 2.1.5IV(lower half). Further progress was obtained in growth with pin core shell NWs with polycrystalline shells instead of amorphous shell as observed previously in the literature. Recently the core-shell p-i-n growth has also been optimized to obtain mono-crystalline n-doped Si shell (see Fig 2.1.5V[**18**]).

The understanding in the growth and doping of Si NWs progressed and with continued interest in Si NWs, the efforts were then directed towards investigating the light absorption in NWs. The preliminary measurements were performed by Kalzenberg et al.,[**21**] on microwires (see Fig 2.1.6I). They observed results comparable to thin film coherent/incoherent absorption ascribing the observed photocurrent spectrum to Fabry-Pérot interferences which are function of the thickness of the slab (Si NW in this case). As one reduces the dimensions of the NWs, different resonances form in the NW depending on polarization and the angle of incidence. The first reports on light absorption in NWs were published by Cao et al.[**22**] on Ge NWs. The representative results on Ge NWs are shown in Fig 2.1.6II with various peaks observed in the absorption spectra of the NWs. They explain the presence of the peaks as resonances arising from efficient/resonant light coupling in the NW core for particular wavelengths which they ascribe to leaky mode resonances. The resonance in the NW have also been explained by the same authors including Mie theory in their later work on the light absorption in Si NWs[**23**]. For photovoltaic applications it is more desirable to work with pin junctions where the high intrinsic fields between the p and n-type

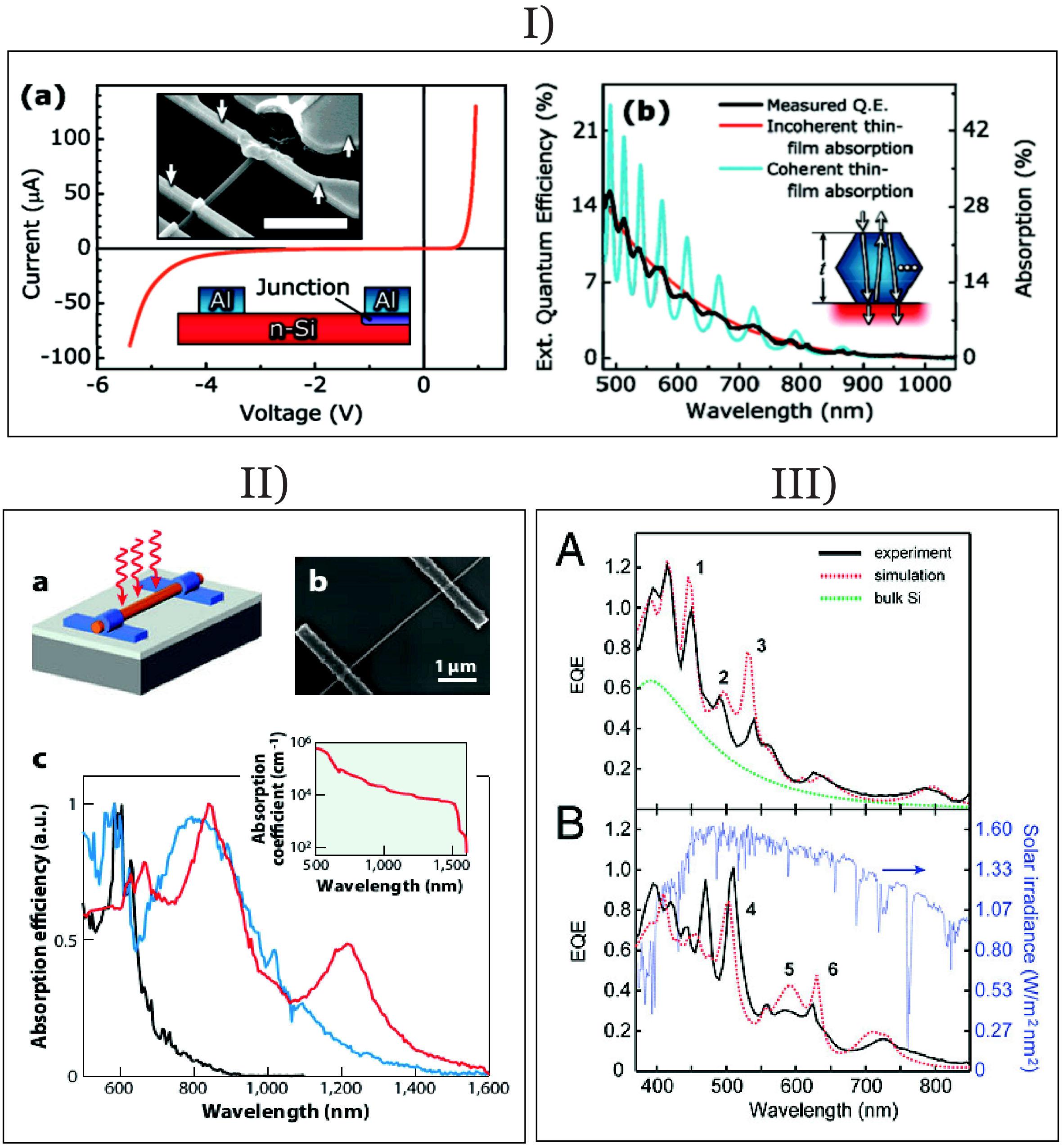

FIGURE 2.1.6. Light absorption in Si NWs: I) I-V and EQE measurements on thick Si NWs[21] II) Light absorption studies on Ge NWs[22] III) Light absorption studies on pin core shell Si NWs[18]

semiconductor enhances the charge carrier separation. Addressing the above point, there are recent reports on the study of light absorption in pin core-shell Si NWs (2.1.6III). The core shell NWs also show the presence of resonances in their absorption spectra with external quantum efficiencies exceeding 100% at many resonances. The light absorption spectra is well reproduced by the simulations (see Fig 2.1.6III) and the high efficiencies obtained can be used for energy harvesting in photovoltaic applications. Further the NW absorption efficiency is much higher in comparison with the bulk Si absorption making them more efficient light absorbers than bulk Si.

Although we will limit ourselves to the light absorption measurement on single Si NWs, an array of Si NW is more practical for solar cell applications than the single Si NW case. Thus it is important to have an overview of the absorption gain in arrays of NWs compared to the other PV technologies, for e.x. thin film solar cells. The Fig 2.1.7I shows the comparison of light absorption between the Si thin film, Si NW and Si nanocone absorber. The details about the data can be obtained from [**17**]. In all the plots the absorption of the NW based solar cell out performs its thin film counter part. The NWs and nanocones in their studies were fabricated by reactive ion etching of the amorphous Si film grown by CVD growth. The authors conclude the gradual reduction in effective refractive index between the amorphous Si substrate and air for the nanocones and NW as the reason for the enhancement. The Fig 2.1.7III shows the enhancement in light trapping by NWs[**26**]. The authors start with 7.5μm thick Si window and perform reactive ion etching to obtain the 2μm and 5μm long NWs. The light transmission through the 2 μm long NWs, 5 μm long NWs and 7.5 μm thin-film layers are compared to give the readers a clear picture of the enhancement in light trapping. The planar sample transmits almost 50% of the light at higher wavelength in the infrared whereas maximum transmission through NWs with 2 μm length is limited to ~10% at the longest wavelengths, with the 5 μm long NW showing negligible transmission throughout the spectral region of interest. They achieve energy conversion efficiencies up to 6% on their etched NWs which they attribute to light trapping in the NW arrays. The Fig. 2.1.7III shows theoretical analysis of light absorption, transmission an reflection in array of NWs of 2.33μm and are compared to thin film Si of same thickness. A significant increase in absorption is observed in NWs compared to bulk for higher energies from 2.5-4eV. Finally Fig 2.1.7IV shows the experimental comparison of light absorption in CVD VLS grown Si NWs on glass and Si substrate compared to light absorbed by Si wafer and thin film of Si on glass. In their work NWs were grown by using Helium and Silane precursor gases along with diborane or phosphine as dopant gases with similar growth processes used for growth on mono-crystalline Si and glass.

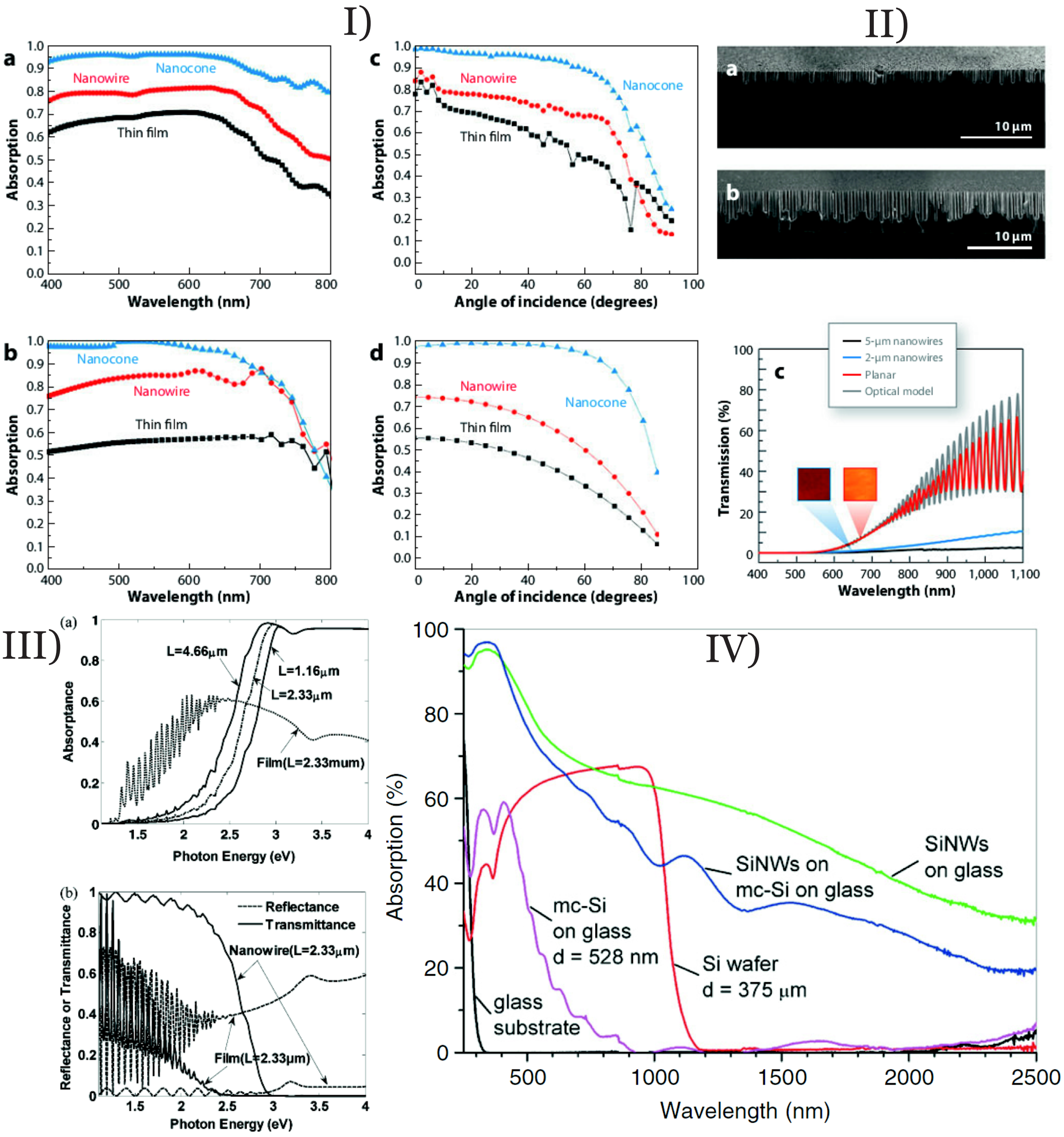

FIGURE 2.1.7. Si NW solar cells. I) Comparison antireflective properties of amorphous Si NWs, nanocones and thin film substrates with a) and c) as measured, b) and d) as simulated plots.[17] II) Comparison of light transmission through a 2μm, 5μm long etched network of NWs with respect to 7.5μm thick crystalline Si film[17] III) Reflectance and transmittance of 2.33 μm long NWs compared to same thickness of Si film[24] IV) Optical absorption of Si NWs on a glass substrate and on mono crystalline Si on glass compared to the absorption of a 375 μm thick Si wafer. [25]

The major objective of our work involve engineering the Si NW growth and doping to make NW junction and to study and engineer the light absorption properties in single Si NWs.

2.2. Engineering the NW growth and light absorption

In this section of the thesis we will discuss the challenges in the doping process using phosphine and diborane for n- and p-type doping respectively. Further we investigate various doping processes in NWs with and without HCl to eliminate the gold diffusion on the surface of NWs in order to limit its elemental contamination. This step is followed by the study of the variation of the resistivity along the NW. In particular we will analyze the problem of the surface doping which can be detrimental to the growth of axial junctions. We complete this study by the dependence of the dopant incorporation and activeness of these dopants on the diameter of the NWs. In the end, we obtain an abacus showing the relation between the apparent wire resistivity and the doping conditions used for the growth which can be readily used for engineering junctions in various configurations as p+i, n+i, p-i-n axial, p-i-n core-shell.

Once the optimum junction configuration is chosen, the next step is to build up an understanding of the free carrier diffusion in the NWs. This is done by Electron Beam Induced Current (EBIC) characterization technique. Finally the optimum device configuration is chosen with reasonable metal-semiconductor contact properties for a good rectification behavior providing utmost photocurrent.

The understanding of the light absorption processes in single NWs is vital for application of NWs in solar cells. The single NW junction fabricated in the previous section efficiently separate the carriers when the junction is illuminated by the light. In this second part, we want to address the question of the absorption efficiency in the Si NWs that we grow at the laboratory, using the built in electric field of NW junctions. As we will see in our study we are capable of performing photocurrent measurements on single NW junctions contacted by lithography. The photocurrent spectrum obtained is then normalized by light intensity to obtain the light induced photo-response of the NW. This photoresponse is closely related to the absorption spectrum of the NW. We used an existing theoretical framework to offer an understanding of the absorption and resonant processes at stake in NWs. We will examine in detail the light harvesting properties of our solar cells and examine the geometrical control of the light absorption by NWs. In particular we will try to answer a fundamental question related to the performance of these devices as efficient photon to electron converters, with an estimate of the external quantum efficiency of a core shell pin structure. In the later half of this part, we oriented our efforts towards the development and the study of strategies aiming at improving even more the efficiency of the light absorption in NWs through the deposition of a dielectric shell, which constitutes a step forward for the field of NW based solar cells.

Part 2

Doping of Si NWs

CHAPTER 3

Résumé

Cette partie s'intéresse à l'étude du dopage de type p et n dans les fils de silicium qui est un pré requis nécessaire à l'élaboration de nanofils à jonction qui seront utilisés dans le chapitre suivant.

Nous commençons cette étude par une brève revue bibliographique des réalisations de nanofils de silicium dopés et nous attardons sur le cas le plus controversé du dopage par le bore. Aux fortes compositions du mélange réactif en diborane, et dans les atmosphères et température de croissance usuellement rencontrées pour la synthèse VLS, une épaisse coquille de silicium amorphe est observée à la surface du fil, préjudiciable à une connexion optimum et concourant à rendre le fil très résistif. Nous proposons dès lors d'incorporer dans le mélange réactif du chlorure d'hydrogène, dont les bénéfices certains en terme d'inhibition de la diffusion du catalyseur et de planéité de la surface du fil ont été démontrés par le passé par notre groupe pour le cas intrinsèque.

En ce qui concerne la morphologie, l'adjonction d'HCl aux recettes de croissance de fils dopés permet d'obtenir des surfaces lisses, dépourvues de dents de scie, et réduit considérablement la croissance non catalysée et la diffusion de l'or depuis le catalyseur, non seulement pour le dopage n (phosphore) mais aussi p (bore). Les fils obtenus sont ainsi beaucoup moins coniques sous chimie chlorée, toute autre condition expérimentale étant constante (température notamment). L'analyse structurale par microscopie électronique en transmission montre que les fils dopés fortement au bore sont cristallins et dépourvus de coquille de silicium amorphe. L'aptitude du chlorure d'hydrogène à stabiliser le catalyseur en bout de fil, ainsi que l'inhibition de la croissance non catalysée sous cette atmosphère permet d'augmenter la fenêtre en température accessible à la synthèse des nanofils à 650°C dans notre cas, concourant certainement à recristalliser toute couche de silicium amorphe et à obtenir une structure peu conique cristalline.

Des mesures de résistivité par la méthode des quatre contacts ont été entreprises sur les nanofils p et n ainsi synthétisés, et peuvent être étendues à l'ensemble de la longueur du fil grâce au dépôt d'un peigne de 16 électrodes. L'expérience menée sur un fil dopé n et non conique montre que la résistivité varie linéairement par rapport à l'axe de croissance, avec un pied de fil moins résistif que la région proche du catalyseur. Nous avons alors approfondi l'étude de l'influence de la morphologie du fil sur sa résistivité apparente et étudié des échantillons où les conditions de croissance en chimie chlorée inhibent à un degré moindre la conicité, ceci permettant d'avoir à disposition des nanostructures où l'effet de la position axiale et du diamètre peuvent être sondés. Nous montrons que la dépendance axiale de la résistivité se retrouve pour les deux dopages. Nous montrons que lorsqu'une surface 2D crue sans catalyse or est exposée à une atmosphère dopante, typique de celle des fils dopés, puis enterrée dans une autre couche supérieure non dopée, une couche delta dopée est alors synthétisée à l'interface des deux couches. Ce résultat apporte un argument fort en faveur d'un dopage de surface significatif des fils dans la méthode de CVD VLS, phénomène à prendre en compte lors de la réalisation de jonctions axiales. L'analyse de la résistivité apparente en fonction du diamètre révèle que le piégeage des porteurs majoritaires sur les bords non passivés des fils impacte le dopage apparent pour les petits diamètres. Deux modèles simples de déplétion pleine et partielle sont présentés et permettent de remonter à Ns, densité de charges piégées en surface.

Afin de donner une vue synthétique de ce travail, un tableau rapportant les résistivités moyennes en fonction de la dilution en espèce dopantes p ou n est donné.

La dernière partie de ce chapitre s'intéresse à la fabrication de jonctions dans les nanofils. Plusieurs configurations ont été testées, à dopage axial ou radial et dopage pin ou pi (ni). Même si la jonction radiale pin est facilement synthétisée, la jonction axiale Schottky où le fil est dégénéré sur la première moitié et non intentionnellement dopé (nid) sur l'autre, émerge comme un dispositif de synthèse cristalline et de fabrication aisés et aux caractéristiques électriques robustes. Nous discutons les caractéristiques des jonctions ainsi obtenues (hauteur de barrière, résistance série, facteur d'idéalité) et donnons une analyse détaillée des processus de diffusion des porteurs minoritaires en utilisant la technique du courant induit par faisceau d'électrons (EBIC). Une configuration du dispositif en deux jonctions est mise en évidence (jonction Schottky à l'interface métal silicium nid et jonction à l'interface entre le silicium dégénéré et nid). Des longueurs de diffusion faibles, de l'ordre de 700 nm

sont mesurées et attribuées à une durée de vie courte des porteurs minoritaires du fait de la prédominance des recombinaisons de surface sur celles de volume.

Summary

The semiconductor, in its undoped form is insulating at room temperature and therefore the intrinsic semiconductor is of little use in making devices. The doping is an important tool to modulate the transport properties of semiconductor. It also necessary to achieve free carrier injection or "spontaneous'' separation by interplay of built in fields through the semiconductor, which are exploited in most devices. Further the majority of devices requires one to fabricate junctions in semiconductor educed by doping consecutive regions with donors or acceptors to create opposite polarity in semiconductor. This makes an efficient control of doping a prerequisite to control the quasi Fermi levels at any point in the nanowire, to control the device properties as per our needs. The first step towards studying the doping begins with optimizing dopant incorporation in Si nanowires as in for homogeneously doped nanowires. The dopant influx is constant during this type of growth with all other parameters kept constant and therefore it is quite easy to correlate the influence of relative dopant gas flow on the active doping achieved in the nanowire by electrical resistivity measurements. The study of homogenous doping in both p and n doping with nanowire axial and radial dependence lays the framework with the basic ingredients needed for the fabrication of good junctions. The next step then is to obtain heterogeneous doping by modulating the doping during the growth by either p-type, n-type or both type of dopants to obtain axial junctions. The growth parameters can also be engineered such that it drives the nanowire axial growth during a certain period of time, after which the growth mode is switched to support 2-D conformal deposition. The different growth modes gives us the freedom of growing radial p-n or hetero junctions as needed. The quality of the nanowire junctions thus fabricated can only be inferred by performing current-voltage(I-V) measurements on diodes and along with electron beam induced current technique, to achieve a full understanding of carrier transport and ideality of our nanowire diodes.

CHAPTER 4

Homogenously doped NWs

There are large number of literature reports on studying and optimizing the in-situ p-type and n-type doping of Si NWs by VLS process using various methods[**10**][**15**][**27**][**14**][**28**]. The first reports of controlled doping in NWs were given by Y. Cui et al[**10**]. The authors proved that the engineering of doping in NWs was possible for p- and n-type doping by introducing dopant gases B_2H_6(Boron: p-type doping) and ablating Au-P(Phosphorous: n-type doping) using a laser assisted growth technique with SiH_4 as silicon precursor. There are also numerous reports implementing doping using conventional CVD VLS growth with silane, diborane and phosphine as the precursor and doping gases. Attempts also have been made for using organic precursors such as trimethylaluminium [**29**] or trimethylborane [**12**] or for the p-type doping in silicon NWs. In our work, we use LPCVD deposition tool equipped with silane, diborane and phosphine gases. A detailed description of the growth equipment and process is provided in Appendix A.

4.1. Challenges in doping of NWs

The p-type doping, although successfully observed in literature[**15**] faces many challenges. We will describe the difficulties encountered for the p type doping to put in perspective our contribution to this field. The p-type doping is usually performed with inorganic (B_2H_6) or an organometallic-Trimethylborane[**12**] precursor. The growth with diborane faces issues at high diborane to silane injection ratio and the literature reports doping values with lesser consistency for different dopant gas dilutions as compared to phosphine[**30**]. This can be attributed to the growth of amorphous Si shell by addition of diborane, therefore giving unreliably high resistivity values as reported by Cui et. al.[**10**]. Increasing the hydrogen pressure in CVD can reduce the amorphous Si shell thickness deposition rate. As suggested by Lew et. al.[**12**], is the use of trimethylborane (TMB) as the growth precursor which avoids the unwanted amorphous Si deposition on NW sidewalls. But they obtain much higher concentration of boron in Si measured by SIMS measurements compared to 4 probe resistivity measurement suggesting difficulties in boron incorporation in NW using TMB. With TMB the doping efficiencies are about 2 order of magnitude[**31**] smaller than obtained with diborane. For the diborane use, apart from the above issues, the growth is riddled with problems pertaining to side wall faceting, Au diffusion on surface and tapering of NWs[**27**]. This is summarized in the work of Fang et al.[**32**] shown in Fig 4.1.1a, where a TEM image of a boron doped section compared with axially grown phosphorous and undoped sections in same growth are shown. The section with boron doping is evidently more rough/faceted with much thicker diameter due to the amorphous shell.

The primary mechanism involved is VLS growth, with precipitation of cracked Si at Au-Si liquid-solid interface, leading to 1D growth. This is usually accompanied by distinct dissociative adsorption of Si on the surface of NW (2D growth). Depending on the exact growth conditions one of the above process dominates the growth. The literature[**27**][**32**] suggests that introduction of diborane during the growth significantly enhances the secondary uncatalyzed 2D growth mechanism leading to faceting in NWs. Pan et al[**27**] observed crystalline core for doping in range of 1E18 $cm^{-3}$and an amorphous shell as shown in Fig. 4.1.1b for doping values of 1E19 cm^{-3}. The faceting could also be linked to the Au diffusion as observed by others in literature[**33**]. The former type of faceting is more prominent for boron than for phosphorous doping and is insignificant for undoped NWs. The diffusion of gold along the sidewalls during the growth is another reason for 2D growth which is present in most of CVD VLS grown NWs. Thus from literature one can conclude that the change in surface morphology can be caused by catalyzed growth by diffused gold or by non-catalyzed 2D growth which is enhanced by induction of Diborane.

We have performed similar experiments with NW growth with various diborane to silane concentrations and observe similar effect of tapering and faceting with increased diborane dilutions. The NWs grown at various dilutions of diborane to silane are shown in Fig 4.1.2. The growth was performed with $pB_2H_6/pSiH_4$ ratios ranging from 2.4E-5 to 1E-3 at temperature of 650 °C and pressure of 1.5 Torr with H_2 flow rate of 1.9 L/min, without HCl. The faceting increases with the B/Si ratio due to preferential 2D growth rates on various crystal phases. The tapering also increases with $pB_2H_6/pSiH_4$ ratio and a diameter enlargement from 5 nm μm^{-1} for $pB_2H_6/pSiH_4$ of 2.4E−5 to 15 nm μm^{-1} for $pB_2H_6/pSiH_4$ of 1E-3 is observed.

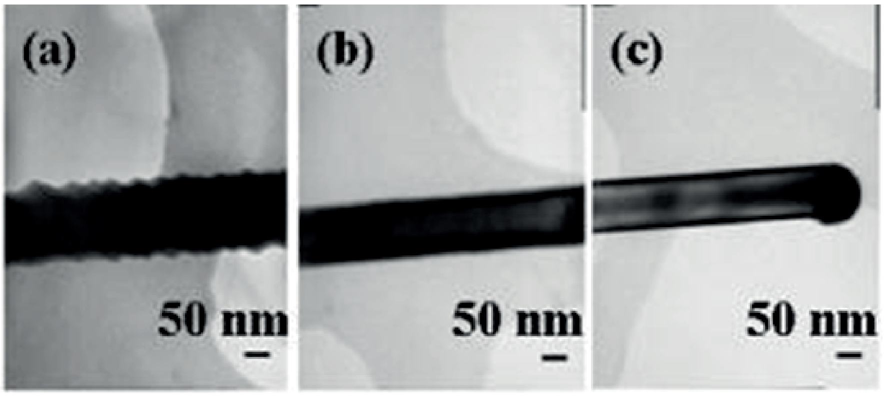

(A) TEM images of an axial modulation doped p-n-i SiNW taken along the wire growth direction. (a) The B-doped (p-type) SiNW region, (b) the P-doped (n-type) SiNW region, and (c) the intrinsic SiNW region.[**32**]

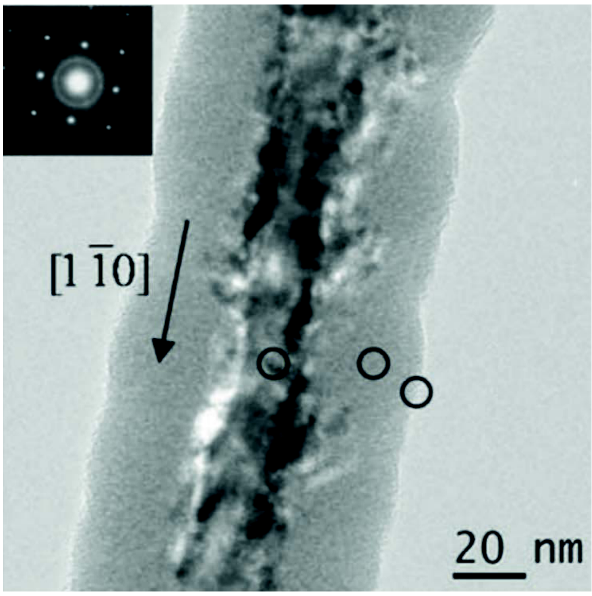

(B) Bright-field TEM image of a typical B_2H_6 highly doped SiNW, showing the core–shell structure. The inset is the corresponding diffraction pattern.[**27**]

FIGURE 4.1.1. TEM on boron doped NWs

We then characterize the n-type NWs grown using silane and phosphine. The n-type doping can be easily achieved by addition of phosphine and unlike diborane, the addition of phosphine has negligible impact on the growth process[**34**]. The n-type doping also faces gold diffusion problem on the sidewalls during growth which can induce some 2D growth. Most of the above challenges can be solved by reduction in the partial pressures of dopant precursor to the silane[**28**]. Regarding diborane, the typical ratios of partial pressures for

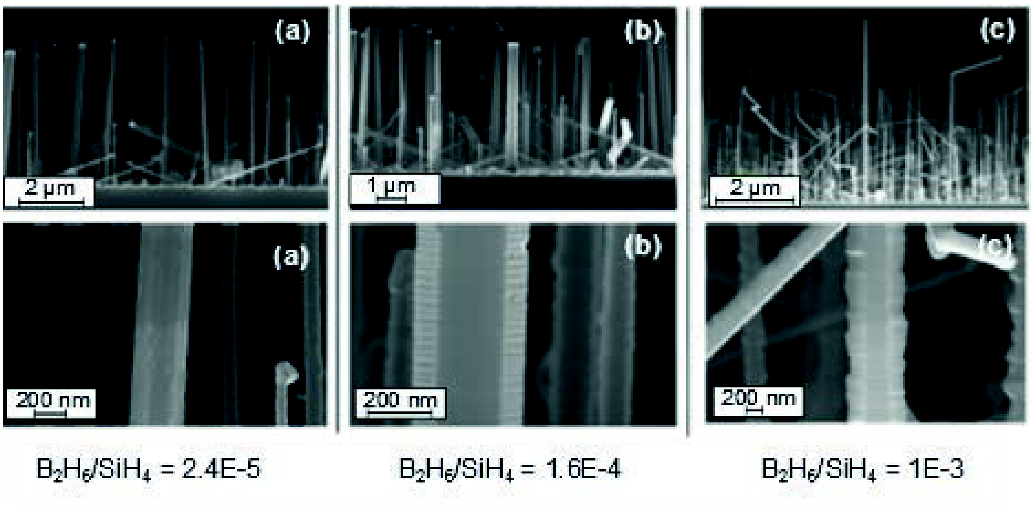

FIGURE 4.1.2. SEM images of p-doped SiNW growth without HCl.[**14**]

$B_2H_6/SiH_4 < 10^{-3}$or $PH_3/SiH_4 < 10^{-3}$ with Au catalyst provides growth with minimal morphological changes, but the problems of shell overgrowth still remains. In our group a solution to this problem has be found by addition of hydrogen chloride (HCl) gas in the precursor mixture during the growth.

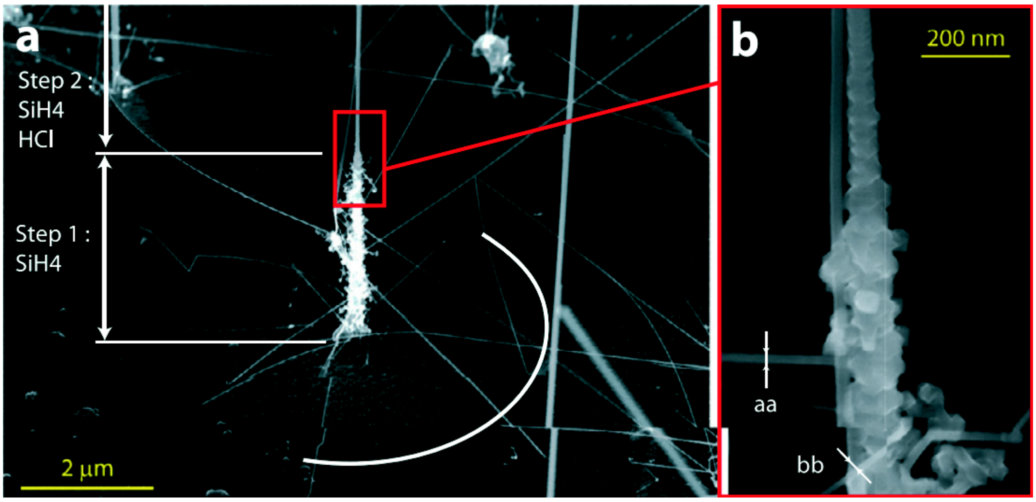

FIGURE 4.1.3. Si NW obtained by 2 step growth at 650 °C with Au catalyst. a) Two step growth consists of silane induced growth followed by addition of HCl to the growth recipe. The Au diffusion can be see around the base of NW. b) A close up view of transition region with small NW originating from diffused catalyst.[35]

Similar growths as above were performed in our group along with the addition of HCl to see its influence on dopant incorporation and morphology. These effects of HCl on NW growth have been studied previously in our group by Oehler et al.[**35**], with the Au catalyst for the case of undoped NWs. A significant reduction in gold migration was observed with HCl assisted growth. This can be witnessed from SEM on an undoped NW (see Fig 4.1.3) grown with and without HCl. In the part grown without HCl, the Au diffusion around the base is clearly visible as a result of the catalyst diffusion during the chamber heat up. This section shows thinner NWs re-catalyzing from the diffused gold. The second section is grown with HCl and shows a relatively smooth surface. This inhibition of migration of catalyst is attributed to the chlorination of the silicon surface by HCl which reduces Au diffusion[**35**]. The surface chlorination also prevents coalescence of catalyst particles at the early stage of the growth sequence (during chamber heat up), thus giving a narrow distribution of diameters on the sample.

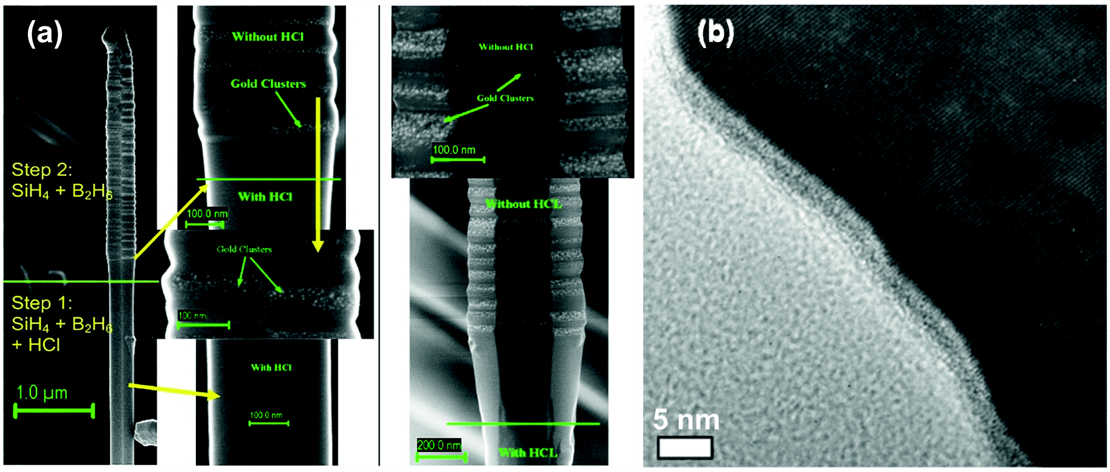

FIGURE 4.1.4. SEM images of boron-doped SiNWs grown in two steps under different conditions: Step 1 with HCl and step 2 without HCl. We clearly observe two regions on the NWs corresponding to the two growth conditions. In the zooms showing the region grown without HCl we can clearly observe gold clusters at the surface with an increase of the diameter and the roughness. The scale bar on TEM is 5 nm.[**14**]

Seeing the positive effects of HCl incorporation, we performed a study of its influence on the growth of doped NWs. The Fig 4.1.4 shows a two step process with silane, diborane and HCl in first half of the growth and without HCl in the second half of the growth[**14**]. The growth was performed at 650 ºC; a total pressure of 3 Torr; H_2 flow of 1 L/min; SiH_4 flow of 50 sccm and $pB_2H_6/pSiH_4 = 10^{-3}$. The growth of the first section was performed with HCl (100 sccm) and the HCl mass flow controller (MFC) was closed in the second half of the growth. The rough and faceted surfaces are obtained under HCl free atmospheres near the top of the NW compared to smooth surfaces with HCl. Further without the presence of HCl the diffusion of Au from the catalyst occurs on these facets. This results in reduction in the size of the catalyst droplet which causes the tapering of the NW by reduction of the catalyst diameter. In the bottom half of the NW grown with HCl the surface is very smooth with no visible gold clusters on the surface. Moreover, the presence of amorphous shell Si as noted in literature[**27**] is entirely absent as seen in the TEM image in Fig 4.1.4b. The thin amorphous shell of ~2 nm seen around the NW is the standard native oxide that usually forms on bare Si (when exposed to air) as opposed to a thick layer of amorphous Si shown by Pan et. al[**27**]. Further the overgrowth of 2D layer during the process is minimized due to surface chlorination of NW with HCl. The Fig 4.1.5 shows the tapering estimate between the HCl and HCl free recipes for different boron doped NWs. A dominant reduction in tapering of the boron doped NWs is observed from ~15$nm \cdot \mu m^{-1}$ HCl free recipe to ~6$nm \cdot \mu m^{-1}$ HCl atmospheres at 650 ºC. Although systematic studies as a function of the growth temperature were not performed, we can hypothesize that the higher process temperatures allowed due to inclusion of HCl (thanks to the stabilization of the catalyst droplet compared with the HCl free approaches) certainly has a beneficial impact on the growth with a higher crystal quality.

In contrast with boron doping, the n-type NWs growth with PH$_3$ is not much influenced by the incorporation of HCl. A small increase in the tapering angle is observed for increasing temperatures, while keeping a constant and smooth sidewall surface. Overall, an increase in growth yield was observed for both HCl assisted n-type and p-type NWs due to inhibited diffusion of catalyst and almost all catalyst particles yielding NWs. A comprehensive set of growth parameters for different doping configurations used is detailed in Annex A-I. In conclusion, the introduction of HCl provides a remarkable structural improvement over non-HCl growth by freezing the gold catalyst diffusion by surface chlorination and sets an interesting stage for modulation of morphological and structural properties of doped NWs.

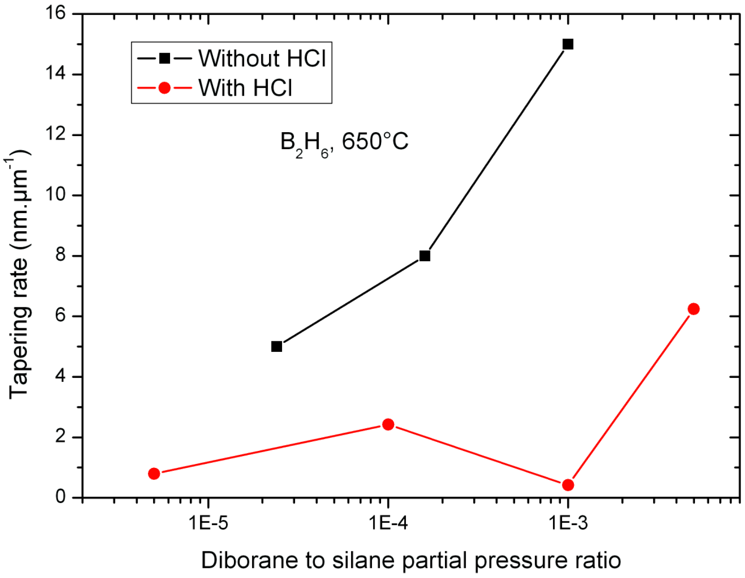

FIGURE 4.1.5. NW tapering vs diborane/silane dilution

4.2. Electrical measurements

In the previous section we have addressed the challenges in growth of homogeneously doped NWs. Once the NWs are grown and after primary step of topographical characterization in scanning electron microscope(SEM), we need a second step of electrical characterization to confirm the type of doping and the resistivity of the NWs. This resistivity values and extracted from the electrical measurements are converted to dopant concentration which can then be correlated with the dopant to silane gas ratios providing us with a table with all necessary data points of precursor gas ratios to doping densities obtained experimentally.

The experimental methods for connecting NWs follows the same basic steps for making 2-probe and 4-probe contacts. First, the as grown NWs are immersed in isopropanol and followed by an ultrasonication step to disperse the NWs. The solution is then drop-casted onto a highly doped Si substrate with an insulating SiO_2 top layer which is followed by standard lithographic process to give 2-probe, 4-probe or 16-probe contacts on isolated NWs as desired. There was no step for gold removal before performing the lithography due to the minimal diffusion of gold on NW surface as explained in previous section. Metal stacks

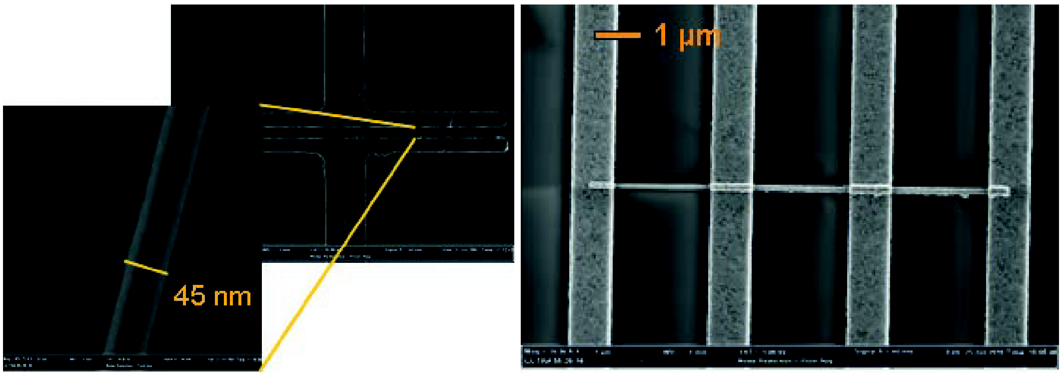

(A) NW contacted in 2-Probes (B) NW contacted in 4-Probe

FIGURE 4.2.1. Single NW contacted in 2-probe and 4-probe configurations

of Ni/Al/Au and Ti/Al/Au of 50/100/50 nm were deposited on expected[1] p-type and n-type NWs. A typical 2-probe and 4-probe device fabricated with above process are shown in Fig 4.2.1. The I-V measurements on the connected 2 probe and 4 probe devices were performed on Keithley 4200 semiconductor characterization setup. The detailed parameters and discussion on device nanofabrication and characterization can be seen in Appendix A.

The device configuration for standard I-V measurements is the basic 2-probes setup as shown in Fig 4.2.2. A constant potential is applied between the two ends of NW and a back gate potential sweep is performed to obtain I_d-V_g(source-drain current vs back gate voltage) curves. The NW goes into accumulation or depletion depending on the doping, when a gate potential is applied on the back gate of the transistor device shown in Fig 4.2.2.

For example, the low p-type doped NW will go into accumulation mode on negative biasing of substrate as shown in Fig 4.2.3. Similarly for n-type NW the channel is conducting when a positive gate voltage is applied. In both cases the carrier concentration should be low enough so that gate field can influence the channel potential and hence the free carrier density across the NW. If the NW is highly doped then excessively large fields are required to cause a similar modulation due to large free carrier density screening the external gate potential. The method is then limited by the dopant concentration in the NWs with limits ranging from undoped to moderately doped(1E18 cm^{-3}) NWs.

---

[1] The doping in the NW is unknown before the electrical characterization but one can assume p- and n-type doping depending on the doping recipes used. The growth for undoped NW usually shows a residual p-type doping. The tests done on large number of NWs with various doping levels allows us to “expect” the doping based on experience accumulated from previous measurements.

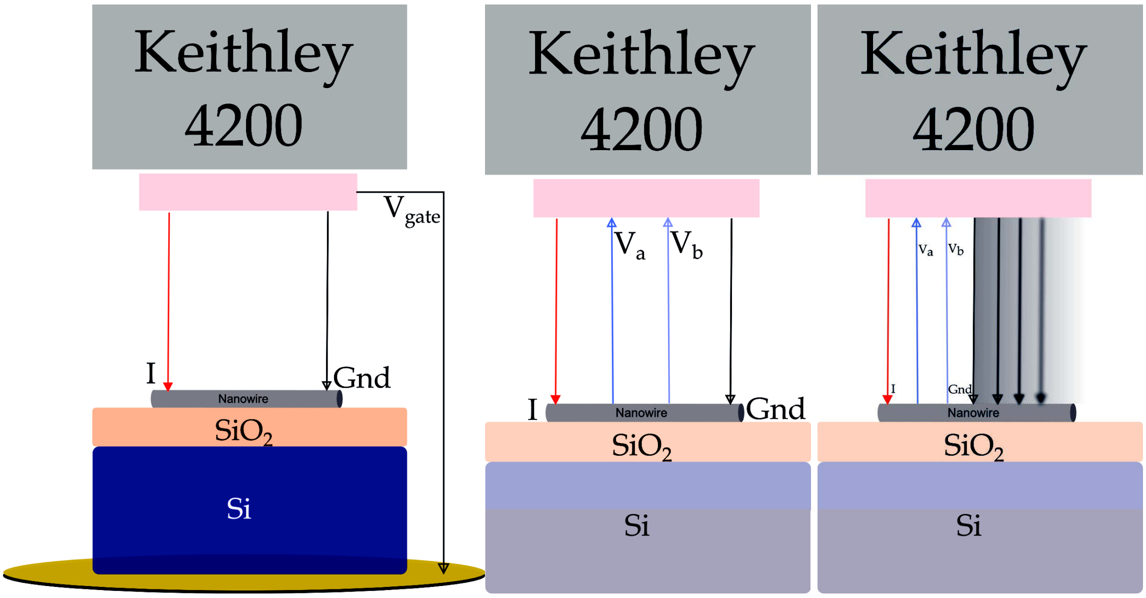

(B) 2-Probe (C) 4-Probe (D) 16 Probe

FIGURE 4.2.2. Schematic of 2-Probes, 4-Probes and 16-Probes measurement

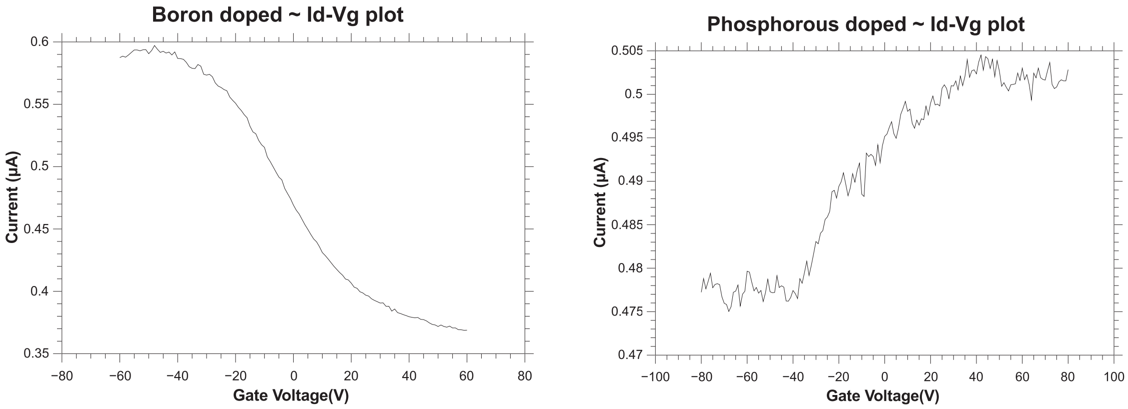

FIGURE 4.2.3. Id-Vg sweep for low doped p-type and n-type NWs with gate bias swept from negative -60/-80 V (left) and -80/+80 V (right).

The 4-probe measurements are essential to obtain an accurate measurement of resistivities. This method eliminates the influence of contact resistances by implementing a difference in potential at two inner probes on NW with respect to the ground probe. The schematic of 4 probe setup is shown in Fig 4.2.2. The current sweep is performed on the outer two electrodes and potential drop is measured on the inner two electrodes. The resistance of the NW is then given by the ratio of the difference in this potential drop with respect to the current sweep. The resistivity (ϱ) can then be easily calculated by knowing the cross section area (A) of NW and the length (L) between the inner probes by $\varrho = \frac{R.A}{L}$ relation. The radius of the NW for extracting cross section area and the length are determined by SEM. The typical 4 probe resistivity measurements are shown below in Fig 4.2.4 for the boron doped growth recipe with HCl and without HCl. The other growth conditions are the same for both recipes with process temperature of 650 ºC, pressure of 3 Torr and diborane to silane gas dilution of 10^{-3}. The resistivity of NWs drops from 106 mΩ.cm to 17 mΩ.cm with HCl.

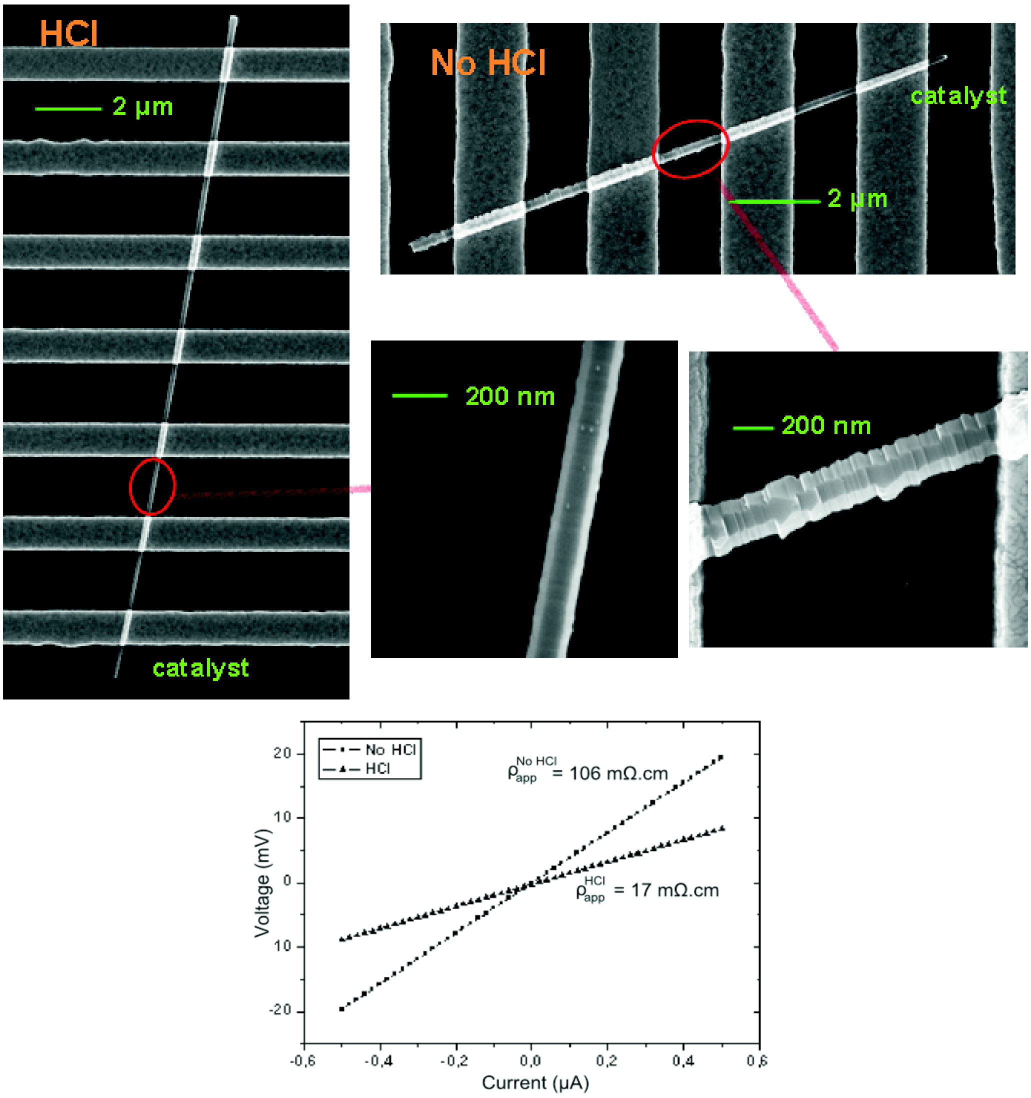

FIGURE 4.2.4. 4-Probe Resistivity Measurement for HCl and HCl free growths for boron doped NW[**14**].

To see the influence of the contact resistance we performed 2-probe[2] and 4-probe measurements. Then the difference in the 2-probe resistance and 4-probe resistance gives the total contact resistance on the NW in the 2 probe configuration. The results are tabulated below in Table 1. The contact resistance is observed to decrease with increasing doping (decreasing resistance) in the NW. Thus the resistivity of the NW plays an important role in the contact resistance measurement since for a given couple metal-semiconductor the doping density governs the width of the depletion region below the contact. For low doping case the metal-semiconductor interface is no more ohmic and forms a Schottky contact. This gives rise to a complicated picture where each contact is forming a diode with the NW. Further, due to the non negligible contact width, one can consider each contact as formed by a continuous distribution of infinitesimal width schottky diodes in parallel[3] with the NW section under it. Now, since the current will flow through the least dissipative path, for each contact, the current enters the contact through the first schottky diode at the edge of the contact and then traverses through the contact (since it is the least dissipative path) and then reenters the NW through the schottky diode at the other edge of the contact.

No.	NW Diameter(nm)	2-Probes (Ohms)	4-Probes (Ohms)	Contact Resistance(Ohms)
1	≈259	1.358E+3	485.13	872.87
2	≈258	2.275E+3	687.31	1587.69
3	≈259	4.279E+3	1.04e+3	3239
4	≈259	1.136E+4	1.37E+3	9990
5	≈257	2.137E+4	1.94E+3	19430

TABLE 4.2.1. Variation in contact resistance with axial doping along a NW

The process can be understood more easily by the schematic in Fig 4.2.5 where the current path is highlighted in red. The phenomenon is very complicated and no alternative exist for measuring such low doping using 4-probes. Thus at low doping levels due to additive and subtractive effect of various diodes, a non linear curve is obtained for 2-probe and 4-probe measurements. This is shown in Fig. 4.2.6, where non-linearity is clearly visible when compared to I-V on highly doped NWs in Fig 4.2.7. For 4-probe measurements for low doping, in some cases a linear region is obtained for either positive or negative current

---

[2] The resistance measurement by 2-probe method gives the sum of contact and NW resistances instead of just the NW resistance as in 4 probe method

[3] In case of a schottky diode the current through the diode varies non linearly with the voltage across the junction depending of the ideality factor of the diode.

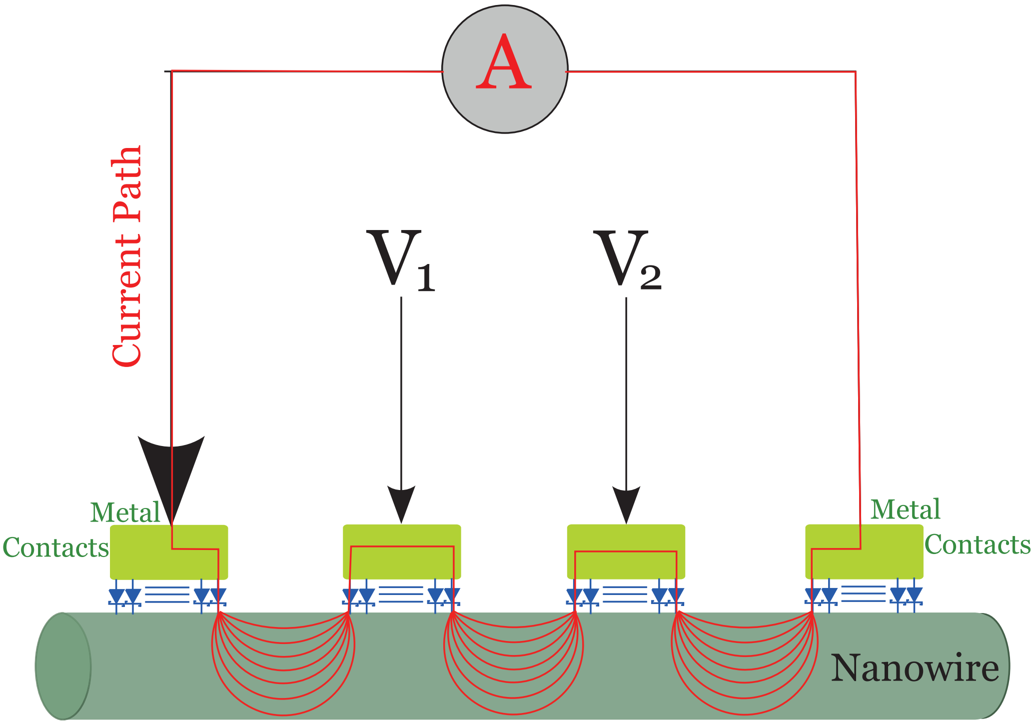

FIGURE 4.2.5. The schematic of 4-probe contact configuration on low doped NWs

sweeps and allows one to roughly extract the NW resistance(see 4-probes in Fig 4.2.6). This could occur in special cases where efficient carrier injection occurs at a weak point such as a sharp edge of the metal electrode.

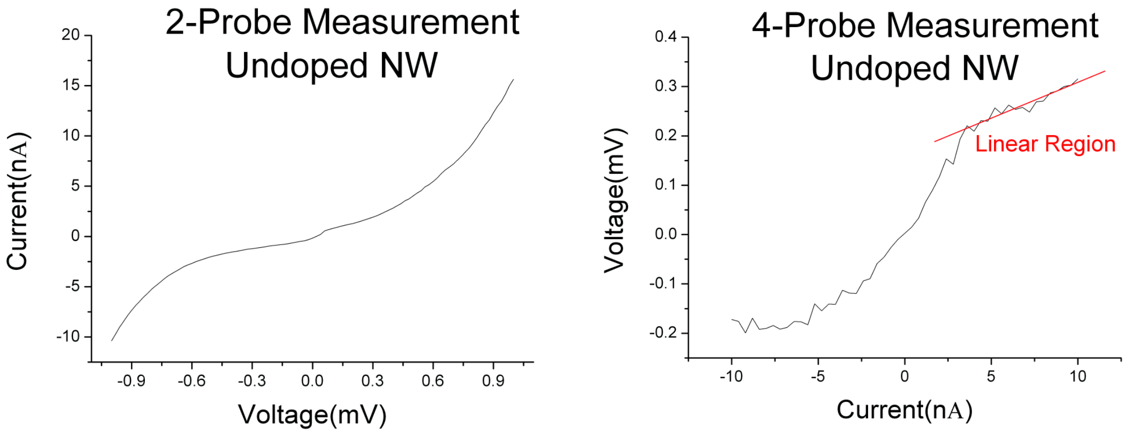

FIGURE 4.2.6. I-V measurement on undoped NW

To conclude, the addition of HCl strongly improves the doping efficiency in Boron doped NWs as well as their structural quality.

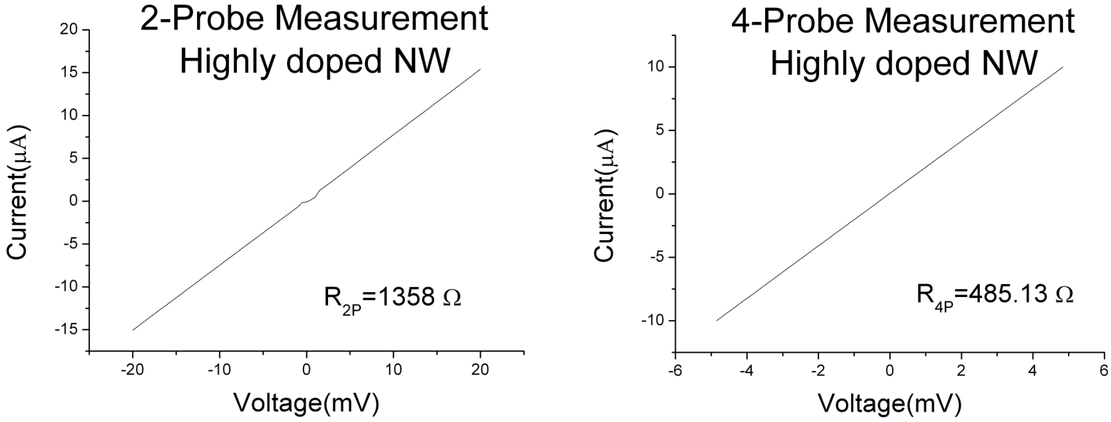

FIGURE 4.2.7. I-V measurements on highly doped NW

4.3. Diameter and axial dependence of doping

4.3.1. Axial dependent resistivity.

In all the following experiments, the ratio of dopant gas to Si precursor is kept constant which should lead to an uniform doping along the NW. We will show that it is not the case in our NWs. In the previous section, we showed that combined use of HCl and doping gas resulted in a great improvement of the doping efficiency and the morphology of doped wires, particularly in term of surface smoothness and reduced tapering. Even though the uncatalyzed 2D growth is seriously reduced in this growth regime, specially for the PH_3 doping, some continuous deposit of doped material on the sidewalls all along the growth might significantly contribute to a decrease in resistivity. With increasing exposure times to the reactive mixture the surface doping increases and thus the resistivity decreases, or in other words, regions close to the NW base are exposed for more time and thus are more doped. This enrichment in doping impurities due to uncatalyzed deposit was very clearly evidenced by Perea et al[**36**], using atom probe tomography on Ge NWs. Under experimental growth conditions that favor surface deposit and thus tapering, i.e. using only GeH_4 as process gas, they showed the formation of an over-doped shell, with phosphorous concentrations of the 1E20 cm^{-3}, around lower doped VLS core having phosphorous concentrations in the 1E18 cm^{-3} to 1E19 cm^{-3} range. In separate experiments, using Kelvin Probe Force Microscopy on a p-doped Si NW, Koren et al[**37**] observed differences in the surface potential of neighboring segments which were radially etched over different depths. They interpreted this result as the signature of a radial distribution of dopants arising from an efficient surface incorporation and diffusion of phosphorous during the growth, as it was observed even in absence of tapering.

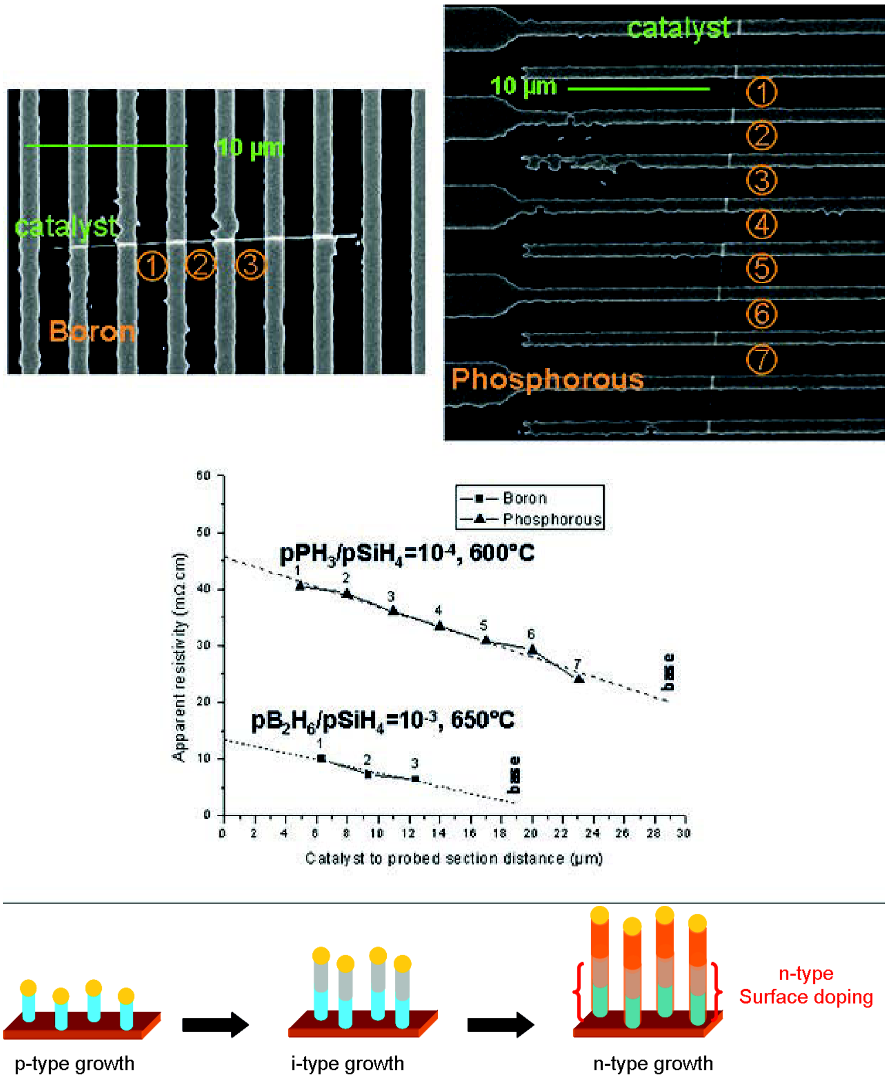

FIGURE 4.3.1. Abscissa dependent resistivity measurements performed on boron and phosphorous doped NWs grown with HCl showing resistivity decrease with increasing surface exposure times to dopant gases. A schematic of surface doping in pin axial NW growth is depicted in lower half.

To prepare our work on the fabrication of junctions where surface doping might play a determinant role, we performed a set of experiments to characterize the axial dependance of the doping distribution in our Si NWs grown with HCl. For this, we performed growth of >20μm long NWs which were later connected in multiprobe configuration. The resistivity measurements by four probe measurements were then performed on individual NW segments as described in Section 3.2. The resulting devices formed by multiple probes on typical doped NWs are shown in Fig 4.3.1. In the Fig 4.3.1, the SEM images show a boron doped NW on the top left image and a phosphorous doped NW on the top right image with growth conditions of 650 °C, $pB_2H_6/pSiH_4$=1E-3 for boron doped wires and 600 °C, $pPH_3/pSiH_4$=1E-4 for phosphorus doped wires. To be accurate in the measurements one must take care of comparing the probed section exposed to dopant gas for similar time scales. We assume that, for all the NWs grown in same growth the doping in NW section adjacent to catalyst droplet should be constant. Due to above reason, the apparent resistivity measurements thus obtained on various segments of the NWs should give more clear picture when plotted against the distance from the catalyst. A linear trend is observed in apparent resistivity with the distance from the catalyst, showing a successive increase in active dopants concentration in NW from the catalyst to the base.

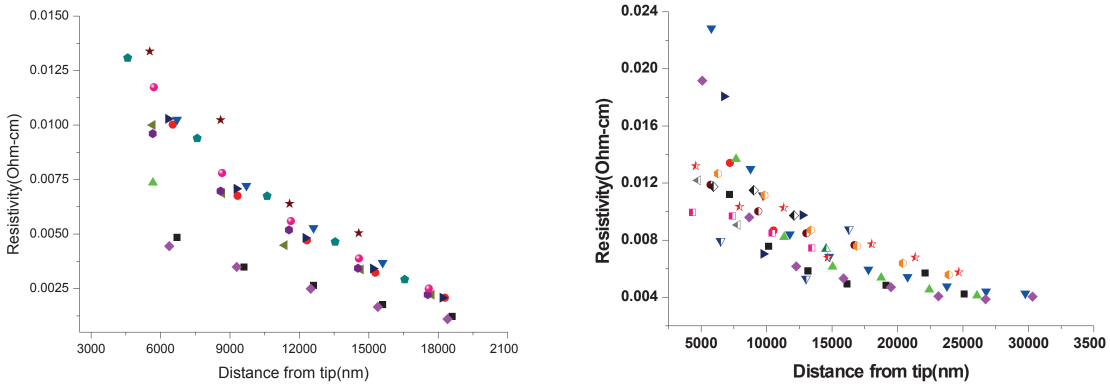

(A) p-type doping with $pB_2H_6/pSiH_4$=1E-3

(B) p-type doping with $pB_2H_6/pSiH_4$=5E-3

FIGURE 4.3.2. Apparent resistivity vs the distance from the catalyst for Boron doped NWs

To have an overall view of resistivity variation in a typical NW during growth process it is more convenient to perform measurements on various NWs grown in the same process recipe. A similar plot of apparent resistivity vs distance from the catalyst gives us a general trend of the change in axial resistivities.Fig. 4.3.2a,b shows such a figure for boron doped NWs with $pB_2H_6/pSiH_4$=1E-3 at 650 °C and $pB_2H_6/pSiH_4$=5E-3 at 650°C respectively. The

Fig 4.3.2 shows axial resistivities for NWs of various diameters plotted on same graph with similar symbols representing the same NW. In this set of experiments, we have chosen a process temperature (650°C for both n and p type doping) that induces tapering for both types of wires in order to explore the axial and the diameter dependence (shown in next section) of the four probes resistivity in the same set of measurements. We see a general trend of increasing resistivity as we probe the section from base to the top of NW near the catalyst. The change in resistivity is a linear variation with the axial position except for smaller diameter where the resistivity increases rapidly with axial position.

Similar plots with axial dependence of resistivity are shown Fig 4.3.3a,b for Phosphorous doped NWs with pPH$_3$/pSiH$_4$=5E-4 at 650 °C and pPH$_3$/pSiH$_4$=1E-3 at 650 °C respectively. The NWs grown with pPH$_3$/pSiH$_4$=1E-3 at 650 °C fall under high dilution limit for phosphorous and thus show an exceptional trend of increasing resistivity with axial position which will be discussed later.

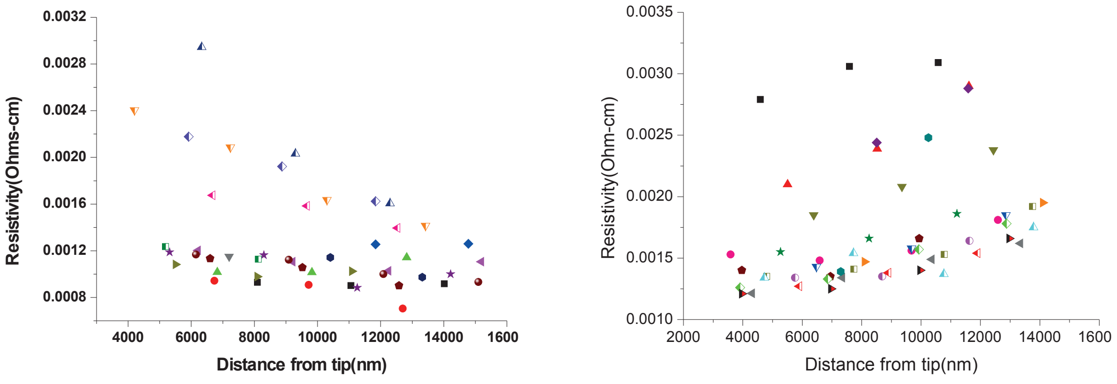

(A) n-doping with pPH$_3$/pSiH$_4$=5E-4

(B) n-doping with pPH$_3$/pSiH$_4$=1E-3

FIGURE 4.3.3. Apparent resistivity vs the distance from the catalyst for Phosphorous doped NWs

Since the growth conditions are kept constant from the beginning to the end of the growth, the axial variation signifies a time dependent phenomenon since the dopant incorporation through the catalyst is expected to remain unchanged during entire growth. Then by carefully analyzing the data, we come to conclusion that such time dependent increase in doping can only occur in three cases:

Case I : Catalyzed surface deposition/incorporation.

In absence of HCl the gold diffuses on the NW sidewalls during the growth and induces a gold catalysed 2D growth on sidewalls. This mechanism is possibly the leading one to account for the surface doping in wires grown without HCl. In our case, previous work carried out on undoped wires[**35**] or on doped wires (see figure 4.1.4) shows that no noticeable gold catalyzed and doped 2D layer is observed under Cl atmospheres.

Case II : Uncatalyzed surface doping.

In VLS growth mode the dopant incorporation in the NW through the catalyst is also accompanied by an uncatalyzed decomposition of dopant precursor on the NW sidewalls, as suggested by the doping radial profile found using the KPFM technique[**37**]. The decomposition of phosphine to phosphorous and diborane to boron induces free dopant species which then diffuse over the first few nanometers of the NW[**38**] and give rise to doping of the surface. As the growth continues, the base of the NW is continually exposed to dopant precursor and is increasingly surface doped.

To test the model of surface doping, we perform an experiment on 2D layers. In this experiment, we simply grew a 150 nm⟺150 nm bi-layer of Si on a (100) n- type silicon substrate (1-10 $ohm \cdot cm$). Four different depositions were tested with:

i) 150 nm⟺150 nm simple bi-layer with no dopant gases.

ii) 150 nm⟺PH_3Flux⟺150 nm bi-layer with phosphine flux in between.

iii) 150 nm⟺PH_3Flux + HCl⟺150 nm bi-layer with phosphine and HCl flux in between.

iv) 150 nm⟺PH_3Flux + HCl + SiH_4⟺150 nm bi-layer with phosphine, HCl and silane flux in between.

The parameters for 2D Si layer growth were 650 ºC, silane flow of 40 sccm, pressure of 3 torr and hydrogen flow of 1 L/mn. The process parameters for gas flux between the two 2D layers is chosen the same as NWs grown with $pPH_3/pSiH_4$ dilution of 5E-3.

Great care was given to purging all the volume of the reactor before restarting the growth for the top 150 nm section of the bi-layer. This configuration is used to assess the existence of a diffused layer of dopants in silicon, and seemed to us adequate to mimic the surface incorporation of phosphorous atoms in the presence of silane gas. Epitaxy of the top unintentionally doped upper layer is also necessary to characterize the doping profile using the capacitance voltage technique. Indeed, in case of direct electrode connection with

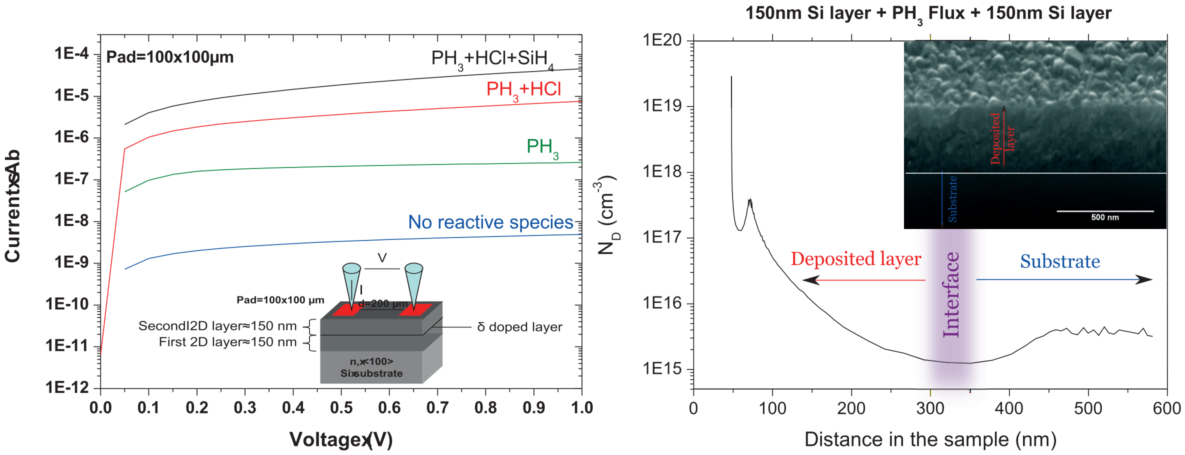

FIGURE 4.3.4. I-V (left figure) and C-V (left figure) measurement on various bi-layer CVD growths. The inset of CV measurement shows an SEM image of 2D layer with labeled substrate and 2D deposition regions.

the delta-doped layer, an overdoping at the surface would generate an ohmic contact with the rest of the semiconductor, thus preventing any C-V dopant profiling. The inset of C-V graph in Fig. 4.3.4 shows a SEM cross section of the overall layers, with a total measured thickness of ~350 nm[4].

The Fig 4.3.4 shows the I-V measurement on the thin films with each contact pad of $100\mu m \times 100\mu m$ separated by $200\mu m$. A qualitative understanding of the doping can be achieved by comparing the different growth scenarios. The simple growth with no interlayer gas flux shows the lowest current level followed by the interlayer PH_3flux. Even higher current levels more than an order of magnitude compared to PH_3 flux are reached by interlayer (PH_3+ HCl) flux and (PH_3+ HCl + SiH_4) flux. The results suggest a successive increasing doping of the delta doped layer from no doping species to (PH_3+ HCl + SiH_4) flux.

The above samples were also characterized by capacitance voltage (C-V) measurements. The samples with interlayer (PH_3+ HCl) flux and (PH_3+ HCl + SiH_4) flux were too highly doped and could not be probed by C-V measurements. The doping profiles extracted from the C-V characteristics are presented on the right of Fig. 4.3.4. They show a constant value around 1E15 cm^{-3}to 1E16 cm^{-3}in regions corresponding to the substrate, in agreement with the value of the resistivity given by the wafer supplier. For smaller probed depths, we clearly see a peak value at approximately 100 nm around 5E17 cm^{-3}, in the region where the

---

[4] The actual deposition thickness varies from ±50 nm from expected 300 nm for different samples.

delta doped layer is expected. The width of this peak which can be ascribed to the diffusion length of phosphorous impurities (10-20 nm) and falls in the range of diameters of the Si NW that we study (note that for small values of applied potential, which correspond to the smallest probed abscissa and thus depletion zones, the high values in the current generates divergences in the value of the measured capacitance that we eliminated from the graph). This is the proof that when a silicon crystal is grown and exposed in-situ to a phosphine bath, some phosphorous atoms bind on the surface and can be embedded by further Si regrowth with subsequent diffusion in the "bulk", leading to the so called surface doping.

Case III: Thermal activation of dopants.

An alternative process which can also lead to axial dependance of the resistivities is the thermal activation of dopants. At growth temperatures the diffusion of dopants is very limited, only over dimensions typical of the NW radius; we disregard the possibility of large scale axial diffusion of dopants. But the exposure of the NW to high temperatures during the growth for long time scale could lead to an activation of inactive dopants in the NW core. Since the base of NW is present in the chamber for longer time scale, it is intuitive to assume more activation of dopants in the base than in the segment near the catalyst. At our growth temperatures (typically 600-650°C) the thermal activation even though present, should be insignificant. Thus we conclude axial change in resistivity is due to a dominant surface doping.

We now return to Fig 4.3.3b, the high dilution case for phosphorous doping. We see a decrease in the resistivity for decreasing distance to tip, which is unexpected in the frame of our current model. One can suppose that beyond a limit value of the dopant to silane dilution ratio, the Si lattice approaches its dilution limit and can not incorporate more phosphorous (in its elemental form) than it can for boron given the relatively larger 2D growth rate for p-type doping. As a result, at high phosphine to silane dilution ratio, clustering and thus loss of accessible doping impurities might occur on the surface of NWs exposed for a long time to the doping atmospheres, which can explain our observation.

To conclude this part, the "core" doping level can thus be extrapolated from the intercept of the resistivity curves with the zero ordinate to get the core doping near the catalyst(calculated only using bigger diameter NWs). For a given wire, this must be done by taking only the linear part of the resistivity-abscissa relation to rule out any radius induced change in the resistivity as we will see in the next section. For boron doped wires, we find a mean value of 0.00537 $\Omega \cdot cm$ (for Fig 4.3.2a) and 0.00657 $\Omega \cdot cm$ (for Fig 4.3.2b).

4.3.2. Diameter dependent resistivity.

There are many reports in literature[**38**][**39**][**40**] [**36**][**41**] showing a radial distribution of dopants in Si NWs grown by VLS mode which was measured by atom probe tomography, capacitance-voltage measurements, scanning spreading resistance measurement, kelvin probe force microscopy and by chemical oxidation and etching techniques. A few theoretical studies have also been directed towards the role of dielectric mismatch in impurity ionization and the trapping of charge carriers on surface traps [**42**][**43**][**44**].

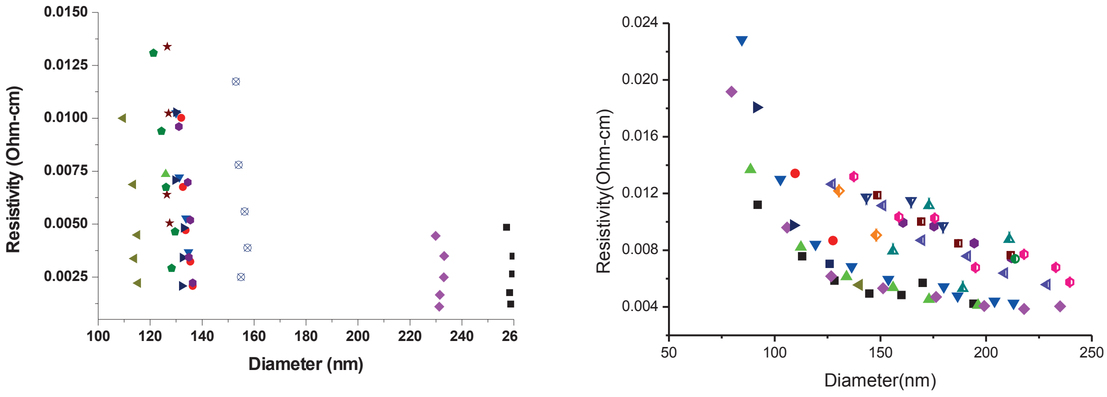

(A) p-type doping with $pB_2H_6/pSiH_4$=1E-3

(B) p-type doping with $pB_2H_6/pSiH_4$=5E-3

FIGURE 4.3.5. Apparent resistivity vs diameter for Boron doped NWs

To assess the influence of diameter on apparent resistivity, the results from the Section 4.3.1, where the resistivity of NWs were plotted vs the axial position, were re-tabulated to obtain the variation in resistivity with respect to the diameter of the NW. The Fig 4.3.5 and Fig 4.3.6 show this variation of apparent resistivity for different diameters. The symbols with similar shapes represent the same NW with different points corresponding to measurements on different axial positions.

The Fig. 4.3.5a,b (and Fig. 4.3.6a,b) show a very distinct trend of increase in resistivity as we move from large diameter NWs to small diameter NWs. This decrease in resistivity can be explained by three possible phenomena:

Case I: Reduction in mobility.

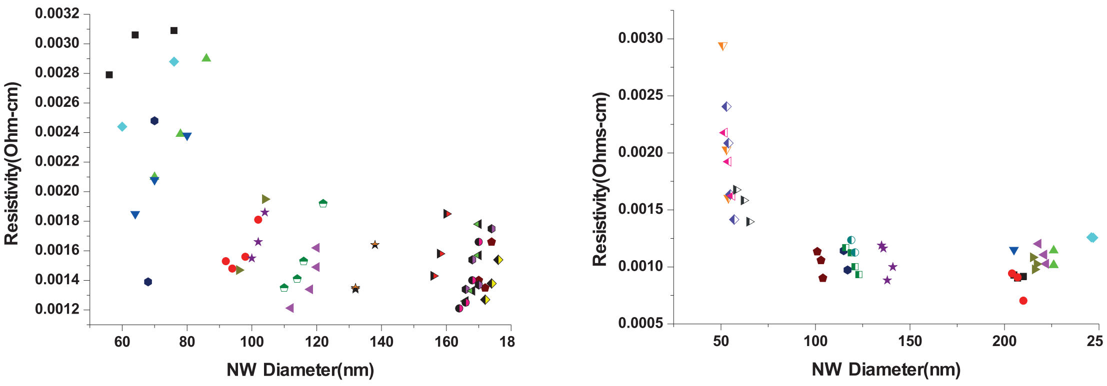

(A) n-doping with $pPH_3/pSiH_4$=5E-4

(B) n-doping with $pPH_3/pSiH_4$=1E-3

FIGURE 4.3.6. Apparent resistivity vs diameter for Phosphorous doped NWs

When one reduces the diameter of the NW, the surface atoms to volume atoms ratio increases rapidly at nanoscale dimensions and importance of surface phenomena increases. Carriers can also feel more significantly the surface roughness induced scattering and in absence of any passivation feel the presence of a large number of trapped charges at the surface.

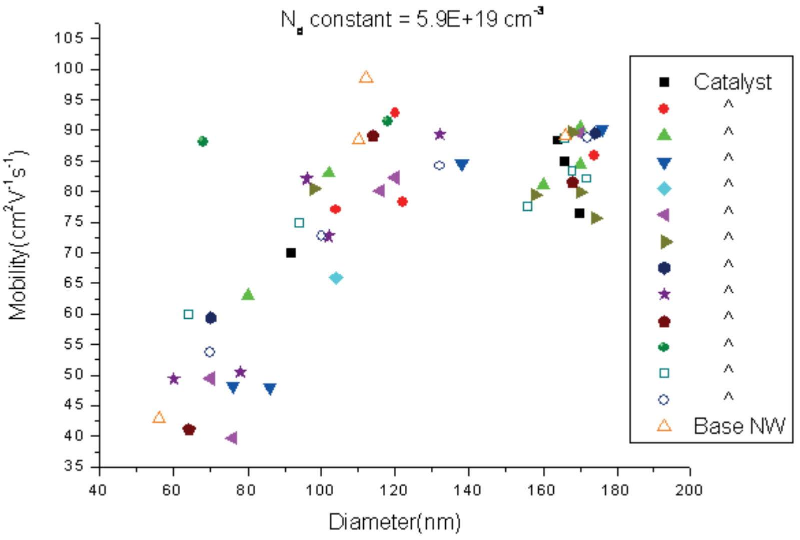

FIGURE 4.3.7. The variation in calculated mobility vs NW diameter

The relation of the resistivity with mobility and doping is given by $\varrho \approx 1/[q\mu_n N_d]$ (assuming full ionization of the impurities). Now, hypothesizing that the change in resistivity of NW is only related to the reduction in mobility, we can fix the donor density N_d by relation between bulk resistivity and dopant concentration. The calculation was performed assuming bulk like mobilities for big NWs and data arranged to consider the same doping level for same distances of probed sections from the catalyst. We then obtain a transformed plot for mobility varying with diameter for the case of phosphorous doping at dilutions of 5e-4 in Fig. 4.3.7. The plot shows a huge reduction from bulk like mobilities of ≈90 $cm^2V^{-1}s^{-1}$in 200 nm diameter NWs to ≈40 $cm^2V^{-1}s^{-1}$ for 60 nm diameter NWs.

However, literature reports show that mobilities in silicon NWs are not influenced for large diameter NWs and the strong influence of surface scattering is seen on mobility only for NW radius below 4 nm[**45**][**46**]. The crystal direction also affects the mobility of the charge carriers but this effect should be prominent only for radius smaller than 6 nm[**47**]. Considering the above reports the dependence of the mobility on NW diameter although present is very negligible for the radii of NWs under consideration.

Case II: Diameter dependent dopant segregation.

The literature has various reports of inhomogeneous dopant placement in the NW core which has been studied for example by Xie et al.[**38**][**37**][**36**]. The electrical measurements performed on NWs after controlled etching of NW after low temperature thermal oxidation showed a transition from bulk like to surface doping as the diameter is decreased <25 nm for both n and p-type NWs. This natural spatial separation of dopants in cross section of the NW could also give rise to the diameter dependent resistivities. In their results, Xie et al. consider a NW <25 nm diameter as small and NWs > 50 nm as big which show bulk like effect in their experiments. Since in our experiments we work on NWs with diameters ranging from 50 nm to 250 nm, it is accurate to quantify our NWs as bulk in their nomenclature. Therefore even though, the diameter dependent dopant segregation plays a minor role in modifying the resistivities in our diameter range it fails to explain the continuous decrease in doping seen for smaller NWs.

Case III: Dopant deactivation.

The ionization energy of the dopant defines the probability for the impurity to ionize and take part to the charge transport phenomena through the emission of a free carrier.

Thus, at a particular temperature the ionization energy of dopants sets the free carrier concentration in the semiconductor. For the single impurity case, the ionization process in the semiconductor leaves a fixed and charged atomic nucleus and induces the presence of an image charge at the semiconductor surface which in turn adds an extra screening term on the coulomb potential of the impurity. One can ignore this effect in bulk semiconductors due to the usually observed big distances between the impurity and the surface. However, one has to take into account the modified coulomb potential due to the neighboring image charges on the NW surface that will affect the work to be done by the ionized free carrier in his course towards the infinity by which one defines the ionization energy. For the single impurity case, the theoretical calculations by Diarra et al.,[**42**] shows that the enhancement of the ionization energy can be seen in NWs with a radius beyond the quantum limit. Indeed, significant increase in the ionization energy is observed beyond a 10 nm radius for a silicon wire immersed in the air, with, for example, values in the 100 meV range for both donors and acceptors, in place of the typical 40 to 50 meV observed in the bulk material. Then this effect can be neglected in our NWs due diameters >50nm and doping concentration in degenerate regime.

Case IV: Surface depletion.

Surface depletion occurs when the surface of a semiconductor is depleted of charge carriers due the presence of surface charges. For the case of silicon, the surface is usually oxidized in air and has a thin layer of native oxide. Various traps can be formed either in the oxide layer or at the interface with silicon. These long lived oxide traps can capture hot free carriers or will be filled by photo-excitation. Fixed oxide traps are formed at or near the interface during the oxide creation and can not be unfilled using electric fields. Interface traps can exchange rapidly charges with silicon and are found all along the band gap. They are due to dangling bonds, extrinsic elements, or stoichiometric “mismatch”. They are amphoteric by nature and can be either negatively or positively charged depending on the value of the surface potential with respect to the intrinsic Fermi level. Further in steady state conditions and for charge neutrality reasons, a part of the free carriers is trapped on the surface, the rest being distributed in an inner conductive core separated from the surface by a depleted layer.

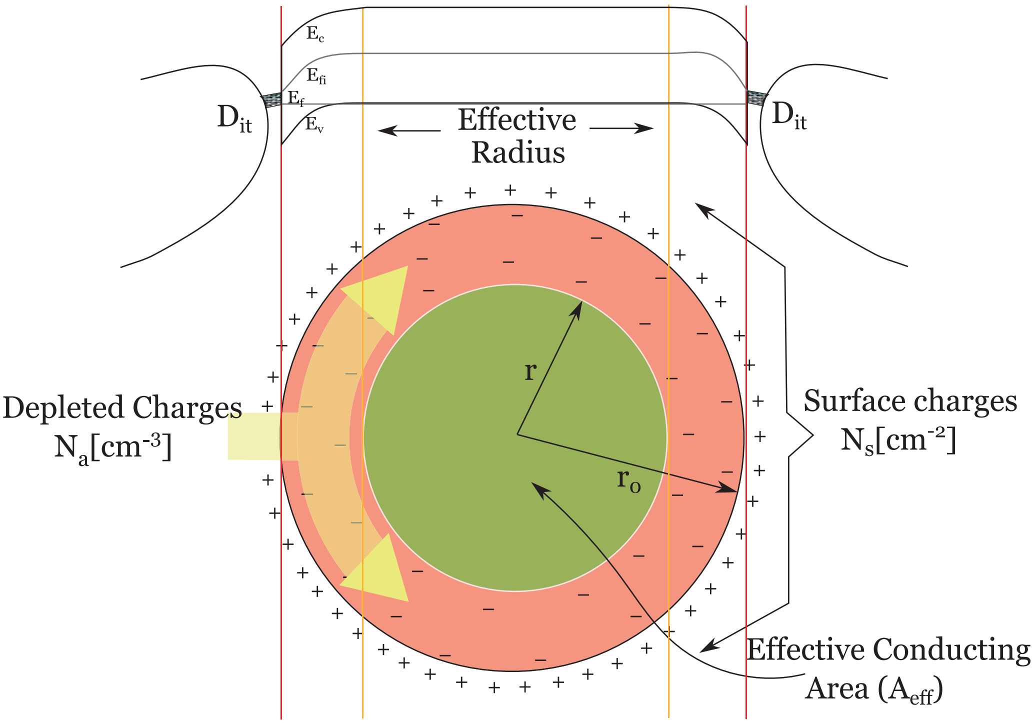

FIGURE 4.3.8. Schematic of radial band bending near the surface of NW due to interface states of density Dit. The negative charges in the semiconductor are attracted to the surface charges and thus leads to the depletion region shown in yellow.

The surface depletion phenomenon in NWs is described in Fig 4.3.8, for the case of positive trapped surface charges and the depletion of the free positive charges (holes) of a p-type Si NW. The accompanying band diagram shows the bending of the bands near the surface due the surface charges induced depletion. Filled surface states describe a band whose bounds are set by the intersect at the surface of the wire Fermi level on one hand and the intrinsic Fermi level E_{fi} on the other hand (indeed in the present case at the thermodynamic equilibrium no trapped hole can be found above E_{fi}). There are two different models in literature for calculating this surface charge density and density of interface traps given by Seo et. al.[**44**] and Schmidt et. al.[**43**]. The first model does not set any condition on the statistics (Boltzmann or Fermi-Dirac) followed by the carriers and no assumption is made on the form of the density of states of the interface traps D_{it}. In the approach by Schmidt et. al.[**43**], an analytical formulation of the potential profile is derived together with the corresponding mean values of the majority carrier densities for a given set of D_{it}, wire radius and doping level, based on the use of the Boltzmann and full depletion approximations and hypothesizing a constant D_{it} across the band gap. The latter is clearly not adapted for the case of degenerate NWs where the carrier distributions are not well reproduced by the Boltzmann approximation. Here, we make use of the first model to account for the apparent resistivity sensitivity to diameter fluctuations and we give in a second step a modified version of the model of Seo et. al., where the full depletion is not reached in the outer shell of the NWs.

Model by K. Seo et al.:

This model relies on simple charge balance between the surface charges and the NW surface depleted region. In an ideal case of NW without any surface depletion, the resistivity vs radius plot follows the standard proportionality: Resistivity ∝ (Radius)^2(assuming a homogeneous radial doping). The deviation of the experimental data from this ideal behavior is used to extract the surface charge density. One can deduce a simple relation between the apparent resistivity and actual resistivity (assuming constant doping) for different diameter by following relation:

$$\varrho_{old}=\varrho_{actual}\left[1-\frac{2}{r_0}\left(\frac{N_s}{N_a}\right)\right]^{-1} \tag{4.3.1}$$

Where ϱ_{old} is the measured resistivity of NWs and ϱ_{actual} is the actual resistivity of undepleted core in the NW[5], so we have $\varrho_{actual} < \varrho_{old}$. The r_0 is the actual radius of the NW and N_s and N_a are the surface charge density and dopant concentration in the NW. The ϱ_{actual} and N_s/N_a are the fitting parameters. The formulation of this model will be detailed in Appendix B.

A Uniform Potential Approach:

We formulated an alternative similar to Seo et al. for extracting the actual doping and surface traps density values. In this approach we begin with the assumption that the potential through the radius of our NWs is constant since most of the wires are degenerate. Indeed, any description of this system by means of a depleted and non depleted region, the so called full depletion approximation, has to be analyzed carefully. The full depletion approximation implies the simultaneous presence of a degenerate (conductive) core with

---

[5] This is same as ideal resistivity one would measure in the absence of surface states.

a quasi Fermi level near the band edge, and an outer shell being depleted enough to be considered as much more resistive than the core. If we consider that a 10 fold decrease in the majority carrier density is enough for setting the semiconductor as partly depleted, the corresponding electric potential drop must be $\Delta V = 0.1V$ across the transition region of thickness Δt_p between the conductive core and depleted shell. Limiting the corresponding field to the reasonable and physical value of $E_b = 3 \times 10^5\, cm^{-1}$ which corresponds to the Si breakdown field, we have $\Delta V/\Delta t \ll E_b$ and thus $\Delta t_p \gg \Delta V/E_b = 3\, nm$. Reasoning similarly for the lower bound of the total partly+fully depleted length Δt_{p+fd} leads to the condition $\Delta t_{p+fd} \gg \Delta V/E_b = 8.5\, nm$ with $\Delta V = 0.3\, V$ as a reasonable value of the potential offset between the core and the surface if the Fermi level is pinned by the surface. This crude but intuitive picture of the constraint on the potential profile suggests that for the smallest diameters, the full depletion approximation does not hold. Instead a gradual and flatter potential decrease is expected across the whole section of the NW, with a value at the origin shifted with respect to the case with zero surface trapping. This in turn leads to a radially gradual charging of the whole NW section. Thus, the apparent resistivity (ρ_{eff}) is the resistivity corresponding to an "apparent" free carrier density $\left(N_{a,\,d}^{eff}\right)$ which can be calculated simply by saying that the number of trapped charges with surface density N_s on the sidewalls equals the integrated difference between the true density of dopants and N_{eff} across all the NW cross-section. In equation, we get $2\pi r_o N_s = \pi r_0^2 \left(N_{a,\,d} - N_{a,\,d}^{eff}\right)$ and thus $N_{a,\,d}^{eff} = N_{a,\,d} - 2N_s/r_0$. From the relations between the dopant density and the resistivity $\rho_{eff} = f\left(N_{a,\,d}^{eff}\right)$, one can retrieve the apparent resistivity by non linear regression with the experimental data on resistivity vs radii with the fitting parameters $N_{a,\,d}$ (actual doping) and N_s(density of surface traps).

We performed the fitting of the experimental data in Fig 4.3.6 (phosphorous doped) and Fig 4.3.5 (boron doped) NWs with our model and that given by Seo et al. The fitting provides us with values of effective doping and effective resistivity of the NW core for the batch of the NWs, along with density of charges trapped on the surface. The results are tabulated in the table below for plots in Fig 4.3.9.

The values between our approach and Seo et al., agree quite well for all the NWs probed. The resistivity and doping values in above table shows the actual/effective values present in the undepleted NW core in Seo's model. Our model gives the effective doping that is

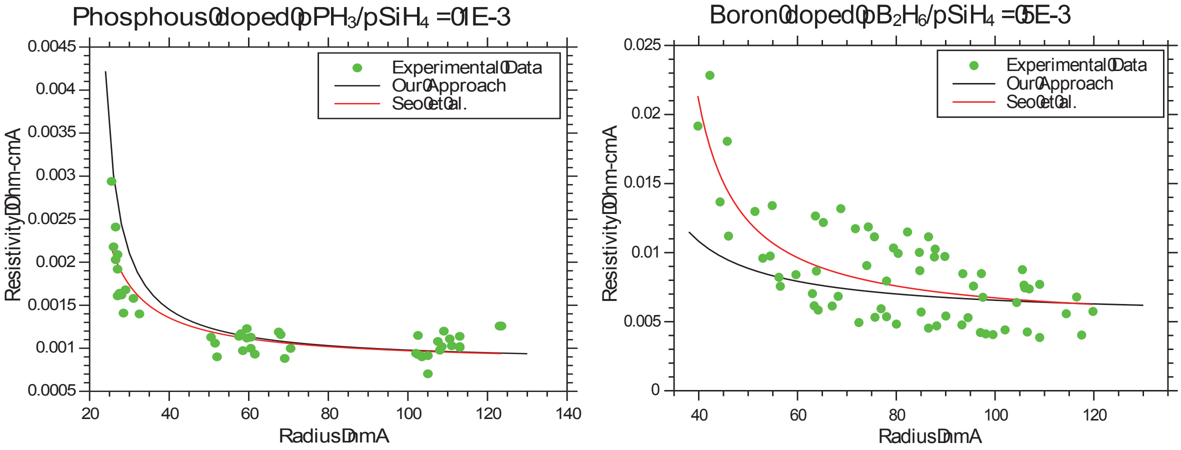

FIGURE 4.3.9. Theoretical fits by our approach and that of Seo et al., with experimental data on resistivity vs radius for phosphorous and boron doped NWs.

	Phosphorous doping		Boron doping	
	Our approach	Seo et al.	Our approach	Seo et al
Resistivity(ohm-cm)	8.7E-3	8.2E-3	5.3E-2	4.6E-2
Effective NW doping(cm^{-3})	9.2E+19	9.8E+19	1.9E+19	2.3E+19
Density of trapped carriers(cm^{-2})	7.7E+13	7.8E+13	2.3E+13	3.5E+13

TABLE 4.3.1. Resistivity, effective doping and density of surface states extracted by different models for different doping.

the doping one should measure in absence of any surface states, given in Table 4.3.1[6]. N_s stands for the integration of the density of interface traps D_{it} over all the occupied surface traps band. The surface densities of trapped carriers are extremely high compared with the passivated Si/SiO_2 interface($\approx 10^{11} cm^{-2}$), but lie in the commonly observed range for unpassivated surfaces. Our approach predicts a number of trapped charges per unit length of wire equal to $2N_s/r_0$. If we consider for instance the case of phosphorous doping and a radius of 60 nm, the volume density of trapped charges is 2.6E+19 cm^{-3} compared with an estimated doping level of 9.2E+19 cm^{-3}, which is actually a significant part of the total number of free carriers "injected" in the NW. The critical radius by which all the free carriers are trapped is 17 nm for phosphorous doping and 30 nm for boron doping. Therefore when doping induced properties are required on smaller NWs, this must be done in conjunction with surface passivation schemes.

---

[6] Note this approximation only hold for either very low density of surface states or for very high doping which is our case

4.3.3. Outcome.

The results of our study of p- and n-type doping of NWs are compiled in a chart showing the resistivity as a function of dopant dilution vs silane flow as shown in Fig. 4.3.10. The results are obtained on NWs 20-30 μm long with 100-200 nm in diameter. As discussed previously, no significant drop in the resistivity is expected for these diameters which thus provides a non biased view of the true doping impurity incorporation rate in NWs The resistivity shown is the mean value as measured from several places on the NW. The plot shows the expected trend of decreasing resistivity values with increasing dopant to Silane ratio[7] and is in agreement with literature[**34**][**31**]. Using the bulk mobilities as the starting point one can estimate the nominal doping concentration in the NWs using the relation between dopant concentration and resistivity in bulk Si. This gives the doping values for doping ranging from ≈4E14 to ≈1E20 cm^{-3} for phosphorous and ≈7.5E15 to ≈1.8E19 cm^{-3} for boron.

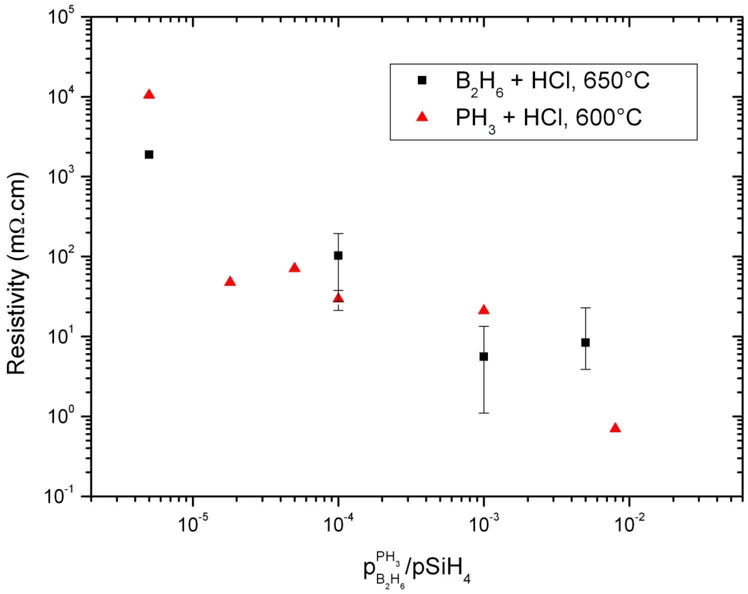

FIGURE 4.3.10. Mean apparent resistivity of SiNWs grown with HCl for phosphorous doping at 650°C and boron doping at 600°C. The y-error bars indicate the resistivities near the tip and base of the measured NWs.

---

[7] The increase in dopant in the gas mixture causes an increase in dopant incorporation in NW core and thus decreasing the resistivity.

Thus to conclude we have overcome the challenges in doping of the NWs by incorporation of HCl in the growth recipe which reduces the NW faceting, catalyst loss and tapering. The grown NWs show crystalline core with thin layers of amorphous shell for both boron and phosphorous doping. We have successfully obtained resistivities as low as $\approx 4 m\Omega cm$ for phosphorous doped NWs and $\approx 0.8 m\Omega cm$ for boron doping. We observe an axial increase in resistivity of the NW from the base to the tip which was due to the surface doping in our NWs during the growth. The resistivity of the NWs was also observed to decrease with increasing NW radii due to the charge trapping on the surface traps of the NW. We determined the actual resistivity in our NWs by fitting of our experimental data with the theoretical models. Finally, we measured resistivities for different dilution of diborane/phosphine to silane, finally giving us a complete picture of resistivity variation with dopant to precursor dilutions. The above results when combined together, provide us with all the necessary tools to realize various axial and radial doping geometries.

CHAPTER 5

NW growth with junctions

5.1. NW pin junctions

Two kinds of junctions have been grown and studied: axial and radial. The axial junction is made by growing a degenerately doped p-type NW with HCl followed by intrinsic and n-type section growth with HCl. The axial NWs faces problems with surface doping of the intrinsic and p-type section during the growth of the final n-type section and results in shorted junctions. The problem of surface doping was avoided later by working at low partial pressures of silane and performing slow growth of the intrinsic section along with intermediate purge steps which helps in flushing the residual dopants from the chamber and the catalyst. We succeed to obtain rectifying junction with I-V on axial pin junction NW shown in Fig 5.1.1a.

The core shell structure avoids the problem of surface doping. In this case, we first grow p-doped core by standard VLS process with HCl. Then the NW is either removed for gold catalyst removal step (or directly) and proceeded with an intrinsic and n-type 2D shell growth in absence of HCl. The detailed process for growth is available in Appendix A-I. We successfully obtain good rectifying junction in core shell configuration. The SEM image of a connected pin core shell NW and typical I-V measurements shown in Fig 5.1.1b.

5.2. NW schottky diodes

The fabrication of axial junctions required great care to avoid the surface doping and the core-shell junction required complicated process for contacting the NWs (See Appendix A-II). We therefore performed the growth of an axial modulation doped (p+i or n+i) schottky diode that offered us an ease of growth and device fabrication.

5.2.1. Growth, measurement and modeling.

The growth was performed at 650 °C under 3 Torr total pressure with silane, HCl gases along with phosphine or diborane as dopant gases. The axial modulation doped junction

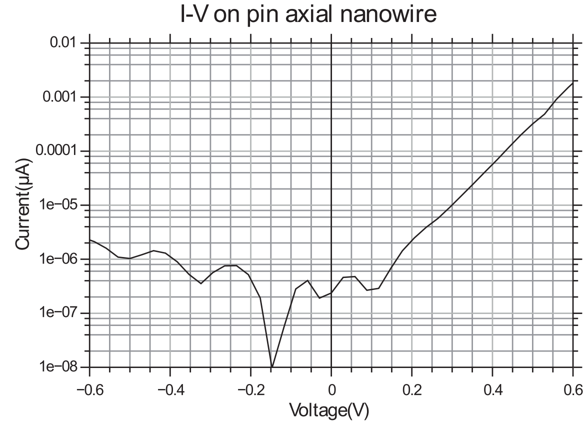

(A) I-V on pin axial junction NW

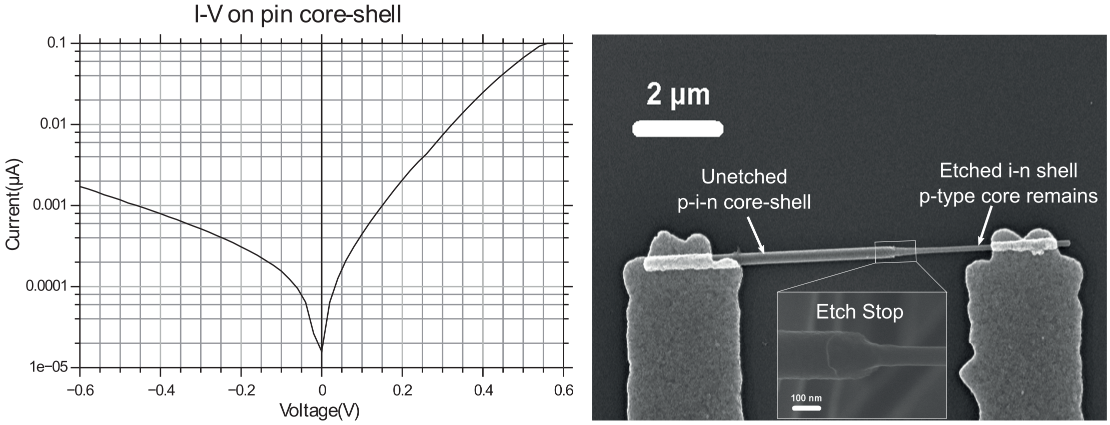

(B) I-V(left) and SEM(right) on pin core-shell junction NW

FIGURE 5.1.1. I-V on pin axial and radial junctions

were grown by heavily p-type (n-type) doping in the first section of the NWs. Next, the dopant gas flux was switched off after reaching around half of the required NW height and undoped section was grown for same duration to obtain p+i (or n+i) junction in the center of the NW.

The schematic of band diagram for formation of Ni and Ti schottky barrier on the intrinsic section of the n+i and p+i NW respectively is shown in Fig 5.2.1 where E_f, E_c, E_v and $\varphi_{b,n}$ are the quasi fermi level, conduction band edge, valence band edge and barrier height respectively. The metal contact is chosen for both type of NWs to obtain an optimum configuration of ohmic(tunneling) contact on one side and schottky contact on the other end (low doped section) of the NW. The contact is chosen by comparing the metal-Si work function

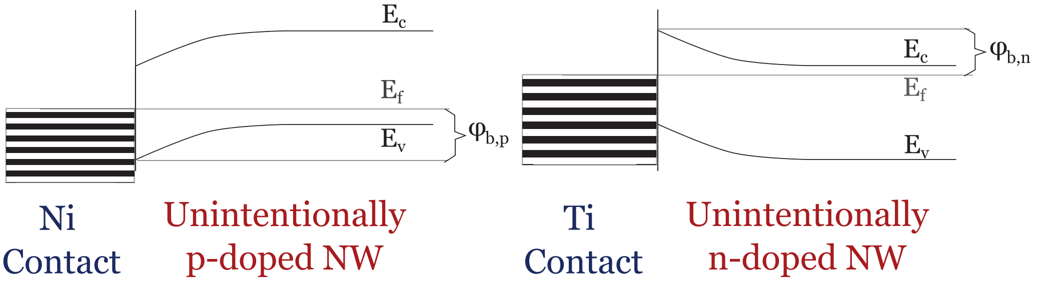

(A) Ni Contact on intrinsic section of p+i NW

(B) Ti contact on intrinsic section of n+i NW

FIGURE 5.2.1. Band diagram for metal semiconductor contact at zero bias.

from literature[**48**] for different dopings. In reality, the trend for Fermi level pinning usually observed at metal semiconductors contacts tends to make the Schottky barrier height independent of the metal work function. Nevertheless, we try to optimize the metal contact by testing different configurations of metal stacks. The thickness of different stack layers in configuration A/B/C/D or A/B/C were A= 5 nm, B=50 nm, C=100 nm and D=50 nm. In a standard stack the first layer is usually 5 nm of Ti layer which acts as a sticking layer and is followed by the actual contact metal layer which is usually Ti, Ni, Al or Pt depending on the type of doping in the NW. The contact metal is followed by a thick Al/Au stack for good contact with the probe tips and a reasonable thickness is needed to avoid breaking the oxide on the substrate by the probe tips. The aluminum layer is introduced in the stack to have a reasonable thickness of metal stack to cover the NW and to keep distance between the deposited gold and the NW[1].

The different contact configurations tested were Ti/Ni/Al/Au, Ti/Pt/Al/Au and Ti/Al/Au on p+i NWs with rectifying behavior observed for all contacts. The diode parameters like ideality factor, saturation current, barrier height are extracted from the I-V curve. The metal stack seems to influence the quality of junction with ideality factor changing from ~1.8 for Ti/Ni/Al/Au contacts to ~2 for Ti/Pt/Al/Au contacts. For all the metal stacks we extract the barrier heights in the range of 0.56-0.62 eV[2] suggesting a pinning of Fermi-level on the surface of Si NWs. Another possibility is that the 5 nm thick Ti sticking layer used for each

---

[1] When annealing the samples at 400ºC we observed pumping of Si from the NW when we used Ti/Au contacts. Thus Al layer is introduced to avoid such a behavior in the future.

[2] The barrier height can be extracted either theoretically from [**49**] or by linking the saturation current density and the barrier height with the experimental graphs in Sze [**48**]

contact sets the contact barrier height (although the deposited thickness is too small for full coverage of NW), since the Ti-Si barrier fits quite well with the findings.

The left half of Fig 5.2.2 shows a typical axial doping modulated NW contacted and the over-image shows band bending expected in such a system. An overlay schematic also shows a cross-section view of p+i NW with ohmic and schottky contact on two ends of NW. The I-V curves on typical devices are shown in right half of Fig 5.2.2.

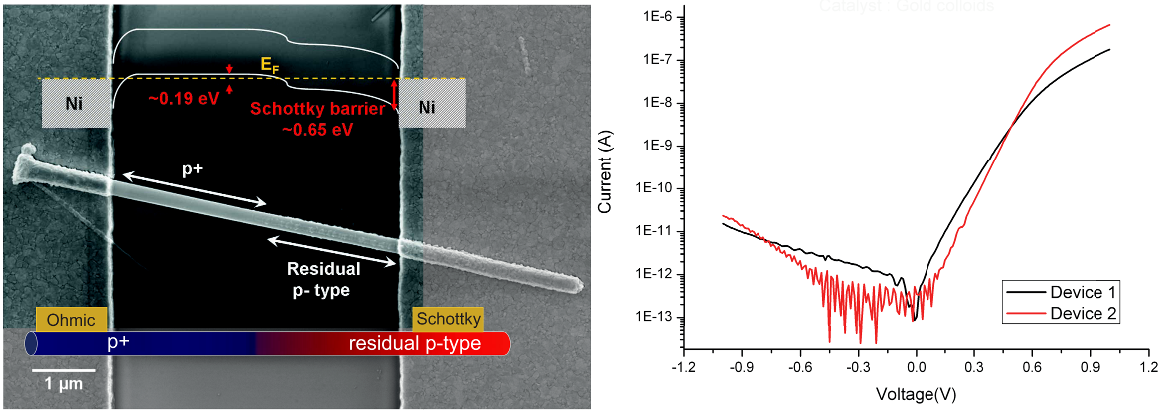

FIGURE 5.2.2. A typical p+i NW connected after lithography and metal deposition and superimposed expected band alignment in the NW(left). I-V curves of typical p+i NW Schottky devices(right).

The density of dopants in the p+i NW can be extracted by modeling the NW diode as an ideal schottky diode in series with a high resistance zone (intrinsic/residual doped region) followed by a low resistance zone (highly doped section), where the resistance are named as R_i and R_{p+} respectively. When forward bias is large enough the series resistance from the highly resistive i-type section (along with the contact resistance) dominates and this series resistance(R_s[3]) can be calculated by following equation where all the terms have their general meaning:

$$\frac{\partial V}{\partial I} = R_s + \frac{n k_b T}{qI} \tag{5.2.1}$$

The value of doping densities in highly doped section is deduced from the dopant to Silane gas dilution ratios. For the NWs grown in above batch we estimate the doping level in the highly doped section in the range of 1E19 cm^{-3} corresponding to a R_{p+}≈10 kΩ. The

---

[3] The total series resistance R_s= R_i + R_{p+}+ contact resistance

fitting of the data in Fig 5.2.2 with the equation above gives us an estimate of the R_i=700 kΩ. This corresponds to a resistivity value of ≈1 Ω.cm and an apparent active dopant density of $N_A \approx$ 10E16 cm^{-3} assuming bulk mobilities, which is a reasonable assumption for thick NWs. From the above doping values, the potential drop in the p+i junction is calculated to be ≈0.19 eV which confirms the expected low barrier heights at this junction. Thus under an applied forward bias we expect the current through the NW varying as a combined contribution of the two diodes working in series. In the reverse bias the schottky diode dominates due to the high barrier height imposed by this junction. This schematic of the band bending is shown as a overplot in Fig 5.2.2, with schottky contact on low doped section, tunneling contact on highly doped section and a junction between p+ and intrinsic section of NW.

5.2.2. EBIC Study.

The above sections deal with electrical and topographical characterization of NWs with I-V measurements, optical and scanning electron microscopes. With the above techniques we can know the structure and overall properties of the junction but they do not give much insight into the carrier transport. The study on the carrier transport is necessary since the carrier diffusion and collection are fundamental aspects of the device, which intricately govern the I-V measurements. Further we also need to experimentally validate our hypothesis of presence of two junctions in our devices with p+ intrinsic junction along with metal-intrinsic semiconductor junction. For this we take help of the Electron Beam Induced Current (EBIC) technique, which is a very versatile technique used for the measurement of the carrier diffusion length, depletion width and also for localizing the junctions in NWs.

The EBIC technique can be easily understood by comparing it with the photovoltaic analogy i.e photo current. In solar cells a photo current is generated when light is irradiated on a p-n or schottky junction where the carriers absorb the light energy and become free carriers which are then separated by the intrinsic electric fields in the depletion region and are collected through the contacts giving photo current on illumination. In fact, the electric field generated can be intrinsic as in semiconductor junctions(pn, p+i, schottky, etc) or external where a semiconductor is polarized. The electron beam induced current in the specimen is very similar to the photo current in a way that minority carrier concentration is increased by an external process (photo -illumination or E-beam bombardment) and this excess minority carriers take place in transport process by diffusion in bulk semiconductor and drift in the space charge region of the p-n/schottky junction. In case of EBIC, the high energy electrons are bombarded on the substrate and they go through multiple scattering events giving rise to various processes such as back scattered electrons, secondary electrons, characteristic X-rays, light and plasmon generation. The latter is responsible for electron hole pair generation in semiconductors through their relaxation. If the material is a bulk semiconductor without any junctions the excess carriers will recombine over time and will not give rise to induced current. In case of a p-n junction, the diffused minority carriers cross the depletion zone and become majority carriers whose flow towards the ohmic contact generates a current measured by an preamplifier and an ammeter connected to the sample. For silicon, the electron hole pair formation energy is ≈3.5 eV. So, a 1 keV beam with incoming current of 1 nA will generate a maximum EBIC current of ≈ 285 nA. This situation is never observed in practice since even in intrinsic regions of pin junctions electron hole recombination always occurs.

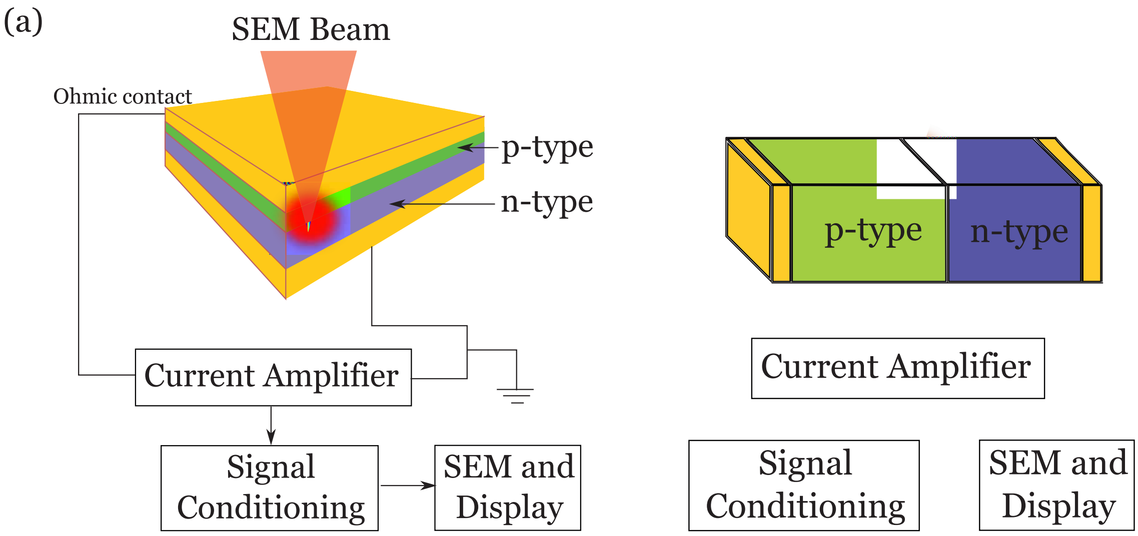

location on the semiconductor surface. The second configuration is when the electron beam scan is performed across the junction such that electron beam is parallel to the junction as shown in Figure 5.2.3b. In this configuration the electron beam induced current is the same over the entire scan area but only the carriers that diffused in the depletion region will be separated by the fields in the junction. The minority carriers generated by scanning the electron beam on p type and n type section will only participate in transport process if they can diffuse to the junction. The EBIC current thus produced in this configuration depends on the distance from the junction and the diffusion length of the minority carriers in respective sections. In the bulk material, this EBIC decay is exponential with the distance from the junction and follows the relation, $I = I_0 e^{\frac{-x}{L}}$ where x is the distance from the junction and L the diffusion length of minority carriers.

Thus EBIC will be used to assess the validity of double junction hypothesis in our devices. Further, the depletion width and diffusion lengths will be extracted from a scan of the NW with quantitative analysis of the EBIC current. This estimation of diffusion lengths at high resolution is extremely important for the correct estimation of the junction yield when used under photo-excitation.

In addition, the surface is expected to play a vital role on the device performance. In nanostructures and in NWs in particular, generated free carriers are considerably more exposed to the surface than in the bulk material, making carrier diffusion processes essentially surface dependent. EBIC, as the technique used for measuring the depletion and diffusion lengths in bulk, can also be readily extended to Si NWs. Despite the lack of theoretical background on the diffusion properties of free carriers in 1D structures, we will use the equations of the EBIC decay in bulk semiconductors to give a crude estimate of the diffusion lengths in our NWs. In the EBIC measurements on our p+i NWs, we worked at low acceleration voltages in order to prevent pumping of the NW section below the contact pads. This particular electron energy thus provides an analysis of transport parameters in the regions of photon absorption only. In parallel, this tool offers a high degree of spatial resolution for mapping the induced current profiles in nanostructures where diffusion lengths are expected to be much smaller than in their bulk counterparts. Indeed, at these acceleration voltages (1 kV), the interaction volume—the region of e-h generation by scattered primary beam in the matter—is restricted to a volume of a few 10 nm in the body of the

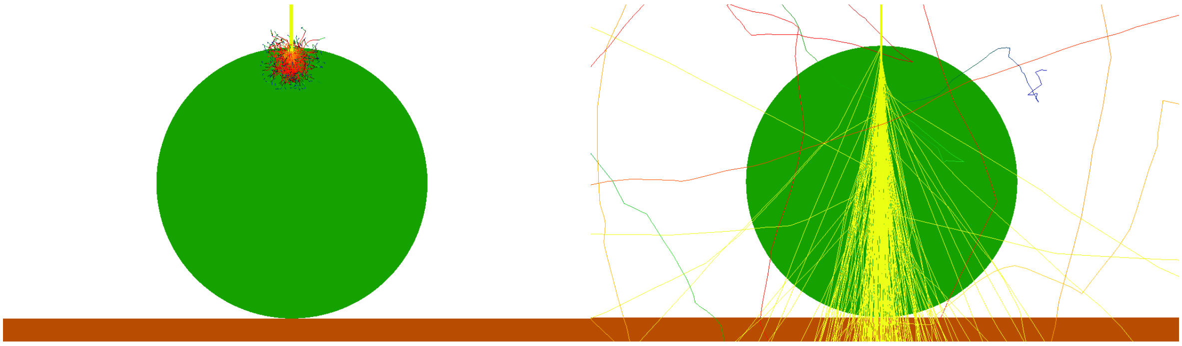

(A) NW on Substrate: 1 KV E-Beam Acceleration Voltage(Spot size=3 nm)

(B) NW on Substrate: 20KV E-Beam Acceleration Voltage(Spot size=1 nm)

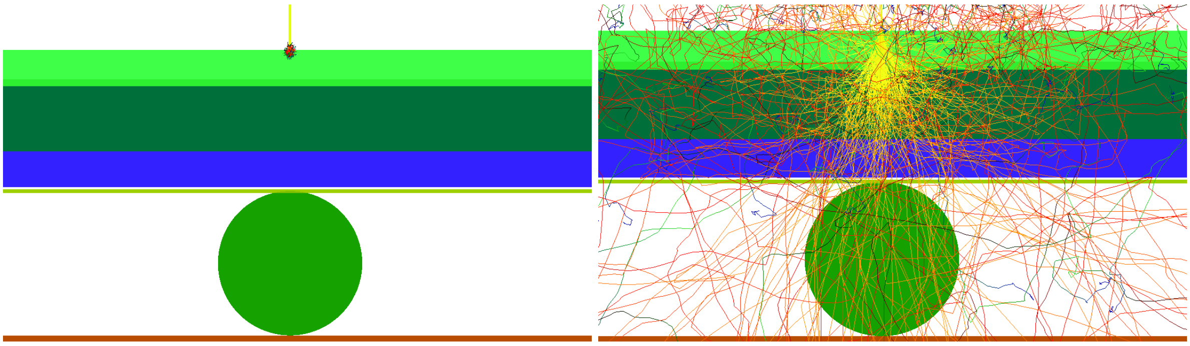

(C) Metal stack on top of NWs: 1 KV E-Beam Acceleration Voltage(Spot size=3 nm)

(D) Metal stack on top of NWs: 1 KV E-Beam Acceleration Voltage(Spot size=3 nm)

FIGURE 5.2.4. CASINO Simulation of Electron paths in Si NW of 200 nm. The color from yellow to blue denotes the decreasing electron energy

Si wire. We calculate with Si, an electron beam interaction width of ~26 nm and depth of ~30 nm through Monte Carlo simulation with 3 nm beam spot size and beam acceleration voltage of 1 kV shown in Fig 5.2.4a. A similar simulation for 20 kV acceleration voltage is shown in Fig 5.2.4b showing a much bigger E-beam interaction region with the NW. The spot size in both simulations are chosen keeping in mind the typical spot diameters experimentally obtained under good focusing conditions. To see the penetration of e-beam through our metal stack we simulated the stack of Ti/Ni/Al/Au with 10/50/100/50 nm and the simulation results are shown in Fig 5.2.4c,d. For 1 kV beam acceleration voltage the e-beam hardly crosses the few tens of nanometers in top gold layer, whereas for 20 kV beam acceleration the highly energetic electrons pass through all the layers in metal stack and interacts with the NW. Thus for above reason a 1 kV beam should be used as it can not cross the whole metal stack above the Schottky junction and is associated with a very small interaction volume necessary to reach the highest spatial resolution in the EBIC mappings. Indeed, spatial resolution depends on the diffusion length and also on the size of the interaction volume where e-h pairs are generated. We must keep the size of the interaction volume small enough compared with the diffusion length to ascribe with a good level of accuracy the measured spatial decay rates of EBIC signal with a length characteristic of the diffusion length.

We use of low accelerating voltage EBIC technique in contrast with previous reports of the minority carrier diffusion length extraction by optical techniques like the confocal Scanning Photo Current Microscopy[**21**]. In optical techniques the e-h generation area can not be decreased down to nanometer resolution due to the diffraction limit, thus setting a lower detection limit of diffusion lengths to the micron scale for such types of measurements. The Fig. 3a shows an EBIC area scan along the p+i NW. The Schottky junction near the metal contact is clearly visible due to the strong EBIC gain observed in this region (Fig 5.2.5a). The enlarged view (see inset of Fig 5.2.5a) reveals a second and weaker peak in the NW section, which can be ascribed to another local built in electric field associated with the p+i junction. The position of this double peak structure confirms that the photo current generation occurs at the Schottky junction and also in the body of the wire due to junction formed by doping modulation. The Fig 5.2.5b shows the EBIC line scans taken along the NW, and shifted in y-axis for clarity. Modeling the theoretical EBIC decay profile in this geometry is a hard task that particularly needs to take into account the effect of the surface recombination. Therefore, it is crudely assumed here that the EBIC decay follows the exponential form $I = I_0 e^{\frac{-x}{L}}$ where x is the distance from the junction and L the diffusion length of minority carriers. This is valid for beams parallel to the Schottky junctions without significant surface recombination for bulk and planar semiconductors. Thus from above relation, the minority carrier diffusion length were calculated in the p+ section (EBIC decay from the p+/nid junction) of the same wire for different voltage biases.

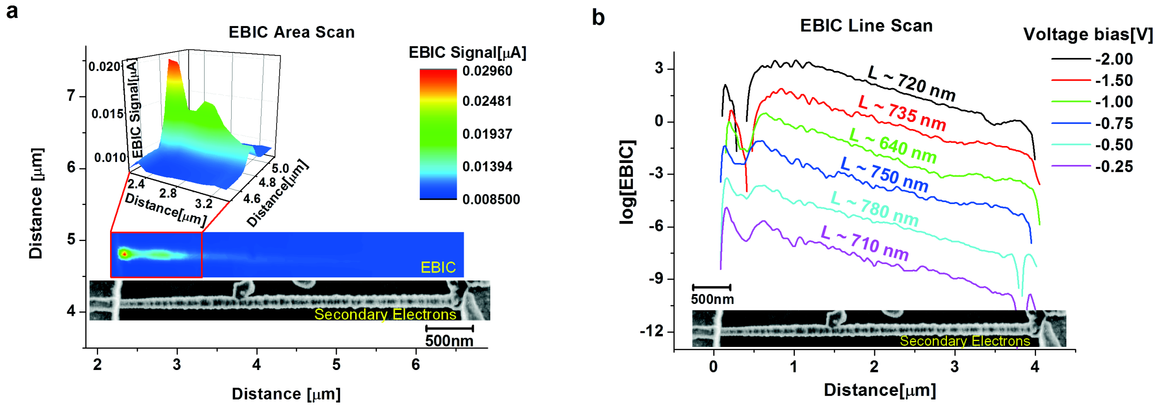

(A) The 2D color plot EBIC area scan at 0.5 V. The inset shows a 3D EBIC plot of the junction region.

(B) EBIC line scans at different reverse bias polarization plotted in log scale.

FIGURE 5.2.5. EBIC characterization on p+ i NW. The curves are vertically translated for clarity. A SEM image is attached to the abscissa to show the actual scan area for 2D plot. For the EBIC line scans the E-beam was scanned along the center of the NW.

The diffusion lengths were obtained ranging from 640 nm to 780 nm. Compared with the bulk case, this value is rarther small which arises from the considerably reduced carrier lifetime in the NW due to an extremely efficient surface recombination on the non passivated surfaces. This agrees well with the previous studies in literature on the passivation of Si NWs which showed no photoluminescence signal from electron-hole (e-h) recombination owing to the extremely high values of the surface recombination velocities. Therefore, a step for surface passivation was necessary to observe efficient e-h recombination, where native oxide was removed chemically and a SiO_2 layer was thermally grown on a chemically cleaned Si surface with a final annealing step in the forming gas. The surface recombination velocities were drastically reduced with the above process, to typically 20-30 cm.s^{-1}, very close to the value 1 cm.s^{-1} for $Si-SiO_2$ interfaces on (100) surfaces. In our study, we expect the surface recombination velocity (S) to be in the range of $(2-10)\times 10^3\, cm.s^{-1}$, a value generally measured for Si surfaces with native oxide. An estimate of e-h lifetime τ can be obtained from $\tau = \tau_b + \frac{2S}{R}$ [50], where R is the wire radius and τ_b is the bulk e-h lifetime[4]. The high surface recombination velocity S for a bad surface with large density of surface states sets the upper limit of the lifetime and thus results in very short lifetimes along with short

---

[4] The lifetime is typically 200 ns in Si under strong carrier injection, which is the case for EBIC

diffusion length. Using the above model, and assuming $D = 15\,cm^2.s^{-1}$ as the diffusion coefficient, we get the value of surface recombination velocity $S \approx DR/\left(2L^2\right) = 15000\,cm.s^{-1}$ which is in good agreement with reports in literature. Due to the extremely high value of S, the active zones of the device are then restricted to tiny wire sections near the junctions. In light of the previous arguments, we can see that passivating the NW surfaces is essential to achieve low values of S that are typically found in thermally oxidized Si NW's. Further, a decrease in S will greatly improve the quantum efficiency of the device by seriously extending the diffusion length in NWs. The diffusion lengths can be improved by various means such as passivating the surface of the NW by performing surface hydrogenation and then growing thermal SiO_2 or deposition of passivating dielectrics(like SiO_2, Si_3N_4, etc) by PECVD, ALD or other techniques. Amorphous Si also acts as an efficient passivation layer and a thin layer can by deposited in-situ in CVD or PECVD equipment after the NW growth .

In the end we performed the I-V measurements on the NW under dark and illumination to confirm the photo current generation in our NW devices.

The p+i NWs were exposed to broad band illumination by a focused Xenon light source[5] to determine the suitability for these NW diodes for future photo current measurement. The NW junctions showing a discernible response to light were chosen for upcoming photo current measurements. The Fig 5.2.6a shows the I-V of a typical p+i device under dark and illumination conditions. A clear shift is seen in the I-V on illumination with short circuit currents of few tens of picoAmps which fall in the good measurement range for our setup. The Fig 5.2.6b shows a steep on off response of the short circuit current and the open circuit voltage to external illumination being turned on and off. The nice photo response behavior observed along with the sufficient photo current on illumination, proves that the modulation doped NW devices will be useful devices for the photo current experiments presented in next part of the thesis.

---

[5] The light intensity was not calibrated at this moment since the purpose was to confirm the light induced carrier generation in preliminary devices

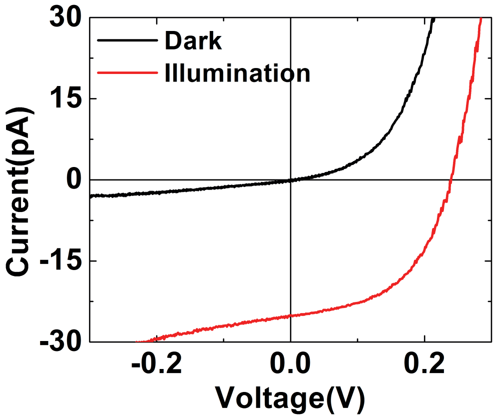

(A) IV in dark and under broadband illumination

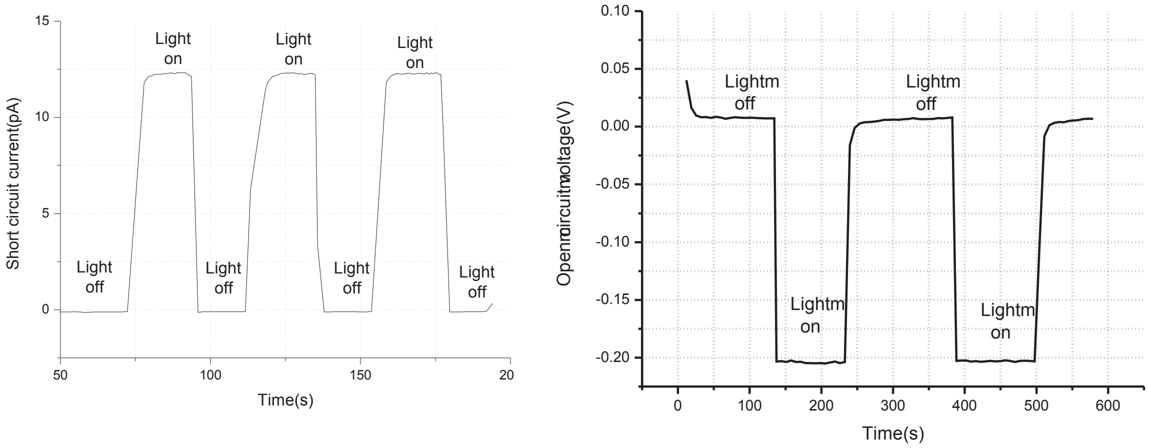

(B) Short circuit current in dark and under broadband illumination

(C) Open circuit voltage in dark and under broadband illumination

FIGURE 5.2.6. Open circuit voltage and short circuit current response

CHAPTER 6

Conclusions

The challenges in the doping of the NWs with boron (p-type) and phosphorus (n-type) were discussed. The challenges were countered by HCl, which is necessary to control the morphology and the structure of Si NWs and to obtain the optimum doping efficiency at 2e19 cm^{-3} for boron and 2E20 cm^{-3} for phosphorus. Optimization in the growth parameters allowed us to obtain a precise table with precursor dilutions for required p and n doping values. Secondly the study for the doping dependence on diameter and axial position were performed. Our data also showed an increase in resistivity of the NWs with decrease in diameter. The diameter dependence of the resistivity in our NWs from 60 nm to 250 nm in diameter fits quite well with surface depletion of dopant by interface traps. We saw an increase in the resistivity of the NWs from the base towards the tip of the NW near the catalyst. After performing dedicated experiments to test the different models we conclude that surface doping is the major effect behind the axial variation of resistivity for doped NWs.

The above study provided us a good foundation of the understanding of the NW growth and doping process. With that knowledge we moved on to growth of various junction like p+i/n+i/in+/ip+/pin (axial or coreshell). In the above configuration the p+i/n+i junctions are best suited owing to the ease of fabrication of good junctions and easy avoidance of surface doping which causes shorts instead of junctions in other axial configurations. The core shell configuration gives good diodes but is much more complicated to fabricate devices and thus will be exclusively used in specific experiments for determination of external quantum efficiencies later in Section 8.4 of the thesis. The p+i/n+i system proved to be a robust system with significant forward to reverse current ratio and an acceptable photocurrent value on broadband illumination. The other parameters were well within the acceptable range necessary for performing photocurrent measurements. The electrical characterization of the NWs were supplemented with techniques like EBIC to localize junction and to measure the minority carrier diffusion length in our NWs. As postulated earlier the EBIC measurement indeed showed two peaks signifying a bi-junction system in our NWs with metal-semiconductor junction in series with a p+i junction. The electron diffusion length were extracted from the line scan along the NW to be around 700 nm in our NW diodes. The above measurements allow us to perform a smooth transition towards studying the optical properties of these NWs in the next chapters.

Part 3

Light absorption in single Si NWs

CHAPTER 7

Résumé

Cette partie donne une étude détaillée des mécanismes d'absorption de lumière et de génération de photocourant dans les structures cylindriques que sont les nanofils de silicium et s'intéresse dans un deuxième temps à des procédés d'optimisation du couplage lumière nanofil.

Nous décrivons tout d'abord les dispositifs expérimentaux de mesure de caractéristiques courant tension et de spectroscopie de photocourant. L'attention est portée à la calibration de ce dernier avec la mesure précise de la densité surfacique spectrale de puissance incidente, permettant à la fois de s'affranchir de la réponse optique de la ligne d'excitation lumineuse et d'autre part de remonter ultérieurement aux rendements de conversion des dispositifs étudiés.

Les premières jonctions irradiées donnent un spectre de photocourant décroissant aux grandes longueurs d'onde, explicable aisément et qualitativement à l'aide d'une loi de Beer-Lambert, mais modulé par des pics et des creux. Ces modulations persistent quel que soit le substrat (silicium oxydé en surface sur 200 nm ou lame de verre d'épaisseur millimétrique) et le type de jonction (axiale pi, ni ou radiale pin) ceci permettant d'exclure tout effet interférentiel issu de réflexions multiples dans le substrat et tout effet dépendant du transport de charges.

Nous nous attachons donc à donner une explication plus poussée des processus d'absorption de lumière dans les fils allant au-delà d'une simple absorption incohérente et utilisons le cadre donnée par la théorie de Mie, dérivée initialement pour rendre compte de l'interaction entre une onde plane et une particule sphérique. Après avoir introduit les concepts fondamentaux utilisés pour des particules de forme arbitraire, tels que la diffusion, l'extinction, l'absorption et les sections efficaces associées, nous donnons les expressions rigoureuses des spectres d'absorption attendus pour des cylindres immergés dans l'air et éclairés par une onde plane en incidence normale. L'accord spectroscopique entre les absorptions expérimentale et théorique est très bon mais ne suffit pas à expliquer la présence des pics d'absorption. Nous procédons alors au calcul analytique du champ électromagnétique (EM) en tout point de l'espace et démontrons que ces pics sont liés à l'établissement de résonances du champ EM dans le volume et en périphérie du fil. Ces résonances sont associées à la présence de modes ayant pour la plupart un fort recouvrement spectral les uns avec les autres, et dont la résultante des sections effectives d'absorption donne le spectre observé expérimentalement. Nous traçons les champs de vecteur de Poynting pour le champ EM en et hors résonance et démontrons que le flux d'énergie en résonance est affecté par la présence du fil sur une section plus grande que la section géométrique, pouvant conduire à une section efficace d'absorption supérieure à l'unité. Ce résultat est corroboré par une comparaison des sections efficaces d'absorption de fils et de films de silicium dans l'air de dimensions caractéristiques identiques (diamètre et épaisseur) montrant une plus forte absorption dans le cas de l'absorption cohérente en géométrie cylindrique.

Des spectres de photocourant sont ensuite acquis sur une collection de nanofils sur substrat isolant pour des diamètres allant de 85 à 225 nm, avec un très bon accord expérience théorie. Nous montrons un décalage spectroscopique progressif des modes avec le diamètre, en accord avec l'observation de branches modales obliques dans le diagramme donnant l'absorption en fonction du diamètre et de la longueur d'onde. La polarisabilité, c'est-à-dire le rapport entre l'absorption TM et TE, donne elle aussi un bon accord et révèle une absorption moyennée sur le spectre moindre en configuration TE (champ électrique transverse à l'axe du fil) qu'en configuration TM.

Nous concluons cette partie par une estimation du rendement quantique externe dans les structures à dopage radial pin. Ces structures nous donnent l'opportunité de connaître exactement l'extension spatiale de la zone active pour la génération de photocourant, rigoureusement égale à la surface de jonction radiale éclairée, contrairement aux jonctions axiales où la dimension de cette zone est donnée par la longueur de diffusion des porteurs minoritaires mesurée en EBIC et qui n'est qu'approximative. Nous trouvons des rendements externes de l'ordre de 40% dans le bleu, en accord avec la théorie, et ici aussi modulés suivant la longueur d'onde par l'entremise des effets de résonance de Mie. Un tel accord implique un rendement quantique interne proche de l'unité dans nos structures.

La seconde section s'intéresse à l'exaltation du couplage lumière-matière dans les nanofils à l'issue de l'adjonction d'une coquille de diélectrique. Nous découpons cette partie en deux, suivant la géométrie prise par le dépôt de diélectrique, à savoir i) un dépôt semi-conforme constitué par l'ajout d'un diélectrique PECVD de même épaisseur que celle du diélectrique sur lequel repose le fil et ii) un dépôt conforme réalisé par PECVD sur une structure suspendue constituant par là-même un cas idéal.

Nous basons les calculs réalisés ici pour les cœur-coquille sur une généralisation de la théorie de Mie appliquée au cas de cylindres coaxiaux permettant de discriminer l'absorption ayant lieu dans le cœur de celle classiquement calculée pour le cœur coquille. Ces calculs, dérivés par ailleurs au laboratoire, permettent d'examiner le cas des cœur-coquille ayant une coquille de diélectrique d'absorption arbitraire, et donc de simuler des systèmes réels.

i) Cas semi-conforme:

L'approche numérique menée en premier lieu sur un cœur coquille Si-SiO_2 (le SiO_2 étant légèrement absorbant) indique un gain de l'absorption moyenne pouvant atteindre un facteur 3 sur des intervalles spectraux significatifs. L'analyse des profils de champ EM indique que le gain d'absorption à une longueur d'onde donnée provient des modulations du couplage entre la lumière et les modes dégénérés à l'énergie en question dont l'ampleur peut être très différente d'un mode à l'autre à l'image du recouvrement entre la coquille et la distribution du champ pour un mode donné.

L'expérience est en bon accord avec la théorie, les pics d'absorption et leur décalage étant bien reproduits, et montre un facteur d'augmentation du photocourant toujours supérieur à l'unité à l'issue du dépôt de SiO_2. L'écart expérience-théorie du facteur d'augmentation, constant avec la longueur d'onde, est interprété comme provenant d'un léger changement de rendement quantique interne consécutif au dépôt de diélectrique.

Pour un cœur de diamètre donné nous calculons l'absorption, intégrée ou non sur le spectre visible, du cœur en fonction de l'épaisseur de SiO_2. Un effet interférentiel de type Fabry-Pérot est mis en évidence avec une périodicité en épaisseur de diélectrique visible sur tout le spectre d'absorption. D'autre part, le photocourant théorique calculé en illuminant un fil cœur coquille par un spectre solaire AM1.5 montre un gain significatif au cours des 80 premiers nanomètres d'adjonction de coquille pour ensuite osciller avec une amplitude moindre. Nous mettons également en évidence un effet clair du paramètre de taille, qui varie comme le rapport du diamètre à la longueur d'onde, sur les gains d'absorption en

TE et TM. Si les fils absorbent d'autant plus en TE et TM que leur diamètre est grand, le gain relatif d'absorption entre un grand et un petit diamètre de cœur est plus fort en TE qu'en TM du fait de l'existence de charge liées à l'interface cœur coquille pour l'excitation TE, dont l'influence va en décroissant lorsque le diamètre de cœur et l'épaisseur de coquille prennent de l'importance.

Une dernière série d'expériences menées dans le cas semi-conforme vise à déconvoluer l'effet réfractif de l'effet d'absorption de coquille dans l'absorption du cœur seulement. L'adjonction d'une couche superficielle de nitrure de silicium PECVD en lieu et place d'une couche de dioxyde de silicium d'indice de réfraction moins grand doit permettre selon nos calculs un meilleur couplage de l'onde incidente au cœur. Si à l'issue du dépôt de diélectrique le décalage des raies d'absorption expérimentales est bien reproduit par nos simulations, il n'en est pas de même pour le gain de photocourant qui s'avère être très largement inférieur à l'unité. Ce constat expérimental s'explique par une sous estimation du coefficient d'extinction du nitrure utilisé, ayant pour effet de diminuer considérablement le flux lumineux arrivant sur le cœur de silicium. Ce résultat met en lumière la nécessité d'élaborer des couches antireflet de coefficient d'extinction extrêmement faible dans le bleu qui constitue la région où la majeure partie de l'énergie est absorbée en cas d'excitation en incidence normale.

ii) Cas conforme:

Plusieurs dispositifs à fil unique suspendus ont été fabriqués, avec un espacement substrat fil de 700 nm, permettant de limiter, voire d'annuler tout recouvrement spatial entre les modes observés dans les fils et ceux du substrat. Lorsque le fil n'est pas recouvert de diélectrique, l'accord expérience théorie est meilleur que dans le cas i), apportant une preuve supplémentaire de la bonne description des processus d'absorption de lumière par la théorie de Mie.

A l'issue de l'adjonction de diélectrique, l'exaltation de l'absorption en lumière non polarisée ou polarisée TE et TM est bien reproduite. Plus important encore, les polarisabilités après plusieurs dépôts successifs sont elles aussi reproduites expérimentalement. Bien que la polarisabilité soit proche de l'unité en raison des diamètres de départ importants du cœur, cet accord avec les calculs suggère que pour les petits diamètres un fort gain d'absorption en polarisation TE peut être attendu par un simple recouvrement avec une coquille de SiO_2.

Summary

The study of light absorption in NWs is highly regarded in literature[**21**][**22**][**51**][**23**] [**20**] with serious effort in understanding the light matter interaction, owing to their potential application in solar cells. Thus before beginning the study we take a short glance at the history of previous efforts for light absorption in single NWs. The first results were performed on silicon NWs of big diameters of $\approx 900nm$ by M. D Kelzenberg et al.[**21**], on as grown unintentionally n-type NWs with the junction fabricated by Al diffusion in NWs from contact. In these structures since the diameter of NWs were thick, a bulk like decrease in external quantum efficiency was observed with increasing wavelength which was closely modeled by the authors with coherent and incoherent thin film absorption, with the former accounting for the local maxima and minima in absorption peaks and the latter accounting for the global absorption line-shape. A shift from the absorption peaks was seen by L. Cao et al.[**22**] in different diameter NWs when studying Ge NWs of $\approx 10 - 100\,nm$ radius. A wavelength dependent light absorption was evidenced in these thin NWs which the authors explain by existence of leaky mode resonances(LMR) with the justification that the light is coupled more efficiently in the NW at the resonance conditions, which exists only for a particular combinations of wavelength and NW radii. The same authors further expand their study to Si NWs[**23**] where they implement the Lorentz-Mie formalism for correlation with experimental data. They observe a similar absorption dependence on wavelength and radii but due to different dielectric properties of Si the absorption enhancement is modest compared to Ge. This change in absorption can also be transformed to change in scattering properties of NWs which has triggered interest due to its intriguing properties[**51**], with large scattering and absorption efficiencies[**52**]. An interesting observation from the Mie theory seen in above reports was to have absorption and scattering efficiencies far exceeding the limiting unity case for bulk, a phenomenon which is unique to nanostructures. Although such high absorption efficiencies are already possible, theoretical studies first performed by W. F Liu et al.[**53**] suggest the possibilities of further enhancement of absorption by coating the NWs by high dielectric constant shells.

In the literature so far the absorption studied on individual NWs is only performed on unintentionally doped NWs and thus other methods(like joule heating) were used to induce a junction for intrinsic fields in the device or external bias needs to be applied to generate extrinsic fields throughout the NW. These systems although sufficient for studying the light absorption do not quite replicate the current photovoltaic devices where intrinsic field are obtained by fabricating/growing different p-n junctions[**54**]. Towards this goal we begin in this part of thesis, the study on optical properties of various as-grown p+i/n+i axial and p-i-n core shell NW diodes. In the second half, we move towards engineering this light absorption in NWs and finally study an ideal test configuration for getting a perfect experimental confirmation.

CHAPTER 8

Experimental setup & methods

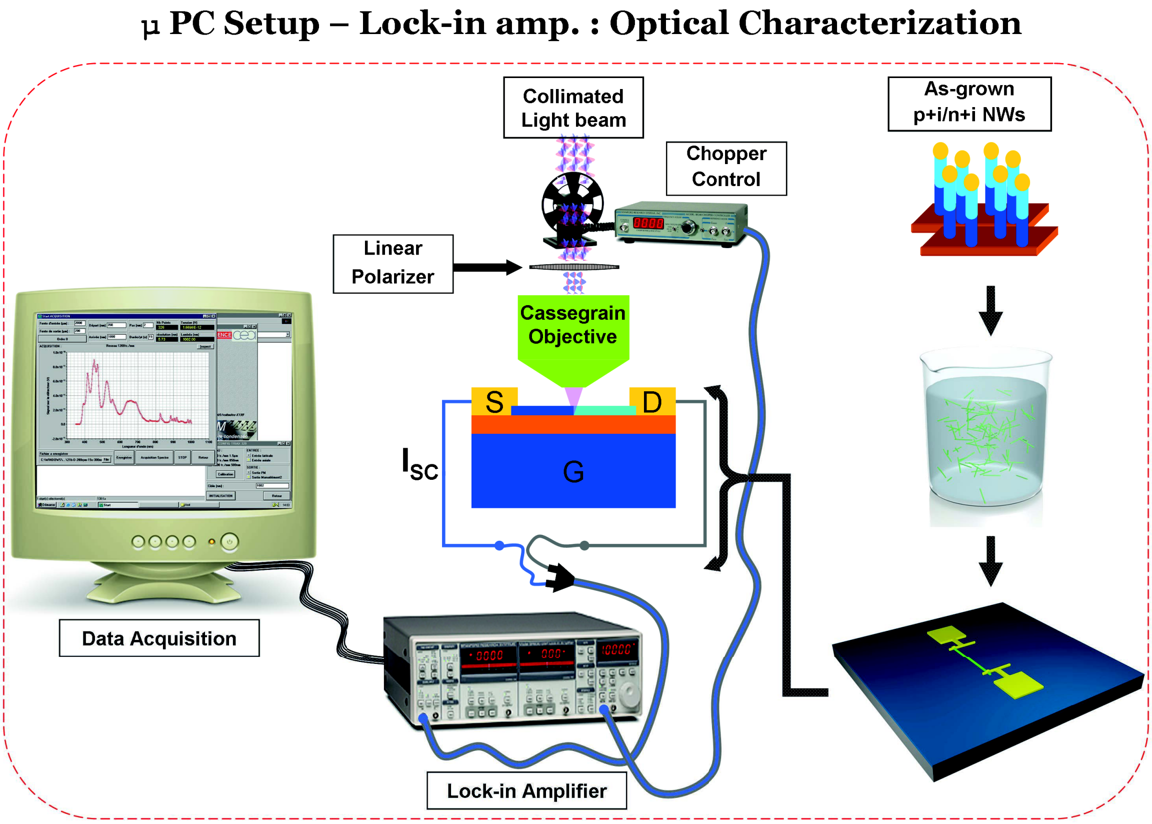

FIGURE 8.0.1. Optical setup-Lockin amplifier: Spectral measurements

The optical setup was home made and was built at the beginning of the PhD, in parallel with the first electrical characterizations on doped NWs. In our setup, monochromatic light is selected from panchromatic source which is then focused on the NW diode generating photocurrent. The core of optical setup consist of a 75W Xenon Light source and the light from the lamp is focused on the input slit of the monochromator, the output of which is connected to lens assembly which focuses light on the sample.

The Xe light source is an optimum choice for photocurrent measurements since the output intensity is almost constant in the area of interest from 350nm to 800 nm. The Xe light source we used had a UV blocking layer to avoid ozone production at these wavelengths which makes the light output threshold of the lamp at ≈370nm. The monochromator was programmed to work on grating blazed at 500 nm, implying a well controlled and optimized output power between 350 and 850 nm, which covers the visible spectrum. The monochromatic/panchromatic[1] light passes through focusing lens assembly at the exit of monochromator consisting of three achromatic doublets where the first lens collimates the light. This is followed by x4 beam expander giving a more collimated light output. The collimated light then passes through first beam splitter. This beam splitter along with transmitting the input light also reflects the lights from white LED source placed perpendicular to the Xe source beam line for illumination of the sample surface . The beam is then transmitted through second beam splitter and falls on the input of a 32x Cassegrain objective which focuses the beam on the sample surface. The light from the sample is reflected back in the Cassegrain to the second beam splitter which reflects the light 90 degrees onto a CCD camera for sample viewing (field of view calculated to be 250 μm). All the lenses used in the optical assembly have the relevant antireflective coating to minimize the power losses. In addition, to reduce the chromatic aberration effects, we worked with achromatic refractive elements.

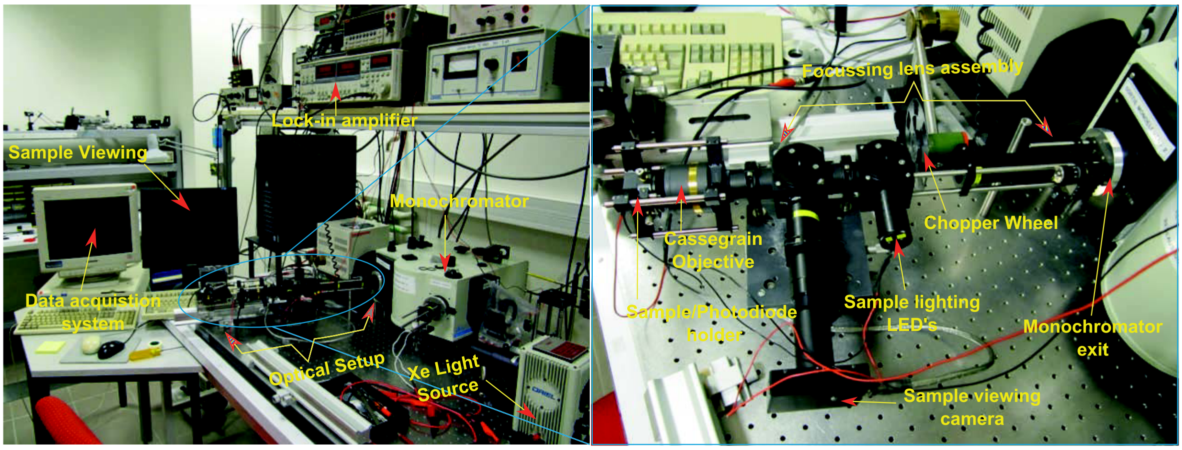

FIGURE 8.0.2. Image of the home built optical setup

---

[1] Setting the monochromator to 0th order reflects most of the input light to output slits

The spectral measurement of photocurrent requires a dedicated current acquisition from the sample with triggering synchronized with the monochromator. Since the photocurrent produced by the device is very small (few tens of pA), the signal is almost completely lost in the noise without the use of a low pass filter and an amplifier. Thus we use high gain lock-in amplifier to increase the signal to noise ratio in photocurrent measured. The schematic of this setup is shown in Fig 8.0.1. A picture of the actual setup is shown in Fig 8.0.2 where the different components can be compared with the schematic. The photocurrent signal is then fed in to the lock-in amplifier which compares the phase of the the chopped beam trigger signal and the photocurrent signal eliminating all the noise at other frequencies. In this configuration due to low intensities of signal range a high quality shielded coaxial cables (to reduce the influence external noise sources) must be used with one of the two contact probes connected to the shell and the other connected to the core of the coaxial cable, to avoid overloading of the lock-in amplifier. To reduce even more the effect of external electromagnetic perturbations on the signal, to secure the sample handling and to avoid electrostatic discharges during the connection, we have made a special sample holder equipped with shielded manipulators directly connected to the lock-in and then set at the same potential. Indeed, bonding the samples on typical holders and then connecting the external pins of the holders to the optical setup has several drawbacks. The technique was tested with our devices but the NWs were mostly destroyed during bonding, transport or in external connections. Moreover this method has an drawback of inflexibility in reuse of sample since the bonding is permanent.

The computer acts as the data acquisition system by controlling the monochromator (slits, blaze wavelength, grating orientation and hence the output wavelength) and fetching the lock-in amplifier output. The monochromator parameters for each scan are set to wavelength step of 1 or 2 nm and a duration per point of 5 s or 10 s respectively. The input slits and output slits are set to 2 mm and 200 µm respectively and the wavelength was swept from 350 nm to 1000 nm for all the samples.

Since the lock-in amplifier measures the first sine component of the input signal[2] , a device generating an instantaneous photocurrent of “I” amperes will not be measured by the lock-in with the same value but with a 0.45 correction factor so that $I_{lock-in} = 0.45I$.This

---

[2] Chopped signal has square waveform which can be expressed by Fourier series as a sum of infinite sine components

relation is important if one requires a quantitative estimate of the current generated by a NW and is necessary in later on for estimation of the external quantum efficiency of our devices.

The optical setup was later modified to include a linear polarizer after the chopper wheel. The polarizer can be rotated with polarization axis parallel or perpendicular to the NW giving a transverse electric(TE) or transverse magnetic (TE) polarized light. This adds one more degree of freedom in the optical measurements and we can now include a study of the dependence of absorption on incident light polarization.

CHAPTER 9

Photocurrent on single Si NW

In the Chapters 4 & 5 we saw the electrical response of the NW diodes and diffusion properties of carriers in these NWs junctions. These studies helped us gain a deeper insight on the junction and surface quality of our as-grown NWs. In this section we begin with micro-photocurrent(μPC) measurements to study the electrical response of NWs under optical excitation. The preliminary study begins with measuring the junction IV under dark and under illumination as shown previously in Fig. 5.2.6. The illumination is performed by tungsten lamp on the IV setup or the illumination setup shown in Fig. 8.0.2 with monochromator set to 0th order. This gives us a basic idea of the photocurrent generation capacity of the device. The time response of the open circuit voltage and short circuit current gives us the transient response of the device with on/off slope and reproducibility of photocurrent probed for each on/off cycle to see the influence of surface traps.

9.1. NW photo-response

As we discussed above, the light from the Xe light source passes through the monochromator, various beam splitters and lenses before falling on the sample and thus is highly modified in the process, each element having its own optical response. The Xe light source also has some modulations over the spectra and strong florescence lines between 800-1000 nm which induces artificial peaks in photocurrent spectra due to high light intensities of these lines. Due to above reasons the photocurrent spectra cannot be compared directly with the theoretical response, but needs to be calibrated/normalized according to the spectral power density falling on the NW. Thus we calculate the NW response (responsivity[1]), for each device by normalizing the NW photocurrent in I_{nw}(A) with the photo-diode current[2] I_{PD}(A), as measured by replacing the sample by the photo-diode in Fig 8.0.1. This gives

---

[1] It is defined as the electrical output generated by a photo-diode per optical power falling on it.

[2] Photodiode current is measured using the same optical setup by replacing the NW with well calibrated commerial Si photodiode with a 5μm aperture.

us a dimensionless quantity signifying the current generated by device calibrated with respect to a commercial photo-diode for the same illumination. This ratio is then multiplied by the responsivity R_{PD}(A/W) of the commercial photo-diode obtained from the data-sheet to get the responsivity R_{nw}(A/W)[3] of the NW device.

The Fig 9.1.1 shows optical measurements on a typical p+i Schottky NW diode. The Fig 9.1.1a shows the photocurrent raw spectra acquired directly from the lock-in amplifier. The Fig 9.1.1b shows the similar photocurrent measured on commercial photo-diode which is illuminated through 5μm aperture placed at the focal point of the Cassegrain objective. The plot in Fig 9.1.1c is the responsivity of the commercial photo-diode extracted from the supplier data-sheet and finally the Fig 9.1.1d shows the actual NW responsivity which is calculated from above plots by the relation $R_{nw} \approx \frac{R_{PD} I_{nw}}{I_{PD}}$. As a reminder, the responsivity in A/W is defined as the ratio between the output photocurrent and the input optical power. Thus $P_{PD} = I_{PD}/R_{PD}$ is the integrated optical power of the focus spot (in Watts) falling on and around the NW, which makes R_{NW}, as presented above, an artificial responsivity for all the illuminated area on the sample (illumination on NW + surrounding). The responsivity is closely related to the external quantum efficiency by

$$EQE = 1240 \times Responsivity(A/W)/\lambda(nm) \tag{9.1.1}$$

As we will see later, it is important to note that for correct evaluation of EQE, an exact calculation of the responsivity should be done by including photocurrent densities (photocurrent/illuminated active area) for both photodiode and the NW devices. This can be viewed as a rescaling of the optical power falling on photodiode (P_{PD}) in the responsivity formula into the optical power falling on the NW (P_{NW}) by a applying a correction factor equal to the ratio between the wire active area and the illuminated photodiode area. However, since the ratio of (illuminated active area on NW)/(illuminated area on photodiode) remains nearly the same, the responsivity will only be modified by a constant factor whatever the wavelength and can be used for comparison with theoretical absorption efficiency by dividing the responsivity by $\lambda/1240$ as seen from Eqn 9.1.1.

---

[3] Ideally the photocurrent per unit area of illumination should be considered, but since the ratio is approximately constant over the spectra and with 5μm aperture on photodiode for our setup, the proportionality is maintained.

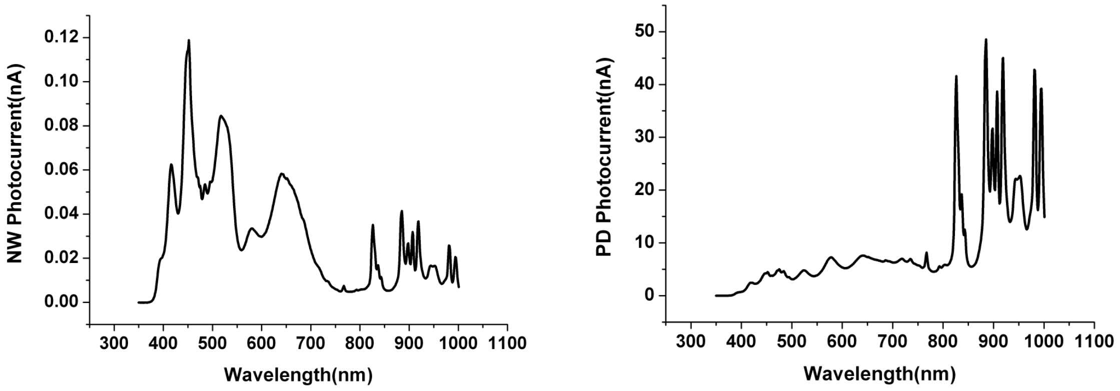

(A) Photo current spectrum on p-i NW

(B) Photo current spectrum from commercial photo diode

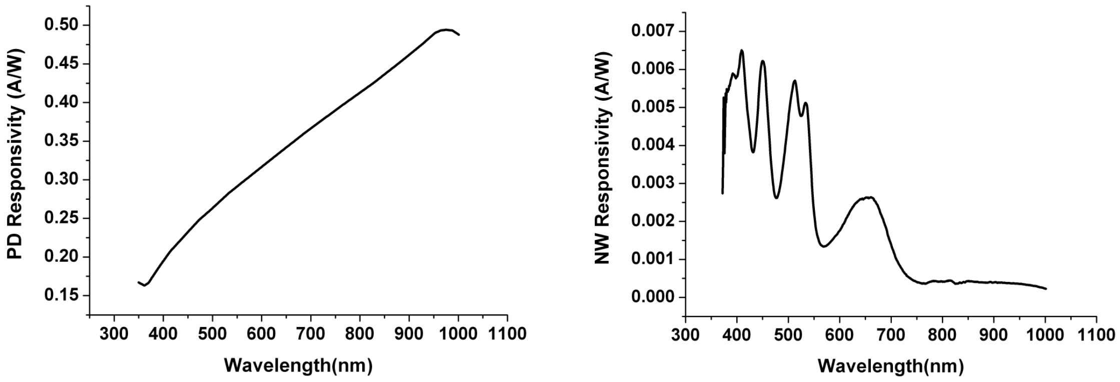

(C) Responsivity of commercial Si photo-diode from datasheet

(D) Responsivity of the NW

Figure 9.1.1. Optical measurement on p+i NW

The responsivity of the device seen from above figure comprises of various modulations with maxima's and minima's over the spectra. The devices were fabricated by lying NWs on Si substrate with 200 nm SiO_2 and thus the response could arise from the absorption modulation by Fabry–Pérot interferences in the underlying oxide. To prove the insignificance of the substrate interference effects in the responsivity of measured NW, similar measurements were performed on different substrates with a Si_3N_4 layer replacing the SiO_2 layer or by changing the substrate entirely to for e.g. glass as shown in Fig 9.1.2.

The above figures for nitride and glass substrate show similar spectral variation as obtained for oxide coated substrate. This implies that the spectral modulations thus seen cannot be due to the substrate interference effects. Another possibility could be that the

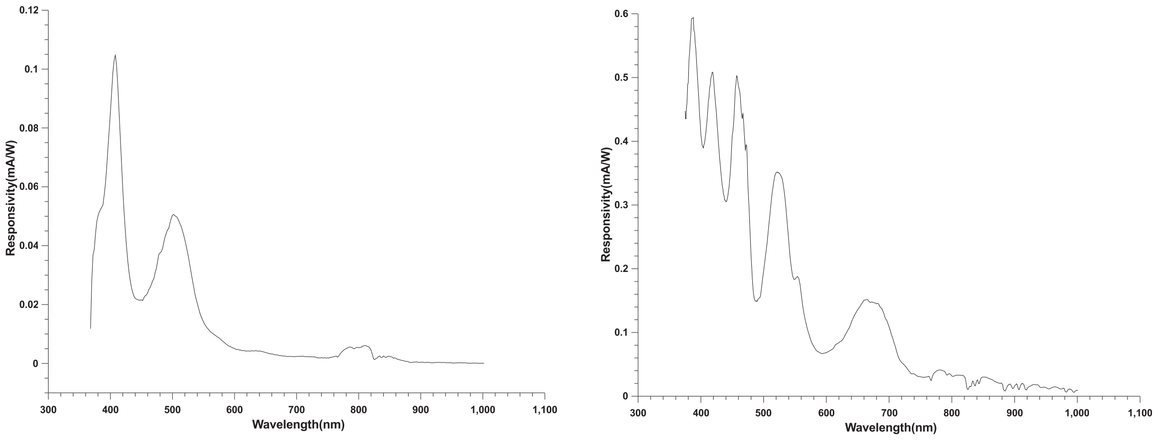

(A) NW Responsivity on 200nm Si_3N_4coated Si substrate

(B) NW Responsivity on 60μm Glass substrate

FIGURE 9.1.2. Typical responsivity on $Si_3N_4$and glass substrates for p+i NWs

peaks depend on the type of junction. To answer this question we performed spectral photocurrent measurements on other junctions like axial n+i and core shell pin NWs.[4]

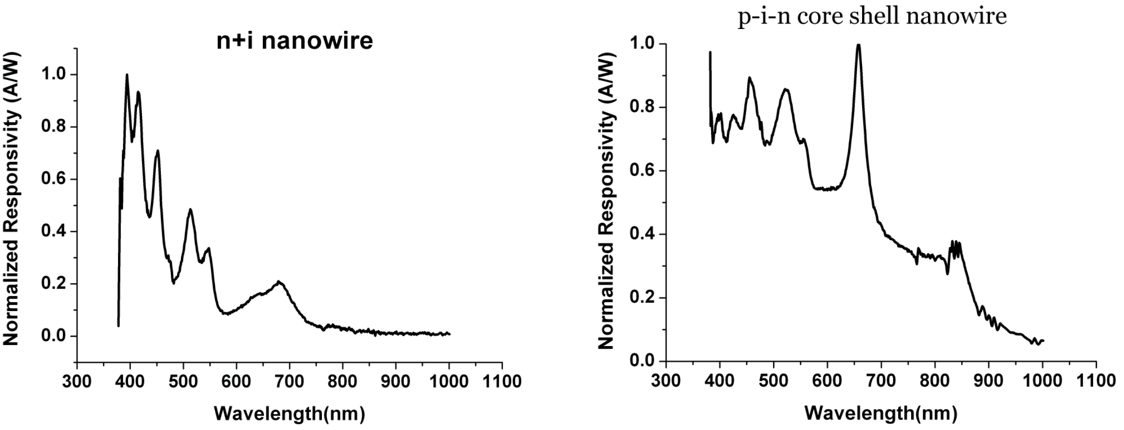

(A) Normalized response of a typical n+i NW

(B) Normalized response of a typical p-i-n core shell NW

FIGURE 9.1.3. Photocurrent spectra on various junctions

The results are shown in Fig 9.1.3, from which it is quite clear that peaks analogous to p+i junction NWs are observed also in n+i axial and p-i-n core shell junction devices. The similarity in the spectra of various junctions proves that the type of junction or the doping

---

[4] We would like to remind the readers that although pin structures are more suitable for photovoltaic application due to a large built in potential, working pin core-shell devices were only fabricated in the latter half of the PhD and thus most of the optical measurements were performed on axial p+i or n+i NWs.

(p+i/n+i) do not suffice to explain the presence of peaks in the responsivity plots[5]. Thus from the above experiments we can conclude that the characteristic peaks in responsivity spectra should be linked to topography and morphology of the NWs and are nearly independent on the doping, junction type or the substrates. A theoretical interpretation of the phenomenon can shed some light on the unusual shape of the absorption spectrum. Towards that goal we begin to elaborate the theoretical framework for light absorption in NWs.

9.2. Theoretical interpretation

To gain an understanding of the peaks in the response spectra of the NWs one needs to understand the light absorption mechanism that subsists at such nanoscale dimensions for NWs. We try to base our understanding on the current theoretical framework of light scattering by nanostructures, first developed by Gustav Mie for gold colloids in suspension in 1908.

9.2.1. Basic concepts of the Mie theory.

It is well known that for a beam of light incident on a glass slab that, a part of the light is reflected, a part is absorbed and remaining is transmitted through the slab. The light which is reflected and transmitted from the slab can also be combined under a unified representation of scattering, where scattering implies a phenomenon of excitation of the obstacle (a glass slab in this case) and a re-radiation by reflection and transmission processes. The interpretation is much more clearer when applied to a non uniform obstacle small compared with the wavelength as shown in Fig. 9.2.1. The Fig 9.2.1a shows a schematic of an incident plane wave with its electric and magnetic field components $(\mathbf{E}_i, \mathbf{H}_i)$ incident on an arbitrary obstacle with field in the object as $(\mathbf{E}_0, \mathbf{H}_0)$ and scattered field as $(\mathbf{E}_s, \mathbf{H}_s)$. For small objects, the concept of reflection and transmission do not hold and are replaced by wave scattering.

The Fig 9.2.1b sets the various energy parameters of interest that are related to different light matter interaction processes with which we are going to deal with later. This figure shows the rate of energy transfer in different regions with incident beam scattered by an arbitrary obstacle and light detected by a detector placed far away from the obstacle. Here the rate of energy transfer in different sections can be divided into W_a, W_s, W_e and W_i for the absorbed, scattered, extinction and incident light. When the incident light falls on the

---

[5] The intensity of modulation is different between n+i and p-i-n core shell NWs which could in fact depend on the type of junction due to more stronger fields and more area for light absorption in p-i-n NWs.

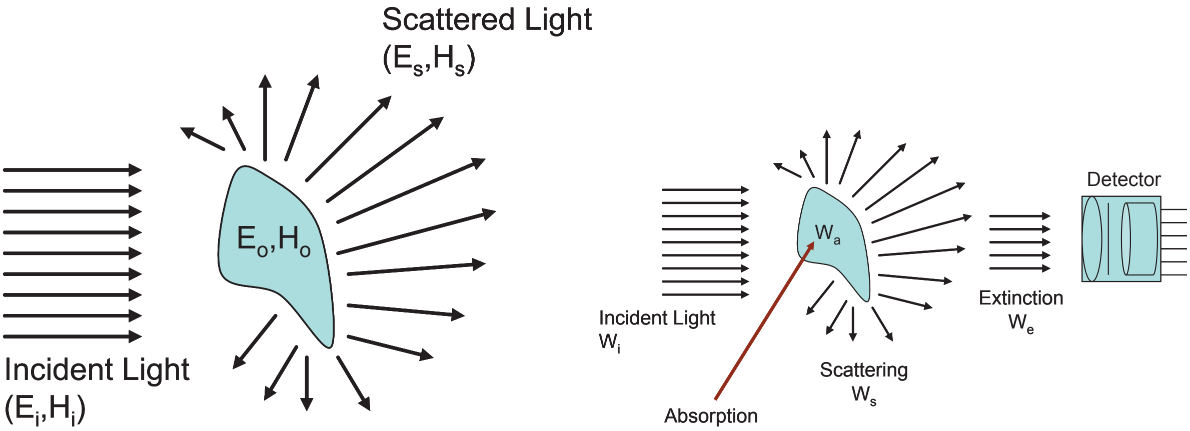

(A) Light scattering from obstacle with EM field annotated in different regions

(B) Extinction of light as seen from detector with rate of incident, absorbed, scattered and extinction energies depicted.

FIGURE 9.2.1. Scattering by an obstacle (Adapted from Bohren & Huffman[**55**])

obstacle, some part of it is absorbed in the obstacle and the other in surrounding medium depending on its dielectric properties, the rest being scattered in all directions with extinction/attenuation in the incident beam being detected by the detector due to the presence of the obstacle.

Therefore, for an obstacle in an arbitrary medium, the extinction is the sum of all the processes that cause loss/attenuation of energy. This includes the removal of energy from the beam by attenuation in the medium, scattering by the obstacle and finally the absorption in the obstacle. Thus the rate of change of extinction energy (W_e) can be formulated from the rate of loss of incident energy(W_i), rate of change of absorbed energy (W_a) by the obstacle and the rate of change of scattered energy $(W_s)^6$ by the obstacle as $W_e = -W_i + W_s + W_a$. For a non absorbing medium the W$_i$ term vanishes to give $W_e = W_s + W_a$, or in words $extinction = scattering + absorption$. Alternatively the extinction can also be calculated from the data of the scattering amplitude in the forward direction [7]. Following the description in[**55**], to calculate the above rate of change of different energies, we assume a imaginary sphere of radius r surrounding the obstacle. Using the complex representation for the Electro Magnetic (EM) fields, it can be shown that the time averaged Poynting vector components for incident, scattered and extinction fields are given by

---

[6] Note that the rate of transfer of the different energies is the rate of the transferred power multiplied by the unit time. Thus W_e, W_i, W_s and W_a actually denotes power instead actual energies.

[7] This conclusion is reached by the optical theorem[**56**]

$$\text{(9.2.1)}\qquad \mathbf{S}_i = \frac{1}{2}Re\left\{\mathbf{E}_i \times \mathbf{H}_i^*\right\}, \quad \mathbf{S}_s = \frac{1}{2}Re\left\{\mathbf{E}_s \times \mathbf{H}_s^*\right\}, \quad \mathbf{S}_{ext} = \frac{1}{2}Re\left\{\mathbf{E}_i \times \mathbf{H}_s^* + \mathbf{E}_s \times \mathbf{H}_i^*\right\}$$

If the fields are known, the net rate of exchange of electromagnetic energy through the surface A made by the imaginary sphere is given by

$$\text{(9.2.2)}\qquad W_e = -\int\limits_A \mathbf{S}_e \cdot \hat{\mathbf{e}}_\mathbf{r} dA, \qquad W_s = -\int\limits_A \mathbf{S}_s \cdot \hat{\mathbf{e}}_r dA.$$

where $\mathbf{S}_{e,s}$ is the time averaged Poynting vector and $\hat{\mathbf{e}}$ is the unit vector perpendicular to surface A. One can easily show that the W_i vanishes if the surrounding medium is non absorbing. Evaluation of W_a is straightforward by using the relation $W_a = W_e - W_s$. This approach gives access to the absorbed energy in the object based on the knowledge of the external parameters W_e and W_s and does not require the calculation of $\mathbf{E_1}$and $\mathbf{H_1}$, where $\mathbf{E_1}$and $\mathbf{H_1}$ are the internal electric and magnetic fields in the NW respectively. Conversely, if $\mathbf{E_1}$ and $\mathbf{H_1}$ are known, we have

$$\text{(9.2.3)}\qquad W_a = -\int\limits_C \mathbf{S_1} \cdot \hat{\mathbf{e}}_\mathbf{r} dA$$

where C is the surface of the object and $\mathbf{S_1} = \frac{1}{2}Re\left\{\mathbf{E}_1 \times \mathbf{H}_1^*\right\}$.

Next we define the scattering cross-sections from $\mathrm{W_e}$, $\mathrm{W_a}$ and $\mathrm{W_s}$ by normalizing by the incident irradiance I_i by

$$\text{(9.2.4)}\qquad C_e = \frac{W_e}{I_i}, \qquad C_a = \frac{W_a}{I_i}, \qquad C_s = \frac{W_s}{I_i}.$$

These cross-sections can be seen as apparent areas projected by the obstacle which interact with the incident beam. These apparent areas can be very different from the projected area of physical obstacle (G) on the incident beam depending on the experimental condition. The cross-sections further allow us to formulate the absorption, scattering and extinction efficiencies as follows

$$Q_e = \frac{C_e}{G}, \qquad Q_a = \frac{C_a}{G}, \qquad Q_s = \frac{C_s}{G}. \tag{9.2.5}$$

The efficiencies are dimensionless quantities and provide an intuitive view of the effectiveness of light coupling with the obstacle.

9.2.2. Mie theory: Particular case of NWs. The above discussion was very general concerning an arbitrary obstacle, but for understanding the light-matter interaction for the NWs a more focused approach is required to give the solutions for the EM field in the problem of the light interaction between an incident plane wave and an object in the cylindrical geometry. For this we follow the context on light scattering by infinitely long cylinders[**55**], directly inspired from the method originally developed by Mie for the spherical case of colloidal particles.

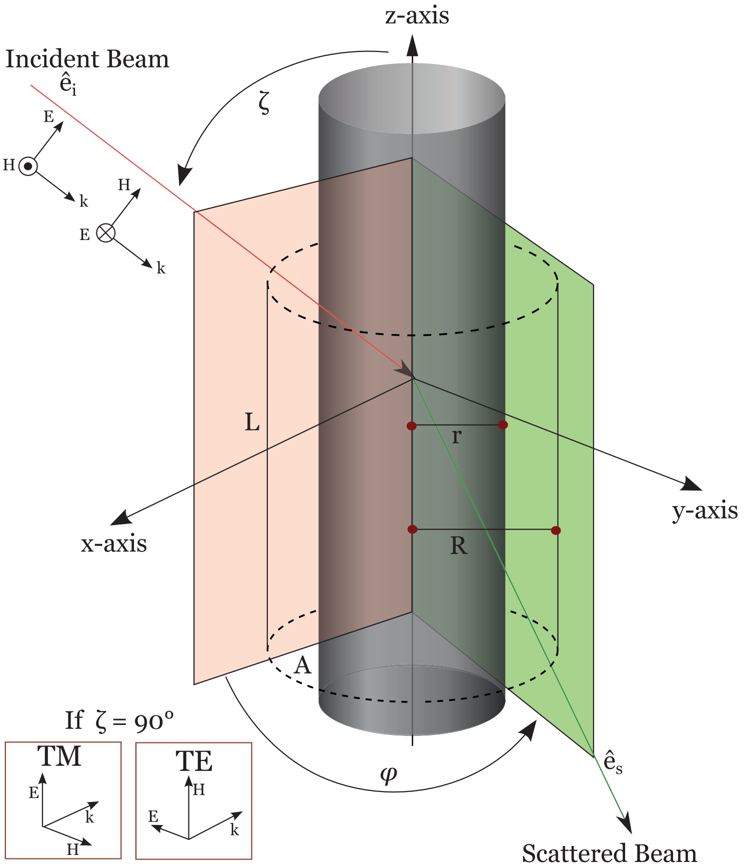

FIGURE 9.2.2. Infinitely long cylinder illuminated by a plane wave

The Fig 9.2.2 shows a schematic of light scattered by an infinitely long cylinder obliquely illuminated by a plane wave. The surrounding medium is assumed to be non absorbing with φ as the angle between the incidence and scattering plane and ζ the angle between the incident beam and the NW axis. The cross-sections obtained for infinitely long cylinders are inherently infinite due to the length parameter, but the light scattered per unit length is of course finite and can be calculated. Thus ignoring the effects of the ends of cylinder, the light scattered per unit length of an infinitely long NW can be approximated by a finite one with ratio W_s/L and W_a/L for a cylinder of length L. This approximation is well satisfied in our case due to high aspect ratios >20 in our NWs. Then following in a similar manner as the previous case of arbitrary obstacle we form an imaginary concentric surface, around the infinitely long cylinder, with the surface area A of radius R and length L. Then the rate at which the energy is absorbed within this volume is given by $W_a = W_e - W_s$, where

$$W_e = RL\int_0^{2\pi}(S_e)_r d\varphi, \qquad W_s = RL\int_0^{2\pi}(S_s)_r d\varphi. \tag{9.2.6}$$

and integration is performed on the radial component of the Poynting vector $\left(S_{e,h}\right)_r$ for a fixed radius r.

The scattering and absorption efficiencies can then be calculated in the configuration I, when the electric field is in the (xz) plane, as

$$Q_{s-I} = \frac{W_{s,I}}{2aLI_i} = \frac{2}{x}\left[|b_{0I}|^2 + 2\sum_{n=1}^{\infty}\left(|b_{nI}|^2 + |a_{nI}|^2\right)\right], \tag{9.2.7}$$

$$Q_{e-I} = \frac{W_{e,I}}{2aLI_i} = \frac{2}{x}Re\left\{b_{0I} + 2\sum_{n=1}^{\infty}b_{nI}\right\}. \tag{9.2.8}$$

Similarly efficiencies for the configuration II, when the electric field is perpendicular to the (xz) plane are

$$Q_{s-II} = \frac{W_{s,II}}{2aLI_i} = \frac{2}{x}\left[|a_{0II}|^2 + 2\sum_{n=1}^{\infty}\left(|b_{nII}|^2 + |a_{nII}|^2\right)\right], \tag{9.2.9}$$

$$Q_{e-II} = \frac{W_{e,II}}{2aLI_i} = \frac{2}{x} Re\left\{ a_{0II} + 2\sum_{n=1}^{\infty} a_{nII} \right\}. \tag{9.2.10}$$

In the above equations a_n and b_n are the scattering coefficients and the size parameter is $x = 2\pi a/\lambda$, with r=a the radius of the NW. In the simplest case of normal incidence($\zeta = 90°$) with a plane wave, which is not so different from our experimental case, the scattering coefficients can be further simplified and are composed of Hankel and Bessel functions of the first kind. We have $a_{nI}\,(\zeta = 90°) = 0$, $b_{nI}\,(\zeta = 90°) = b_n$, $a_{nII}\,(\zeta = 90°) = a_n$ and $b_{nI}\,(\zeta = 90°) = 0$. Then a_n and b_n can be described as below, where m is the complex ratio of the refractive index of cylinder to that of the medium:

$$a_n = \frac{mJ_n(mx)J'_n(x) - J'_n(mx)J_n(x)}{mJ_n(mx)H_n^{(1)\prime}(x) - J'_n(mx)H_n^{(1)}(x)} \tag{9.2.11}$$

$$b_n = \frac{J_n(mx)J'_n(x) - mJ'_n(mx)J_n(x)}{J_n(mx)H_n^{(1)\prime}(x) - mJ'_n(mx)H_n^{(1)}(x)} \tag{9.2.12}$$

and the prime standing for differentiation with respect to the argument.

The efficiencies in unpolarized case for normal incidence can then be calculated by below relation,

$$Q_s = \frac{1}{2}(Q_s^{TE} + Q_s^{TM}), \qquad Q_e = \frac{1}{2}(Q_e^{TE} + Q_e^{TM}). \tag{9.2.13}$$

where TM stands for the configuration I and TE for the configuration II.

With the above relations along with the relation between absorption, scattering and extinction we can calculate the unpolarized absorption efficiency as $Q_a = Q_e - Q_s$. For a given radius the ratio Q_a/E_{ph} (E_{ph} photon energy) is proportional to the NW responsivity R_{NW}, and thus can be correctly correlated with our experimental data.

Figure 9.2.3a shows the responsivity spectra of a NW with ≈225 nm diameter superimposed with the corresponding Mie fit for theoretical case of 220 nm NW for unpolarized case. A nice correlation is observed between the theory and the experimental responsivity

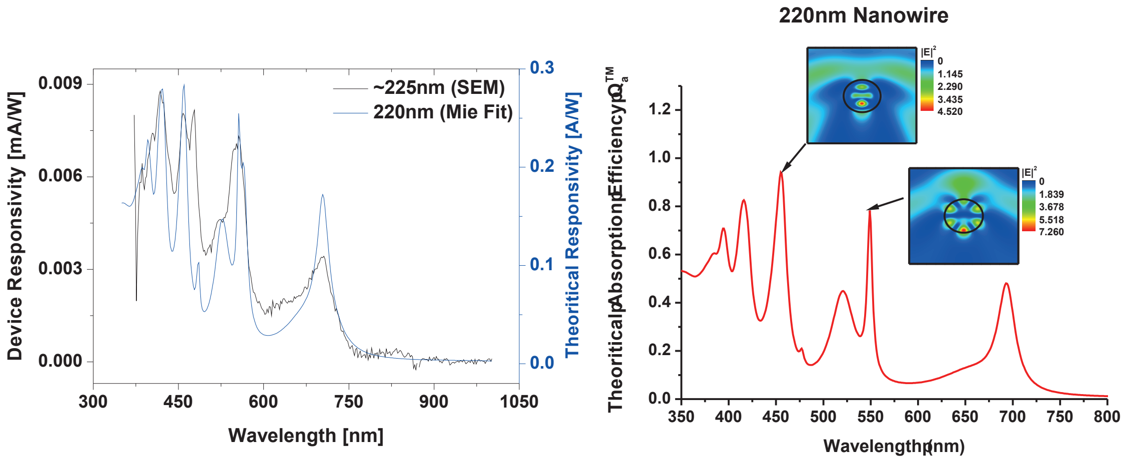

(A) Theoretical Responsivity (Q_a/E_{ph}) vs Experiment R_{nw}

(B) Theoretical Q_a for TM polarization with electric field plots in NW.

FIGURE 9.2.3. Light absorption in NWs. The inset in (B) shows simulated $|E|^2$ field plots in NWs with a plane wave illumination from the top.

suggesting that theoretical description nicely accommodates the experimental case of a NW on a substrate illuminated with focused light.

9.2.3. Formation of modes and modal energy distribution.

Even though theory fits well, the reason behind the enhancement in the absorption is not quite evident. To go deeper in our understanding, we performed analytical simulations of the field amplitudes in and out of a NW when irradiated by a plane wave for remarkable wavelengths. Here we adopt the TM polarized case which is plotted in Fig 9.2.3b for peaks at 455 nm and 549 nm .

The field plots in Fig. 9.2.3b are calculated for a Si NW of 216 nm diameter in the air. The spectrum clearly shows the presence of well defined field localizations at specific places in the NW core with large enhancement factors compared to the background field, the incident electric field strength being set at 1 $V.m^{-1}$. This particular shape of field distribution in the NW core is seemingly well defined as the guided modes usually observed in waveguides which implies that we are in a resonant system. Thus going by that analogy, there is formation of electromagnetic modes in the core of the NW at particular combinations of wavelength with the diameter and dielectric constants of the wire and surrounding. The intensity of the modes depends on the strength of the light coupling in the NW core. From the corpuscular point of view, and at resonance, we can see a photon as trapped by the wire cavity, turning and being eventually absorbed or finally escaping from the wire due to the inherently leaking nature of these modes.

From the set of equations 9.2.13,9.2.11 and 9.2.12, one can clearly see the absorption efficiency Q_a as the sum of individual absorption efficiencies Q_a^n. The n number has a physical meaning since the radial expansion of the EM fields scales as $e^{in\varphi}$. Thus, for constant n, Q_a^n gives the absorption spectrum of eigenmodes having the same order of symmetry with respect to the wire axis. Actually we have $Q_a^n = Q_a^{-n}$, so that Q_a^n as considered above improperly represents the summation of the absorption at n and $-n$ and physically accounts for photons propagating in the clockwise or anticlockwise directions. For this n, which is also equal to the effective number of wavelengths around the wire circumference, is referenced as the azimuthal number. However, n is not sufficient to fully characterize an eigenmode and another discrimination by the other physical coordinate, namely the radius, has to be done. The radial number l, describing the number of radial field maxima within the cylinder, allows naming a mode as $TM_{n,l}$ or $TE_{n,l}$.

The Fig 9.2.4 shows the absorption spectrum in Fig 9.2.3b splitted in its first 4 n numbers, which are in practice enough to describe the total absorption with a good accuracy, and the curve labeling with the corresponding $TM_{n,l}$ modes. For improving our understanding of the field building up in the wire, we plot on the same figure the squared of the field modulus for the TM_{21}, TM_{22} and TM_{23} modes, taking the $n = 2$ term in the series expansion of the field. In this configuration the plot gives the mode profile in the wire as excited by the relevant harmonic of the incoming plane wave[8]. It can be easily seen that all the mode profiles have a $2n$ symmetry order along the wire axis and an increasing number of radial maxima for decreasing wavelengths. Of interest are the regions of spectral overlap between to different modes. As an example, we plotted the TM_{03} mode which is nearly degenerated with the TM_{22} mode. Fig. 9.2.3b shows the squared modulus of the total field, which has a rather different profile than the two previous modes taken apart. This is of course due to the interference effect.

9.2.4. Light coupling to a NW: an intuitive view. A very intuitive understanding of the light coupling to a NW can be done by comparing the field pattern and the Poynting

---

[8] We could have also set the field at the wire origin arbitrarily at 1, or in other words placed a point source at the origin, set the boundary conditions and finally retrieved the radiated field by the source, but the used approach was more straighforward.

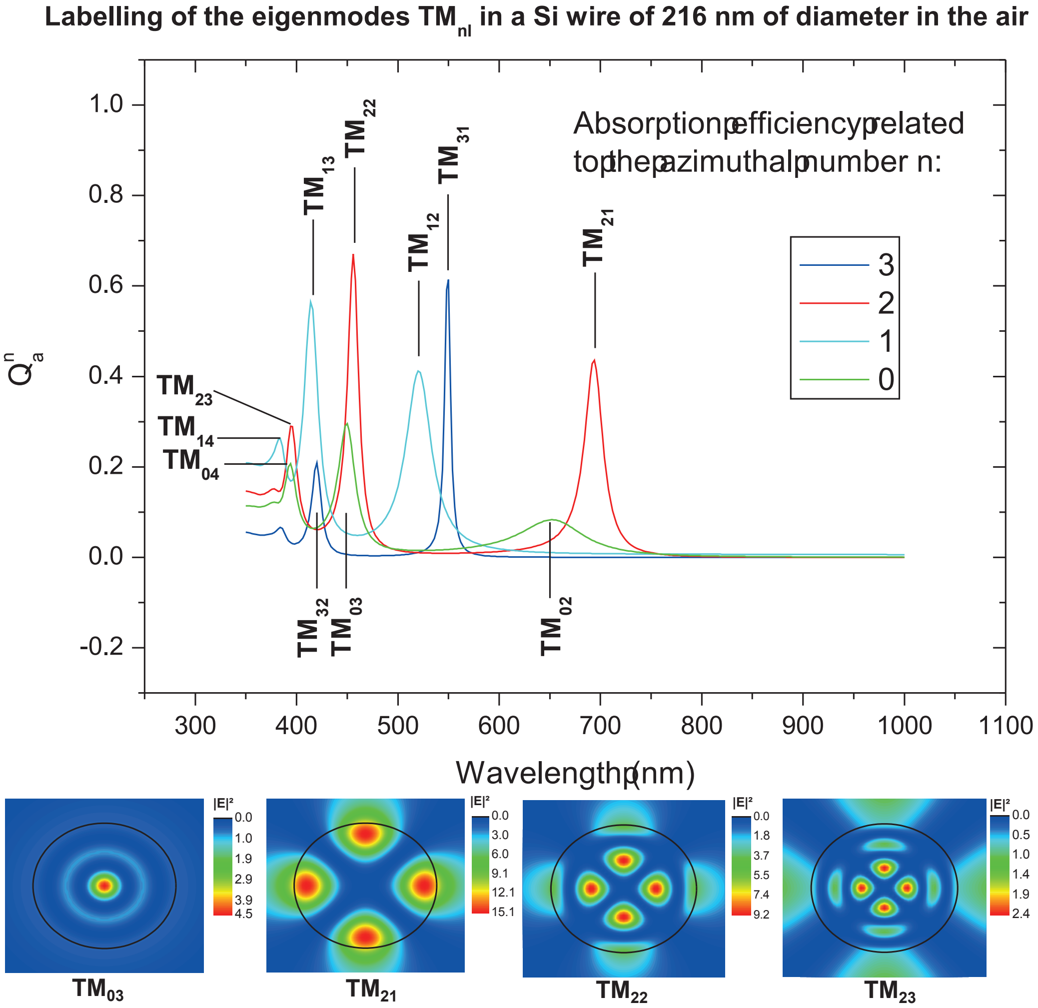

TM_{03} TM_{21} TM_{22} TM_{23}

FIGURE 9.2.4. Decomposition of TM absorption spectra of 216 nm in Si NW in individual modes. The $|E|^2$ field profiles for TM_{03}, TM_{21}, TM_{22} and TM_{23} modes are shown in 2D plots below the graph

vector field in and out of absorption resonance. This is done here analytically for a 220 nm diameter NW in the air illuminated by a plane wave coming from the right side of the field plots shown in Fig. 9.2.5 for resonant ($\lambda = 704$ nm) and non resonant ($\lambda = 490$ nm) conditions (see the joined absorption efficiency spectrum). Here, the electric field amplitude of the incoming plane wave is set at 1 $V.m^{-1}$. For the resonant condition under study, a $n = 2$ mode is formed in the NW leading to significant field intensity in the wire body with 4 field lobes distributed near the wire boundary. More interesting is the case of the Poynting vector field which shows negligible divergence of the upstream energy flow in the far field but rather complex patterns in the wire region with an energy flow vortex associated with each field lobe. These vortices can be viewed as arising from the sum of the leaking energy

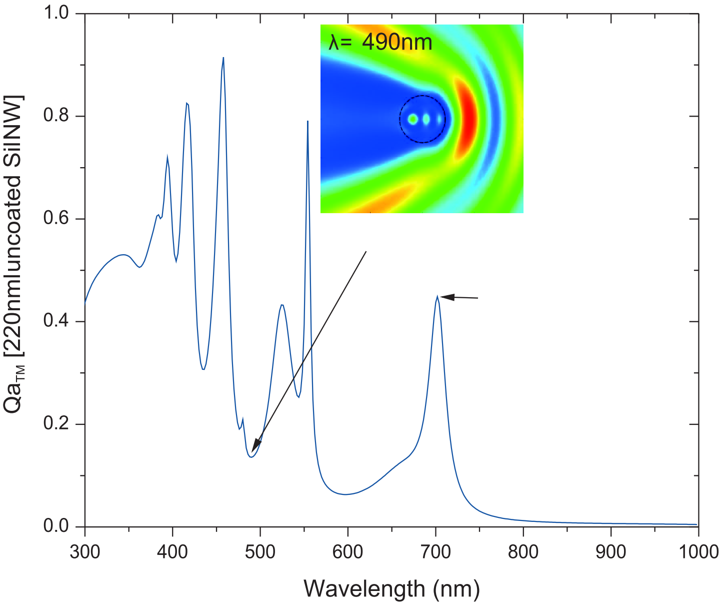
λ= 490nm
QaTM [220nmluncoated SiINW]
Wavelength (nm)
0.0
0.2
0.4
0.6
0.8
1.0
300
400
500
600
700
800
900
1000

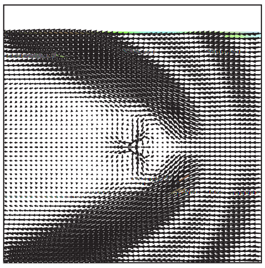

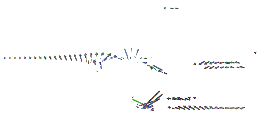

energy harvesting by a nanostructure can occur over an effective cross section well bigger than its geometrical counterpart. Absorption in the wire thus results from the intricate path of the energy flow near the wire surface with multiple entrance and exit processes in the lobe regions associated with an enhanced energy flow. On the contrary, the out of resonance case shows a Poynting vector field gliding on the wire. A very high field strength is observed just in front of the wire surface, which results from the interference between a strongly back-scattered field and the incoming field.

The modes, also tagged as leaky mode resonances in literature have already been shown in passive Ge NW[**22**] or for Si[**23**] NW based devices and active metal-semiconductor-metal Ge NW devices[**57**]. Contrary to the literature we define the active region by doping engineering, similar to current solar cells, which provide intrinsic fields in individual NWs eliminating the need for biasing the NW to extract photocurrent. However the nature of the modes/resonances in the NW remain the same as described before and only depends on the geometry, the dielectric properties of the NW and that of the surrounding medium.

9.2.5. Advantage of the cylindrical coherent absorption over the planar one. Resonant absorptions can also be observed in planar structures such that Silicon On Insulator (SOI), consisting in a top Si layer lying on a 400 nm burried oxide.

The Fig. 9.2.6 shows the absorption spectra of three different thickness SOIs (~100nm, ~160nm and ~190nm) obtained upon external bias. We do observe resonance peaks which can be explained via coherent planar absorption. For comparison theoretical calculations were performed by transfer matrix modeling code developed by G. Burkhard et. al.[**58**] and can be found at [**59**]. The fit performed with experimental slab thickness provided excellent correlation for all the samples, although the magnitude of experimental efficiencies are an order below the calculated ones, which could be due to non ideal measurement geometry[9]. To give an account of the absorption gain in NWs compared to thin films, we also plotted in Fig. 9.2.6 the theoretical absorption efficiencies of Si slabs immersed in the air, whose expression can be found in [**55**] and is considerably simpler than for NWs, and Q_a of Si NWs in the air with a diameter set to the slab thickness. One can clearly see that the absorption efficiency in NWs is close to unity with values exceeding 1 for smaller diameter NWs

---

[9] We used our standard lithographic process for making 2 probe measurements where the distance between the two contacts varies. The substrate was illuminated to have an average distance of around 150 μm between the illumination spot and the contacts.

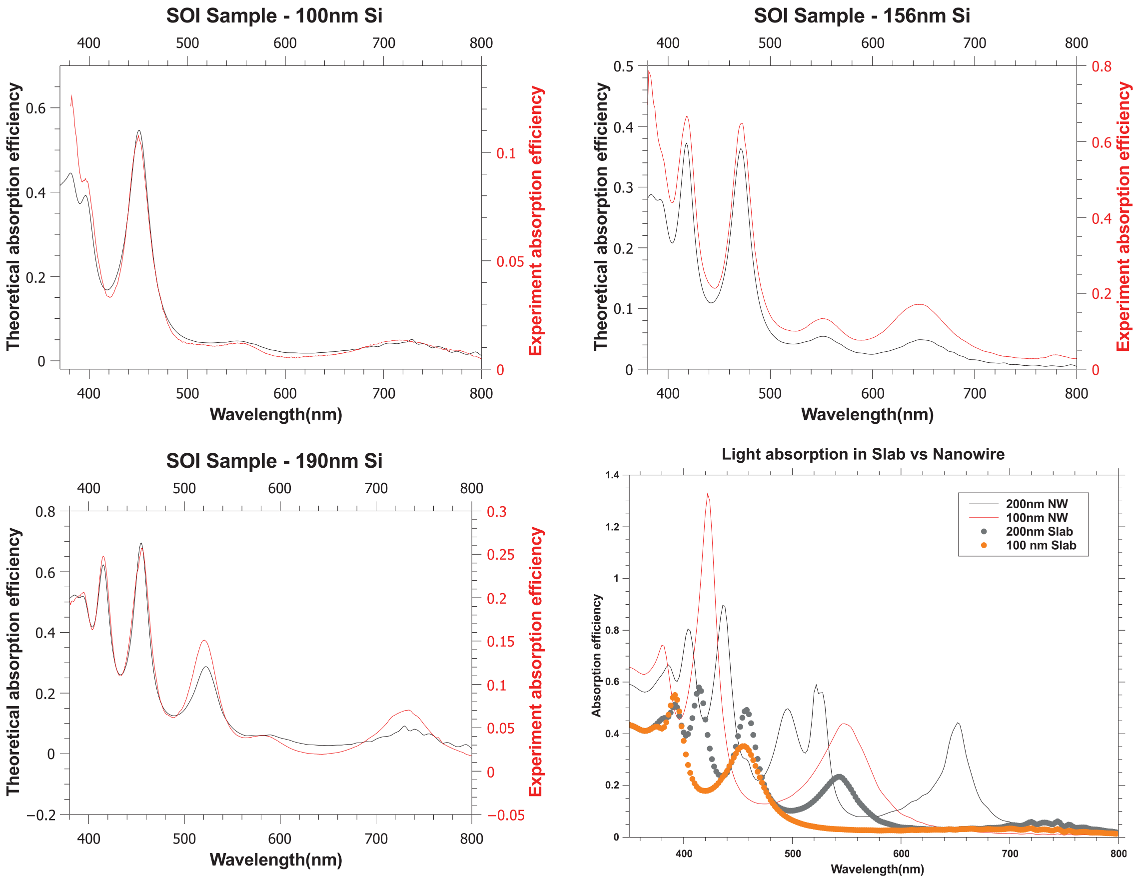

FIGURE 9.2.6. Light absorption in SOI with top Si thickness of ~100nm, ~156nm and ~190nm. The experimental results are compared with theoretical model developed by G. Burkhard et. al.[**58**][**59**]. The analytical spectra of NW absorption efficiency is plotted on the same plot for comparison of absorption enhancement in NWs.. The plot on the lower left shows a comparison between the absorption efficiency over the spectra for 100nm and 200nm thick slab and respective diameters for Si NWs

whereas for the 2D slab the absorption efficiency is close to or lower than 0.8. Even if the resonances arise in both cases from coherent effects in the nano-object, the higher absorption efficiency observed in NWs is due to the particular light path in this structure making the light matter interaction length probably higher than in slabs. Thus NWs provide a significant advantage over their thin film counterpart with more efficient light coupling and absorption, which constitutes one of the motivations of this work.

9.3. Tuning absorption: Diameter & polarization

9.3.1. Absorption diagram.

The theoretical framework in the previous section provides us means to perform analytical calculation for comparison with our experimental data which shows surprisingly good correlations. With the above results we expand the scope of our analytical calculations by including diameter of the NW as another variable, making it a three parameter system with Q_a depending on NW diameter and wavelength. This map of unpolarized absorption efficiency for a single NW in air is plotted as a function of NW diameter on ordinate and wavelength on the abscissa as shown in Fig. 9.3.1 for a plane wave excitation. The diameter range and wavelength range were best chosen to fit our diameters of NWs and the measurement range respectively.

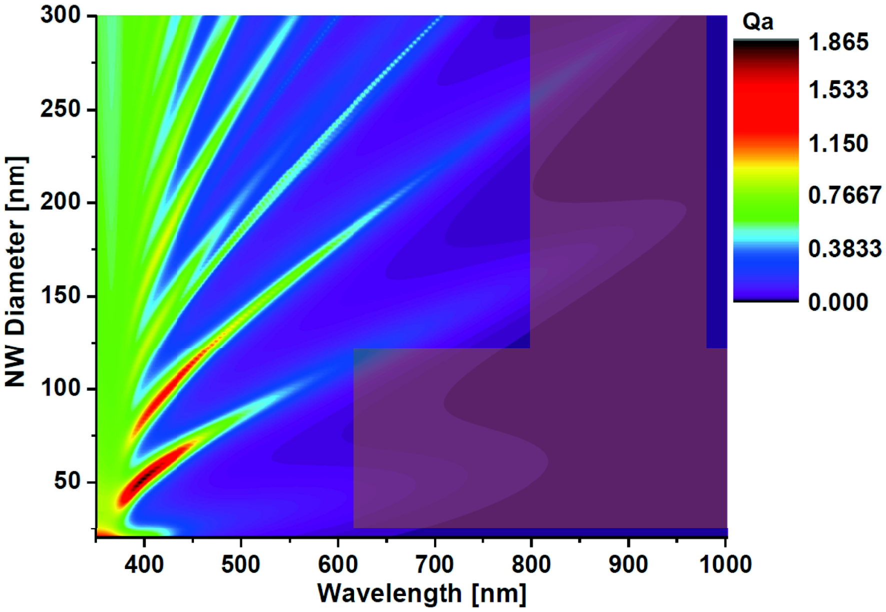

FIGURE 9.3.1. Mapping of the absorption efficiency (Q_a) of single Si NW in the air plotted as a function of the diameter and wavelength for unpolarized excitation.

The sharp contrast in the color scales at lower wavelength are observed over the entire diameter range corresponding to resonances in absorption. Fig 9.3.1 makes it very evident that the magnitude of resonances reduces as we move towards higher diameters and thus the resonant absorptions are less efficient at higher diameters. When the wire diameter is increased further near 1μm the peaks in these microwires can be also easily explained by a coherent 2D interference model. This is nicely elucidated by Kelzenberg et. al., for microwires of ≈900nm diameter[**60**] where a consideration of coherent Fabry-Perot like resonances between the set of parallel facets normal to the beam is sufficient to account for the experimental responses. The microwires in the above case are considered as a planar cavity despite their hexagonal cross section. In our study, the physical cross section of the NWs is below the incident wavelength, which makes the description of the field in our objects by circular like functions more relevant.

9.3.2. Diameter dependance of the photocurrent in uncoated NWs.

To experimentally see the dependence of diameter on wavelength, NWs with well defined diameters were grown and photocurrent measurements were performed on individual NWs. The results are reported in Fig 9.3.2 with distinct NWs ranging from ≈80 nm to ≈225 nm.

The theoretical responsivity $\lambda\,[nm] \times Q_a/1240$ maintains a direct proportionality with the experimental responsivity all across the spectrum and hence should give better fits when comparing theory with experiment. This theoretical responsivity of all the NWs characterized is plotted against the experimental responsivity in Fig 9.3.2.

The theoretical fits show remarkable correlation following the modulations of the experimental response. In all the NWs almost all the peaks in theory can be fitted with experiment with a shift in the peak spectral position with a change in diameter as small as 4 nm within our spectroscopic resolution. The results highlights the fine sensitivity of the technique and can indeed been put to use for applications in size measurement[**61**]. A further analysis of Fig 9.3.2 reveals that the peaks are red shifted when we go from 85 nm NW to 220 nm NW and towards higher diameters as expected from the theory. This shows a strong dependence, even experimentally, of the absorption efficiency on NW diameter. Importantly the plots also exhibit high sensitivity and sharp resonances, with the full width at half maximum of a few tens of nanometers for smaller NWs. These sharp resonances and energy sensitivities can be reverse engineered for fabricating sensors to detect for instance a particular wavelength in an incident polychromatic source or to increase the detector sensitivity when coupled with a light source.

9.3.3. Polarization dependance of the photocurrent in uncoated NWs.

The discussion in previous section on theoretical interpretation of light scattering also provided us an insight on the polarization dependence of scattering and extinction, thus

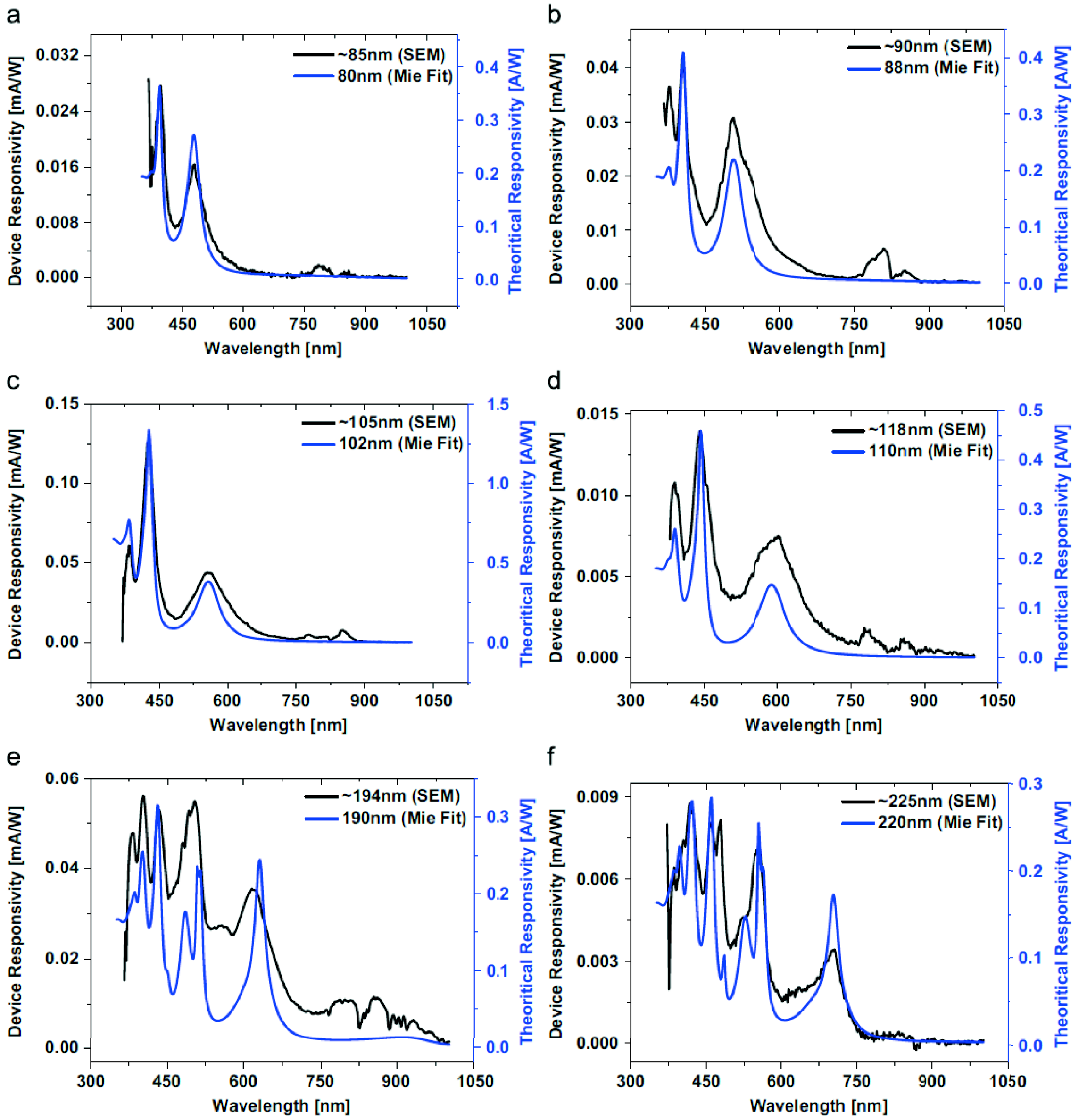

FIGURE 9.3.2. Experimental device responsivity in black and analytical responsivity spectra in blue vs wavelength for different diameters (a) ≈85 nm SEM measured diameter and 80 nm Mie fit (b) ≈90 nm SEM measured diameter and 88 nm Mie fit (c) ≈105 nm SEM measured diameter and 102 nm Mie fit (d) ≈118 nm SEM measured diameter and 110 nm Mie fit (e) ≈194 nm SEM measured diameter and 190 nm Mie fit (f) ≈225 nm SEM measured diameter and 220 nm Mie fit. (Illumination with unpolarized light under normal incidence)

causing absorption to depend on polarization. If we separate the absorption efficiencies for TE and TM polarization based on polarized scattering and extinction equations from Eqn.9.2.13 we get,

$$Q_{a,TM} = \frac{1}{2}(Q_{e,I} - Q_{s,I}), \qquad Q_{a,TE} = \frac{1}{2}(Q_{e,II} - Q_{s,II}). \tag{9.3.1}$$

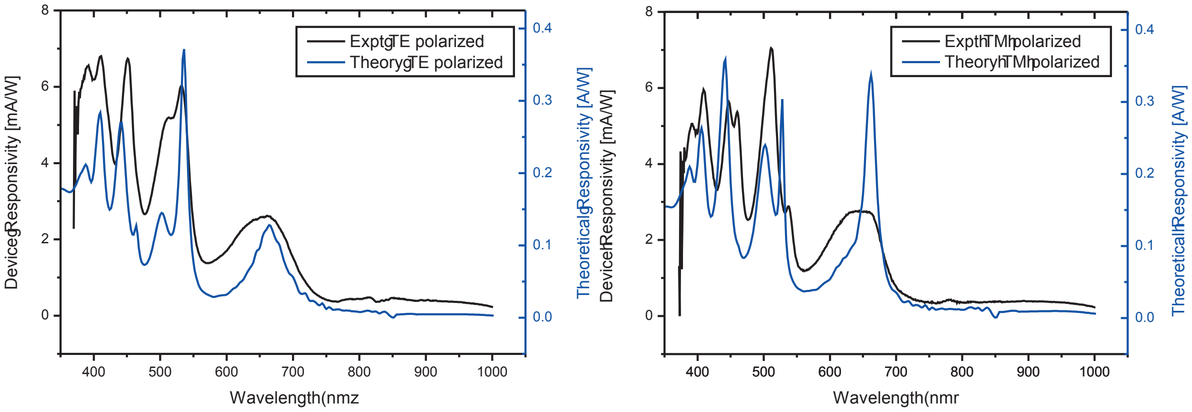

(A) Responsivity under TE polarization (B) Responsivity under TM polarization

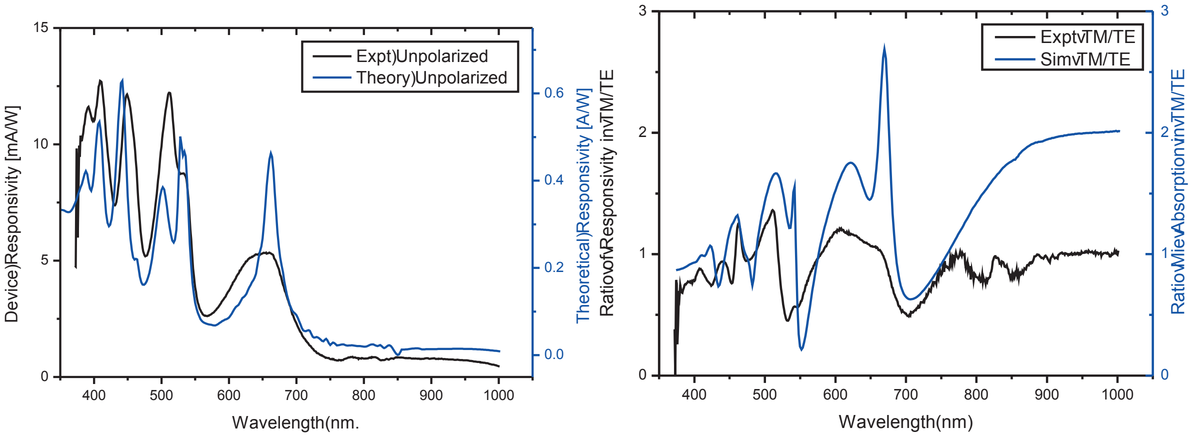

(C) Responsivity in Unpolarized case calculated by TM+TE (D) Ratio of responsivity in TM/TE polarization

FIGURE 9.3.3. NW response under TE and TM polarization for ≈200nm NW

The results for NW responsivity for TE and TM polarized light excitation are plotted in Fig 8.3.3. The responsivity observed from TE and TM polarization in Fig 9.3.3a,b plots is fairly different with slight shifts in resonances and considerable variation in the magnitude of the peaks. Fig 9.3.3c shows the unpolarized case which is here reproduced by summation of responsivity in TE and TM over the spectral range. The good fit obtained here shows that the unpolarized response can be correctly retrieved from the TE and TM response. Finally, an interesting way to see the difference in TE and TM polarized light absorption is by taking the ratio of the NW response in TM polarization to TE polarization. We define this ratio as the polarization sensitivity, which reflects the sensitivity of light absorption for the two polarizations. This polarization sensitivity for TM/TE responsivity ratio is plotted in Fig 9.3.3d. The plot shows a series of modulation with sharp maxima and minima indicating a high polarization sensitivity which is in agreement with the theoretical ratio. However, the slight y-offset observed between experiment and theory can be accounted by slightly different focusing conditions on the sample between the TE and TM acquisitions, thereby suggesting that the experimental TE photocurrent spectrum has been over estimated with respect to the TM one due to non optimized focusing conditions.

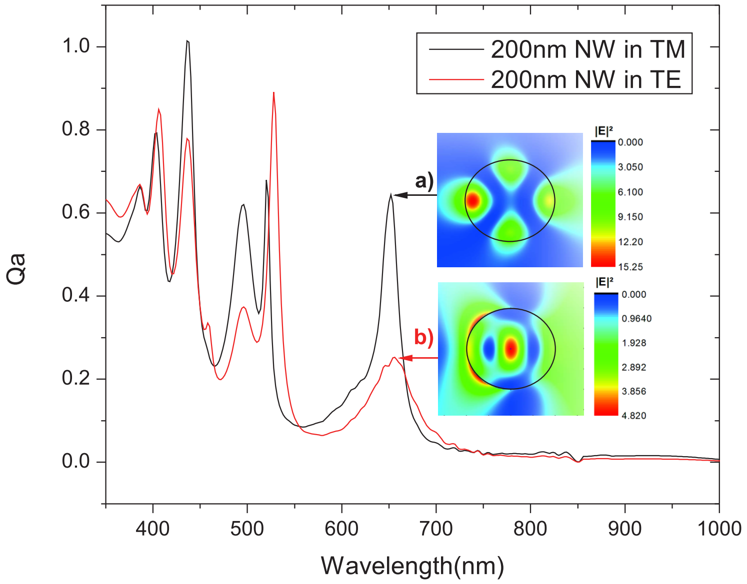

FIGURE 9.3.4. Difference between TE and TM polarization. The top graph shows Qa variation with wavelength for 200nm diameter NW under TM and TE excitation. The inset 2D plot shows the squared modulus of electric fields in NW at position a) and b) marked on Qa spectra.

To understand the polarizability line-shape, we plotted in Fig. 9.3.4, a comparison of the TE and TM Q_a spectra calculated for the same wire. We can easily see that most of the TE and TM modes are degenerate, but associated with different absorption efficiencies, leading to polarizabilities different from one. However, some TE and TM modes are more shifted, leading to peaks and valleys in the polarization sensitivity spectrum. Of interest are the drastically different absorption efficiencies theoretically observed at 650 nm, for which the mode profiles are plotted in inset of Fig. 9.3.4. The field distribution is strikingly different between the TE and TM polarizations since, as it is found generally for TE excitation, a strong field discontinuity is observed at the boundary between the wire and the air. As discussed in more details in Appendix C, TE excitation generates bound charges at the wire surface which, in turn, are associated with a depolarization field inhibiting the electric field propagation in the wire body, and thus the light absorption. This situation also holds for the TM excitation, but with bond charges located on both ends of the NW, thus generating a negligible depolarization field. A closer evaluation of the magnitude of the theoretical polarization spectrum reveals that the average polarization sensitivity is greater than 1. This can be interpreted in terms of a globally more efficient absorption of TM polarized light as compared to TE polarized light, and will be used later as a way to improve the light coupling efficiency in core shell structures.

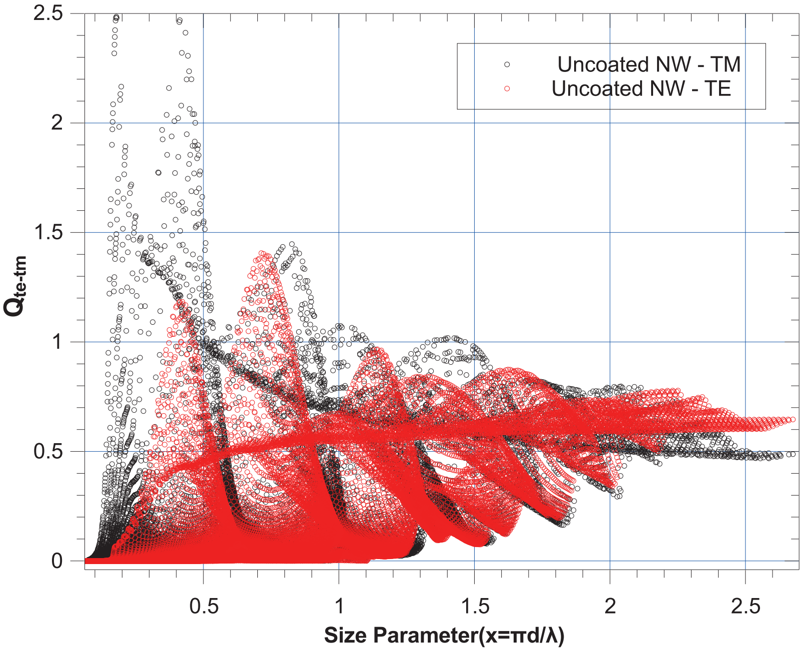

FIGURE 9.3.5. Plot of absorption efficiencies in TE and TM configuration with respect to size parameter.

To conclude this section, and in order to give an overall view of the wire polarization sensitivity, we plotted in Fig. 9.3.5 the traces of the TE and TM absorption efficiencies as a function of the size parameter $x = \pi d/\lambda$, where d is the wire diameter. It is clear that both traces converge towards similar efficiencies when the wire diameter is higher than wavelength, i. e. for large x, or in other words when the light does not see the NW shape. Conversely, for small x, or when the diameter is much smaller than the wavelength, the TM absorption is significantly higher than the TE one, since the light effectively sees the wire structural anisotropy.

Thus the large structural anisotropy for the NWs plays an important role for optimum light absorption at particular wavelengths due to the loss of light collection in the TE configuration. This is a serious drawback if one needs to use NWs for solar cells. Since, although the sunlight we receive is unpolarized , any light absorber one uses should be able to efficiently harvest any kind of polarized/unpolarized light. There are already efforts directed towards changing this polarization sensitivity in Si NWs by other means[**62**]. For photovoltaic application another important factor is quantum efficiency of the diode which we will analyze in the next section of the thesis.

9.4. EQE estimate: p-i-n coreshell system

The section on theoretical interpretation explains the relation between the experimental response obtained from the NWs with the theoretical absorption efficiency calculated using Mie theory. In photovoltaics an important parameter showing the performance of the solar cell is its external quantum efficiency (EQE). The EQE gives the ratio between the number of carriers emerging from the solar cell to the number of incident photons of particular wavelength falling on given area of the cell. This ratio can be roughly estimated experimentally with $EQE = 1240 \times Responsivity(A/W)/\lambda(nm)$, by ignoring the projected area of illumination as explained earlier. This is sufficient for qualitative comparison of peaks since it does not affect the spectral location of resonances. However, when one needs an exact evaluation of EQE, the situation is quite different and we need to take into account the photocurrent generated per unit area of illumination both for NW diodes and the reference photodiode in order to accurately know the power falling on the wire active zone. This makes the calculation of EQE for our p+i/n+i NW unreliable unless we know the exact active area of photon absorption. Although an estimate of the active region of these devices can be obtained from the diffusion lengths obtained from the EBIC measurements, there is still a considerable variation in their value as the active length is estimated with a 25% margin of error (from 750 nm to 1000 nm). Such variation is unacceptable in calculation of EQE where current solar cell market can be easily dictated by having a margin of 1% increase in efficiency. Further in the absence of surface passivation for as grown NWs studied until now, the surface traps on the wire sidewalls can further reduce the active area. The high surface recombination velocities at these unpassivated surfaces are highly detrimental and do not provide high external quantum efficiencies.

The only way to get more reliable estimate of EQE is by knowing the exact value of illuminated active area. Thus we switch our investigations to a new set of NWs with p-i-n junction, fabricated in a core shell geometry. The core-shell structure with sandwiched intrinsic region allows us to easily calculate the projected area of illumination as diameter x length i.e. $2rL$. The active area of the reference photodiode can be conveniently estimated by placing an aperture with 5 μm diameter ($2a$), a region in which the surface power density is assumed to be constant enough to allow extrapolation to the wire active region.

For the growth aspect, the p-i-n NWs were grown by the process mentioned in section 5.1 and for nanofabrication, the process for contacting the core and shell separately can be found in appendix A. The photocurrent measurements for these p-i-n wires were performed in exactly same fashion as the p+i/n+i characterized before. After the photocurrent measurements the dimensions of the p-i-n region length and diameter were measured under SEM. The NW in Fig 9.4.1 had a p-i-n region diameter of 274 nm ($2r$) and length of 1.5 μm (L). Thus the EQE in this case was calculated as

$$EQE = 1240 \times \frac{NW \;\; Photocurrent}{\lambda(nm) \times 2rL \times 0.45} \times \frac{\pi a^2 R_{PD}}{PD \;\; Photocurrent} \tag{9.4.1}$$

An important thing to recall from the Chapter 7 on experimental methods is that the output of the lock-in amplifier is not the actual signal. It gives an apparent photocurrent signal which is given by $0.45 \times NW \;\; Photocurrent$ and thus a correction factor of 0.45 needs to be applied to retrieve the actual photocurrent. This has been included in Eqn 9.4.1 by normalizing with 0.45. With the above equation, we now possess all the parameters to calculate the EQE in our p-i-n NWs.

The results are plotted in Fig 9.4.1 for TE, TM and unpolarized light along with an SEM of a connected core shell NW. We see an overall nice correlation between EQE from experiments and the absorption efficiency from the theory. The theoretical external quantum efficiency is EQE= ηQ_a, where η is the internal quantum efficiency, so comparing the experimental EQE and Q_a allows a direct estimate of the internal quantum efficiency. The

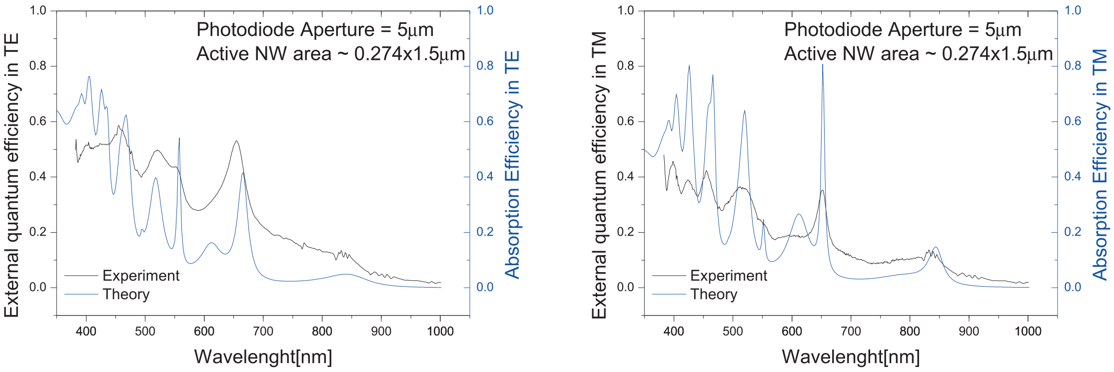

(A) EQE and $Q_{a,TE}$ with TE polarized light

(B) EQE and Qa with TM polarized light

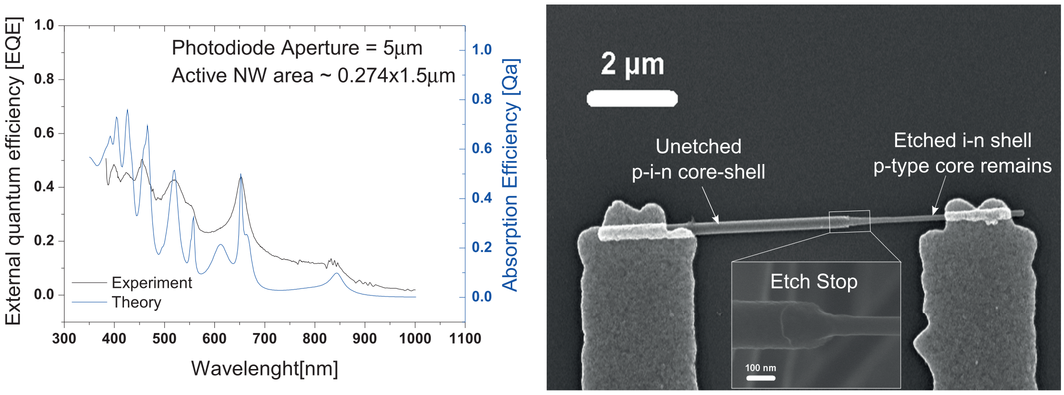

(C) EQE and Qa in unpolarized light

(D) SEM of a connected pin core shell NW

FIGURE 9.4.1. Theory vs experimental efficiencies in p-i-n core shell NWs. The SEM image shows a typical core shell NW connected between contacts

quantitative agreement observed between the experimental EQE and Q_a for both polarizations and unpolarized cases suggests that our radial pin structure does not suffer from important parasitic internal recombination processes and is efficient for carrier separation with internal quantum efficiencies close to the unity. Despite the apparent low EQE observed in our structures compared with bulk solar cells, one must keep in mind that the particular excitation geometry (normal excitation with respect to the wire axis) does not allow maximum light-NW coupling. However, the potentially high internal quantum efficiencies found with this set of experiments makes our core shell structures relevant and potentially very efficient when used under an in-axis excitation, as proposed in the literature.

The peaks are not as sharp as expected in the theory, which can be attributed to the SiO_2/Si substrate, or non circular NW geometry. Moreover, all focusing optics were optimized for use above 500 nm and thus experimental EQE is expected to be less than theory for $\lambda < 500nm$. The EQE values can further be tuned by changing the morphology of NWs as reported by Kempa et. al.,[**18**], where they show large EQE enhancements in Si pin core-shell NWs compared to bulk. Finally, the EQE measurements shown above were performed on single NWs but the similar process can be applied for arrays of NWs where the field coupling between different NWs plays an important role in overall light absorption as reported by Cao et. al.,[**63**]. The current work along with the above literature highlights the performance of silicon NWs at the scale of individual NWs and when applied to an array of NWs, can pave a critical way in future for efficient thin film photovoltaic.

The path we sought for metal-semiconductor junctions can provide reasonable EQE and can be further developed by improving the diffusion lengths and surface quality in NWs. This is achieved in current photovoltaic industry by passivating the surface with silicon dioxide[**64**](or silicon nitride[**65**]) which gives a high quality interface with Si with minimum interface traps and low surface recombination velocities. The light trapping mechanisms like nanostructured surfaces and antireflective coatings are also employed to increase the light absorption by multiple internal reflection[**64**]. For NWs, the surface passivation is even more important, particularly for small diameters, where for significantly high surface trap density, parasitic recombination could result in dramatic loss of performance. This could be achieved by coating/passivating the surface by a dielectric such as SiO_2. Further, could such coating provide effects for light trapping like antireflective coating ? Would one obtain an enhancement in light absorption by coating the NWs ? How would the unpolarized/polarized light absorption scale with dielectric thickness ? How would the absorption vary with different dielectric coatings ? These are the questions that one needs to answer to rationalize the requirement for oxide coating and will be tackled in the next chapter on the influence of change in the dielectric surrounding on the light absorption.

CHAPTER 10

Engineering light absorption: Dielectric surrounding

By now we know the phenomenon of light interaction with the single Si NW and the process of photocurrent generation by light absorption in these NWs. We also saw that the absorption of light depends on the diameter of the NW and that the unpolarized light absorption can in fact be split into the absorption of TE and TM components of the electromagnetic wave. Another interesting aspect to study would be the influence of dielectric surrounding on the light coupling in the core of the NW. Analyzing Eqn. 9.2.11 and 9.2.13 we see that they contain a parameter m which is the ratio of the complex refractive index of the NW to the refractive index of the medium. This shows that indeed the light absorption in NWs also depends on the dielectric constant of the surrounding medium. As used previously the infinite surrounding medium set as the air is a good approximation in our case but for studying the dependence of the NW light absorption on the dielectric surrounding, it is not practically feasible to have an infinite medium of arbitrary dielectric constant with the light source and entire setup enclosed in it. Also to study the effect of dielectric medium we would like to observe the influence of different thicknesses of dielectric on the light absorbed in the NWs. To perform such a study we need to have a core-shell system with Si NW as the core and an arbitrary dielectric as the shell, with the complete core shell system in a non absorbing surrounding ($\varepsilon_r = 1$).

The theoretical interpretation of the light absorption for cylinders developed in section 8.2 can only be used for an uncoated NW with an homogenous dielectric constant immersed in an infinite and homogeneous, non absorbing, medium. Thus for the core-shell system we need to develop a revised theory of the light interaction with core-shell nanocylinders which could be applicable for dielectric coated Si NWs, which we will address in the following part for arbitrary, absorbing or non absorbing dielectric shells. Once the analytical calculation are performed, the experimental data can be readily compared with theory on NWs surrounded/coated with various dielectrics like SiO_2 or Si_3N_4. Finally to conclude this work we build a model system with a freestanding NW in the air and compare it with the previous case of NWs on a substrate with a dielectric coating.

10.1. Theory of light absorption in core-shell nanocylinders

This part gives the formulation of the light absorption by core shell NWs which was developed by group members during the PhD. Such a problem is treated in literature by Kerker et. al.,[**66**] but the authors give the expansion coefficients for the scattered wave only, which limits the description of the absorption properties to the overall core-shell structure.

Our group members developed a modified version of Mie theory to be able to distinguish the light absorption separately in the core and shell of a core shell infinite cylinder. Without going in the details we explain the final form of the equations obtained. For the scattering and absorption efficiencies, we get similar equation as Eqn.9.2.7, Eqn.9.2.8, Eqn. 9.2.9 and Eqn. 9.2.10 but with different expressions for the scattering coefficients a_n and b_n. To know the absorbed energy by the core only of a core-shell system, one must work with the internal fields $\mathbf{E_1}$ and $\mathbf{H_1}$ instead of the above observables (incident and scattered fields relative to the structure) which include the contributions of both core and shell. Therefore, in order to evaluate the net rate of energy transfer through the core shell interface, we have to evaluate $W_a^c = -\iint_{A_{r=a}} \mathbf{S_1} \cdot \mathbf{n}\, d^2A$, where $\mathbf{S_1} = \frac{1}{2} Re\left(\mathbf{E_1} \times \mathbf{H_1^*}\right)$, with $r = a$. We find:

$$W_a^{c,\,I} = 2\pi a L I_0 \frac{\mid k_1^2 \mid}{\mid k_3^2 \mid} Re\left(\Gamma_0 + 2\sum_{n=1}^{\infty} \Gamma_n\right) \tag{10.1.1}$$

$$W_a^{c,\,II} = 2\pi a L I_0 \frac{\mid k_1^2 \mid}{\mid k_3^2 \mid} Re\left(\Phi_0 + 2\sum_{n=1}^{\infty} \Phi_n\right) \tag{10.1.2}$$

where the Γ_n and Φ_n coefficients contain cylindrical Bessel functions and are calculated based on the knowledge of the wave expansion coefficients of the internal EM field $(\mathbf{E_1}, \mathbf{H}_1)$ in the core.

This modified version of the Mie theory will be used in extensively in this chapter to give an analytical treatment of the observed photocurrent in core shell NWs under TE, TM excitation or different configurations of core shell NWs.

10.2. Dielectric shell enhanced core absorption in core shell like NWs on a substrate

The theoretical framework in the previous section makes a significant contribution to the theory of light scattering in core shell structures and with its help, for the first time unambiguously we can analytically calculate the light absorbed individually in core and shell of the NW. With that in hand, we can now proceed with the experimental verification of the theory. But before we begin, one should realize that the theoretical analysis considers a NW suspended in air covered completely with a homogenous shell of dielectric. This is very difficult to realize in experiment and would require more sophisticated and time consuming processes. So, in order to explore in detail the light matter interaction in core shell NWs, we begin with a more simplified structure whose geometry roughly mimics the theoretical one. This is shown in Fig. 10.2.1 where an ideal core-shell geometry used in the theory and the actual experimental case are depicted. To ensure the fabrication of a wide set of samples with varying morphological parameters, we deposited a PECVD dielectric layer on a NW lying on a substrate coated on its surface with the same dielectric. The thickness of the oxide layer is chosen to be the same than the thermal SiO_2 layer below the NW on the substrate. Thus the NW sees almost a constant thickness of oxide all around its axis, except along the sample plane where it sees an infinite dielectric thickness.

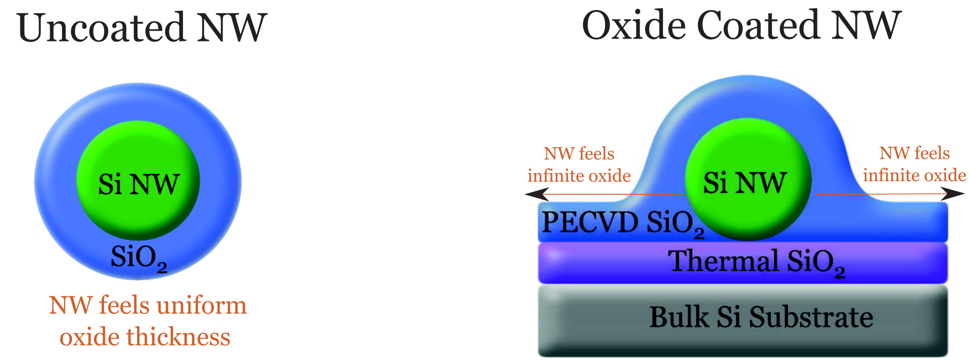

(A) Ideal case for theoretical analysis

(B) Actual case for experimental study

FIGURE 10.2.1. Light absorbed in dielectric coated NW: Theoretical vs experiment structure

We divide our study of the dielectric shell enhanced core absorption into four sub sections. The goal of the following sub sections is to deconvolute the contributions in the core absorption coming from the geometry of our coaxial cable, the pump conditions (polarization effects), or from the shell permittivity. For this, we will address:

a) The change in the core absorption as a function of its diameter for constant dielectric thickness (experiment)

b) The change in the core absorption as a function of the dielectric thickness for a constant core diameter (calculations)

c) The influence of the shell refractive index and extinction coefficient on the core absorption (experiment)

The first case provides us the answer to the question of change in the absorption(gain/loss) with coating while the second case shows the influence of the oxide thickness on the light coupled in the NW which highlights antireflective property if any. The last case should provide an understanding on the dependence of the core absorption on the shell permittivity (in order to examine the role of the shell layer as an antireflective coating [**64**][**67**]).

10.2.1. Modulation of the light absorption in core shell NWs: constant shell thickness and varying core diameter.

The analytical calculations were performed using the theoretical results given in the previous sections. The absorption efficiency of the core is calculated similarly as for the uncoated NWs by $Q_a = \frac{W_a}{2rLI_i}$, where W_a is the absorbed power in the NW core only and r is the radius of the core. This provides the core efficiency which can be directly compared with the uncoated case to extract the gain/loss by coating with the dielectric. This efficiency also gives us an idea of the shell induced change of the effective core absorption cross section, which is particularly relevant to examine the expected shell induced absorption enhancement.

As a starting point, it is important to note that the permittivity is an inherent parameter in the calculation of Q_a and thus actual values of permittivities for the oxide (or nitride in the following) must be used. For this the refractive indices and extinction coefficients were obtained for the deposited dielectrics by spectroscopic ellipsometry on the actual devices. Appendix A-II shows the $(n',\, n")$ (or $(n,\, \kappa)$) couples for the SiO_2 and Si_3N_4 dielectrics deposited with the PECVD technique. It can be seen in particular that unlike for SiO_2 the recipe for the deposit of the silicon nitride layer is not optimized for optical purposes since it has a significantly higher extinction coefficient than that of silicon dioxide, nearly reaching that of Si. For this reason, we restricted our study in this section to silicon oxide shells and used the nitride in a last section to examine the effect of strongly absorbing shells on the core absorption.

The PECVD technique was used for deposition of SiO_2 since it is conformal. The dielectric thickness was chosen to be $\approx 200nm$, aiming for symmetric $200nm$ deposited oxide on the top of the NW as that of 200 nm thermal oxide below the NW on SiO_2/Si substrate. Due to the process variations during the deposition, the actual thickness obtained was around $\approx 230nm$ which was the thickness also used for our calculations.

10.2.1.1. *Numerical approach.*

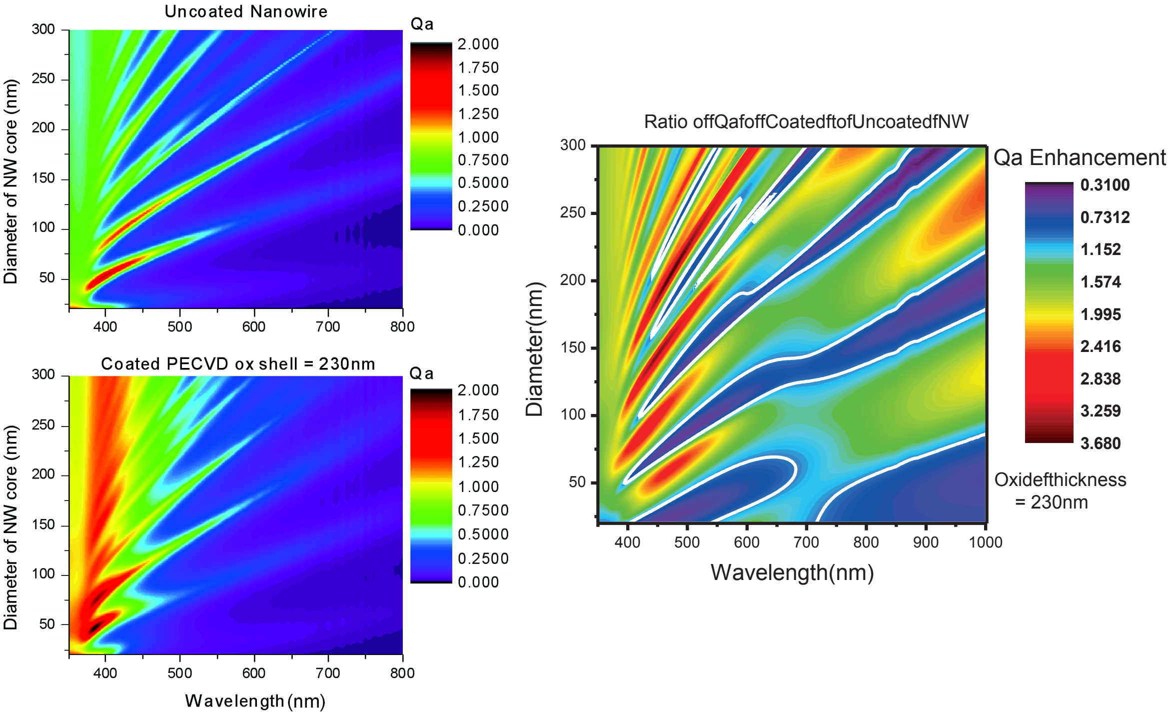

FIGURE 10.2.2. Absorption efficiency comparison between the uncoated and 230nm PECVD oxide coated NWs. The Qa contour plots for uncoated and 230nm oxide coated NWs in top left and bottom left respectively. The ratio of contour plot of coated NW to uncoated NW is shown in Qa enhancement plot on the right. The white lines on the left plot are the contour lines with Qa enhancement factor of 1.

The theoretical absorption efficiency in unpolarized case for coated and uncoated NWs are plotted in Fig 10.2.2a. The left half of the figure compares the absorption efficiency in a 2D contour plot with diameter vs radius for both cases. The gain in absorption efficiency is clearly visible from the 2D plots with peak absorption increased from 1.83 in uncoated case to 2.02 for the coated NW. As a guide to the eye, the magnitude of the color scale for 2D plot for uncoated case is chosen to be the same as for the coated case and do not signify the peak values. Further the absolute increase in absorption is significant at the lower wavelengths whereas in the infrared the absorption increase[1] is weaker with most of the light not absorbed. By fine analysis we can also conclude that the position of the sharp modal branches protruding from the origin of the 2D plots are almost unharmed by the presence of the oxide. This proves that we do observe an absorption gain in most of the regions through strengthening of the modal absorption without a significant shift of their resonance frequency. This absorption gain can be nicely represented by taking the ratio of Q_a between the coated and uncoated cases, as reported in 10.2.2 (right plot), which we can view as an "absorption enhancement factor". We have also plotted on this graph white contour lines on the boundaries between the gain and loss regions. As we can see, the regions with a gain cover an area higher than with a loss, with mean enhancement factors around $1.5-3$.

In order to give an overall estimate of the dielectric induced increase of the core absorption all across the visible and infrared bands, it is interesting to simulate the photo-response of a NW when illuminated by a broadband spectrum. This integrated photocurrent will thus give a mean value of the shell induced core absorption modulation all across the spectrum, by integrating the regions of gain and loss. Particularly relevant in the frame of our study (for photovoltaics) is the choice of the AM1.5 spectrum for illuminating our devices.

The photocurrent in a core shell NW of inner and outer radii a and b under an AM1.5 illumination, based on a constant internal quantum efficiency of 1, is given by $I_{ph}\left(a,\, b\right) = \frac{2aL}{1240}\int_{\lambda_1}^{\lambda_2} Q_a^{c,\,UP} AM1.5\left(\lambda\right)\lambda d\lambda$, where $Q_a^{c,\,UP} = W_a^{c,\,UP}/2aLI_0$ is the core absorption efficiency, $AM1.5\left(\lambda\right)$ is the AM1.5 solar spectral irradiance (in $W.m^{-2}.nm^{-1}$), a and λ are in nm, L is the length of the NW in meters and I_{ph} in nA. The lower and upper bounds in the integral are set at λ_1=300 nm and λ_2=1000 nm to select a reasonable window of integration that takes into account the high energy cutoff of the solar spectrum and the low energy cutoff of silicon absorption.

---

[1] The absorption increase can be seen be comparing the two 2D plots for uncoated and coated case in Fig 10.2.2. It is important to note that absorption enhancement in Fig 10.2.2 is a ratio of uncoated to coated 2D plots and thus give a gain factor by coating which is very different from absolute increase in absorption which can be obtained by taking a difference instead of ratio of the two plots.

Based on this, we find $I_{ph}^{naked} = 2869$ nA, 7217 nA, 13332 nA and $I_{ph}^{200\,nm\,SiO_2}$ =3811 nA, 9966 nA and 19909 nA for 1 meter long Si NWs of inner radii 75 nm, 140 nm and 220 nm respectively. This is a relative increase of harvested energy by the core of 32.8%, 38.1% and 49.3% respectively and confirms that coating a NW with SiO_2 strongly improves the light matter coupling.

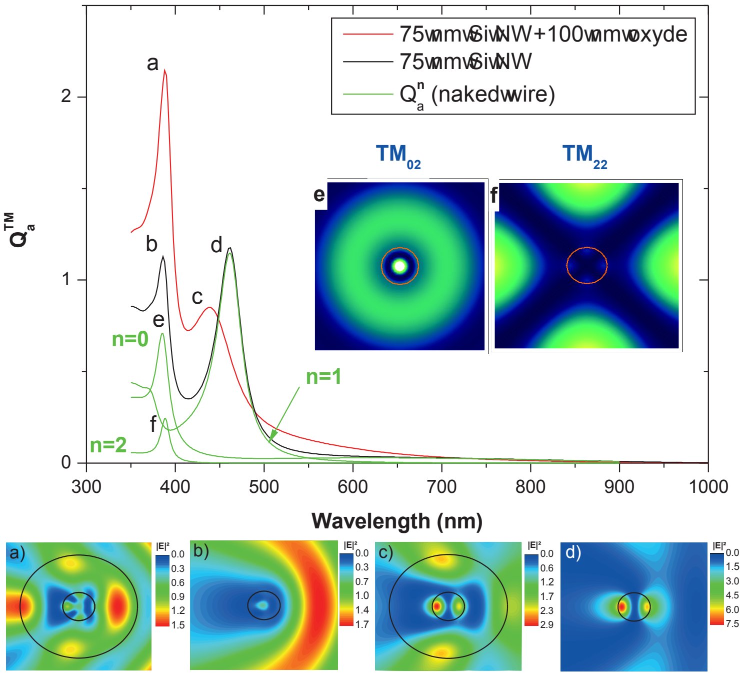

FIGURE 10.2.3. Spectral modulation of analytical absorption efficiency for TM polarization in 75 nm NW. The line color red and black represent oxide coated and uncoated NWs respectively. The 2D plots in insets a), b), c) and d) shows the $| E |^2$ field plots at the marked resonances. The inset shows the two dominant degenerate $TM_{02}$and TM_{22}modes excited at ~387 nm for the uncoated NW, which majorly contribute to the field pattern in plot b) .

In order to understand the effect of the shell on the coupling efficiency between the core and the light, we plotted in Fig 10.2.3 the absorption spectrum and some $| E |^2$ field plots in the TM configuration for a 75 nm Si NW uncoated or coated with a 100 nm SiO_2 PECVD (the incoming plane wave is set at $E_{io} = 1\,V.m^{-1}$ and comes from the right). One can see that the UV resonance is significantly enhanced by the coating with Q_a increasing from 1.13 to 2.14. The visible resonance is slightly shifted and even damped upon coating. We show on the same figure the field profiles for the a and b peaks in the UV and c and d peaks in the visible for both uncoated and coated configurations. The field profiles for the UV resonance clearly shows the enhancement in the light coupling for oxide coated NW with much more intense mode profiles in the NW core. However, the field patterns strongly differ in the core for both cases. This can be understood by plotting the first three Q_a^n components of the TM absorption (green curves on the absorption spectrum). One can clearly see that for the uncoated wire the UV peak actually comprises two main sub-components with $n = 0$ and $n = 2$ for which we plotted the corresponding TM_{02} and TM_{22} modes, labeled e and f on the figure. It can be easily seen from the total field patterns in the UV (a and b plots) that in the air the TM_{02} mode is preferentially excited and that after coating the TM_{22} mode largely dominates over the TM_{02} mode. Such differences in the mode coupling for the same set of wavelength and shell thickness are probably due to the modification of the field distribution at the core surface after capping. The new field distribution favors the presence of an electric field and the build up of modes with a lesser degree of spatial confinement, mainly located on the outer part of the core. As we can see from the spectral analysis, for the visible resonance, no mode mixing can occur since the visible absorption line is ascribed to a single and non degenerate mode. Thus, in this case, any change in the absorption arises from the dielectric induced change in the light coupling with the same mode. We can easily check this effect by plotting the field patterns corresponding to the c and d peaks. We do see a similar profile but a slight difference in their magnitude, accounting from a coating induced sensitivity to light coupling with the core, an effect encountered in 2D layers with antireflective films.

10.2.1.2. *Experimental approach.*

The discussion until now was restricted to the analytical calculations performed with the experimental parameters. Next we study the actual photocurrent of the device and compare the NW responsivity before and after coating it with a layer of 230 nm of PECVD SiO_2. The results are plotted in Fig. 10.2.4 for 80 nm to 220 nm diameter Si NWs. For each NW, the graph is subdivided vertically into 3 three sub-graphs/sections.

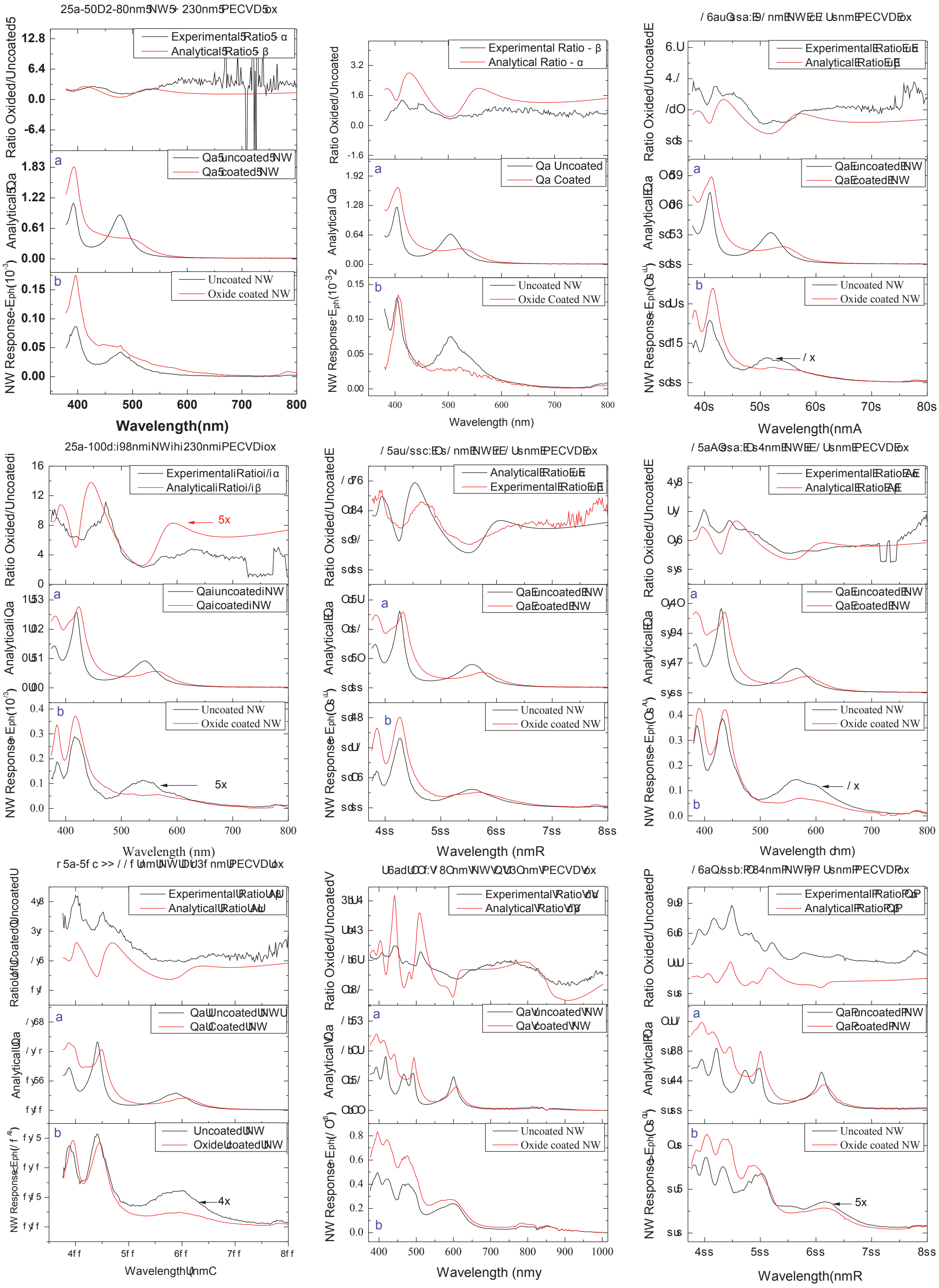
25a-50D2-80nm5NW5+ 230nm5PECVD5ox
Experimental5Ratio5 α
Analytical5Ratio5 β
Ratio Oxided/Uncoated5
Qa5uncoated5NW
Qa5coated5NW
Analytical5Qa
Uncoated NW
Oxide coated NW
NW Response Eph(10-3)
Wavelength(nm)
Experimental Ratio - β
Analytical Ratio - α
Ratio Oxided/Uncoated
Qa Uncoated
Qa Coated
Analytical Qa
Uncoated NW
Oxide Coated NW
NW Response Eph(10-3)2
Wavelength (nm)
25a-100d:i98nmiNWihi230nmiPECVDiox
ExperimentaliRatioi/iα
AnalyticaliRatioi/iβ
5x
QaiuncoatediNW
QaicoatediNW
Uncoated NW
Oxide coated NW
Wavelength (nm)
Uncoated NW
Oxide coated NW
NW Response Eph
4x
Wavelength (nm
5x
Wavelength (nmR

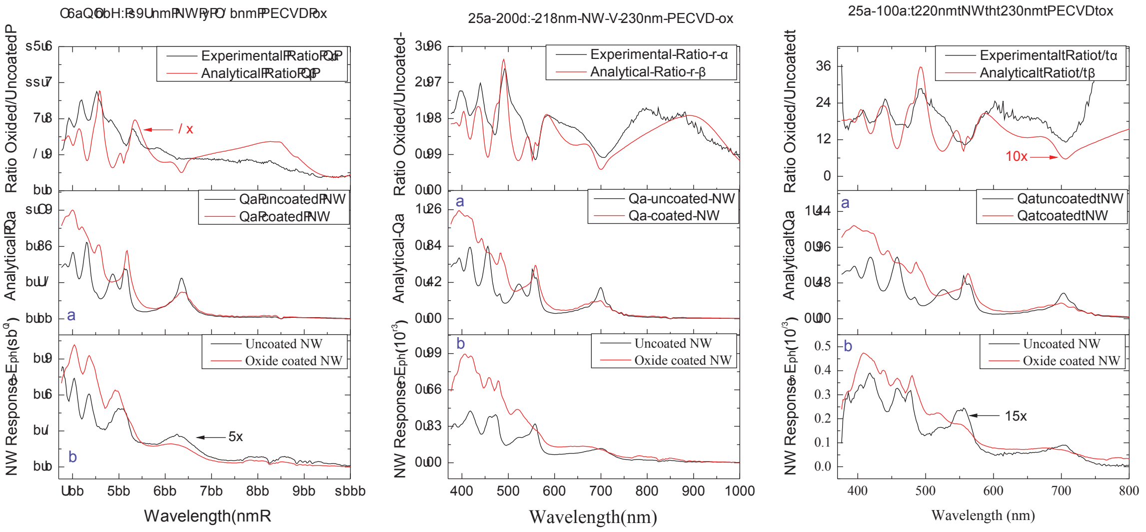

FIGURE 10.2.4. Complete data-set comparing absorption in uncoated NW to that of coated NWs for experimental data in lowest section, analytical comparison in middle section and absorption enhancement between theory and experiment in top section of each plot. Each graph comprises of measurement on single NW before and after coating with 230nm of PECVD oxide.

The experimental responsivity of a NW is plotted in the lowest section, the analytical plots of absorption efficiencies for experimental parameters are shown in the middle section and the top section shows the plots for absorption enhancement factor over the spectrum. To highlight the difference between the coated and uncoated cases, respective line plots for both cases are juxtaposed on each section.

First, the increase in the responsivity upon capping is observed for all the NWs studied experimentally, which constitutes a strong evidence of the shell induced enhancement of the core absorption. Secondly, a good overall correlation is observed between the theoretical responsivity and the experiment for the oxide coated NWs with most of the resonance shifts and modulations being fairly reproduced by the theory. Finally we calculate the absorption enhancement and compare the theory with experiment in the first sub-graph of Fig. 10.2.4 for all the NWs. As long as all the other experimental parameters are kept constant we can even obtain a better fit between experiment and theory with absorption enhancement, since the ratio magnifies the difference between the uncoated and coated absorption. The experimental absorption enhancement compares well with theory with enhancement factors around 2 for most of the NWs. Thus we see even experimentally that the absorption in NW core is doubled or more by coating the NW with 230 nm PECVD. Indeed, the relative changes in the photo current being proportional to the product between the internal quantum efficiency change and external quantum efficiency change upon coating, and the internal quantum efficiency being nearly independent of the photon energy, one can deduce that the spectral modulations observed in the ratio of the photo current spectra are due to a change in the core absorption efficiency only. The nice peak correlation between the experiment and the theory is thus a very strong proof supporting the phenomenon of dielectric induced enhancement of light absorption.

The absorption enhancement for devices even exceeds the calculated theoretical gain. This is presumably due to the enhancement of internal quantum efficiency by efficient surface passivation when the NW diodes are coated with PECVD SiO_2. Particularly striking is the case of the 220 nm core diameter NW. A 10 fold correction ratio is applied on the theoretical absorption gain to have a very nice fitting with the unmodified experimental gain over a broad wavelength band. This 10 fold enhancement can be ascribed to a 10 fold change in the internal quantum efficiency but is an exception compared with the other NWs having a much smaller correction factor. Indeed, in our experiments, we have deliberately chosen to preserve the electronic surface state of our NWs by keeping the usual native oxide (detrimental) on the NW surface prior the dielectric deposition. In such a case, and since the surface recombination is mainly driven by the very first interface atoms, the internal quantum efficiency is not expected to dramatically change during this process. The relative low values for the mismatch of the absorption enhancement for most of the wires support our approach. The PECVD deposition conditions (280 °C) also affect the metal semiconductor junction properties due to annealing which could result in a change in diode properties like series, shunt resistances and ideality, thus causing an increase or decrease in photo current.

One can identify another source of disagreement between experiment and theory as coming from the variation in beam intensity over time or a slight change in focal plane of illumination [2] between uncoated and coated NW (and photo-diode), which can result in a non-negligible variation in the photo current and thus spectral distortion of the enhancement curves. Also due to the chromatic aberration in the lens system on the setup, the

---

[2] It is very difficult to maintain the exact plane of focus between the uncoated and coated NW due to the coating and physical limitations of instrumental setup for fine focusing.

low wavelength were significantly unfocused for the experiments which underestimates the photocurrent at wavelengths $< 450\,nm$.

10.2.2. Modulation of the light absorption in core shell NWs: varying shell thickness and constant core diameter.

To assess the influence of the dielectric thickness on the absorption efficiency of the NW, we perform multiple calculations for the core Q_a spectrum with gradually increasing the SiO_2 thickness from 20 nm to 300 nm with the same dielectric parameter as before. The simulations were performed for two diameters (75 nm and 220 nm) of NWs for comparison. The Q_a for 75 nm and 220 nm NWs are plotted in contour plots for oxide thickness vs wavelength in Fig. 10.2.5.

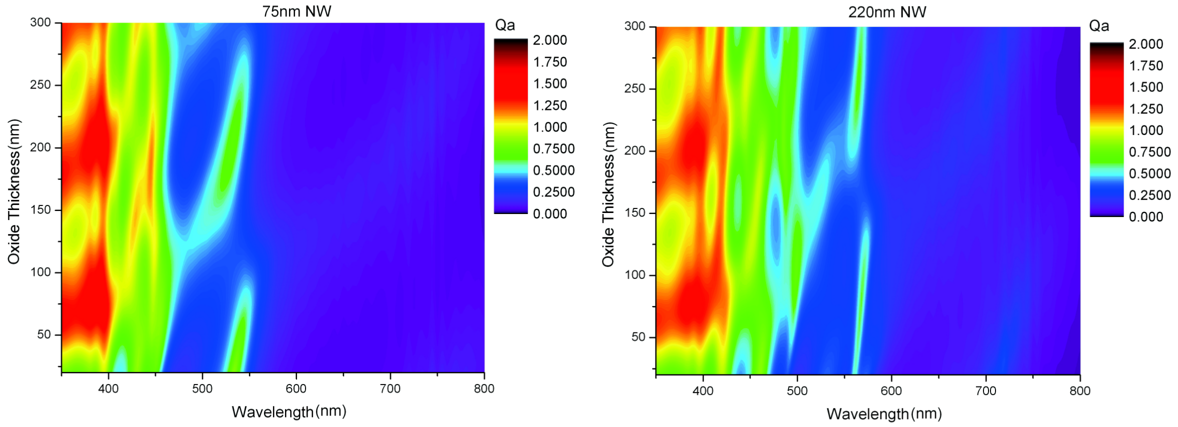

FIGURE 10.2.5. Analytical contour plot of absorption efficiency variation with respect to oxide thickness and wavelength. Plots for two typical diameters 75 nm in figure on left and 220 nm in figure on right are shown to highlight the evolution of profiles with diameter.

At first glance, the contour plots for both NWs (also true for other diameters not plotted here), show a nearly periodic variation of the resonances (in Qa) with respect to the oxide thickness along the y-axis. The periodicity in Q_a with oxide thickness is even striking for high absorption regions with wavelengths around 400 nm. Such a periodicity in light absorption with oxide thickness is usually observed in Si bulk/thin-film samples. The periodic pattern seen in such structures are very typical of Fabry–Pérot interferences where depending on the wavelength, angle of incidence and the dielectric constant of materials involved, the light interferes constructively or destructively at regular intervals of oxide thickness giving rise to such periodic patterns. The similarity of both results with above phenomenon suggests that we might have an interference phenomenon with constructive/destructive light interference with varying shell oxide thicknesses. With the above conception we can infer that at the specific thickness, and at the oxide surface, destructive interference between the incoming beam and back-reflected beam by the core will occur when the thickness of the layer is $\lambda/2n_{SiO_2}$. In such a case, efficient energy transfer occurs up to the core, leading to maximized Q_a; the oxide acts as an antireflective coating. Similarly the constructive interferences on the oxide surface increases the reflection of light (acting as reflective coating), causing a decrease in absorption at these thicknesses. The Fabry–Pérot interferences in particular, for a specific wavelength and angle of incidence, depend solely on the dielectric parameter of the different material layers. This suggest that for our case Air/SiO$_2$/Si NW stack, the spectral location of the interference peaks should remain the same regardless of the diameter of the NW. This can be easily tested by comparing the 75 nm plot with the 220 nm plot in Fig 10.2.5. For instance, if we consider the 500-600 nm range for both cases, one can easily measure the period of the Q_a modulation in term of shell thickness t. We find $\Delta t \approx 200$ nm for both 75 and 220 nm diameters. Taking $n_{S_{iO_2}} \approx 1.5$ and $\lambda \approx 550$ nm, and using the $\lambda/2n_{SiO_2}$formula for the thickness period for destructive (also for constructive) interferences at the surface of planar films, we get $550/2 \times 1.5 = 183$ nm, in good agreement with the measured period taken from our analytical treatment.

Such dielectric core shell antenna have already been studied by Liu et al [**68**][**69**] by analytical calculation[3] and very recently by Yu et al[**70**] with FDTD simulations but they are only limited to theoretical calculations making this work the state of art experimental demonstration of dielectric induced absorption enhancement in Si NWs. The Fig. 10.2.6 shows the electric field profiles in TM configuration in a 220 nm core NW for different shell thicknesses along a wavelength of 556 nm. The points representing the field plot configuration are marked as A (uncoated case), B (local maximum in absorption), C (local minimum in absorption) and D (local maximum in absorption) on the contour plot of Q_a for incident TM polarization. The field profiles in the core shell show the presence of mode with 6 lobes clearly visible in the uncoated NW.

---

[3] They calculate the absorption for entire core shell nanowire by traditional Mie theory.

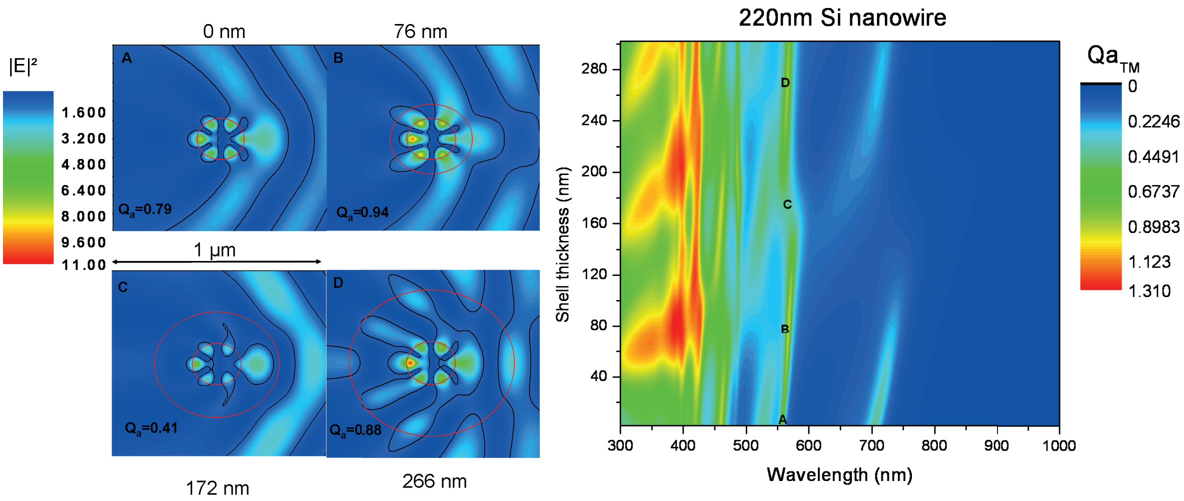

FIGURE 10.2.6. The $|E|^2$field plots in the NW with different thickness of oxide for 220nm NW. The various field plots on the left side are can be correlated to different maxima's and minima's in Qa 2D plot on the right for varying shell thickness labeled as A (uncoated), B (76nm oxide), C (172nm oxide), D (266nm oxide) for 556nm wavelength. The plots represent TM configuration.

As the oxide thickness is increased to 76 nm with an absorption maxima, the mode profiles remain unchanged in the NW suggesting that the same resonant mode is excited but with increased field coupling in the NW core. In the next step the shell thickness is further increased to 172 nm with an absorption minimum. We see a significant reduction in the electric field coupled in the oxide with an enhanced scattering of the incoming wave. In the last step we move to second maximum at 266 nm where as expected, we see field being squeezed inside the NW through the oxide with an antireflective property.

To conclude this section, and in order to fully examine the effect of the coating over a broad range of wavelength, we give the photocurrent change upon capping with various oxide thicknesses and under a solar illumination. Fig. 10.2.7 gives the theoretical photocurrent of three different diameter NWs (75, 140 and 220 nm of diameter) illuminated with a normal incident beam having an $AM\,1.5$ spectral irradiance for TE, TM and unpolarized cases (here we have improperly set $AM\,1.5^{TE}$ and $AM\,1.5^{TM}$ to the unpolarized $AM\,1.5$ irradiance; this simply doubles the resulting photocurrent). As expected, both the TE and TM photocurrent show intensity modulations with the oxide thickness with a typical period around 110-120 nm, corresponding to an effective "working wavelength" close to 350 nm where most of the absorption takes place.

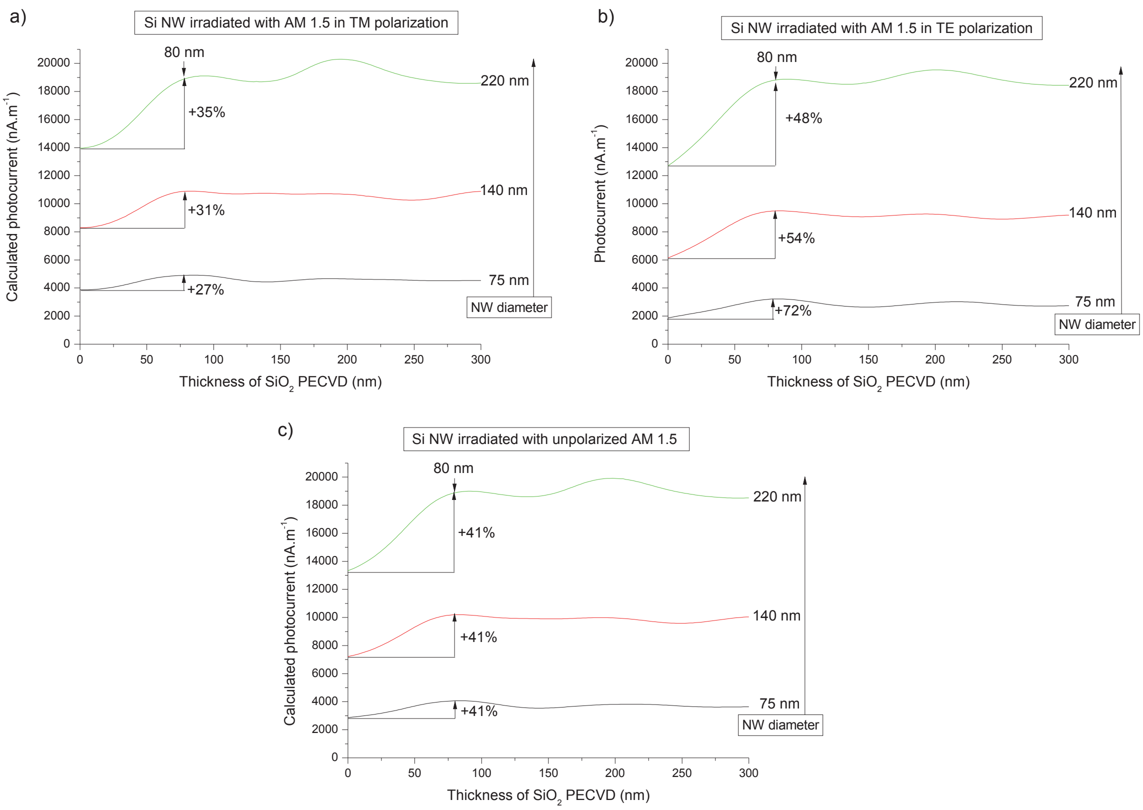

FIGURE 10.2.7. Integrated photo current calculated over AM1.5 spectral illumination for varying thickness of PECVD oxide shell for 75nm, 140nm, 200nm NW in a) TM polarized light, b) TE polarized light and c) Unpolarized light.

Interestingly, the effect of the oxide absorption does not affect dramatically the photo current since no decrease in the photo current with an increase with the shell thickness is observed. This is probably due to the net positive balance between the antireflective gain coupled to a lens effect concentrating the energy from the shell edges to the core and the EM energy dissipation in the weakly absorbing shell. We also see that the overall gain in TM increases as the size parameter of the NW core increases (diameter varying from 75 nm to 220 nm) whereas for TE polarization the gain reduces with increasing size parameter NW.

Another interesting observation is that a very vigorous increase in the photo current is observed for the first tens of nm of oxide capping, e. g. between 0 and 80 nm. Passed this critical thickness t_0, the photo current oscillates with the thickness with an amplitude much more modest than its initial increase at low thickness. This "magic" thickness could be a key parameter in the eventual use of NWs as thin film absorbers. To finish, the relative increase of the photo current between $t = 0$ and $t = t_0$ is much higher for TE than for TM upon coating. This is ascribed to a sensitivity of the core depolarization field to the shell dielectric constant for TE excitation. Decreasing the magnitude of the dielectric mismatch at the core shell interface helps in building a strong electric field in the core body with a decreased counter influence of the depolarization field.

10.2.3. Influence of the shell permittivity on the core absorption: refraction versus extinction effects.

The permittivity (both real and imaginary) of the the dielectric shell plays an important role in enhancing the light coupling in the NW.

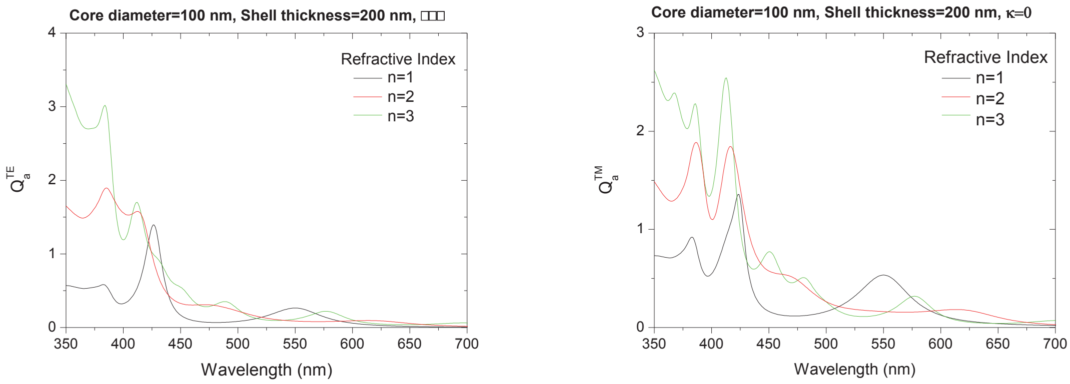

FIGURE 10.2.8. The Q_a^{TE} and Q_a^{TM} absorption spectrum for different refractive indices $n = 1$, $n = 2$ and $n = 3$.

Here, we give a summary of these results by plotting the absorption efficiency spectra in TE and TM cases for a constant core shell geometry (Si core of 100 nm of diameter and a dielectric shell of 200 nm of thickness) but different shell refractive indices n (the extinction coefficient is set at zero).

The Fig. 10.2.8a, b shows that for both polarizations, the mean absorption efficiency increases with increasing n from 1 to 3 due to enhanced light coupling in the NW core. Considering dielectrics as ideal and non absorbing, selecting shells with the higher refractive index should ensure, in principle, an efficient light coupling to the core. Up to now we have used a SiO_2 capping with typical n around 1.5. The above calculations suggest that taking a dielectric shell with a higher n between 1.5 and 3 should improve the photo current level in our core shell systems. This is in agreement with literature where a theoretical report by Liu et al.[**69**] and Yu et al.[**70**] shows similar increase in absorption on coating Si NWs with oxide shell and also for amorphous silicon shell by Lui et al.,[**68**].

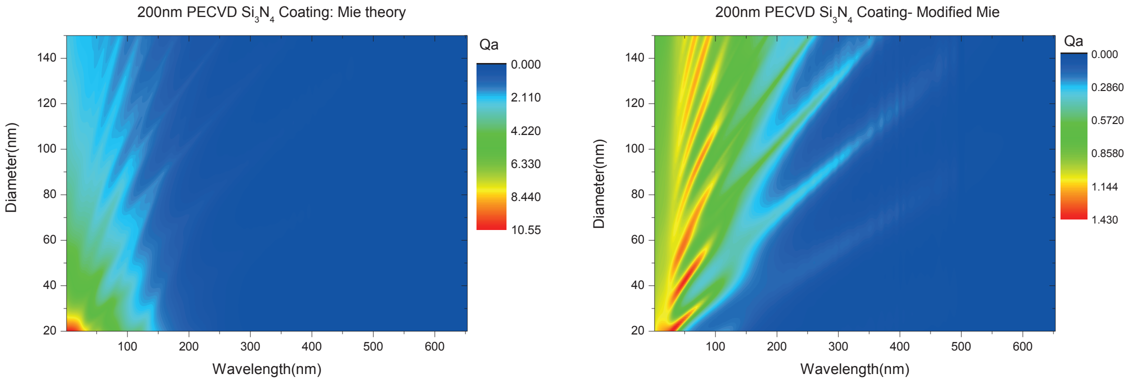

(A) The 2D plot for Mie calculation of absorption efficiency of core-shell NW by standard standard mie theory on the left and the absorption efficiency of just core by modified version of Mie theory on the right. The experimental $n + ik$ values were used in both cases for oxide.

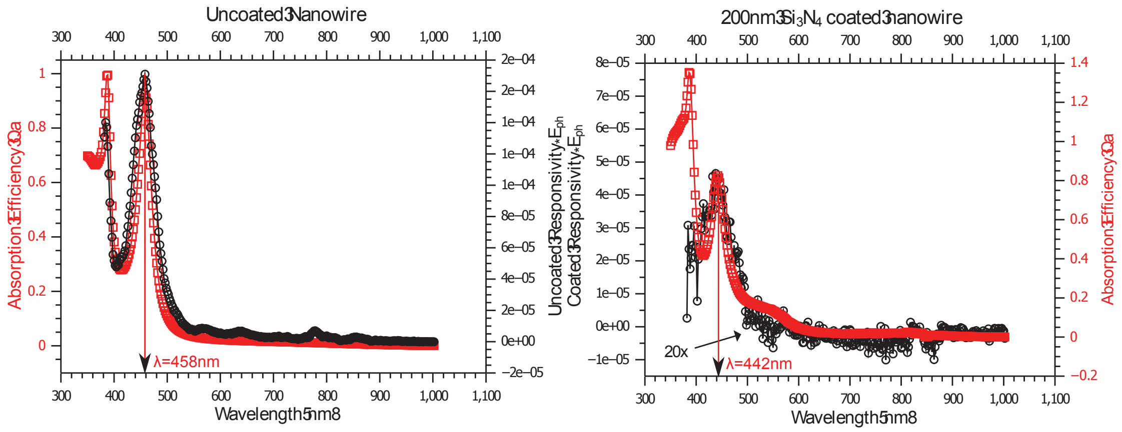

(B) Comparison of uncoated 75nm NW before and after 200 nm PECVD nitride coating.

FIGURE 10.2.9. Light absorption in NWs coated with 200 nm PECVD nitride.

To test this hypothesis, we oriented our choice towards the use of a silicon nitride capping with a typical n around 2 in the spectroscopic range of interest. Towards this goal, we studied the case of a Si NW diode coated with a 200 nm PECVD Si_3N_4 fabricated on a Si_3N_4 (200nm)/Si (bulk) substrate. Unlike for capping by the silicon dioxide, the photo current on the 75 nm NW is surprisingly greatly reduced after nitride capping so that it was very difficult to extract the device responsivity after the coating. The device responsivities are plotted in Fig. 10.2.9b for both cases (left for a uncoated wire and right for a coated wire). The experimental plot for coated NW is increased 20 times to have the responsivity on a similar scale than that of the uncoated NW. To understand this surprising result at first view, we proceed by steps in order to deconvolute the effect of the refractive index and that of the extinction coefficient.

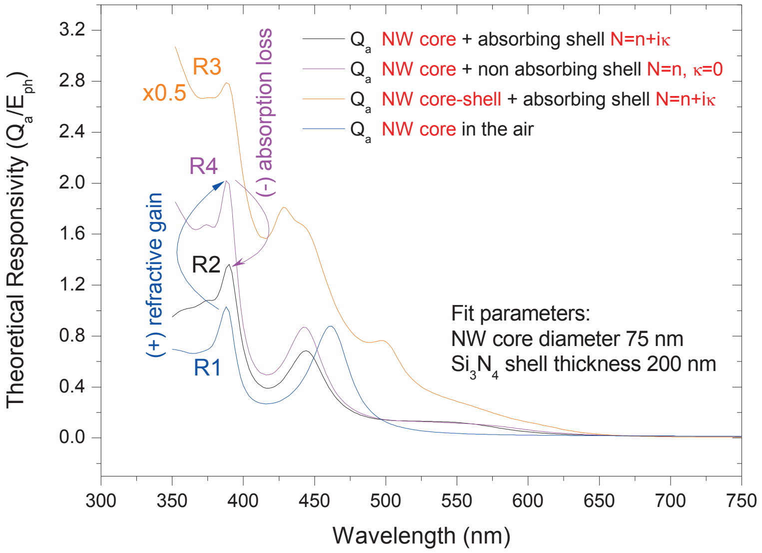

FIGURE 10.2.10. Absorption efficiency of 75nm NW with 200 nm PECVD Si_3N_4shell. The curve in black shows a system of absorption efficiency of NW core with absorbing shell; pink curve shows the absorption efficiency of NW core with assumption that shell does not absorb (k=0); orange curve shows the total absorption efficiency of core shell NW with absorbing shell and the blue curve shows absorption spectra of a NW in air.

Shown in Fig. 10.2.10 are the theoretical responsivities of the core under several configurations. First we report the core responsivity in the air as $R_1 = W^{air}_{a\,c}/\,(2aE_{ph}LI_0)$, where $W^{air}_{a\,c}$ is the absorbed optical power by the wire in the air, supposed to be similar to the wire responsivity before capping. Second we plot the core responsivity as given in our approach $R_2 = W^{abs\,cs}_{a\,c}/\,(2aE_{ph}LI_0)$, where $W^{abs\,cs}_{a\,c}$ is the absorbed power in the core when "immersed" in the absorbing shell, which is expected to reproduce with the best accuracy our experimental responsivity after capping. Third, we plot another expression for the core responsivity as $R_3 = W^{abs\,cs}_{a\,cs}/\,(2aE_{ph}LI_0)$, where $W^{abs\,cs}_{a\,cs}$ is the absorbed power by the real (absorbing) core shell. This approach is actually commonly used in works on core shell structures where the only core shell scattering expansion coefficients are used instead of their core counterparts[**71**][**72**][**73**]. This formula overestimates the true absorbed power in the core since it abusively attributes the overall core shell absorption to the core despite the significant power dissipation in the shell. Finally, we plotted another form of the core responsivity as $R_4 = W_{a\,c}^{ref\;cs}/\,(2aE_{ph}LI_0)$, where $W_{a\,c}^{ref\;cs}$ is the absorbed power by the core in a core shell having a purely refractive shell set at a constant and real index of refraction ≈ 2.06. This last approach allows an estimate of the absorption gain in the core arising from the only refractive contribution of the shell.

As expected, R_1 fits nicely with the experimental responsivity before capping, (see in Fig. 10.2.10) but we also see that R_3 does not show a good agreement with the experiment after capping. However R_2 and R_4 fit nicely with the data and well reproduce the line blue-shift observed upon capping (see Fig. 10.2.9b), which shows the interest of our approach. Of interest is the theoretical behavior of the UV line where one can clearly see the intricate effect of the refraction and absorption of the shell on the core absorption. Indeed, in the UV region, a great increase in the absorption efficiency is first observed after capping with a purely refractive shell, due to the combination of the decreased depolarization field in the core and the antireflective effects (denoted as refractive gain in Fig. 10.2.10). Once the absorption is switched on in the shell, we observe a significant decrease by about 1/3 of the absorption efficiency due to a partial absorption of the incoming light in the shell, which was of negligible effect up to now for the oxide coating (denoted as absorption loss in Fig. 10.2.10). While our approach accounts nicely of the blue absorption line-shape after capping, we apparently fail in explaining the 20 fold decrease in the mean photo current level after capping, while our calculation even predicts a slight increase. A closed view to the experimental spectrum in the UV region below 400 nm reveals a very strong collapse of the UV line after capping, whereas theory predicts a UV peak with a similar intensity than the blue one. We presume that this discrepancy arises from an underestimated extinction coefficient of the nitride in the UV region, as we discussed just above, increasing the absorption in the shell and rigidly decreasing the responsivity spectrum without modifying noticeably its line-shape. As a result, the huge 20 fold decrease in photo current after capping is attributed to a stronger nitride absorption than predicted by the ellipsometric model in the UV and a part of the blue.

To conclude this part, Fig. 10.2.10 compares the absorption efficiencies calculated in two ways for nitride capped Si NWs. In the orange curve, the core absorption efficiency is plotted considering the overall core shell absorption (the nitride is taken as absorbing), and in the black curve we show the core absorption efficiency considering the absorbed energy by the core only. Note the dramatically different shapes and absolute intensities of both distributions.

10.3. Quest for an ideal system: NWs and core shell structures in the air

The experimental measurements in the previous sections always dealt with Si NW devices fabricated on a Si substrate with 200 nm thick oxide or nitride coatings which provides us an ease of fabrication and characterization. But this sets a limitation in term of deposited dielectric thickness since the deposited oxide thickness must be the same as the substrate oxide/nitride thickness. The theory on the other hand is also incapable of calculating the absorption in such complex structures and thus relies on a much simpler model of NW capped by a shell with a cylindrical geometry. The knowledge of above issue naturally raises a question: Does the presence of a substrate influence the light absorption in NWs ? How much does it influence the absorption: enhancement or reduction ?

10.3.1. Light absorption in NWs suspended in air.

The main difficulty for this study rests on the realization of the actual structure for creating a connected NW suspended in air between the contacts. The fabrication of NW in air structure relies on two approaches: Either by creating the air gap between the NW and substrate in advance by drop-casting the NW on a substrate with narrow gaps which requires physical or chemical etching[4] or engineering the drop-casting with the lithographic process such that one ends up with suspended NWs. The second process was chosen and the suspended structure was fabricated by a bi-layer resist lithography with NWs drop-casted between two resist layers naturally giving suspended NWs. The fabrication process is explained further in Appendix A.

---

[4] Another way by etching could be, drop-casting first on the substrate later creating the air gap by preferentially etching the substrate under the NW

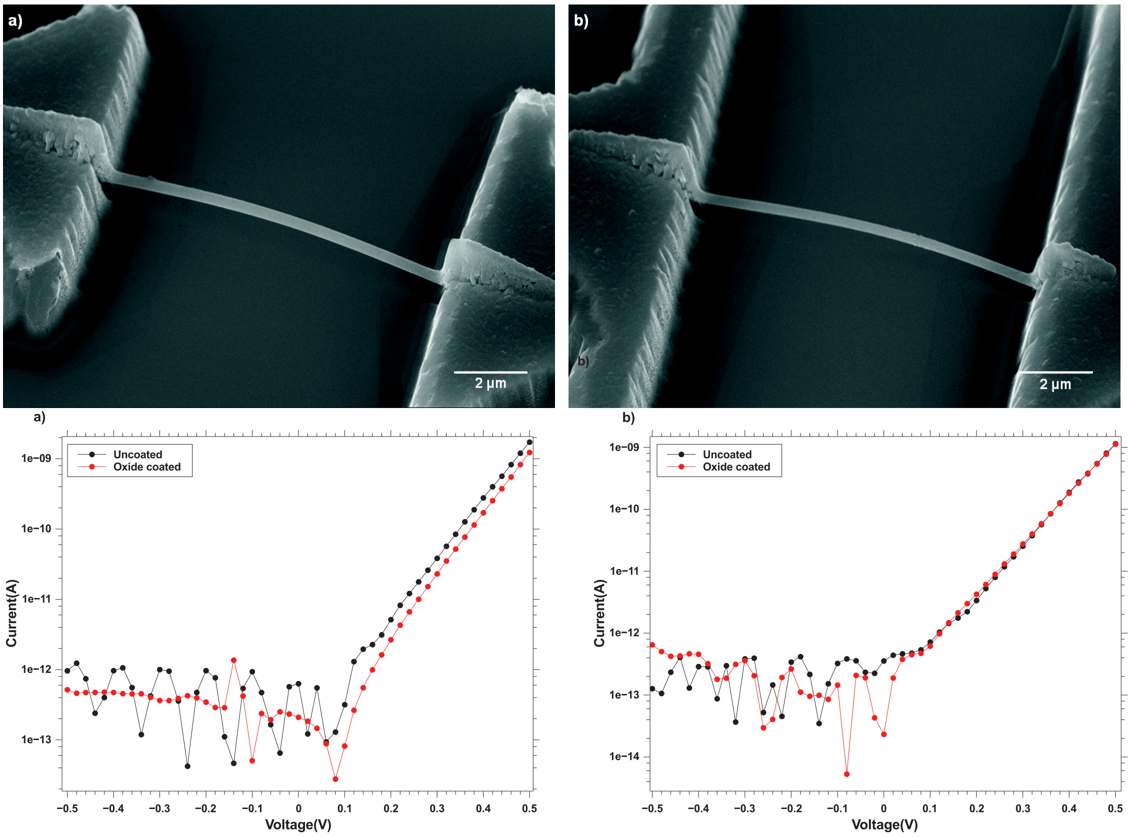

FIGURE 10.3.1. SEM and IV on suspended NWs. The SEM images show samples a) ~216nm NW and b) ~188nm NW where NW is clearly seen suspended in air. The I-V plots of the above NWs are shown below in uncoated case (and later on as we will see a coated case with PECVD SiO_2)

The SEM image of two suspended Si NW devices are shown in Fig 10.3.1. The distance between the NW and the substrate was chosen ≈700 nm, which is high enough to have a negligible electromagnetic coupling with substrate. The lower half of Fig 10.3.1 shows the I-V measurement on the two above samples and the device has as a similar diode like behavior as observed on previous n+i samples. The devices fabricated in such a fashion also tend to be strained. This is due to the thick metal deposited (almost 1 µm) to have a nice contact with the NW which are at an height of 700 nm above the substrate. During the metal contacting, the highly anisotropic metal evaporation process causes the thick metal stack (1 μm) to also deposit both on the bottom of the contact trenches and on the exposed ends of the NW, leaving a void below the wire. This particular configuration is believed to be responsible of the small bending observed in the SEM images (see the Appendix A-II for the detailed schematic of the process flow).

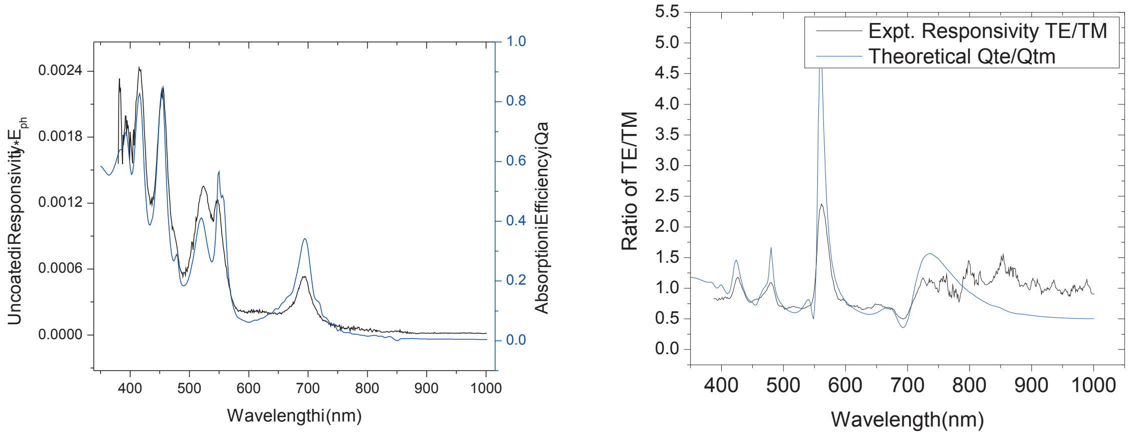

(a) Unpolarized Mie fit with diameter of ≈216 nm(left) and polarization sensitivity ratio (right): Sample a) in SEM in Fig 10.3.1

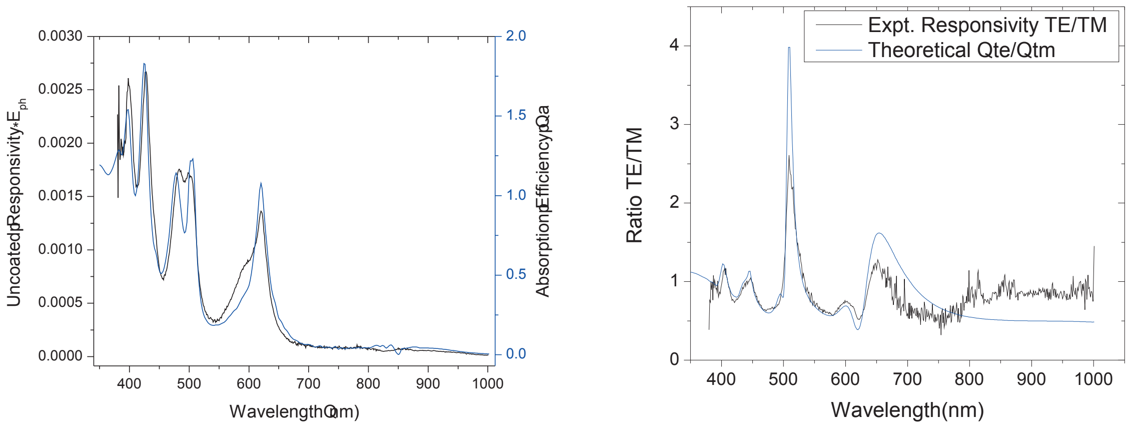

(b) Unpolarized Mie fit with diameter of ≈188 nm(left) and polarization sensitivity ratio (right): Sample b) in SEM in Fig 10.3.1

FIGURE 10.3.2. Responsivity vs wavelength plots for NWs in air

The Fig 10.3.2 shows the experimental curves for responsivity*E_{ph} and absorption efficiency of the NW in air for 216 nm and 188 nm (fitted) diameter NWs. The NW response shows an excellent fit with the theory with the number of resonances from the theory exactly matching the number and spectral position of peaks from experiment. The ratio of responsivity and Qa for TE/TM is also plotted for both NWs in the right half of Fig 10.3.2 which also shows an excellent correlation with the theory. There was no normalization step performed on the experimental responsivity in TE and TM for taking the ratio and the plot against the theory inherently gave the fits plotted without any need for rescaling. This shows that ideal case of NW in air is indeed reproduced by our suspended NW configuration with a high accuracy. The above results establish that the negligible but evident small mismatch observed between the experimental dataset and theory in the previous chapter is indeed due to the modified light interaction due to the presence of the substrate.

10.3.2. Dielectric enhanced absorption.

The structure of the suspended NW gives us a big advantage of choosing the deposited oxide thickness at will, irrespective of the substrate material. In the suspended structure we have the possibility to modulate the air-gap from 0 to 1000 nm depending on the thickness of the bi-layer recipe used. This gives us an added freedom in dielectric depositing up to half of the air-gap to have a clean geometry with deposited oxide on the NW detached from the substrate. Therefore we have an opportunity of making multiple measurements on the same NW in order to follow the wire response upon different coating thicknesses. The study on dielectric thickness theorized in Section 9.2.2 can then be easily realized by photocurrent measurements on the same sample after each oxide deposition. The air gap along with almost conformal PECVD deposition gives us a NW core with an almost uniform oxide shell similar to the ideal core-shell geometry simulated.

The Fig. 10.3.3 (left) reports experimental responsivities for the 188 and 216 nm core diameter wires as uncoated or with 50 nm and 150 nm SiO_2 capping. We can see a very good agreement between the experimental ratio and the theoretical one, in all the visible and infrared range. The minor deviations observed with 150 nm coating is due to non conformal deposition which will be explained later. The right half of 10.3.3 shows the absorption enhancement factor plotted for different oxide thicknesses in TE and TM configuration. The TE and TM absorption enhancement plots can be individually seen to have an idea of the gain in absorption on coating. The comparison of the gain enhancements between the TE and TM configurations give us a complete view of the absorption increase observed in NWs after coating in unpolarized light, which could be due to either coating induced enhancement of either TE or TM contribution. The experimental polarized absorption enhancement curves in 10.3.3b (right) show similar behavior as the theoretical curves with peak experimental absorption enhancement of ≈2 for uncoated to 50 nm coated NW and ≈3 for uncoated to 150 nm coated NW. An overall increase in absorption enhancement is

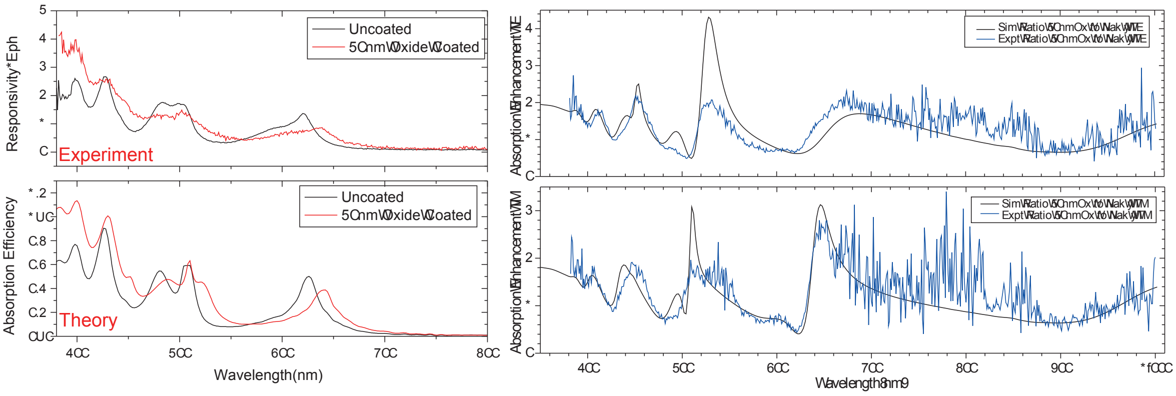

(A) 188 nm (Mie Fit) diameter NW with spectral absorption efficiency (left) and absorption enhancement in TE and TM (right).

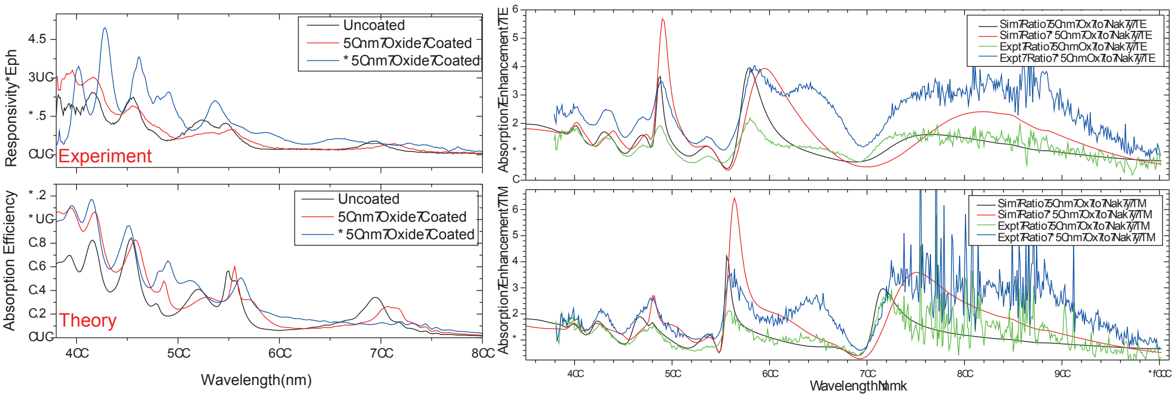

(B) 216 nm (Mie Fit) diameter NW with spectral absorption efficiency (left) and absorption enhancement in TE and TM (right).

FIGURE 10.3.3. Absorption efficiency and absorption enhancement of suspended NWs

observed for most of the spectrum range by increasing the thickness of oxide coating from 50 nm to 150 nm.

10.3.3. Polarized light absorption with dielectric coating.

We have already seen the polarization dependence of absorption in Section 7.3.3 with large polarization sensitivities Q_a^{TM}/Q_a^{TE} for uncoated NWs. We perform similar calculations again for calculating Q_a^{OX-TM}, Q_a^{OX-TE} for the 230 nm PECVD SiO_2 coated NWs and plot the polarization sensitivity as Q_a^{OX-TM}/Q_a^{OX-TE} with respect to the diameter and wavelength in a contour plot shown in Fig 10.3.4. The figure on the right shows the coated case which can be then readily compared with the uncoated case shown on the left.

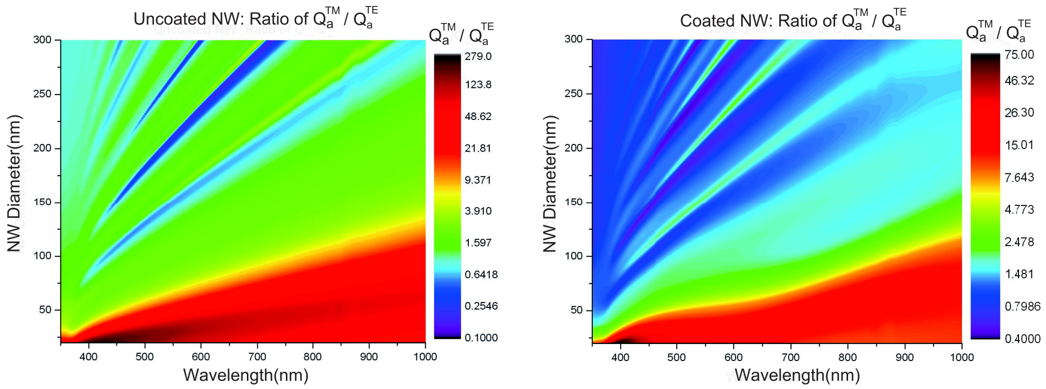

FIGURE 10.3.4. Polarization anisotropy (Q_a^{TM}/Q_a^{TE}) plotted for uncoated and coated NW calculated theoretically.

If we compare the two plots in Fig 10.3.4, keeping in mind the different color scales, we see a huge reduction in the polarization sensitivity from uncoated to coated NWs. The peak magnitude of polarization sensitivity is reduced by almost a factor of 4, from 279 for uncoated to 75 for the coated NW. This results on polarization sensitivity when combined with absorption enhancement observed in Fig 10.2.2b provides us with further insight in absorption gain mechanism by coating. An increase (factor >2) in absorption along with the decrease (factor >3.5) in polarization sensitivity by coating can only suggest a TE absorption gain higher than the TM one. The anisotropy in polarized light absorption is even more evident for smaller diameter NWs and decreases as the diameter increases, which is a direct proof of the geometric anisotropy[5] being converted into polarization anisotropy. The addition of an oxide shell on the NW thus reduces the geometric anisotropy due to an increase in the diameter of the core-shell system resulting in a decline of the polarization sensitivity. Thus by coating the NWs with oxide they become more efficient absorbers of unpolarized light.

The NWs in air make perfect structures for such an experiment and we replot the Fig. 10.3.3 to have the polarization sensitivity variation with wavelength.

This polarization sensitivity for the same NWs in Fig. 10.3.3b is plotted vs wavelength in Fig. 10.3.5. From the two dimensional maps of the polarization sensitivity shown in

---

[5] The geometric anisotropy here refers to the quasi one dimensional structure of NW where length is much greater than the diameter

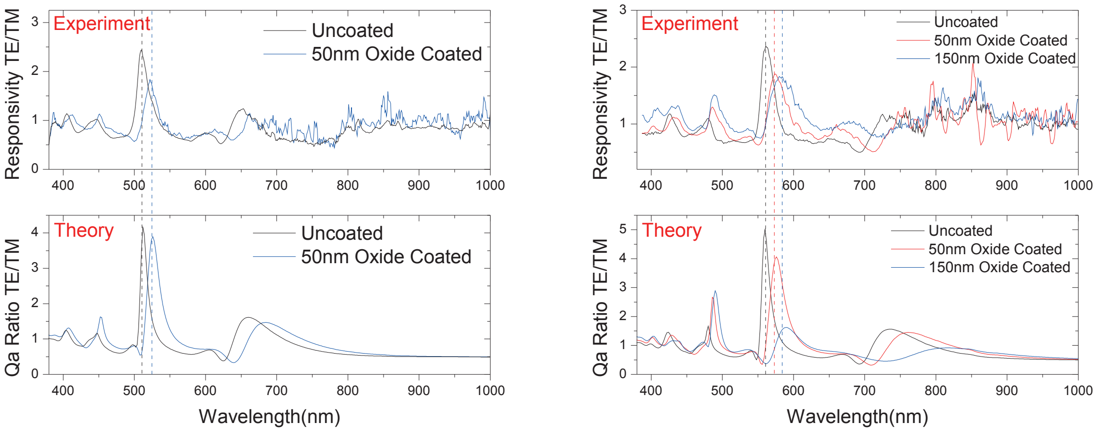

FIGURE 10.3.5. Polarization sensitivity of suspended NWs for 188nm(left) and 216nm(right)

Fig. 10.3.4, we can clearly see that a good balance between the TE and TM absorption can be found for a core diameter in the 200 nm range, as it is experimentally observed here. The quantitative agreement observed in the present case with two different diameter NWs, with polarization sensitivity of both diameters fitting nicely with theory, along with the 2D plots in 10.3.4 is a strong proof showing that the absorption enhancement observed upon capping arises from strong increase in the TE absorption as the overall core shell diameter increases. The results also supports the previous study on the dependence of absorption on oxide thickness, since it shows an improvement of the photocurrent output after coating.

Finally by coating NWs, this reduction in polarization sensitivity obtained is highly advantageous for the photovoltaics and paves a new way for the improvement of NW based solar cells. In applications requiring high polarization sensitivities the Fig 10.3.4 along with Qa enhancement in Fig 10.2.2 can serve as a guide for engineering devices sensitive to the light polarization state.

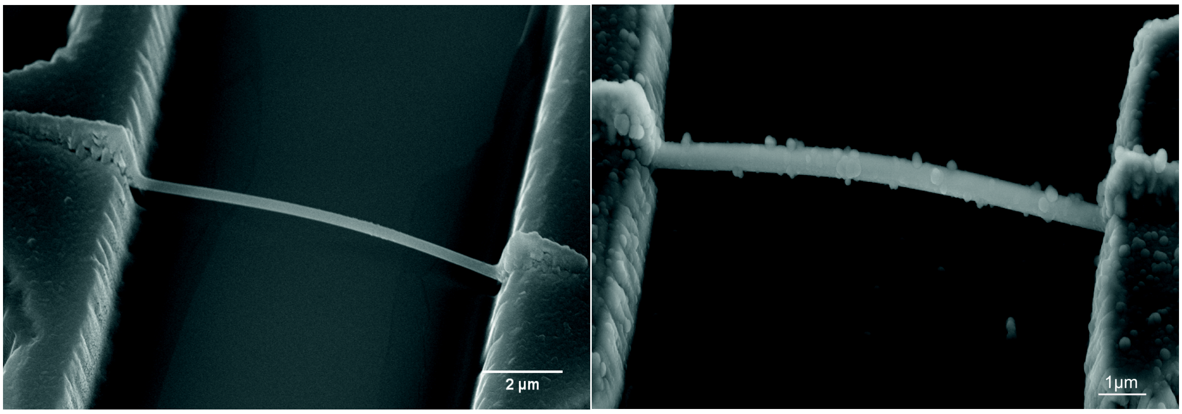

FIGURE 10.3.6. SEM of suspended NW after second deposition(nodules on NW)

The quality and conformity of PECVD deposited oxide largely depends on the surface used for the deposition. Due to the above reason, during the second deposition the deposition recipe sees a different surface (previously deposited oxide) instead of the silicon surface as seen in the first deposition. This change in initial conditions caused the formation of nodules during the second 100 nm layer deposition of PECVD oxide for the NWs characterized in Fig 10.3.3b. The Fig 10.3.6 shows the SEM image of this suspended NW after the two deposition steps. The formation of various nodules due to nonuniform growth is clearly visible over the entire NW. The presence of these nodules on the NW causes thickness of the shell to vary over the surface of the NW and thus affects the light absorption in the NWs, in particular through scattering. The deviation from a uniform core shell structure are reflected in the responsivity measurements in Fig 10.3.3b where 150 nm oxide spectra does not provide a reasonable fit with the theory unlike for the 50 nm coating. Nevertheless the ratio of TE/TM absorption is independent of such artifacts and one can proceed with quantitative comparison of the polarization ratio between oxide coatings of different thickness. Unfortunately, the deviation of the morphology from the core-shell geometry (for the last 100 nm deposition step) prevents us in measuring the relative change in the external quantum efficiency from 50 nm to the next 100 nm oxide deposition with a high level of accuracy.

We also performed measurements to see the effect of asymmetric deposited oxide thickness on the light absorbed in TE and TM polarization. To achieve that, we modulated the thickness of the deposited PECVD SiO_2 on previously studied NWs (one of the wires studied in Fig. 10.2.4) by adding more 100 nm oxide to reach an overall thickness of 330 nm (See

Appendix A-II). In the above case the cumulative effect of the Fabry-Pérot like resonances in the oxide along with the unequal oxide thickness on the top and bottom of NW induces significant changes in the NW response. The resulting responsivity in the TM polarization was relatively unharmed but in TE polarization the absorption spectra was highly modulated showing no correlation with theory.

CHAPTER 11

Conclusion

The detailed analysis of the light absorption in Si NWs was presented and various means to modulate this absorption was proposed with concluding work on an ideal geometry of NW in the air.

To study the light absorption in Si NWs, diodes were fabricated and their properties were studied by I-V and EBIC measurements. The experimental setup required for performing the photocurrent measurements was assembled with suitable resolution to localize NW and the precision to measure the short circuit current levels as low as ~5E-14 amperes. The setup provided an efficient measurement of photocurrent without needs for bonding the sample thus enabling multiple photocurrent measurement on the same sample after subsequent lithography, etching or metal/dielectric deposition process steps. The photocurrent measured was converted into responsivity to have a more standardized measurement. The responsivity measurement done on NW junctions provided novel peaks in the spectral plots very different from the bulk. The presence of similar spectral peaks were confirmed by changing the junction type and the substrate giving a basic understanding of the dependence on the NW material and morphology. To have a better understanding of the resonances the theoretical calculations were performed by the help of the Mie theory. The theory provided means to calculate the absorbed power in the NW which was converted into absorption efficiency for easy comparison with NW responsivity. The experimental measurements gave fair correlation with the theory and showed much better fits compared to the literature. The reasonable fit along with the literature reports confirmed the presence of resonant light absorption at the scale of the NWs under study. The theoretical calculation with the electric field plots in the NW core showed formation of modes in the core of the NW with intensity of the modes varying with wavelength and diameter.

The theoretical description not only strengthened our understanding of the light interaction and absorption in such NWs but also provided various tools to ensure the peaks in spectrum indeed arise from Mie resonances. The prospect of tuning the basic set of parameters on which these resonances depend on provides an opportunity of better understanding the physical reasons behind the resonances and in later run can cater possibility of new applications. The dependence of the absorption was studied for two most feasible parameters that could be varied, namely light polarization and NW diameter. A highly anisotropic polarized light absorption was perceived with the NW absorbing light much more efficiently in TM polarization than the TE polarization. The presence of a particular TE or TM mode depends on the diameter of the NW and thus as the diameter is increased so does the number of modes, that can exist in it. Thus the number of resonances gradually increases with the diameter of the NW. The resonant light absorption was highly sensitive to the diameter with the spectral shift in resonances seen for change in diameter as small as 4nm. The high spectral sensitivity of the resonances and the dependence on diameter could be used to make devices with application tailored response or for measuring the NW diameters with a high resolution. The EQE of the single NW were performed on p-i-n core shell junction with a peak EQE of ~40% for a typical device.

Most of the part dealing with the light absorption in NWs was dedicated to understanding the influence of dielectric coating on the light absorption in a single Si NW. This importance of the chapter is derived from the extensive use of dielectric coatings used in photovoltaic industry for passivation and anti-reflective property. The theory of light absorption previously used was only limited to uncoated NWs, thus a modified version of Mie theory was developed for core shell coaxial cylinders having an absorbing/non-absorbing shell which is capable to isolate the absorbed light in the core and the shell. The preliminary experiments were performed on the previous NWs by PECVD deposition of 230 nm SiO_2. The results confirmed the possibility of an absorption enhancement by coating the NW with an oxide. The experimental absorption almost doubled over most of the spectrum by coating with 230 nm oxide for the entire range of diameters. The theoretical studies performed on the absorption enhancement provide enhancement factors as high as 3.68 with respect to uncoated NWs. The advent of dielectric coating provides us with more degrees of freedom to modulate specific parameters like dielectric thickness and refractive index. The analytical calculation showed periodic modulation in absorption efficiency for varying dielectric thickness. This is presumably due to Fabry–Pérot like interferences in the oxide shell causing the periodic fluctuation in absorption. The change in real part of refractive index was discussed and shown to increase the core absorption with increasing the shell refractive index. On the contrary, increase in the complex refractive index showed an increasingly detrimental effect of the dissipation in the shell at the expense of the absorption in the core of the nanowire.

Finally, an ideal case of NW in air was tested to validate the influence of substrate on the light absorption. The ideal structure with suspended NW was fabricated with a novel method without any etching steps. The experimental results show an excellent correlation with the theory with all the theoretically predicted resonances perfectly reproduced in the experiment. The study confirmed substrate interaction as one of the main factors affecting the light absorption in NWs lying on the substrate. The NW in air structure also provides excellent fits with the theory for coating with a 50 nm PECVD oxide and also confirmed our theoretical results showing a sequent reduction in polarization sensitivity when increasing the thickness of the dielectric coating from 50 to 150 nm.

Part 4

Conclusion and Perspective

We have studied the p and n-type doping in Si NWs and addressed the issues of NW faceting, inhibition of amorphous shell deposition by adding HCl during the growth. Incorporation of HCl also provides other benefits like reduction in catalyst diffusion and so reduced tapering, passivation of the sidewalls with Cl and we obtained doping efficiencies enhanced by an order of magnitude for boron doped NWs. The change in resistivity along the NW axis and with NW diameter was attributed to surface doping and surface depletion respectively. We successfully grew p+i schottky, pin axial and pin core-shell junctions and fabricated good rectifying diodes. The quality of the schottky junction diodes were studied by I-V measurements and the minority carrier diffusion length of $\approx 700\,nm$ were extracted from EBIC measurements.

The study of the light interaction with single Si NWs was studied with microphotocurrent spectroscopy with sharp minima's and maxima's in the spectral response of NW pinpointed as Mie resonances. The NWs can have optical cross-section greater than their physical cross-section and therefore couple and confine light more efficiently than their thin film counterparts. The NW diameter, dielectric constant of the coating, thickness of coating later and incoming light polarization are the major controlling factors for tuning the light absorption. Finally a perfect correlation between theory and experiment was obtained for suspended NWs giving the strongest confirmation of Mie absorption processes in our NWs.

The works performed in this thesis are state of the art and are/were foremost results in our field at the time of the study. This work provides an important contribution in various fields of NW growth/doping, electrical studies and optical or light absorption measurements for NWs in general. The extensive study performed on p- and n-type doping is unique since most of the results found in the literature regarding the doping are sparse and focused on particular growth process. The light absorption in NWs is currently the foremost and the most detailed study with each parameter studied separately.

The goal for this research work was to aid the incorporation of Si NWs in photovoltaics. Last but not the least, we would like to point out a few shortcomings of our studies with respect to solar cells. The current study was exclusively performed on single horizontal Si NWs and cannot be directly applied for photovoltaics since the NWs usually have a very weak absorption in infrared due to their small diameters. Therefore an array of vertical NWs is preferred to absorb as much light as possible where the applicability of our light absorption studies are limited. Nevertheless, our work see's wide variety of NW based applications ranging from control of doping for better NW devices, sensing, electronics, nanophotonics and solar cells.

Here we give a short perspective of the studies that could be performed based on our work with some of our preliminary results. Our studies on Si NWs can be readily extended to Ge NWs (or any NW in that case). Indeed, the first study on light absorption in NWs by Mie theory was also performed on Ge NWs[**22**]. Thus with the axial n+i Ge NWs readily available from our growth equipment, we performed some basic set of IV and photo current measurements. The preliminary results on the response of Ge NW is plotted in Fig 11.0.1. We see an absorption spectrum comparable to that of obtained by [**57**] with band stop around ~ 1580 nm for 240 and 280 nm NW. Our experimental background could be used to probe the electrical and optical properties of strained Ge NWs since interest in strained and doped Ge has recently increased due to the observation of the first germanium laser grown on silicon, under a planar waveguide configuration.

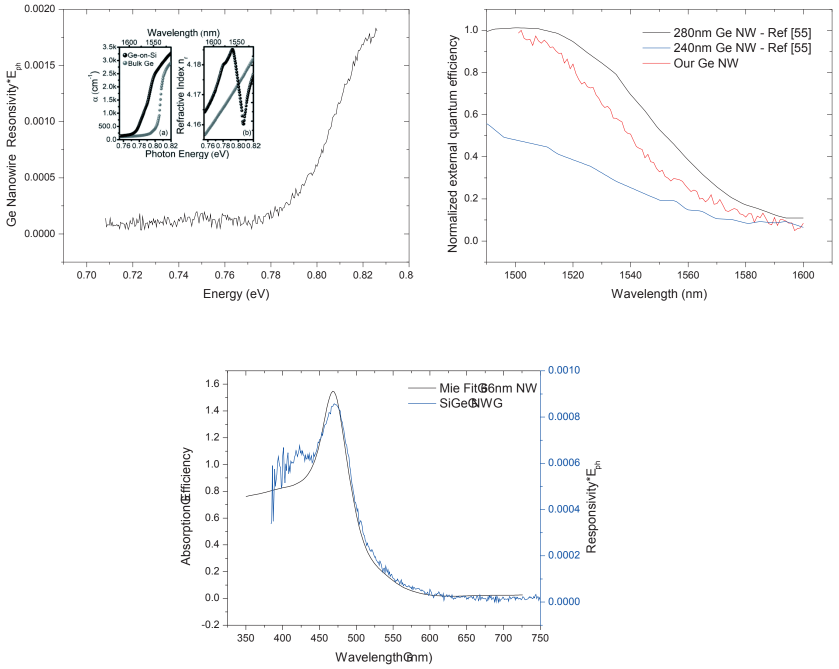

FIGURE 11.0.1. Absorption in Ge NWs. (Top) Light absorption in Ge NW. On left, the Responsivity*Eph is plotted vs energy (eV). The inset show absorption cut off at bandgap in bulk[**74**]. On right, normalized EQE is plotted vs wavelength for the same NW on left and is compared with EQE of 280 nm and 240 nm Ge NWs from literature. (Bottom) Mie Fits of analytical absorption efficiency with experimental Responsivity*Eph for $Si_{39}Ge_{61}$ NW

Also alloys of Si and Ge can be mixed in various compositions Si_xGe_{1-x} to have intermediate properties between Si an Ge. A preliminary experiment on Si_xGe_{1-x} n+-i NW with Si composition between 35-55% was tested. The absorption efficiency and experimental response is shown in Fig 11.0.1. Based on the correlation with the absorption spectra obtained for different refractive index data for Si_xGe_{1-x} $x=0.39$ and $x=0.51$, a successful fit was observed for $x=0.39$ thus experimentally deducing the approximate composition of the SiGe alloy.

Part 5

Appendices

A Growth and methods

I CVD growth

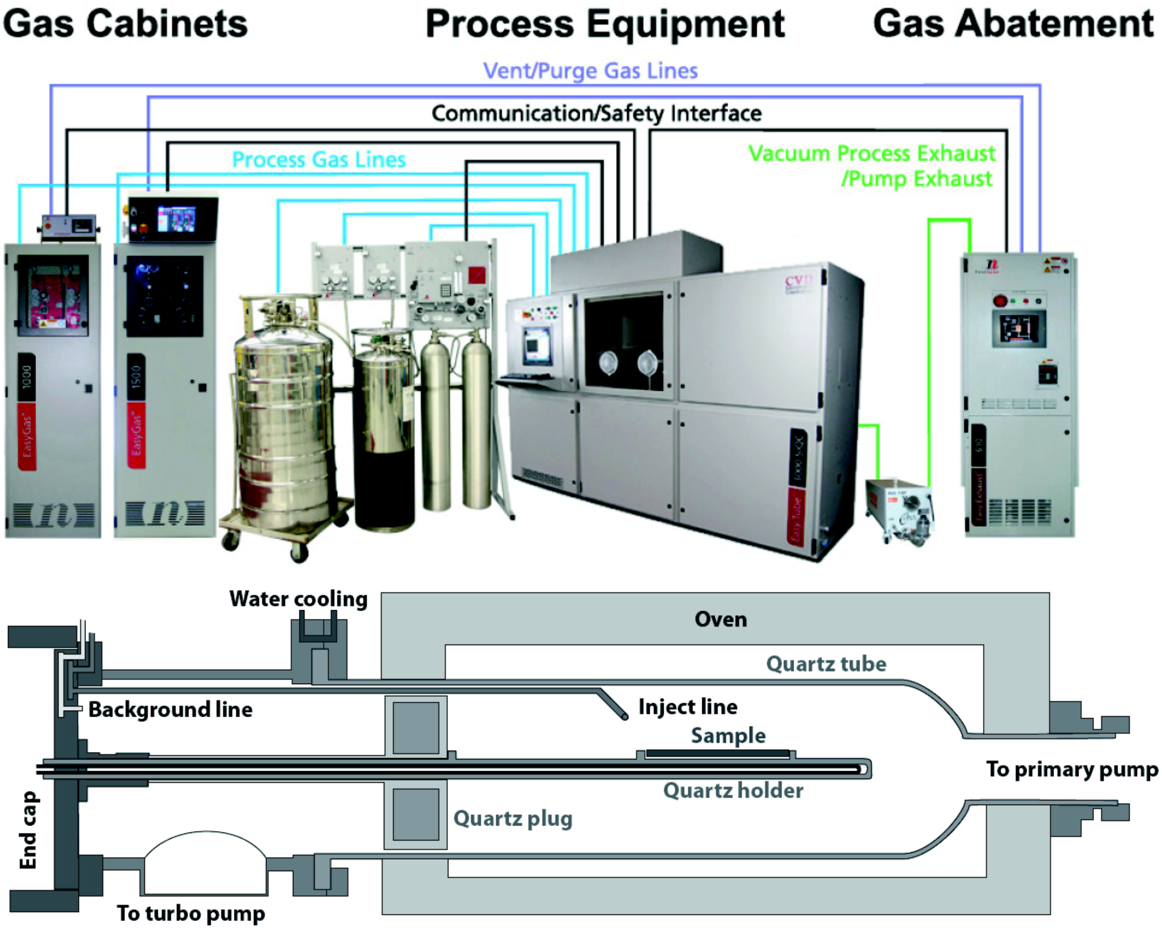

FIGURE 11.0.2. EasyTube3000 First Nano CVD in top figure and a schematic of a EasyWire CVD adapted from ([75])

The CVD growth was performed in a low-pressure CVD reactor (EasyTube3000 First Nano) equipped with SiH_4, B_2H_6, PH_3, HCl and H_2 gas lines. The Silane, Diborane and Phosphine are diluted with hydrogen gas to have a specific precursor gas ratios for the required doping. All the input gas lines are equipped with mass flow controllers(MFC) to accurately control the ratio of precursor gases and sensors to detect process values(PV) of various gases in realtime. The hydrogen gas is also used as carrier gas with a constant background flux to transport the growth precursors through the CVD chamber. The CVD reactor used is hot-wall reactor and thus the wall of entire chamber is pre heated to desired setpoint before passing the process gases. The actual CVD gas line connections and a schematic of reactor can be seen in Fig 11.0.2.

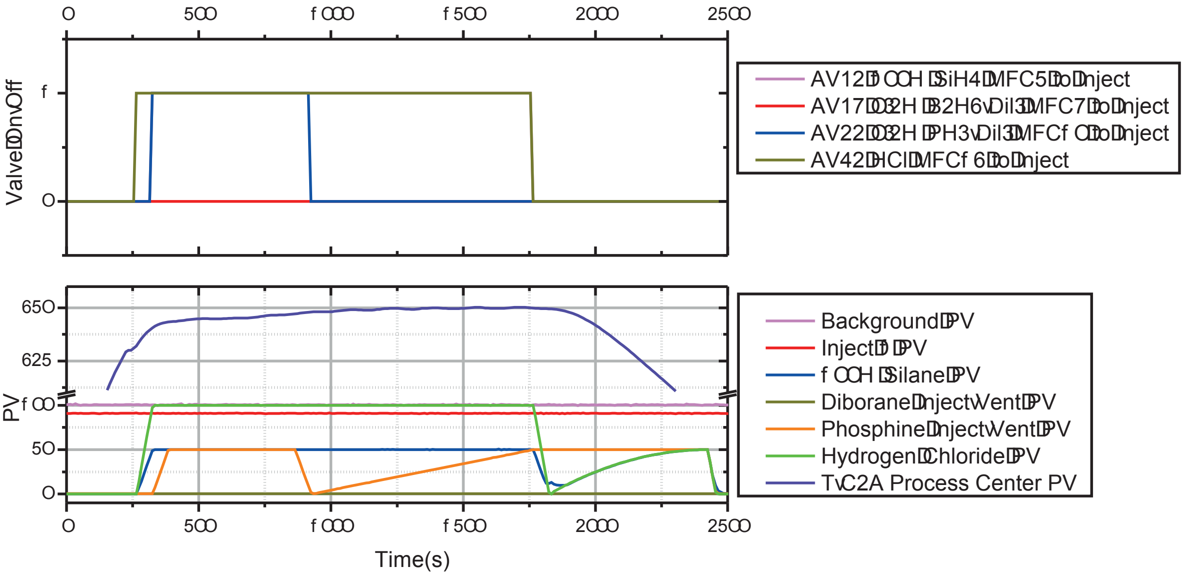

(A) Axial n+i NW

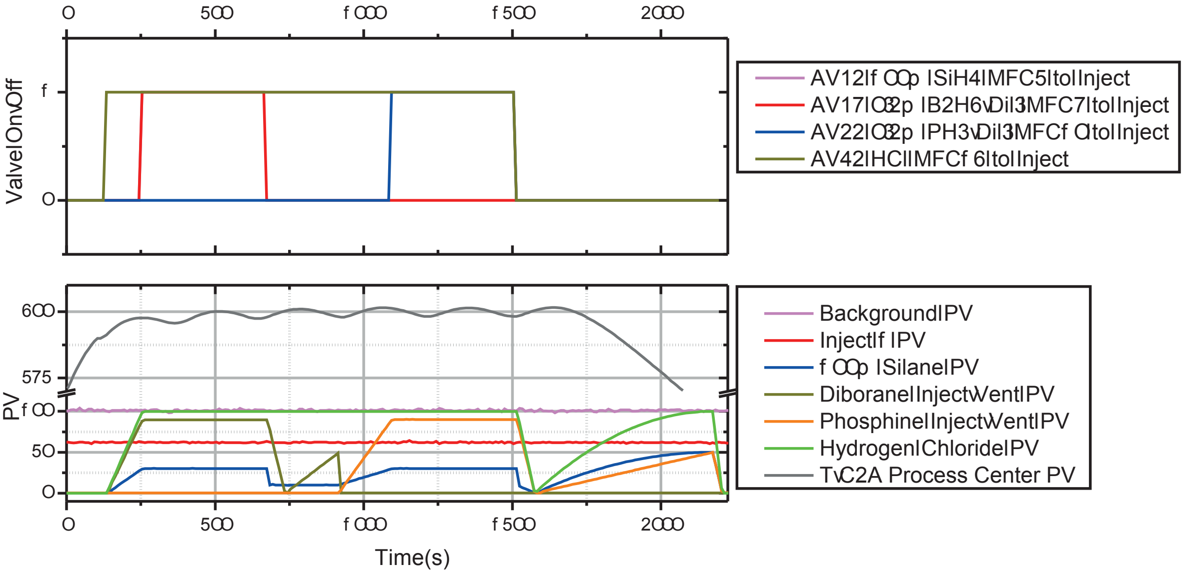

(B) Axial pin NW

FIGURE 11.0.3. The actual process value and MFC reading for different growth parameters during different growths

The Fig 11.0.3 shows the MFC values(gas inject =1, no gas inject = 0) and process values showing the flow of different gases over the growth time. The scale does not represent the actual flow rates due to different dilution of process gases but should merely be used to interpret the qualitative increase or decrease of individual gases. The temperature process value shows the actual temperature in the chamber during the growth.

A growth process for n+i NW is shown in Fig 11.0.3a. The background H_2PV of and injection H_2PV in inject line is set constant throughout the process. The temperature is slowly ramped to the process temperature of 650 °C. The HCl, Silane and Phosphine gases are introduced in the process lines and when the required PVs are reached the MFC5, 7 and 10 for the respective gases are opened(set to inject) and gas flows in the chamber. The pressure in the chamber is regulated by the primary pump which continuously tracks the pressure set-point to process value. The growth rates for different doping is pre calibrated by trial and error. Once the growth time is reached for specific length of NWs the MFC's are switched from inject and a N_2 purge is done with vent line connected. The n+i NWs require the phosphine gas to be switched off after the growth length of n+ section is reached. This can be seen at ~580sec where the MFC for phosphine to inject line switches off and the process value reduces from 50 to 0. The later increase in Phosphine PV in is due to the N_2purge of the line. In the mean time Silane and HCl MFC are still on and thus results in growth of the intrinsic section. After the growth is finished the Silane and HCl MFC are switched to off followed by a N_2purge of respective lines. A similar process for growth p-i-n axial junction can be seen in Fig 10.0.6b. The growth of p-i-n core shell junctions can be performed in similar fashion with growth stop after p+ core and HCl flows stop with temperature increase for 2D growth of i-n section.

Growth of radial junctions.

The growth process of the radial junctions is very different from the axial NW. Such a growth can be performed in two ways:

Case I:.

The core of the core shell system is grown first by a high doping recipe to obtain a degenerately doped core e.g p-type for pin core-shell NW. The growth parameters are Diborane/Silane dilution of 3E-3, 100 sccm of HCl at 600ºC and pressure to 3 Torr for 20 min. The as grown sample is then removed from the CVD chamber and is dipped in IKI[1] to remove the gold catalyst from the tip of NWs. This step is performed to eliminate any gold on the sidewalls and the catalyst which can either diffuse during the shell overgrowth or act as catalyst and continue NW axial growth which is unnecessary. A mild HF clean is

---

[1] Lugol's solution: Elemental iodine dissolved in potassium iodide (KI) diluted in distilled water is widely used to dissolve gold

performed after IKI step to remove the native oxide (easily formed in air). The sample is then transferred in the CVD chamber for shell growth. In this second step the growth parameters are modified to change the growth regime from axial/catalyst induced 1-D growth mode to 2-D/thin film growth mode. The intrinsic shell with 50sccm of Silane at 650ºC for 4 min followed by n-type shell with Phosphine to Silane dilution of 3E-3 at 650ºC for 3.30 min was deposited in this step. The HCl flow is switched off for shell growth to allow conformal deposition. Fig 11.0.4a shows typical pin core shell NWs growth by this approach.

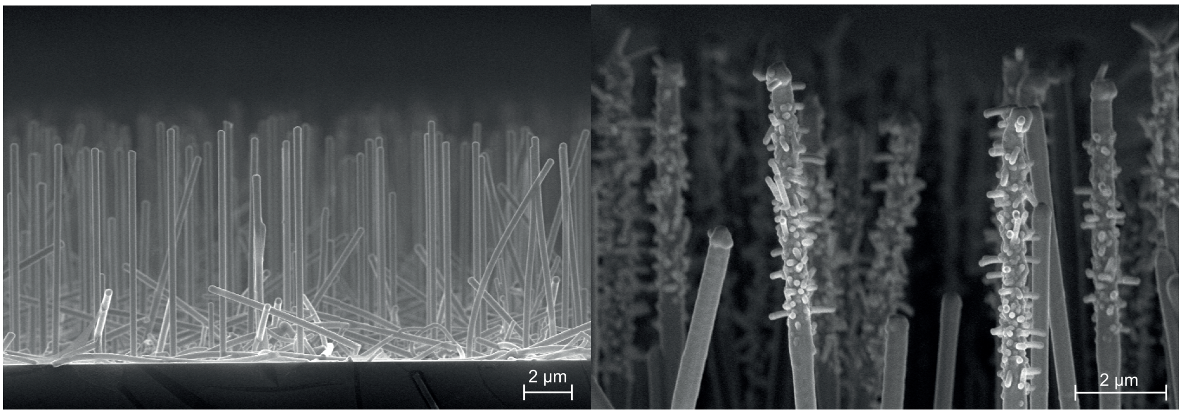

(A) Core shell pin NW by 2-step growth with intermediate IKI clean

(B) Core shell pin NW growth by one shot growth

FIGURE 11.0.4. Core shell p-i-n Si NWs grown by different processes

Case II:.

In the above approach, even though the gold contamination is reduced due to the IKI removal step, the sample has been transferred from clean LPCVD chamber to ambient room conditions with formation of surface oxide. This oxide even though etched using HF, the surface of the NW transferred back in the CVD chamber is never the same as it was after the growth in the CVD reactor. Thus an alternative approach could be to perform a one shot growth, with core and shell of NW grown in the same CVD growth. In this type of growth the process parameters need to be adjusted to minimize diffusion of catalyst and to embed the catalyst in the intrinsic 2-D shell to avoid shorting of the junction through the catalyst. Thus to grow a pin core shell NW by this method, we begin with p-type core by standard growth recipe's with HCl as described before. This is followed by 2D deposition(no HCl) of the intrinsic layer and simultaneously burying the catalyst. Finally the n-type deposition is performed on the intrinsic shell using the same process as intrinsic layer with an addition of dopant gas. The Fig 11.0.4b shows a SEM image of a core shell pin NW grown by this one shot growth process with Diborane/Silane dilution to 3E-3, 100sccm of HCl at 600ºC and pressure to 3Torr for 40 min for core and 50sccm of silane for undoped shell at 650ºC or 4 min followed by n-type shell with phosphine to silane dilution of 3E-3 at 650ºC for 3.30 min with no HCl.

The SEM image in Fig 11.0.4b clearly shows a characteristic thicker region near the tip of the NW with multiple NW hairs protruding from it. The region shows uncontrolled 1-D growth through the catalyst due to insufficient capping of the catalyst during 2-D growth where the parameters favored a concurrent 1-D growth through the catalyst. Furthermore the NW hairs near the tip are due to the splitting of catalyst when the growth transition was performed from 1-D core to 2-D shell regime. It might be possible to obtain a more cleaner growth with this one step growth process by the proper tuning of the growth parameters. Such a study is out of the scope of this thesis and thus we will limit ourselves by working with samples thus obtained from above growth processes. A schematic of the two growth process is shown in Fig 11.0.5.

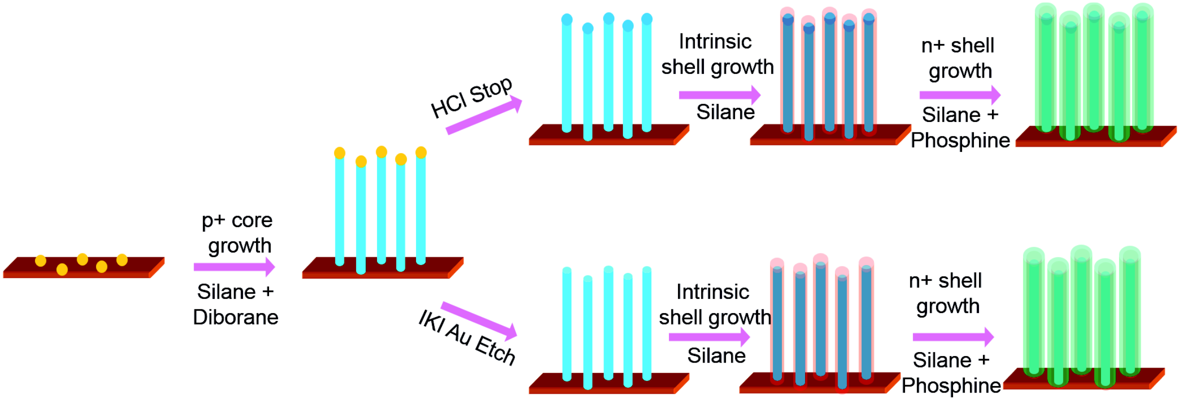

FIGURE 11.0.5. Schematic two growth processes of core shell NW device

Problems are faced for making the contacts on a core shell NW as one needs to connect core on one contact and shell on the other contact for a two probe device (this difficulty made the extensive use of core shell NWs difficult in the following of this work). Here we can use the selectivity of tetramethylammonium hydroxide (TMAH)[2] for etching of p+ doped Si with respect to n+ and intrinsic doped Si to etch the shell (in+). The etch although

---

[2] Etchants like KOH or Ethylenediamine can also be used due to similar doping selectivities of 1E3 between degenerate boron doped Si and undoped/n-doped Si.

possible is quite complicated due to, i) the temperature of solution needs to be maintained at 60 ºC, ii) a large section of NW needs to be masked by materials which can resist TMAH (all resists dissolve in TMAH) to avoid etching of shell over entire length of NW and iii) since the etch rate also drastically depends on the surface morphology, it varies between different samples which makes it difficult to calibrate the etch rate. After the etch is performed, the samples need to be checked in SEM to confirm a complete removal of i-n+ shell. This is necessary to avoid shorting of junction if by mistake both contacts connected to the shell of NW. A schematic of the above process is provided in the next section with various process steps involved in fabrication of single core shell NW device.

II Nanofabrication

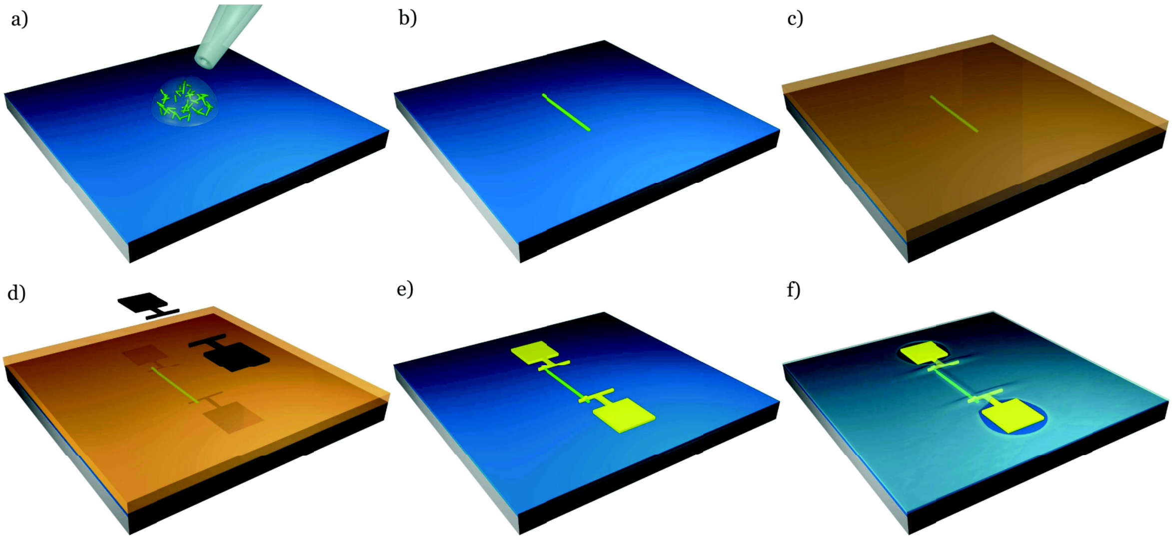

FIGURE 11.0.6. Lithography process schematic a) NW solution dropcasting b) Drying c) Resist spin coating d) Lithography e) Contacted NW after metal deposition and lift off f) Schematic of sample PECVD oxide deposited sample with holes etched on contact pads for dielectric dependence measurements.

The highly experimental nature of the work required a majority of the the time to be dedicated for fabrication and optimization of the devices. The reproducibility of a device/results largely relies on the diligence with which the previous work is executed. Thus we provide here a detailed description of the fabrication and characterization processes that adjoins main body of the thesis. The complete nano-fabrication processes were performed in PTA clean room[**76**] and a typical process for fabrication of device is shown in Fig. 11.0.6.

The fabrication steps depends on the type of the device that needs to be fabricated are classified below for different devices:

Undoped and axial junctions :

(1) The sample with as-grown NWs was immersed in isopropanol solution followed ultrasonication for 5-10 sec giving dispersed solution of NWs.
(2) The NW solution is then drop-casted on thoroughly cleaned Si wafer with 200nm of oxide(or 100nm of nitride)
(3) The sample is spin coated with MAN2410 resist spun at 4000rpm and baked at 90 ºC for 90 sec. The samples were then exposed under the Karl Suss MJB4 mask aligner for 5.2-5.5 sec of exposure to deep UV 254nm. This was followed by a mild edge bead removal step to well planarize the surface of the deposited resist.
(4) The sample were developed by in AZ326 MIF developer for ~45 sec with vacuum contact settings after which they were immediately rinsed under running water for 1 min followed by N_2 blow drying. The settings easily provided 1 μm resolution needed for fabricating devices with 16 probes.
(5) Finally, the samples were loaded in metal deposition tool and a 1 min Ar etch was performed before evaporation. The stack with Ti/Al/Au of 50/100/50nm for n-type and Ni/Al/Au 50/100/50nm for p-type NWs and unintentionally doped NWs.
(6) The lift off was performed by immersing in Acetone for atleast 2 hours. After lift off the samples were cleaned in isopropanol followed by 10min mild plasma ashing to remove the residual photo-resist. This process can be visualized from Fig 11.0.6a-e.

Core shell NWs.

The as-grown core shell pin NWs cannot be used directly to make devices since the core is enclosed by the shell. The carriers generated in pin junction on illumination are separated in p-type and n-type region which should be connected by two terminals to retrieve the photocurrent. Thus the shell needs to be etched on one end of the NW for making the contact to the core. The fabrication was tested by various processes as below:

RIE Dry Etching :

The reactive ion etching is a useful technique to Si with both isotropic and anisotropic etching possible with suitable choice of parameters. The as grown NWs were coated upto almost 3/4th of length with photoresist. The exposed tip of the NWs can then be etched by an isotropic RIE etching recipe to etch intrinsic and n+ shell. The recipe was calibrated on bulk samples and obtained almost isotropic etch (see Fig 11.0.7a). However for the etch test on NWs the RIE etch was highly anisotropic with only vertical etching of the tip region of the NWs(see Fig 11.0.7b). The parameters of the recipe parameters were modified to increase isotropic nature and etching rate but the etching on NW did not proceed as expected on the bulk samples.

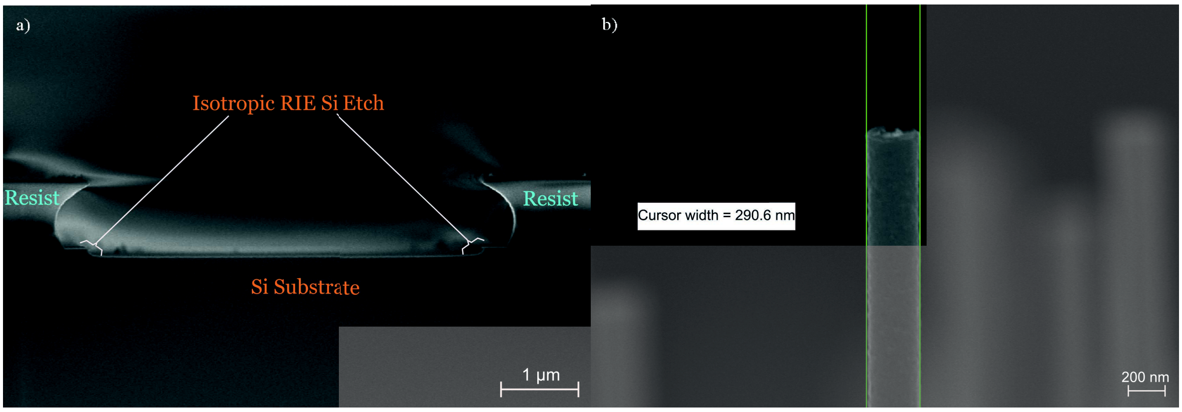

FIGURE 11.0.7. SEM image of RIE etching test, a) on Si substrate patterned with resist b) on NW

Wet Chemical Etching :

The Potassium Hydroxide (KOH) and Tetramethylammonium Hydroxide (TMAH) have unique attribute of doping dependent etching of Si with etch rates for intrinsic and n-doped silicon as high as 10^3times higher than that of p-type silicon. This can be used to our advantage for selectively etching the n+i shell leaving us with p+ core as required. The process follows the similar pattering with as-grown NW sample coated with thick resist (AZ4562). The Fig 11.0.8 a shows the thick resist coating covering the NWs completely with ~20 μm thickness. The 20 μm thickness needed 2 coating steps of the resist to obtain such thick layers. The top view of the NWs is shown in Fig 11.0.8b with almost complete coating of NWs. The Fig 11.0.8c shows the SEM with resist spin coating on ~10 μm long NWs with less density. The reduced density of NWs prevents them from clumping together as in Fig 11.0.8b and the uniformity of resist is better since only one resist spinning step is involved. The spin coated resist was then annealed at 90 ºC for 3 minutes to make it more chemical resistant and a short UV exposure with 10 sec development was performed to etch the resist film on the NWs. Finally to be sure of the NW surface to be clean of resist, a 10 min plasma etch was performed to etch ~500nm of resist on the top of the sample to give clean exposed NW tips as shown in Fig 11.0.8d.

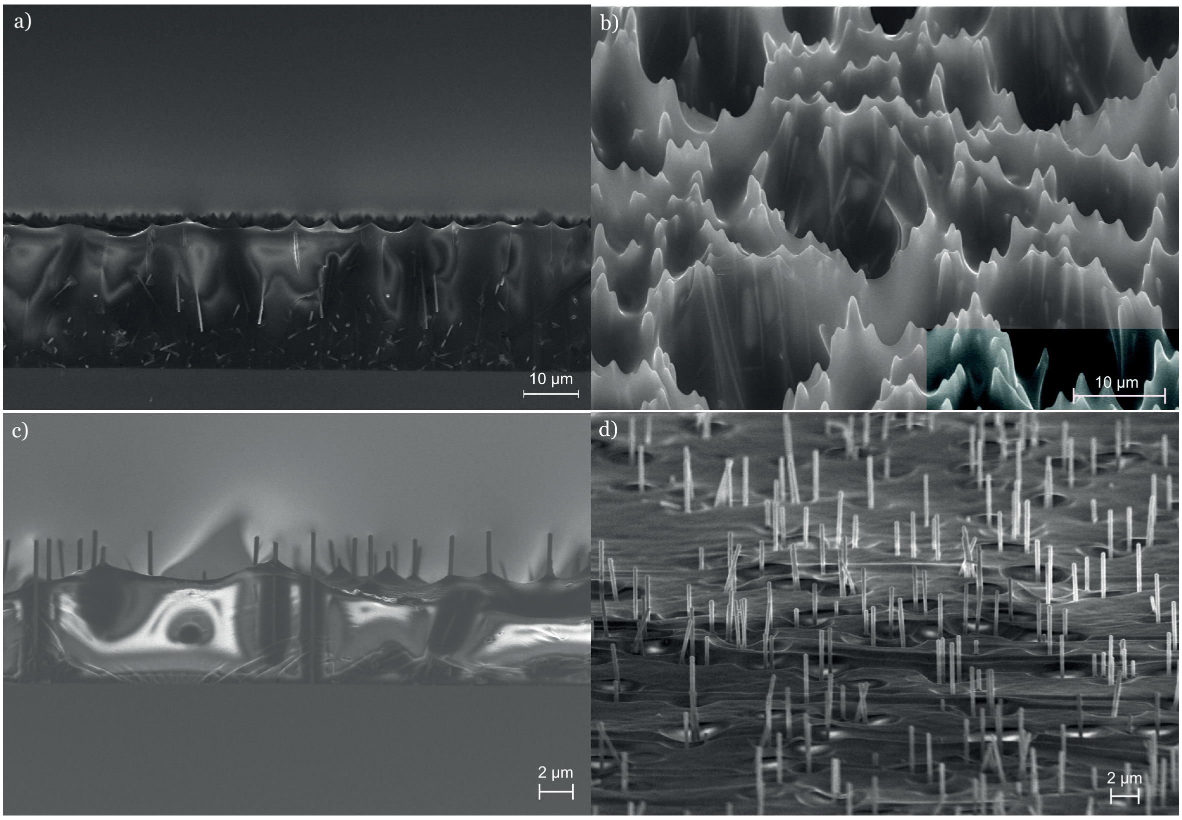

FIGURE 11.0.8. SEM images of pin core shell NWs a), b) after spin coating and c), d) after etching the resist in developer.

The samples were annealed again at 130 ºC for 3min to completely cross link the resist. The samples were dipped in 25% TMAH solution at 60 ºC to etch the exposed NW tips. Due to the capillary action and a strong etching of even hardened resist in TMAH, all the n+i shell of the NWs from the top to the bottom resist coated sections were completely etched by TMAH leaving only p+ core.

Au/Cu Electrodeposition :

The as grown NWs ~10 μm long were spin coated with thick photoresist/SOG ~1-2 μm height. Then an electrodeposition step of Au (from $AuCl_3$solution) was performed to deposit around 200nm of Au on the exposed NW section on the resist. The electrodeposition step cover the exposed NWs isotropically with a gold layer. The etching of n-type and i-type

Si shells then can be easily performed by dipping in TMAH. This leaves us with NW core area exposed on the bottom of the NW. The Au on the top section is removed by dipping in IKI solution.

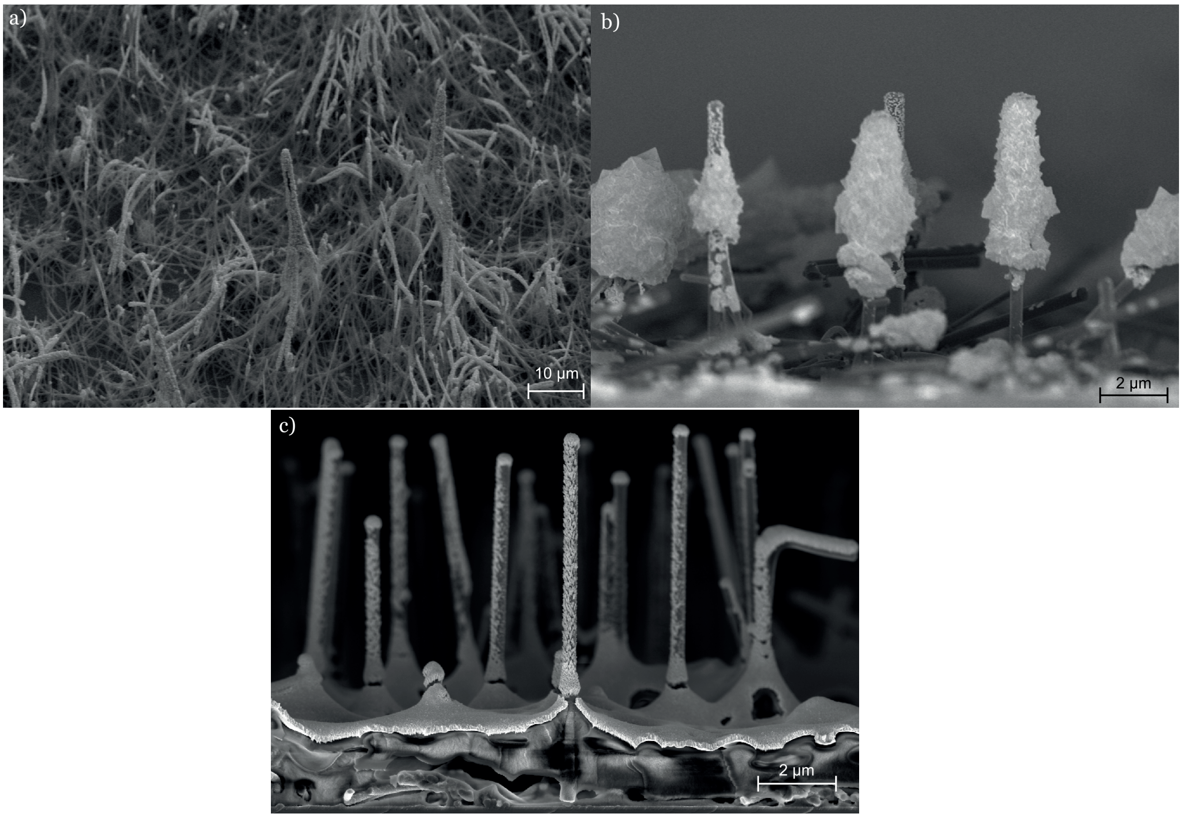

FIGURE 11.0.9. Masking the NW surface with Au, a) & b) for electrodeposition and c) evaporation

The above process has a drawback of nonuniform electrodeposition of Au which depends on the diameter and conductivity of the each p-i-n NW(on as-grown sample) for electrodeposition causing huge deposits on some NWs where as insufficient coating on the other NWs. The samples with Au electrodeposition with SOG/resist removed are shown in Fig 11.0.9a and b. The non-uniformity of the deposition is clearly visible with different thickness of Au on various parts of image. A deposition with evaporation was also tried with 300 nm deposition in 30 min with sample tilted with solid angle of 60 degrees to the source over the deposition time, to have more uniform deposit. However deposition in this case does not form coating of metal on the surface (Fig 11.0.9c). The non uniformity and non conformity of the deposition in above methods prevent us from using the above sample for the next TMAH etching step where the above issues would be reproduced.

PECVD vs Chemical oxidation :

The difficulty in uniformly etching the shell on one section of the NW relays the importance of the masking process used for etching. A uniform etching requires a conformal masking layer. A conformal mask can obtained by PECVD deposition of SiO_2/Si_3N_4 or by chemical/dry oxidation of NWs to form a thin layer of SiO_2. The as-grown samples were transferred to a PECVD deposition tool for ~200nm oxide layer followed by the wet chemical etching process described before. Just before the TMAH etching step the samples are dipped in 1% Hydrogen Fluoride (HF) for removal of the oxide on the tips of NWs protruding from the resist. The HF solution although efficient in removing the oxide also shows a significant capillary etching the oxide layer embedded in the resist. Further the PECVD SiO_2 deposited does not have uniform composition with some areas etched much faster due to non uniform etching.

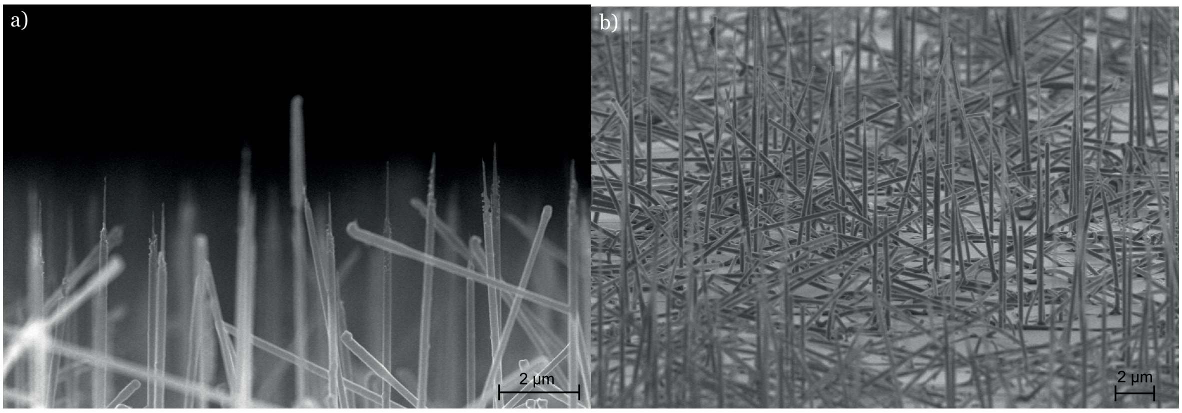

FIGURE 11.0.10. SEM on chemically oxidized pin core shell NWs with tips etched in 0.5% HF and 25% TMAH solution

The oxidation of NW surface by oxidizing agents has been reported in literature to form few nanometer of oxide on the surface of Si[**77**][**78**]. The as grown pin NWs were immersed in 40% HNO_3 solution at 100 °C followed by 68% HNO_3solution at 120 °C for 20 min each. The HNO_3solution was allowed to cool to room temperature before removing the samples. The samples were then cleaned in deionized water and annealed on hot plat at 450 °C for 1 hour. The resulting NWs were characterized under SEM but no discernible oxide layer was seen suggesting a thickness less than <10nm. Test samples for [100] and [111] orientation were chemically oxidized and checked by ellipsometry which shows a thickness of 2-3 nm of chemical oxide. The etch with vapor HF were performed with 20s vapor HF ~6 μm of over etch and 40s vapor HF etched all the shell. Thus liquid etch is a better choice as etch rate can be controlled by dilution. The 1% HF solution was diluted further to obtain 0.5% HF. This solution was used to measure the etch time of oxide grown on test [100] and [111] Si bulk samples (by measuring the time for the Si surface to dewet after immersion in 0.5% HF) found to be 26 sec and 17 sec respectively. The higher time was chosen and the NW samples were immersed exactly for 26sec. After the HF step, the sample was immediately cleaned in acetone for removal of resist followed by dipping in 25% TMAH at 60 °C. The dipping time in TMAH is very critical and etching for more time causes etching of core along with the shell forming needles shown in Fig 11.0.10a or etching entire core and shell. The time for etching was optimized to 90sec giving etched NWs shown seen with careful examination of Fig. 11.0.10b with core-shell intact at bottom and just core exposed at the tip. The samples obtained above were then immersed in IPA and the devices were fabricated by standard process in Fig 11.0.6. A schematic of the etching process is shown in Fig. 11.0.11 for the entire process described above.

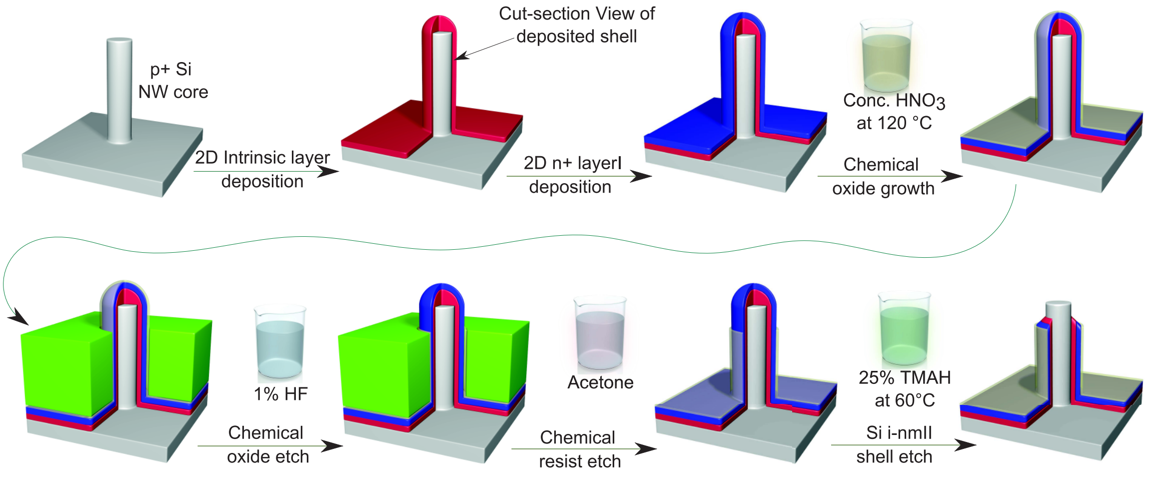

FIGURE 11.0.11. Schematic of pin core shell NW device fabrication

NWs in air :

The fabrication of NW in air was performed by special lithography process to obtain a suspended NW structures after the lift-off process.

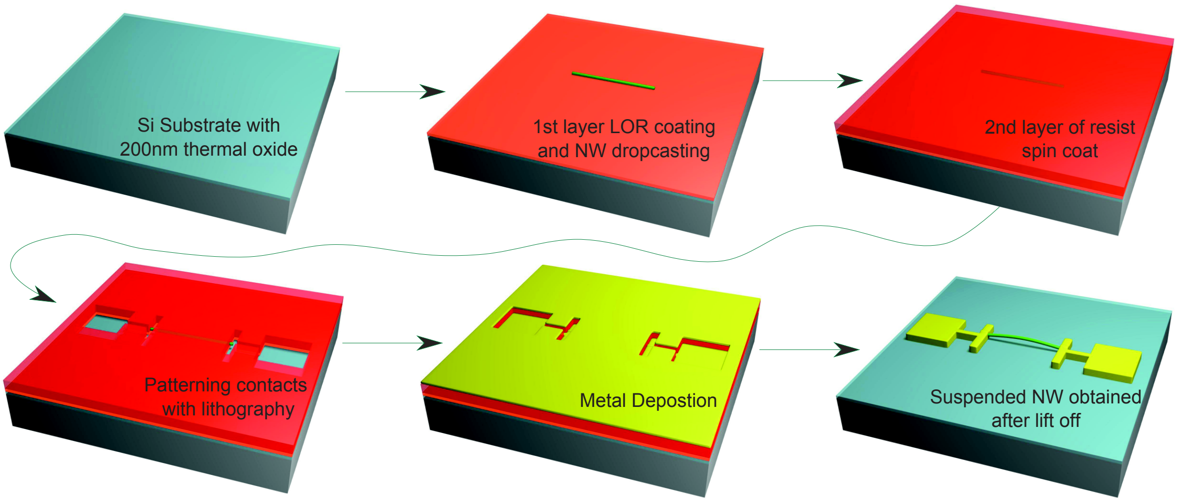

FIGURE 11.0.12. Schematic of process flow for fabrication of suspended NWs

(1) The oxidized Si wafers were cleaned with acetone and IPA followed by hot plate annealing for 5 min at 180 ºC.

(2) The lift off resist LOR 7a was spin coated cleaned wafer pieces at 3000 rpm for 60 sec for a thickness of ~700nm. The sample was then annealed at 150 °C for 5 min to harden the resist making it insensitive to IPA.

(3) The axial NWs in IPA, prepared by the process in previous section, were then drop-casted on the lift off resist coated samples. The sample was allowed to dry in air to evaporate IPA.

(4) AZ2070 resist of 7 μm was then spin coated at 3000 rpm on the samples with pre-baking at 110 C for 3 min. The NWs were then aligned under the mask aligner and 20 sec exposure with UV 350nm. The post annealing bake at 110 ºC for 2 min is required to enhance the selectivity.

(5) The samples were developed in MIF 326 developer for 100 s with mild agitation to have and undercut >1um. Immediately the samples were rinsed under flowing water to prevent etched resist from redeposition. A mild O_2plasma clean was performed for 3 min to etch the residual resist.

(6) The metal stack of Ti/Al/Ti/Au of 10/700/10/100 nm was deposited to contact the NWs(700nm above the substrate).

(7) The lift off was performed by dipping in NMP remover at 60 °C for few hours followed by DI clean and mild O_2 etch for 10 mins. A schematic with major fabrication steps is shown in Fig 11.0.5.

Dielectric coating :

The dielectric coating of Si_3N_4 or SiO_2 was performed by standard PECVD deposition with SiH_4+ $NH_3$and SiH_4+ N_2O gases respectively for nitride and oxide depositions. Since the deposition is performed at 280 °C the samples must be free of any organic contamination. The dielectric coating is uniform with some anisotropy owing to the plasma assisted deposition process. The thickness of the films were measured by Horiba Auto SE ellipsometer with spot size of 25 μm near the NW region. The optical properties of the Si_3N_4 and SiO_2films deposited by PECVD and LPCVD are compared in Fig 11.0.13a and b for real and imaginary refractive indices of the dielectrics. The higher values of real refractive indices for PECVD depositions are accompanied by high values of complex refractive indices. The larger values of extinction coefficients indicate larger absorption of light at that particular wavelength in the dielectric.

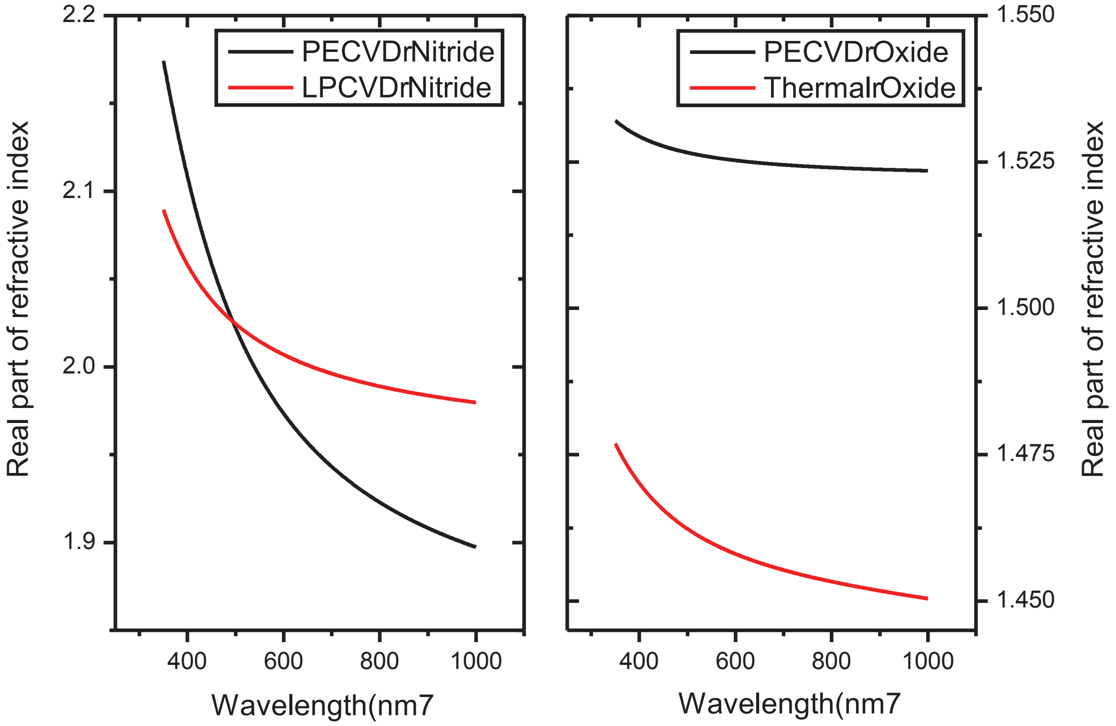

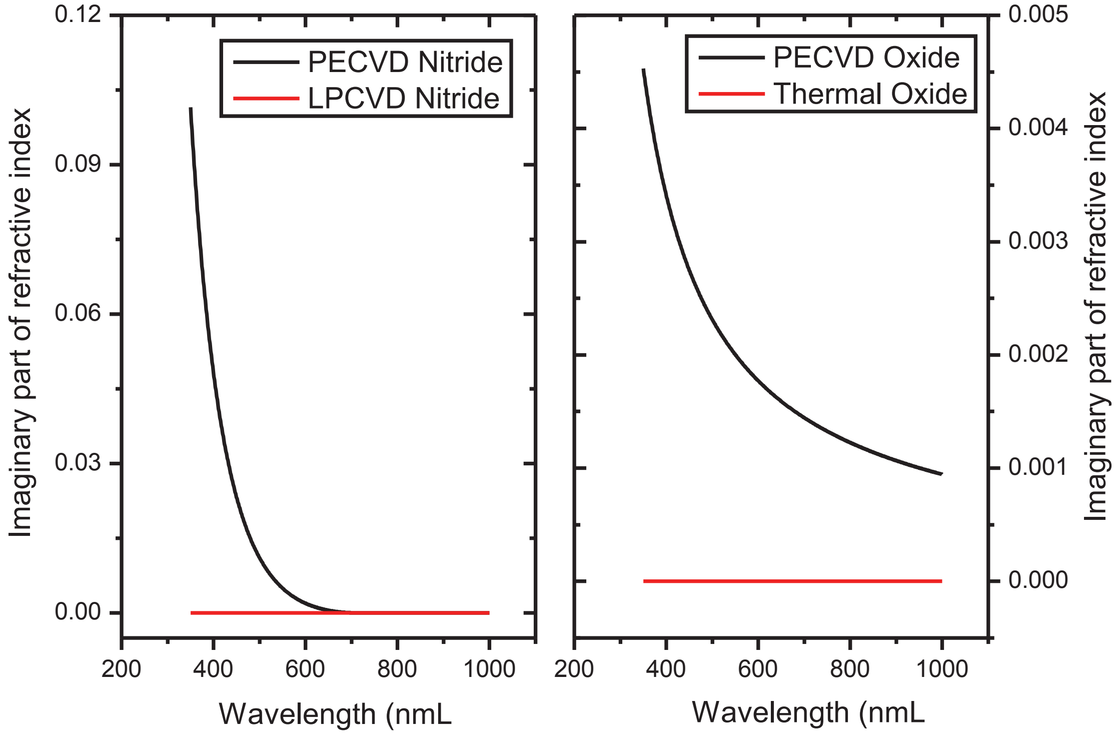

FIGURE 11.0.13. Spectral variation of real and imaginary part of refractive index for various oxides and nitrides

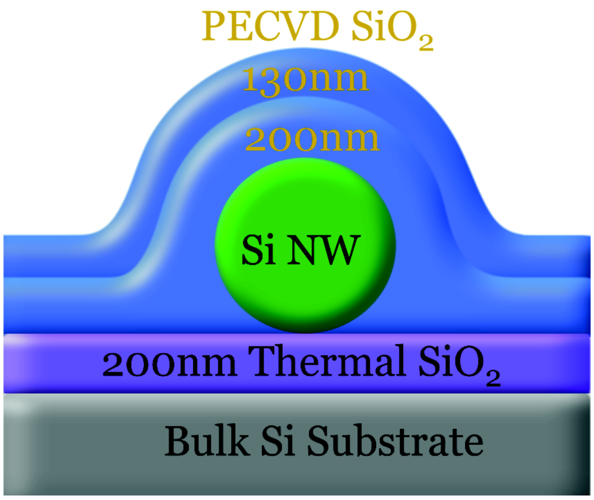

FIGURE 11.0.14. Schematic of 330 nm PECVD oxide coated NW

Absorption in NWs with dissimilar top and bottom oxide thicknesses :

The NWs with first coating ~200 nm oxide were re-coated with 130 nm of PECVD oxide, which makes the total thickness of PECVD oxide to 330 nm. Since the thickness of the thermal oxide below the NW is constant(200nm), the NW now sees a 330 nm oxide on the top and a 200 nm thick oxide on the bottom. Thus the NW see's a nonuniform thickness of dielectric thickness in the vicinity as shown in Fig 11.0.14.

The non-uniformity in the oxide coating affect the process of light scattering and absorption by NW core and causes further deviation from ideal absorption efficiencies calculated theoretically. The normalized theoretical and experimental responsivity is plotted for a NW of ≈210 nm diameter in fig 11.0.15 for uncoated case in top and 330nm coated case in bottom figures. The uncoated NWs shows a nice correlation with theoretical spectra. as expected with almost all theoretical resonances reproduced in experiment. On the other hand, the plots with 330 nm PECVD coating on the same NW show various differences in resonances but gives a satisfactory fit over the spectrum. The resonances in TM configuration shows a better correlation than that of TE polarization. This suggests that absorption of TE polarized light is more susceptible to non uniformity in oxide thickness compared to TM polarized light.

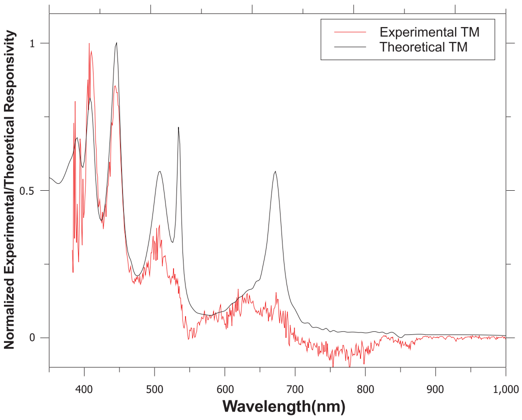

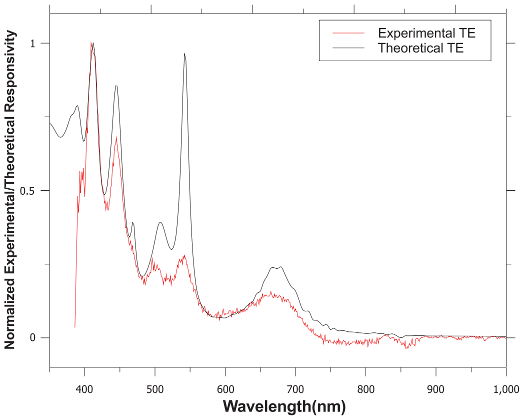

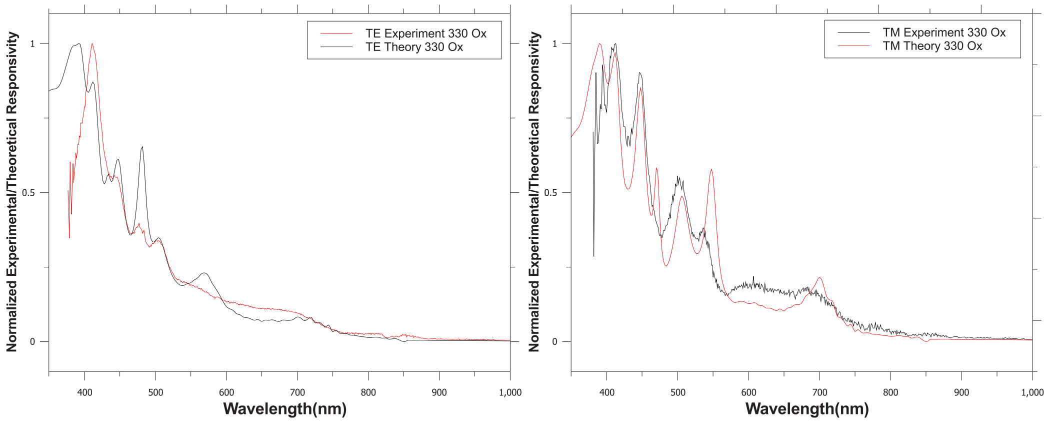

FIGURE 11.0.15. Uncoated(top) and 330nm PECVD coated(bottom) ≈210nm NW

In the above case the cumulative effect of the Fabry–Pérot like resonances in the oxide along with the unequal oxide thickness on the top and bottom of NW induces significant changes in the NW response. The resulting responsivity in the TM polarization was relatively unharmed but in TE polarization the absorption spectra was highly modulated and does not fit with the theory, also due to the above reasons the polarization sensitivity(not shown here) ratio Q_a^{TE}/Q_a^{TM} shows no correlation with theory.

III Characterization

Electrical and optical characterization.

The electrical characterizations were performed using Keithley 4200 semiconductor characterization setup(SCS). Our SCS is equipped with 4 probes with 2 preamplifiers (capable of detecting current as low as few femtoamperes) and other standard probe with detection limit of few picoamperes and a ground sense. The measurements on the NWs were always performed with probes connected to preamplifiers for for low noise measurements.

The schematic of optical characterization setup and measurement details are presented in Chapter 7. Here we present a few supplementary details which can help in providing better understanding of the measurement and addressing some of readers doubts. In the optical setup, a Cassegrain objective was chosen with silver as the reflective coating due to its high and broadband refection coefficient of light (>95% between 0.4 and 20 µm) and achromatic doublets were uses for focusing the light to minimized the chromatic aberration in the focused beam. The typical scan setting for monochromator were 1-2nm of wavelength step; 2000μm of input slit; 200 nm of exit slit with a grating set at 500 nm of blaze wavelength. The above configuration should give a spectral resolution of ≈5 nm across the NW. Since the width of the absorbing area(NW) is much small(50-250nm) compared to width of the focused light beam(20-30μm), the actual spectral resolution obtain on NW is much smaller than the above value. For the the sample illumination, a series of white LED's were used. The light source employed consisted of a 75W ozone free arc lamp and the intensity of light was for 10-20 minutes after turning on the lamp, before starting the photocurrent experiments.

The Low noise co-axial BNC cables were used for connecting the sample output to the lock-in amplifier (Stanford Research Systems SR-830), with one contact of NW connected to the core of BNC and other connected to the shell of the BNC connector. The frequency of lock-in was triggered through chopper control which was set to ≈78 Hz. The chopping frequency was best chosen depending on different factors as noise, sample vibration and the stability in photocurrent. All the electrical connections on the setup were shorted before connecting the NW device to avoid any electrical discharge through the resistive NW.

SEM and EBIC characterization.

The setup for EBIC consists of the following:

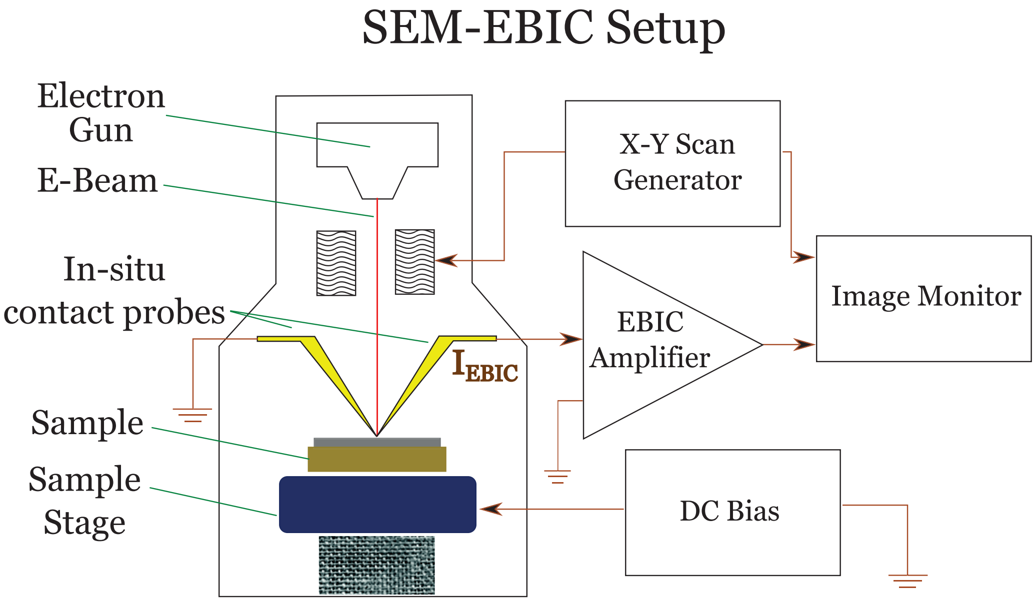

FIGURE 11.0.16. Schematic of operation of EBIC measurement[79]

1. A high resolution Scanning Electron Microscope

2. An external low noise amplifier

3. A sample holder with contact probes with either in-situ or ex-situ contacting.

4. A high vacuum coaxial connections for connecting data acquisition system with sample holder

The current produced due to the electron beam in the sample (I_{EBIC}) is usually hundreds folds larger than the primary beam current(I_{BEAM}) absorbed by the sample. This is due to the following relation,

$$I_{EBIC} = n \cdot I_{BEAM} \cdot (E_b/E_{eh})$$

where $E_b$is the primary beam energy and E_{eh} is the electron-hole pair creation energy and n is the collection efficiency. Thus assuming the acceleration voltage of 1KeV and collection efficiency of 100% and the E_{eh}(for Si is 3.6 eV), the $I_{EBIC}$is ~278 time greater than I_{BEAM}.

A schematic of operation of EBIC is shown in Fig 11.0.16 from [79].

B NW Doping vs diameter

I K. Seo et al

The model proposed by K. Seo et al[**80**] relies on simple charge balance between the surface charges and the NW surface depleted region. We begin by assuming a homogenous surface charge density on NW surface as $N_s$and a dopant concentration of $N_a$or N_d ($N_{a,d}$) in NW. Furthermore, a full depletion approximation[3] is adopted with the effective conducting area of the NWs with conducting core radius (r) is A_{eff}. The structure can be easily visualized by Fig 11.0.17.

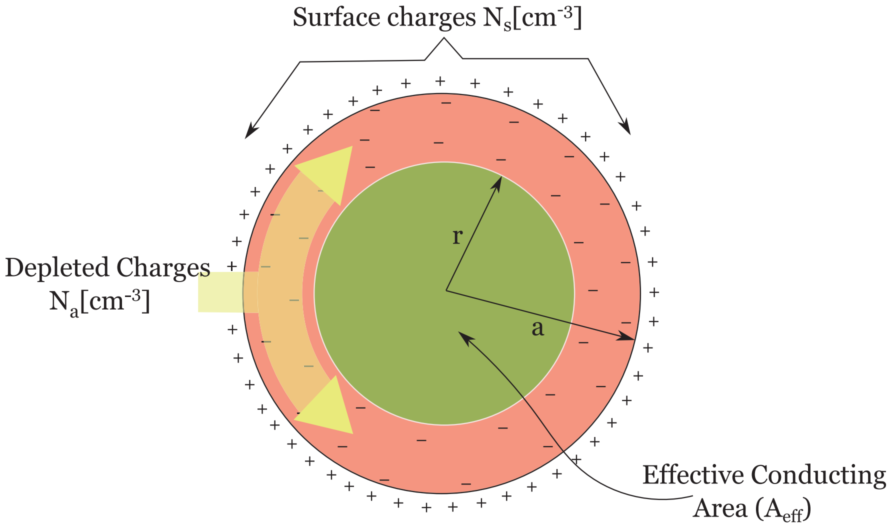

FIGURE 11.0.17. Schematic of surface depletion in NW

To satisfy the charge neutrality condition, the depleted charges in the depletion region must be equal to the surface charges.

$$\int_s N_s ds = \int_v N_{a,d} dv \tag{11.0.1}$$

---

[3] Full depletion approximation assumes an abrupt transition between the depleted region and the non depleted region

Then, assuming uniform surface and depletion charge density we get

$$N_s 2\pi a L = N_{a,d}\pi\left(a^2 - r^2\right)L \tag{11.0.2}$$

Rearranging the terms in above equation we get,

$$\pi r^2 = \pi a^2\left(1 - \frac{1}{a}\frac{2N_s}{N_{a,d}}\right) \tag{11.0.3}$$

where πr^2 is the effective area of conducting area and $\pi a^2$is total NW area i.e measured experimentally. Thus we obtain,

$$A_{eff} = A_{measured}\left(1 - \frac{1}{a}\frac{2N_s}{N_{a,d}}\right) \tag{11.0.4}$$

The measured resistivity is given by $\rho_{measure} = \frac{RA_{eff}}{L}$ and actual resistivity is given by $\rho_{eff} = \frac{RA_{eff}}{L}$, substituting in 11.0.4 and rearranging we get

$$\rho_{measured} = \rho_{eff}\left(1 - \frac{1}{a}\left[\frac{2N_s}{N_{a,d}}\right]\right)^{-1} \tag{11.0.5}$$

The above equation can be fitted with the experimental data on $\rho_{measured}$ vs radius to have extract the fitting parameters as ρ_{eff} and $\frac{2N_s}{N_{a,d}}$.

Since the experimental data measures resistivity, the $N_{a,d}$ can be converted to resistivity[**81**] by

$$\mu = \mu_{min} - \frac{\mu_{max} - \mu_{min}}{1 + \left(\frac{Na,d}{N_r}\right)^{\alpha}} \tag{11.0.6}$$

where $\mu_{max}, \mu_{min}, N_r$,$\alpha$ are fitted parameters given as follows:

	$Phosphorous$	$Boron$
μ_{max}	68.5	44.9
μ_{min}	1414	470.5
N_r	$9.2E+16$	$2.23E+17$
α	0.711	0.719

The mobility is also related to resistivity by $\rho \approx \frac{1}{q\mu N_{a,d}}$. Substituting in Eqn 11.0.5 gives us the relation between the experimentally measured effective resistivity with effective doping.

$$\rho_{eff} = \frac{1}{qN_{a,d}\left[\mu_{min} - \frac{\mu_{max}-\mu_{min}}{1+\left(\frac{Na,d}{N_r}\right)^{\alpha}}\right]} \tag{11.0.7}$$

Substituting the ρ_{eff} extracted from fits in Eqn. 11.0.7 with all the parameters known, we obtain a nonlinear equation in $N_{a,d}$. The root of nonlinear equation gives the effective doping in NW$N_{a,d}$. The surface doping N_s can then be extracted by substituting $N_{a,d}$ in second fitting parameter $\frac{2N_s}{N_{a,d}}$ from Eqn. 10.0.5.

II Uniform Potential Approach

The reduction in the dopant density of the NW with doping (Na) due to doping compensation due to surface/interface traps (Ns) can also be solved by assuming a uniform potential distribution in NW. The model assumes a uniform influence of Ns on the doping (Na,d) in entire cross-section of NW resulting in an effective reduction of doping from Nd to Neff over the entire NW cross-section. Since the NW is highly doped (in the degenerate regime), thus any surface trap induced depletion region in the NW has to be extremely small. One can thus crudely follow the above assumption that the potential all across the wire radius is flat, leading to a constant free carrier density in all the volume of the wire, except very close to the surface. Thus, the apparent resistivity (ρ_{eff}) is the resistivity corresponding to an "apparent" free carrier density (Neff) can be calculated simply by saying that the number of trapped charges on the sidewalls equals the integrated difference between the true number of dopants (ideal surface with no traps as Nd or Na) and apparent number active dopants (with surface traps and overall density as Neff) across all the NW cross-section.

For a NW of radius a, one can formulate following equations for charge neutrality :

$$2\pi a N_s = \pi a^2 (N_{d,a} - N_{eff}) \tag{11.0.8}$$

Rearranging the above equation

$$N_{eff} = N_{d,a} - \frac{2N_s}{a} \tag{11.0.9}$$

Similarly, as in previous section one can convert N_{eff} to ρ_{eff} by one substituting Eqn 11.0.9 in 11.0.5 we get

$$\rho_{eff} = \frac{1}{q\left[N_{d,a} - \frac{2N_s}{a}\right]\left[\mu_{min} - \frac{\mu_{max}-\mu_{min}}{1+\left(\frac{\left[N_{d,a}-\frac{2N_s}{a}\right]}{N_r}\right)^{\alpha}}\right]} \tag{11.0.10}$$

The above equation gives the relation between the effective resistivity measured vs radius(a) of the NW. The experimental data can be fitted with above equation by non linear regression to give the true doping $N_{d,a}$ and surface trap densityN_s as fit parameters.

C NW in polarized light

For a NW illuminated with light, the change in the absorbed EM energy can be ascribed to a change in the electric field distribution inside the NW since the volumetric rate of absorbed EM energy scales as $\mid E \mid^2$ in a non magnetic media. Thus any polarization dependence in the absorption efficiency must reflect the ability of the electric field to penetrate in the body of the NW. Under an applied external electric field, the bond charges to the silicon nuclei will move from their common "center of gravity" to give rise with the charged nucleus to a dipole and a macroscopic polarization P. Since in the nature the effect goes against its cause, this polarization and its associated electric field, the so called depolarization field, tend to decrease the magnitude of the total electric field strength in the dielectric. It can be shown that the continuity of the tangential component of the EM fields across a boundary of discontinuity is a sufficient condition for energy conservation across that boundary[**55**]. In other words, we have at the boundary $[\mathbf{E}_2 - \mathbf{E}_1] \times \mathbf{n} = \mathbf{0}$ and $[\mathbf{H}_2 - \mathbf{H}_1] \times \mathbf{n} = \mathbf{0}$, where 1 and 2 stand for the two media on both sides of the boundary and **n** is the unit vector normal to the surface. For TE excitation, the electric field has a tangential and radial component. As a result, the condition for conservation of energy at the boundary can sustain a discontinuity in the electric field arising from a depolarization field associated with a radial polarization of the material **P** and surface charge density $\sigma_b = \mathbf{P}.\mathbf{n}$. The ability to build a polarization upon an applied external electric field is material dependent and is directly related to the dielectric constant of the material under study, so that the magnitude of the field depolarization can be intuitively connected to the dielectric mismatch at the boundary. In the TM excitation on the contrary, the electric field is always tangential to the boundary so that no field discontinuity can be observed radially. Since in the volume the bound charge density is $\rho_b = -\nabla . \mathbf{P}$, a constant and non zero bound charge density would make the polarization diverging across the wire axis, leading to the conclusion that the bound charge density must be zero and **P** must be constant. The bound charges will be observed only on both ends of the NW and will generate a negligible depolarization field, contrary to the TE case where the bound charges on the wire sidewalls build a considerably higher depolarization field. The Fig 9.3.4 illustrates the drastically different field patterns that we calculated for a 200 nm diameter Si NW in the TE and TM polarizations. We see that for TM excitation no discontinuity can be observed, unlike for the TE field where one can easily localize the regions of high surface charge density. Note the values for the field maxima (the electric field strength of the incoming plane wave has been set at 1 $V.m^{-1}$ for both plots and the light comes from the right side) with a threefold decrease in term of $\mid E \mid^2$ between TM and TE cases.

Bibliography

[1] Survey of energy resources. Technical report, World Energy Council and London, 2010. Accessed: 20/08/2012. 11

[2] M. G. Thomas, H. N. Post, and R. Deblasio. Photovoltaic systems: an end-of-millennium review. *Progress in Photovoltaics: Research and Applications*, 7(1):1--19, 1999. 11

[3] H. Chan, S. B. Riffat, and J. Zhu. Review of passive solar heating and cooling technologies. *Renewable and Sustainable Energy Reviews*, 14(2):781 -- 789, 2010. 11

[4] A. Yilanci, I. Dincer, and H.K. Ozturk. A review on solar-hydrogen/fuel cell hybrid energy systems for stationary applications. *Progress in Energy and Combustion Science*, 35(3):231 -- 244, 2009. 11

[5] W. Shockley and H. J. Queisser. Detailed balance limit of efficiency of p-n junction solar cells. *Journal of Applied Physics*, 32(3):510--519, 1961. 12

[6] C.Y. Kuo and C. Gau. Vapor–solid–solid growth of crystalline silicon nanowires using anodic aluminum oxide template. *Thin Solid Films*, 519(11):3603, 2011. 15

[7] V. Sivakov, G. Andrä, A. Gawlik, A. Berger, J. Plentz, F. Falk, and S. H. Christiansen. Silicon nanowire-based solar cells on glass: Synthesis and optical properties, and cell parameters. *Nano Letters*, 9(4):1549, 2009. 17

[8] M. Kim, Y. Park, I. Kim, T. Park, Y. Sung, and H. Choi. Self-catalytic growth of silicon nanowires on stainless steel. *Materials Letters*, 64(21):2306, 2010. 17

[9] A. M. Morales. A laser ablation method for the synthesis of crystalline semiconductor nanowires. *Science*, 279(5348):208, 1998. 17, 18

[10] Y. Cui, X. Duan, J. Hu, and C. M. Lieber. Doping and electrical transport in silicon nanowires. *The Journal of Physical Chemistry B*, 104(22):5213--5216, 2000. 18, 33

[11] X. B. Zeng, X. B. Liao, B. Wang, S. T. Dai, Y. Y. Xu, Z. H. Hu X. B. Xiang, H. W. Diao, and G. L. Kong. Optical properties of boron-doped si nanowires. *Journal of Crystal Growth*, 265(1-2):94, 2004. 18

[12] K. Lew, L. Pan, T. E. Bogart, S. M. Dilts, E. C. Dickey, Y. Wang J. M. Redwing, M. Cabassi, T. S. Mayer, and S. W. Novak. Structural and electrical properties of trimethylboron-doped silicon nanowires. *Applied Physics Letters*, 85(15):3101, 2004. 18, 19, 33

[13] S. Chung, J. Yu, and J. R. Heath. Silicon nanowire devices. *Applied Physics Letters*, 76(15):2068, 2000. 18

[14] P. Gentile, A. Solanki, N. Pauc, F. Oehler, B. Salem, G. Rosaz, T. Baron, M. Den Hertog, and V. Calvo. Effect of hcl on the doping and shape control of silicon nanowires. *Nanotechnology*, 23(21):215702, 2012. 19, 33, 36, 37, 42

[15] L. J. Lauhon, M. S. Gudiksen, D. Wang, and C. M. Lieber. Epitaxial core–shell and core–multishell nanowire heterostructures. *Nature*, 420(6911):57, 2002. 19, 20, 33

[16] E. C. Garnett and P. Yang. Silicon nanowire radial p–n junction solar cells. *Journal of the American Chemical Society*, 130(29):9224, 2008. 19, 20

[17] E. C. Garnett, M. L. Brongersma, Y. Cui, and M. D. McGehee. Nanowire solar cells. *Annual Review of Materials Research*, 41(1):269, 2011. 19, 22, 23

[18] T. J. Kempa, J. F. Cahoon, S. Kim, R. W. Day, D. C. Bell, H. Park, and C. M. Lieber. Coaxial multishell nanowires with high-quality electronic interfaces and tunable optical cavities for ultrathin photovoltaics. *Proc Natl Acad Sci U S A*, 109(5):1407--1412, 2012. 19, 20, 21, 114

[19] T. J. Kempa, B. Tian, D. R. Kim, J. Hu, X. Zheng, and C. M. Lieber. Single and tandem axial p-i-n nanowire photovoltaic devices. *Nano Letters*, 8(10):3456, 2008. 20

[20] B. Tian, X. Zheng, T. J. Kempa, Y. Fang, N. Yu, G. Yu, J. Huang, and C. M. Lieber. Coaxial silicon nanowires as solar cells and nanoelectronic power sources. *Nature*, 449(7164):885, 2007. 20, 83

[21] M. D. Kelzenberg, D. B. Turner-Evans, B. M. Kayes, M. C. Putnam M. A. Filler, N. S. Lewis, and H. A. Atwater. Photovoltaic measurements in single-nanowire silicon solar cells. *Nano Letters*, 8(2):710, 2008. 20, 21, 71, 83

[22] L. Cao, J. S. White, J. Park, J. A. Schuller, B. M. Clemens, and M. L. Brongersma. Engineering light absorption in semiconductor nanowire devices. *Nat Mater*, 8(8):643--647, 2009. 20, 21, 83, 103, 149

[23] L. Cao, P. Fan, A. P. Vasudev, J. S. White, Z. Yu, W. Cai, J. A. Schuller, S. Fan, and M. L. Brongersma. Semiconductor nanowire optical antenna solar absorbers. *Nano Lett*, 10(2):439--445, 2010. 20, 83, 103

[24] L. Hu and G. Chen. Analysis of optical absorption in silicon nanowire arrays for photovoltaic applications. *Nano Letters*, 7(11):3249, 2007. 23

[25] Th Stelzner, M. Pietsch, G. Andrä, F. Falk, E. Ose, and S. Christiansen. Silicon nanowire-based solar cells. *Nanotechnology*, 19(29):295203, 2008. 23

[26] E. Garnett and P. Yang. Light trapping in silicon nanowire solar cells. *Nano Letters*, 10(3):1082, 2010. 22

[27] L. Pan, K. Lew, J. M. Redwing, and E. C. Dickey. Effect of diborane on the microstructure of boron-doped silicon nanowires. *Journal of Crystal Growth*, 277(1–4):428 -- 436, 2005. 33, 34, 35, 38

[28] P. Madras, E. Dailey, and J. Drucker. Spreading of liquid ausi on vapor–liquid–solid-grown si nanowires. *Nano Letters*, 10(5):1759, 2010. 33, 35

[29] F. Oehler, P. Gentile, T. Baron, M. Den Hertog, J. Rouvière, and P. Ferret. The morphology of silicon nanowires grown in the presence of trimethylaluminium. *Nanotechnology*, 20(24):245602, 2009. 33

[30] V. Schmidt, J. V. Wittemann, and U. Gosele. Growth and thermodynamics and and electrical properties of silicon nanowires. *Chemical Reviews*, 110(1):361, 2010. 33

[31] Y. Wang, K. Lew, T. Ho, L. Pan, S. W. Novak, E. C. Dickey, J. M. Redwing, and T. S. Mayer. Use of phosphine as an n-type dopant source for vapor–liquid–solid growth of silicon nanowires. *Nano Letters*, 5(11):2139, 2005. 34, 60

[32] F. Li, P. D. Nellist, and D. J. H. Cockayne. Doping-dependent nanofaceting on silicon nanowire surfaces. *Applied Physics Letters*, 94(26):263111, 2009. 34, 35

[33] C. Wiethoff, F. M. Ross, M. Copel, M. H. Hoegen, and F. J. M. Heringdorf. Au stabilization and coverage of sawtooth facets on si nanowires grown by vapor−liquid−solid epitaxy. *Nano Letters*, 8(9):3065, 2008. 34

[34] H. Schmid, M. T. Bjork, J. Knoch, S. Karg, H. Riel, and W. Riess. Doping limits of grown in situ doped silicon nanowires using phosphine. *Nano Letters*, 9(1):173--177, 2009. 35, 60

[35] F. Oehler, P. Gentile, T. Baron, and P. Ferret. The effects of hcl on silicon nanowire growth: surface chlorination and existence of a 'diffusion-limited minimum diameter'. *Nanotechnology*, 20(47):475307, 2009. 36, 37, 49

[36] D. E. Perea, J. E. Allen, S. J. May, B. W. Wessels, D. N. Seidman, and L. J. Lauhon. Three-dimensional nanoscale composition mapping of semiconductor nanowires. *Nano Letters*, 6(2):181, 2006. 45, 52, 54

[37] E. Koren, N. Berkovitch, and Y. Rosenwaks. Measurement of active dopant distribution and diffusion in individual silicon nanowires. *Nano Letters*, 10(4):1163, 2010. 45, 49, 54

[38] P. Xie, Y. Hu, Y. Fang, J. Huang, and C. M. Lieber. Diameter-dependent dopant location in silicon and germanium nanowires. *Proceedings of the National Academy of Sciences*, 106(36):15254, 2009. 49, 52, 54

[39] X. Ou, N. Geyer, R. Kogler, P. Werner, and W. Skorupa. Acceptor deactivation in individual silicon nanowires: From thick to ultrathin. *Applied Physics Letters*, 98(25):253103, 2011. 52

[40] M. T. Björk, H. Schmid, J. Knoch, H. Riel, and W. Riess. Donor deactivation in silicon nanostructures. *Nature Nanotechnology*, 4(2):103, 2009. 52

[41] E. C. Garnett, Y. Tseng, D. R. Khanal, J. Wu, J. Bokor, and P. Yang. Dopant profiling and surface analysis of silicon nanowires using capacitance–voltage measurements. *Nature Nanotechnology*, 4(5):311, 2009. 52

[42] M. Diarra, Y. Niquet, C. Delerue, and G. Allan. Ionization energy of donor and acceptor impurities in semiconductor nanowires: Importance of dielectric confinement. *Physical Review B*, 75(4), 2007. 52, 55

[43] V. Schmidt, S. Senz, and U. Gösele. Influence of the si/sio2 interface on the charge carrier density of si nanowires. *Applied Physics A*, 86(2):187, 2006. 52, 56

[44] K. Seo, S. Sharma, A. A. Yasseri, D. R. Stewart, and T. I. Kamins. Surface charge density of unpassivated and passivated metal-catalyzed silicon nanowires. *Electrochemical and Solid-State Letters*, 9(3):G69, 2006. 52, 56

[45] S. Jin, M. V. Fischetti, and T. Tang. Modeling of electron mobility in gated silicon nanowires at room temperature: Surface roughness scattering and dielectric screening, and band nonparabolicity. *Journal of Applied Physics*, 102(8):083715, 2007. 54

[46] E. B. Ramayya, D. Vasileska, S. M. Goodnick, and I. Knezevic. Electron transport in silicon nanowires: The role of acoustic phonon confinement and surface roughness scattering. *Journal of Applied Physics*, 104(6):063711, 2008. 54

[47] T. Hiramoto, M. Saitoh, and G. Tsutsui. Emerging nanoscale silicon devices taking advantage of nanostructure physics. *IBM Journal of Research and Development*, 50(4.5):411, 2006. 54

[48] S. M. Sze. *Physics of semiconductor devices*. Wiley, 2 edition, 1981. 65

[49] A.N. Saxena. Forward current-voltage characteristics of schottky barriers on n-type silicon. *Surface Science*, 13(1):151 -- 171, 1969. 65

[50] O. Demichel, V. Calvo, A. Besson, P. Noé, B. Salem, N. Pauc, F. Oehler, P. Gentile, and N. Magnea. Surface recombination velocity measurements of efficiently passivated gold-catalyzed silicon nanowires by a new optical method. *Nano Letters*, 10(7):2323, 2010. 72

[51] L. Cao, P. Fan, E. S. Barnard, A. M. Brown, and M. L. Brongersma. Tuning the color of silicon nanostructures. *Nano Lett*, 10(7):2649--2654, 2010. 83

[52] G. Bronstrup, N. Jahr, C. Leiterer, A. Csáki, W. Fritzsche, and S. Christiansen. Optical properties of individual silicon nanowires for photonic devices. *ACS Nano*, 4(12):7113, 2010. 83

[53] W. F. Liu, J. I. Oh, and W. Z. Shen. Light trapping in single coaxial nanowires for photovoltaic applications. *IEEE Electron Device Letters*, 32(1):45, 2011. 84

[54] J. Nelson. *The Physics of Solar Cells*. Imperial College Press, London U.K, 2003. 84

[55] C. F. Bohren. and D. R. Huffman. *Absorption and scattering of light by small particles*. Wiley, New York, 1983. 94, 96, 103, 177

[56] R. G. Newton. Optical theorem and beyond. *American Journal of Physics*, 44(7):639, 1976. 94

[57] L. Cao, J. Park, P. Fan, B. Clemens, and M. L. Brongersma. Resonant germanium nanoantenna photodetectors. *Nano Lett*, 10(4):1229--1233, 2010. 103, 149

[58] G. F. Burkhard, E. T. Hoke, and M. D. McGehee. Accounting for interference and scattering and and electrode absorption to make accurate internal quantum efficiency measurements in organic and other thin solar cells. *Advanced Materials*, 22(30):3293, 2010. 103, 104

[59] Thin film calculate. `http://www.stanford.edu/group/mcgehee/transfermatrix/`. Accessed: 24/09/2012. 103, 104

[60] M. D. Kelzenberg, D. B. Turner-Evans, B. M. Kayes, M. A. Filler, M. C. Putnam, N. S. Lewis, and H. A. Atwater. Photovoltaic measurements in single-nanowire silicon solar cells. *Nano Lett*, 8(2):710--714, 2008. 105

[61] G. Brönstrup, N. Jahr, C. Leiterer, A. Csáki, W. Fritzsche, and S. Christiansen. Optical properties of individual silicon nanowires for photonic devices. *ACS Nano*, 4(12):7113--7122, 2010. 106

[62] J. K. Hyun and L. J. Lauhon. Spatially resolved plasmonically enhanced photocurrent from au nanoparticles on a si nanowire. *Nano Letters*, 11(7):2731, 2011. 111

[63] L. Cao, P. Fan, and M. L. Brongersma. Optical coupling of deep-subwavelength semiconductor nanowires. *Nano Lett*, 11(4):1463--1468, 2011. 114

[64] A. Mavrokefalos, S. E. Han, S. Yerci, M. S. Branham, and G. Chen. Efficient light trapping in inverted nanopyramid thin crystalline silicon membranes for solar cell applications. *Nano Letters*, 12(6):2792, 2012. 114, 118

[65] W. Soppe, H. Rieffe, and A. Weeber. Bulk and surface passivation of silicon solar cells accomplished by silicon nitride deposited on industrial scale by microwave pecvd. *Progress in Photovoltaics: Research and Applications*, 13(7):551, 2005. 114

[66] M. Kerker and E. Matijević. Scattering of electromagnetic waves from concentric infinite cylinders. *Journal of the Optical Society of America*, 51(5):506, 1961. 116

[67] H. Nagel, A. G. Aberle, and R. Hezel. Optimised antireflection coatings for planar silicon solar cells using remote pecvd silicon nitride and porous silicon dioxide. *Progress in Photovoltaics: Research and Applications*, 7(4):245, 1999. 118

[68] W. F. Liu, J. I. Oh, and W. Z. Shen. Light absorption mechanism in single c-si (core)/a-si (shell) coaxial nanowires. *Nanotechnology*, 22(12):125705, 2011. 127, 131

[69] W. F. Liu, J. I. Oh, and W. Z. Shen. Light trapping in single coaxial nanowires for photovoltaic applications. 32(1):45--47, 2011. 127, 131

[70] Y. Yu, V. E. Ferry, A. P. Alivisatos, and L. Cao. Dielectric core-shell optical antennas for strong solar absorption enhancement. *Nano Lett*, 12(7):3674--3681, 2012. 127, 131

[71] W. Q. Xie, W. F. Liu, J. I. Oh, and W. Z. Shen. Optical absorption in c-si/a-si:h core/shell nanowire arrays for photovoltaic applications. *Applied Physics Letters*, 99(3):033107, 2011. 133

[72] Y. Dan, K. Seo, K. Takei, J. H. Meza, A. Javey, and K. B. Crozier. Dramatic reduction of surface recombination by in situ surface passivation of silicon nanowires. *Nano Letters*, 11(6):2527, 2011. 133

[73] M. M. Adachi, M. P. Anantram, and K. S. Karim. Optical properties of crystalline−amorphous core−shell silicon nanowires. *Nano Letters*, 10(10):4093, 2010. 133

[74] J. Liu, X. Sun, L. C. Kimerling, and J. Michel. Direct-gap optical gain of ge on si at room temperature. *Optics Letters*, 34(11):1738, 2009. 149

[75] F. Oehler. *Etude et compréhension des mécanismes de croissance catalysés des nanofils de silicium obtenus par Dépôt Chimique en phase Vapeur*. PhD thesis, University de Grenoble, 2010. 153

[76] P.t.a grenoble. `http://www.ptagrenoble.fr`. Accessed: 20/08/2012. 159

[77] K. Imamura, M. Takahashi, Asuha, Y. Hirayama, S. Imai, and H. Kobayashi. Nitric acid oxidation of si method at 120 °c: Hno3 concentration dependence. *Journal of Applied Physics*, 107(5):054503, 2010. 164

[78] T. Matsumoto, Asuha, W.-B. Kim, M. Yamada, S. Imai, S. Terakawa, and H. Kobayashi. Low temperature formation of sio2 thin films by nitric acid oxidation of si (naos) and application to thin film transistor (tft). *Microelectronic Engineering*, 86(7–9):1939 -- 1941, 2009. 164

[79] Ebic overview. `http://www.pointelectronic.de/produkte/diss5-ebic.html`. Accessed: 24/09/2012. 171, 172

[80] K. Seo, S. Sharma, A. A. Yasseri, D. R. Stewart, and T. I. Kamins. Surface charge density of unpassivated and passivated metal-catalyzed silicon nanowires. *Electrochemical and Solid-State Letters*, 9(3):G69, 2006. 173

[81] B. van Zeghbroeck. *Principles of Semiconductor Devices*. 2007. 174

List of Publications

Articles.

A. Solanki, P. Gentile, V. Calvo, G. Rosaz, B. Salem, V. Aimez, D. Drouin, and N. Pauc. Geometrical control of photocurrent in active Si nanowire devices. *Nano Energy* 1(5):714, 2012.

P. Gentile, A. Solanki, N. Pauc, F. Oehler, B. Salem, G. Rosaz, T. Baron, M. Den Hertog, and V. Calvo. Effect of HCl on the doping and shape control of silicon nanowires. *Nanotechnology* 23(21):215702, 2012.

L. Dupré, D. Buttard, P. Gentile, N. Pauc, and A. Solanki. High density core-shell silicon nanowire array for the realization of third generation solar cell. *Energy Procedia*, 10:33, 2011.

Oral Presentations.

N. Pauc, B. Salem, P. Gentile, T. Baron, V. Calvo, F. Oehler, O. Demichel, G. Rosaz, and A. Solanki. Mesures électriques sur nanofils : aspects physiques et technologiques. *GDR* Rouen, 2010.

A. Solanki, N. Pauc, P. Gentile, V. Calvo, G. Rosaz, B. Salem, V. Aimez, D. Drouin, and N. Magnea. Light absorption and carrier diffusion in single Si nanowires studied via microphotocurrent spectroscopy and electron beam induced current. *E-MRS Nice*, 2011.

A. Solanki, N. Pauc, P. Gentile, V. Calvo, G. Rosaz, B. Salem, V. Aimez, D. Drouin, and N. Magnea. Light absorption and carrier diffusion in single Si nanowires studied via microphotocurrent spectroscopy and electron beam induced current. *GDR* Villeneuve d'Ascq, 2011.

A. Solanki, N. Pauc, P. Gentile, V. Calvo, G. Rosaz, B. Salem, V. Aimez, D. Drouin, and N. Magnea. Influence of the dielectric environment in the absorption properties of single silicon nanowires. *GDR* Porquerolles, 2011.

A. Solanki, N. Pauc, P. Gentile, V. Calvo, G. Rosaz, B. Salem, V. Aimez, D. Drouin, and N. Magnea. Influence of the dielectric environment in the absorption properties of single silicon nanowires. *E-MRS* Strasbourg 2012.

A. Solanki, N. Pauc, P. Gentile, V. Calvo, G. Rosaz, B. Salem, V. Aimez, D. Drouin, and N. Magnea. Influence of the dielectric environment in the absorption properties of single silicon nanowires. *ICSNN* Dresden 2012.

A. Solanki, N. Pauc, P. Gentile, V. Calvo, G. Rosaz, B. Salem, V. Aimez, D. Drouin, and N. Magnea. Size and Dielectric Coating Induced Optical Absorption Enhancement in Silicon Nanowires. *MRS* Boston 2012.

Abstract. In this work we present the characterization of the light absorption properties of single silicon NWs (NW) using photocurrent spectroscopy along with the preliminary work done at the wire scale to characterize the dopant incorporation and the fabrication of junctions. First, we start with a description of the growth methods used to synthesize active NW's for photocurrent generation, with results obtained on the use of hydrogen chloride in the CVD VLS growth of doped NWs. This method offers highly straight structures, widened process temperatures allowing in particular very efficient boron incorporation—ionized acceptors densities up to 1.8E19 cm^{-3}—and inhibited gold diffusion, thereby greatly reducing elemental contamination from the catalyst. Focus is made on the junction formation, the study of its electrical characteristics and the influence of morphological parameters—radius, axial position—to obtain the desired doping properties. In a second part, we present the photocurrent response of a set of different diameter active Si NWs and correlate our results with an analytical treatment of the photon absorption at the nanoscale using the Lorentz Mie theory adapted to the cylindrical geometry under study. Very good agreement is found between experiment and theory for both polarization spectra (TE-TM). Absorption resonances are resolved, corresponding to leak resonant modes, and can display absorption efficiencies higher than one, making downscaling an efficient tool to increase energy harvesting capabilities. In a last part, we adapt the antireflective coating strategy used in solar cells to improve the coupling of the incoming light to Si NWs. For this, SiO2 and Si3N4 films are deposited on NWs using PECVD, providing a set of structures coated with a high level of conformity. Based on the new set of spectra we obtain the relative gain curves and compare them with analytical calculations specifically derived for getting the absorption in the core of coaxial nanocylinders only, which allows estimating the magnitude of the absorbed energy in the dielectric shell.

Keywords: Nanowires, Photovoltaics, Mie theory, Dielectric, Light absorption, Photocurrent

Résumé. Ce travail présente la caractérisation des propriétés d'absorption de lumière par des nanofils uniques (NF) de silicium en utilisant la spectroscopie de photocourant, ainsi qu'une étude préliminaire des processus d'incorporation des dopants et de réalisation de jonctions dans les NFs. Tout d'abord, nous commençons par décrire les méthodes de croissance utilisées pour synthétiser des NFs actifs pour la génération de photocourant, avec l'utilisation du chlorure d'hydrogène dans les procédés classiques de croissance CVD catalysée or de fils dopés. Cette méthode offre des structures très faiblement coniques, élargit les températures de procédé, permettant en particulier d'incorporer très efficacement le bore, avec des densités d'accepteurs ionisés allant jusqu'à 1.8E19 cm^{-3}, tout en inhibant la diffusion d'or depuis le catalyseur. L'attention est ensuite portée à la fabrication de jonctions, l'étude de ses caractéristiques électriques, ainsi que sur l'influence de paramètres morphologiques (rayon, position axiale) du fil sur sa résistivité apparente. Dans une seconde partie, nous étudions la réponse en photocourant d'un jeu de NFs actifs de différents diamètres et corrélons nos résultats à un traitement analytique de l'absorption des photons à l'échelle du nano objet dans le cadre de la théorie de Mie adaptée au cas cylindrique. L'accord expérience-théorie est très bon pour les deux polarisations (TE-TM). Des résonances dans le spectre d'absorption sont mises en évidence, correspondant à l'excitation de modes propres du fil, et associées à des sections efficaces d'absorption pouvant être supérieures à l'unité. Dans une dernière partie, nous adaptons la stratégie de dépôt antireflet utilisée dans les cellules solaires pour améliorer le couplage de la lumière incidente aux NFs. Pour cela, des dépôts de SiO_2 et Si_3N_4 sont réalisés sur des NFs via la technique de PECVD, nous fournissant par là-même un jeu de structures pourvues d'un dépôt de diélectrique à haute conformité. Se basant sur les spectres d'absorption ainsi acquis, nous obtenons les gains relatifs d'absorption induits par le dépôt de diélectrique et les comparons aux calculs analytiques développés spécifiquement pour obtenir l'absorption dans le cœur seulement du cylindre coaxial, ceci nous permettant également d'estimer la partie du rayonnement incident absorbé dans la coquille diélectrique.

Keywords: Nanofils, Photovoltaïque, Théorie de Mie, Diélectriques, Absorption de la lumière, Photocourant